DTU Physics
Department of Physics

High Resolution Three Dimensional X-ray Microscopy
Simulations & Experiments

PhD Thesis

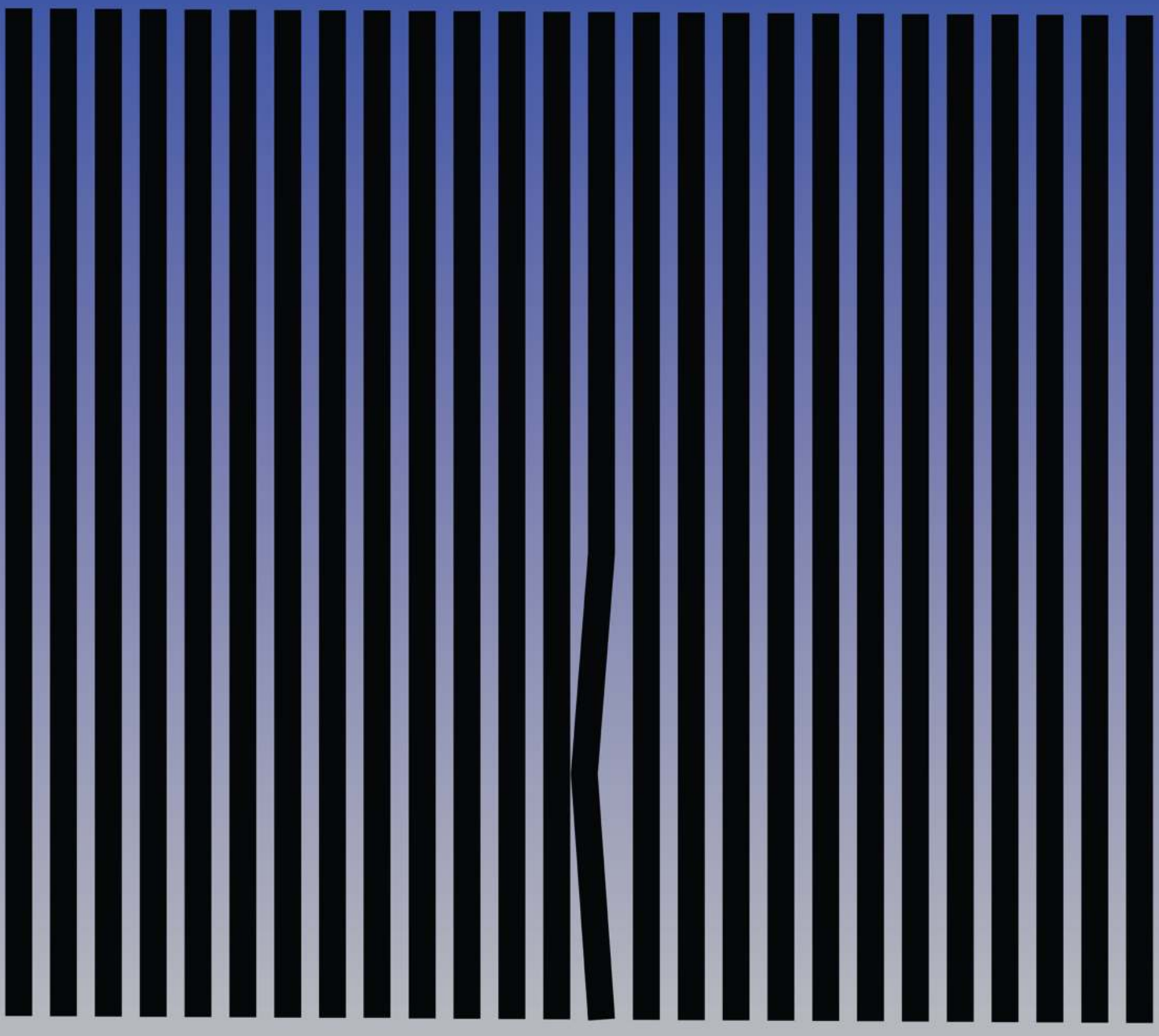

High Resolution Three Dimensional X-ray Microscopy
Simulations & Experiments

PhD Thesis
June, 2021

By
Mustafacan Kutsal

Copyright: Reproduction of this publication in whole or in part must include the customary bibliographic citation, including author attribution, report title, etc.
Cover art: *Untitled*, Sinan Cem Kızıl, 2020
Published by: DTU, Department of Physics, Fysikvej, Building 307, 2800 Kgs. Lyngby Denmark
www.fysik.dtu.dk
ISSN: [0000-0000] (electronic version)
ISBN: [000-00-0000-000-0] (electronic version)

ISSN: [0000-0000] (printed version)
ISBN: [000-00-0000-000-0] (printed version)

Approval

This thesis has been prepared over three years at the Section for Neutrons and X-rays for Materials Physics, Department of Physics, at the Technical University of Denmark, DTU, in partial fulfilment for the degree Doctorate in Philosophy, PhD. The project was supervised by Prof. Henning Poulsen of Department of Physics at the Technical University of Denmark and Dr. Carsten Detlefs of European Synchrotron Radiation Facility.

Mustafacan Kutsal
Kongens Lyngby, Denmark, June 30th, 2021

Mustafacan Kutsal - s176523

.....

Signature

.....

Date

Abstract

Deformation processing of metallic materials is one of the key routes for the production of industrial and consumer goods. The control of the microstructural evolution is essential for optimization of the materials' service performance. Therefore, the characterization of the deformed microstructures has a key role to play in the understanding and subsequently the improvement of these materials. Optical and electron microscopy techniques have been the dominant methods for mapping microstructures. However, these methods probe the (near-)surface only. For these methods, 3D information can be reached by serial sectioning, but the destruction of the sample limits their use to static studies.

Owing to their high penetration, X-ray microscopy techniques offer an alternative non-destructive route for volumetric characterization of materials. The development of three dimensional X-ray diffraction (3DXRD) microscopy created a new paradigm for 3D mapping of grain ensembles with spatial and angular resolutions of $2-10\,\mu$m and $0.01-1\,^{\circ}$, respectively. The reconstructed data provide a detailed 3D-EBSD type map of the microstructure, identifying the local orientation, the spatial position and shape of grains and their lattice parameters.

Deformation microstructures are hierarchical structures that spans from μ m-sized grains to atom-sized crystal defects. Specifically, the deformation transforms an ideally strain-free grain structure into a banded microstructure of $\approx 1\,\mu$m-sized crystallites called cells, or *subgrains*. Furthermore, the structure is locally heavily textured. Therefore, a high angular resolution is required for differentiating the individual subgrains. Existing 3DXRD methods fail to meet both the requirement to spatial and angular resolution.

In order to enable in situ 3D mapping of deformed microstructures within representative volumes, in this thesis, I present work towards establishing a new *high resolution* modality for 3DXRD, HR-3DXRD, with a 10 times superior spatial and angular resolution.

HR-3DXRD is based on several concepts, that are novel in connection with 3DXRD.

- Diffraction information acquired at an intermediate sample-to-detector distance, $\boldsymbol{L}$,
- The use of a large (virtual) compound detector with a relation between pixel size and field-of-view (FoV) that is much larger than what is commercially available,
- 3D mapping of sub-micrometer objects by means of a tessellation algorithm, requiring only the registration of the center-of-mass (CoM) and integrated intensity of diffraction spots.

Full scale numerical simulations of HR-3DXRD on phantoms representative of deformed microstructures reveal that diffraction spot densities are not prohibitive, and that indexing is possible. Moreover, while much outside of the range of applicability they were created for, existing 3DXRD indexing algorithms can be adapted to HR-3DXRD. The resulting 3D maps are space-filling and exhibit a spatial and angular resolution of $0.1\,\mu$m and 2×10^{-5} degrees. The main limitation is shown to be the signal-to-noise ratio.

A main challenge of HR-3DXRD is the generation of the compound image, from a series of partial diffraction images, acquired at different positions of the 2D detector. It is shown that pattern recognition and stitching algorithms can provide the required sub-pixel accuracy.

Five experimental tests have been performed, all using *ad hoc* set-ups in four different grain-mapping beamlines. The main sources for degradation of the quality of mapping are identified and remedies suggested. Preliminary results are presented for indexing and grain maps on one of the systems.

Acknowledgements

This PhD project has been supervised by Prof. Henning F. Poulsen of DTU Physics and Dr. Carsten Detlefs of European Synchrotron Radiation Facility. I would like to express my sincerest gratitude to my supervisors for their guidance and encouragement about the thesis studies, but also for their vast kindness and understanding, as well. Also, I'd like to further thank Prof. Poulsen and Dr. Detlefs for their incredible help and leadership in the many synchrotron experiments performed during the span of this thesis work. Your enthusiasm and countless advice will always inspire me; not only for becoming a better scientist, but also for being a better human being too. In the last year of the PhD studies, Prof. Grethe Winther of DTU Mechanical Engineering and Dr. Henning O. Sørensen of DTU Physics has joined the supervision team for the numerical simulations work. I would like to present my deepest gratitude for their immense help and support about the work.

I would like to acknowledge the travel supports from European Synchrotron Radiation Facility and DanScatt. I would like to further acknowledge European Synchrotron Radiation Facility, Advanced Photon Source and Deutsches Elektronen-Synchrotron for provision of beamtimes in ID11 and ID06, 1-ID-E, and P21.2, respectively. Furthermore, I would like to acknowledge the contributions of all the beamline scientist in the mentioned experimental stations. Also, I would like to acknowledge Jérôme Kieffer of European Synchrotron Radiation Facility for his great help in the preparation of the multi-panel calibration tool.

In the first half of the project, I got the become a part of ESRF's ID06-Hard X-Ray Microscope beamline team with Carsten Detlefs, Philip K. Cook, Can Yıldırım. I would like to say that it was a huge honor to work side-by-side with such incredible scientist. I would like to thank them for everything that I've learned from them, their comradery through the stressful experiments and also for bearing with my rookie mistakes. Their good taste in music and all the laughter we had shared will always be pleasantly remembered.

I would like to thank Mario Beltran, Mariana Mar Lucas and Dirk Müter for their kind friendship through the dark and lonely winters of Denmark. I would also like to thank Hugh Simons, Jeppe Ormstrup, Ashley Bucsek, Sonja Rosenlund Ahl, José 'Tato' Xavier Sierra Trujillo, Leora Dresselhaus-Cooper and Helle Lynnerup Grunnet-Jepsen for their scientific discussions and various contributions for the PhD project.

Lastly, I would like to say that a tree flourishes not only with the sunlight it bathes in, but also through the nourishment it gets from the earth through its roots. As a human being, I could never have been completed this work without the nourishment I got from my personal "roots". This work could have never been completed without the devoted love, endless mental support and also selfless financial support of my dearest family; my grandparents Sevim & Esen İlhan Yücel and my parents Canan & Osman Kutsal. I think there are no words in any known language that could express the extent of my gratitude for their great support. Through thick and thin, they gave me the utmost courage to face all the struggles and more importantly, the will to survive them. Therefore, I would like to dedicate this work to my "roots" in this universe we are floating in, my dearests, and the brightest stars in my sky; to Sevim, Esen İlhan, Canan and Osman. I love you.

List of Publications

First author papers

- **Paper 1** M. Kutsal, P. Bernard, G. Berruyer, P.K. Cook, R. Hino, A.C. Jakobsen, W. Ludwig, J. Ormstrup, T. Roth, H. Simons, K. Smets, J.X. Sierra, J. Wade, P. Wattecamps, C. Yildirim, H.F. Poulsen, C. Detlefs, The ESRF dark-field x-ray microscope at ID06, IOP Conf. Ser. Mater. Sci. Eng. 580 (2019) 012007. https://doi.org/10.1088/1757-899X/580/1/012007.
- **Paper 2** M. Kutsal, H.F. Poulsen, G. Winther, H.O. Sørensen, C. Detlefs, High resolution 3DXRD: 3D mapping of deformed metal microstructures, (2020), *in preparation, to be submitted to Journal of Applied Crystallography*

Co-authored papers

- **Paper 3** H.F. Poulsen, P.K. Cook, H. Leemreize, A.F. Pedersen, C. Yildirim, M. Kutsal, A.C. Jakobsen, J.X. Trujillo, J. Ormstrup, C. Detlefs, Reciprocal space mapping and strain scanning using X-ray diffraction microscopy, J. Appl. Crystallogr. 51 (2018) 1428–1436. https://doi.org/10.1107/S1600576718011378.
- **Paper 4** N. Mavrikakis, C. Detlefs, P.K. Cook, M. Kutsal, A.P.C. Campos, M. Gauvin, P.R. Calvillo, W. Saikaly, R. Hubert, H.F. Poulsen, A. Vaugeois, H. Zapolsky, D. Mangelinck, M. Dumont, C. Yildirim, A multi-scale study of the interaction of Sn solutes with dislocations during static recovery in α-Fe, Acta Mater. 174 (2019) 92–104. https://doi.org/10.1016/j.actamat.2019.05.021.
- **Paper 5** J. Ormstrup, E. V. Østergaard, C. Detlefs, R.H. Mathiesen, C. Yildirim, M. Kutsal, P.K. Cook, Y. Watier, C. Cosculluela, H. Simons, Imaging microstructural dynamics and strain fields in electro-active materials in situ with dark field x-ray microscopy, Rev. Sci. Instrum. 91 (2020) 065103. https://doi.org/10.1063/1.5142319.
- **Paper 6** C. Yildirim, H. Vitoux, L.E. Dresselhaus-Marais, R. Steinmann, Y. Watier, P.K. Cook, M. Kutsal, C. Detlefs, Radiation furnace for synchrotron dark-field x-ray microscopy experiments, Rev. Sci. Instrum. 91 (2020) 065109. https://doi.org/10.1063/1.5141139.
- **Paper 7** K. Hlushko, J. Keckes, G. Ressel, J. Pörnbacher, W. Ecker, M. Kutsal, P.K. Cook, C. Detlefs, C. Yildirim, Dark-field X-ray microscopy reveals mosaicity and strain gradients across sub-surface TiC and TiN particles in steel matrix composites, Scr. Mater. 187 (2020) 402–406. https://doi.org/10.1016/j.scriptamat.2020.06.053.
- **Paper 8** L.E. Dresselhaus-Marais, G. Winther, M. Howard, A. Gonzalez, S.R. Breckling, C. Yildirim, P.K. Cook, M. Kutsal, H. Simons, C. Detlefs, J.H. Eggert, H.F. Poulsen, In-Situ Visualization of Long-Range Defect Interactions at the Edge of Melting, (*in print*, 2021).

Contents

1 Introduction

Deformation and subsequent heat treatment of metals and alloys has been a staple manufacturing route of commodities since the dawn of the human civilization. Throughout history, discoveries such as smelting and cold deformation processes induced widespread usage of metals and their alloys for the production of tools, from everyday items to machines of war. Despite its several thousand year old history, metallurgy topics (e.g. metal refinement/purification, casting, forming/shaping and alloy design) were long regarded as artisanal abilities under the general umbrella of faux-science, alchemy. Reaching the end of the 19^{th} century, the discoveries and advancements in physics and chemistry enabled metallurgy to contextualize the underlying factual information of such processes. With the turn of the 20^{th} century, metallurgy had gained a modern scientific understanding to its means of *techne* production in an epistemological manner.

Deformation processing of metals is one of the key routes for the production of commodities. Referencing the so-called *materials science tetrahedron*, the structure-performance relationship of deformation context has been started to draw attention with the introduction of optical microscopy (OM) characterization in the $18 - 19^{th}$ century. OM methods have enabled a new paradigm for understanding the structure of crystalline materials, as for the first time, OM provided a probe for studying the granular microstructure of polycrystals. Nowadays, OM characterization is a well-established technique for characterization of not deformation, but all microstructures in general. The discovery of X-ray diffraction (XRD) at the turn of the century sets another great milestone for the characterization of metals. The crystallographic information conveyed in XRD measurements have opened an atomistic paradigm for understanding the structure-performance relationship in metals and alloys.

During the 20^{th} century, XRD characterization of metals (or crystalline solids in general) had grown to become a go-to tool for studying structural changes. As a characterization technique, initial works with XRD had focused on crystal structure determination with white beam radiation. Later, developments on X-ray optics and detectors provided — now indispensable— tools for the production and detection of monochromatic radiation with adequate collimation. These developments led to powder diffraction-type studies of deformation microstructures, in which the substructure and strain measurements are developed through powder line analysis. In a similar time-span, electron diffraction and microscopy techniques become available for studying materials with spatial resolutions reaching the interplanar spacings in crystals. Starting from mid-60's, transmission electron microscopy (TEM) has proved to provide invaluable information through structural and scattering-wise characterization of the deformation microstructures.

The last decades of the 20^{th} century have witnessed two groundbreaking developments in materials characterization: the development of orientation imaging capabilities through electron backscatter diffraction (EBSD) mapping in scanning electron microscopes (SEM), and the emergence of highly brilliant synchrotron radiation sources. EBSD mapping relies on indexing of Kikuchi diffraction patterns obtained by raster scanning the surface of the sample. Such indexing allows determination of the orientation of each raster position. This enables fast orientation mapping of the surface microstructures in a readily available laboratory tool, SEM. The latter development provided production of X-rays flux in mm-to-μm sized cross-sections that is several orders-of-magnitude higher than the laboratory scale X-ray sources (e.g. cathode tubes, rotating anode, etc.). Comparing to reflection

based laboratory XRD routines (e.g. with Bragg-Brentano geometry), the high energy X-rays of high brilliance provided better X-ray penetration, therefore, enabling development of bulk sensitive X-ray scattering studies. The high brilliance further enabled X-ray imaging and microscopy methods for microstructure characterization. In late 1990's, the joint work between Risø Laboratory and European Synchrotron Radiation Facility (ESRF) led to the development of orientation imaging capabilities by making use of the high brilliance X-rays, called *three-dimensional X-ray diffraction microscopy, 3DXRD* (also called as *high energy diffraction microscopy, HEDM*). 3DXRD microscopy utilizes the spotty diffraction patterns from polycrystals. The three-dimensional (3D) mapping is done via assignment and subsequent refinement of the indexed diffraction spots to the found orientations. The indexing and refinement procedures determines the grains in the microstructure through their orientation, center-of-mass position in direct space and six lattice parameters. Owing to its unique capabilities, 3DXRD techniques have grew to become a competent tool for bulk characterization of crystalline microstructures in the last twenty years.

The chemical and/or topological ordering in most of the metallic microstructures occurs in three-dimensions. In this regards, the mentioned visible light or electron-based characterization techniques have three main downfalls: OM, TEM and SEM are surface sensitive techniques providing surface-limited 2D information about the microstructure. As a natural result, the 3D extension of these techniques require destructive processing of the sample surface, hence hindering their in situ characterization capabilities. Lastly, the metallurgical sample preparation methods for providing an adequate surface finish may alter the studied microstructure through surface relaxation. This may cause the structural features of interest to vanish, thus leading to inaccurate experimental observations.

The X-ray microscopy methods offer a new route for non-destructive characterization of microstructures. Specifically, 3DXRD and its modalities offer a non-destructive approach for orientation mapping of crystalline microstructures. The high penetration depth remedies the mentioned limitations of optical and electron microscopy techniques. Usually, 3DXRD techniques are performed with incident beams with thick cross-sections. Through stacking of such cross-sections, the complete orientation map of the sample can be obtained without damaging the microstructure of the studied sample. Secondly, 3DXRD experiments are performed with a rather simple experimental setup of collimating optics, a sample rotation stage and a detector. Such simple setup provides large spaces around the sample that can be utilized for various sample environments, therefore, enabling non-destructive in situ mapping of the microstructure. Lastly, 3DXRD experimentation require little to no sample preparation. This enables 3DXRD to study samples of with e.g. rough surface finish or irregular shapes within its regular usage.

Upon deformation, the grains in a metallic microstructures break down into mosaic pattern in multiple length-scales. In a generic deformed microstructure, the deformation is accumulated through linear defects mediating the deformation, called *dislocations*. These linear defects may form stochastic tangles or form extended 3D structures through the formation of intragranular boundaries. These banded intragranular microstructures may extend in deformation bands on the intergranular scale. Hence, the structuring of deformation microstructures span from atomic sized defects to μm or mm-sized bands.

Since their conception, orientation imaging with electron microscopy methods (TEM and SEM-EBSD) have been used as a central characterization tool for characterization of deformation microstructures. As mentioned above, the surface-limited sensitivity of such studies poses a bottleneck for the complete 3D characterization of these microstructures. In comparison, 3DXRD methods offer a non-destructive approach for volumetric map-

ping of deformation microstructures with bulk sensitivity. Over the last decade, 3DXRD experimentation has been adopted for visualization of deformation microstructures in multiple length-scales. However, the spatial and angular resolution dictated by the deformed microstructures have limited their use for complete characterization of the deformation processes.

Recently, the resolution problem of 3DXRD microscopy has started to pushed below the microstructural requirements through differing experimentation and analysis methods. However, in relation to plastic deformation, 3DXRD is inherently limited by a spatial resolution of $2\,\mu$m and the overlap of diffraction spots [1–3], caused by the fast multiplication of the number of subgrains with increasing external strain. In practice, 3DXRD mapping has not been successful beyond 20% deformation. The previous attempts of 3DXRD mapping of the deformation microstructures had presented only the local averages of the observables for each grain. Yet, these maps had provided no information about the constituents of the deformed microstructure, i.e. the subgrains. *Hence, as of today, there exists no non-destructive method that provides a visualisation of the plastically deformed metal microstructures within representative sample volumes at industrially relevant degrees of deformation of* $50\% - 90\%$ *and beyond.*

In previous works, it was shown that the diffracted intensity from subgrains is sufficient to be detected by a high resolution x-ray detector, if spot overlap can be avoided, and moreover that the subgrains themselves tend to be near-perfect single crystals [4, 5]. Inspired by these works, in this thesis I aim to design, optimize and demonstrate an X-ray mapping technique — and associated data analysis chain — that may visualize the subgrains in metals in 3D with a target resolution of 300 nm, and register their crystallographic orientation with a superior angular resolution of better than 10^{-3} degrees.

The method exploits the following concepts, that are novel in connection with 3DXRD:

- Diffraction information acquired at an intermediate distance, where high resolution in both direct and reciprocal space can be achieved.
- The use of a large (virtual) compound detector with a relation between pixel size and field-of-view that is 4 times what is commercially available.
- 3D mapping of sub-micrometer objects by means of a tessellation algorithm, requiring only the registration of the center-of-mass (CoM) and integrated intensity of diffraction spots.

At the outset of the Thesis, the main challenges were foreseen to be;

1. Potential use of existing software: The adequacy of using the existing simulation and analysis software dedicated for Mode-II CoM mapping[1] was not previously studied for HR-3DXRD-type experimental datasets.
2. Experimental configuration: The accuracy of the experimental parameters needed to achieve sub-micrometer precision for the analysis was unknown. Consequently, it was unclear if existing experimental setups were adequate for HR-3DXRD.
3. Indexing: The existing polycrystal indexing methods are not designed to handle the very small misorientations involved with HR-3DXRD.

[1] For definitions and details of 3DXRD modalities, including Mode-II CoM mapping, please refer to Section 2.2.1.

4. No existing synchrotron beamlines readily accommodated the specifications HR-3DXRD requires, implying that many details of the set-up including calibration aspects had to be designed from scratch and/or *ad hoc* during beamtime.
5. Implementation of hardware that accommodates the compound detector principle.

This thesis documents my work towards realizing HR-3DXRD. Due to the shutdown of ESRF lightsource during the last 1.5 years of my PhD project, the experimental part of the presented thesis was performed prior to completing the data analysis chain.

The thesis will start by introducing basic and key concepts in deformation microstructures in metals, and X-ray microscopy techniques with an emphasis on 3DXRD microscopy in Chapter 2. Then, in Chapter 3, the *high resolution* concept for 3DXRD will be introduced. Here, the experimental configuration will be given and it will be compared to the available 3DXRD methods. In Chapter 4, the limitations of HR-3DXRD will be explored through a series of numerical simulations. The chapter will conclude by presenting a numerical proof-of-concept study of HR-3DXRD with a physically representative phantom reflecting a common deformation substructure. The thesis will continue by presenting the efforts for experimental realization of HR-3DXRD in Chapter 5. Lastly, the thesis will conclude with Chapter 8, by presenting the outcomes and future plans regarding the study.

2 Background

This chapter will present state-of-the-art prior to introducing the *HR-3DXRD* technique. The chapter will begin with a focus on the material aspect by introducing a brief overview of deformation microstructures in metals and metallic alloys. Then, we will continue with the experimental aspects by discussing various X-ray microscopy techniques and their application on microstructural imaging, with a highlight on 3DXRD and its modalities.

The reader is assumed to have a basic knowledge on kinematical theory of X-ray diffraction and basics of synchrotron radiation sources in order to follow the presented information in this chapter. For further reading, please refer to [6] & [7], and [8] & [9], respectively.

2.1 Deformation microstructures

Plastic deformation of crystalline materials occurs through the accommodation of a minute portion of the exerted mechanical energy in the crystal lattice by creation and accumulation of defects of various dimensionality. These defects, e.g. point defects like vacancies or line defects such as dislocations, cause local discontinuities in the lattice, by which the exerted mechanical energy is stored. Further exertion of mechanical energy would pose these defects, dislocations, to move within the microstructure, leading to *plastic deformation* and development of the microstructure. The cross-interaction between the mobile and stationary dislocations can hinder the former's mobility along its path, in turn increasing the strength of the material. We should point out that the presence and mobility of the dislocations eases the plastic deformation. Hypothetically, the absence of dislocations would lead deformation to require forces that are orders of magnitude higher than what is actually observed.

This section aims to present the basic concepts in deformation and its microstructural implications in metals and alloys. The background section will introduce the basic concepts of stored energy and the linear defect of concern, dislocations, and its impact on the microstructure. Then, the section will finish with a brief review of the origins and organization of deformation microstructures and its evolution under the influence of thermal and mechanical forces.

2.1.1 Basic concepts in deformation microstructures

Plastic deformation of metals and alloys are categorized in regard to the absolute temperature of the processing; cold and hot deformation. As a rule of thumb, the process is called cold deformation if the absolute processing temperature is below 60% of the material's absolute melting temperature, $T < 0.6T_m$, and vice versa for the hot deformation. Such distinction can be made, as it is known that the kinetic activity of the microstructure (i.e. mobility of microstructural features, such as defects) is a direct function of homologous temperature, $\frac{T}{T_m}$. For the sake of clarity, the following text will focus on cold deformation and its related microstructures.

As mentioned above, some of the energy exerted to the material during plastic deformation process is accumulated in the crystal lattice. From a thermodynamic perspective, the internal energy change of the microstructure upon plastic deformation can be explained with the first law of thermodynamics [10],

$$\Delta \boldsymbol{U} = \boldsymbol{W} + \boldsymbol{Q} \tag{2.1}$$

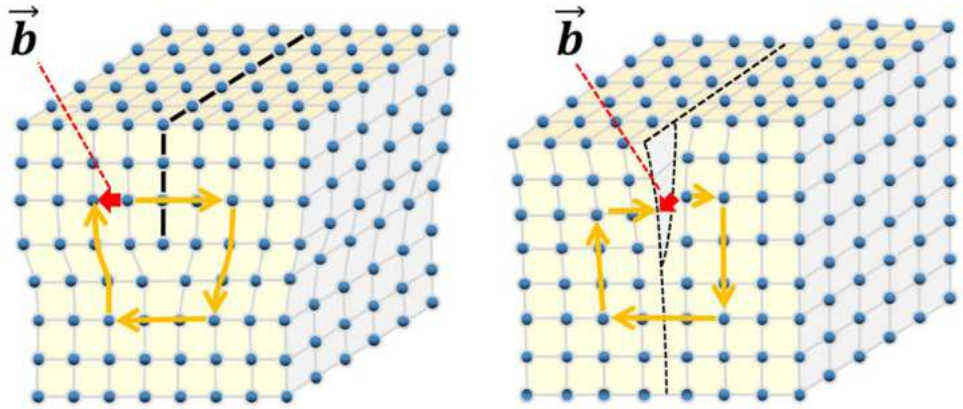

Figure 2.1: Sketches of (a) edge and (b) screw dislocations. Burger's circuit in the deformed state for both cases are shown in red. Figure retrieved from [11].

where ΔU is the internal energy change, W is the mechanical work done on the sample and Q is the dissipated heat due to plastic deformation. Analyzing the equation above, we can say that the exerted mechanical energy to the sample can be termed as W and Q is the energy required for plastic deformation to occur (e.g. activation energy for defect mobility, etc.) [10]. The deformation processes show mostly exothermic behavior due to internal friction of the microstructure, therefore they cause a temperature rise of the sample. Therefore, the internal energy change, ΔU, denotes the energy accumulated in the microstructure with various crystalline defects, such as dislocations. In a broader sense, ΔU can be referred to as "*stored energy*", as it implies the energy stored in the microstructure through defects and their structuring. For the sake of clarity, the text will further focus on dislocations as the main crystalline defect for mediating the plastic deformation.

Edge dislocations are defined as extra half planes introduced to the perfect lattice that lie exclusively on closed-packed planes of the lattice (Figure 2.1(a)). Whereas, screw dislocations are defined as the shear of the perfect lattice that occur exclusively on closed-packed planes of the lattice (Figure 2.1(b)). Dislocations are characterized by their amount of shearing inside the lattice called a *Burger's vector*, $\vec{b}$, which can be determined by forming a Burger's circuit (yellow lines in Figure 2.1) around the dislocation line. If $\vec{b}$ is found to be perpendicular to the dislocation line, it is called as an *edge dislocation*, whereas if $\vec{b}$ is parallel to the dislocation line, it is called as a *screw dislocation*. Dislocations are loops where different parts of the loop have edge, screw and mixed edge/screw character. The motion of dislocations are also called *slip*, and closed-packed directions and planes that the mobile dislocations move on are also called "slip directions" and "slip planes", respectively. For further detailed theoretical coverage on dislocations, please refer to Weertman & Weertman [12] and Hull & Bacon [13].

Cubic materials are deformed by either slip or twinning mechanisms. The deformation is mainly mediated through either of these mechanisms depending on a material property called stacking fault energy, γ_{SFE}, that represents inclination for forming errors on the natural stacking sequence of atoms. γ_{SFE} also represents a materials ability to *cross-slip*, which is the process of expansion of a dislocation loop to another symmetrically equivalent close-packed plane, which contains the Burgers vector. Cross-slip is favoured by high γ_{SFE}, as it limits the splitting of dislocations into partials.

The deformation of materials with low γ_{SFE} (such as Ag, brass, Au, $\gamma - Fe$, etc.) is

Table 2.1: List of closed-packed planes and directions for fcc and bcc Bravais lattices. Table adopted from [14].

	Slip system	
Structure	Plane	Direction
fcc	{111}	<110>
bcc	{110}	<111>
	{112}	<111>
	{123}	<111>

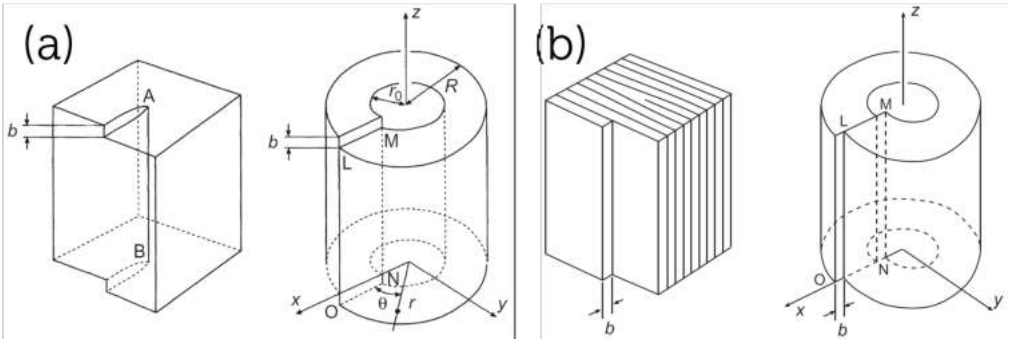

Figure 2.2: Schematic illustration of (a) screw and (b) edge dislocation of an infinite and straight screw and edge dislocations in a cylindrical elastic medium. Figure retrieved from [13].

dominated by twinning, whereas for materials with high γ_{SFE} (such as bcc-metals and Al, etc.), the main mode of deformation is through slip and cross-slip of dislocations. Regarding the scope of the text, the following section will focus on deformation by slip, therefore, through dislocations.

Dislocation slip is dependent on the crystal structure, as close-packed planes vary for different crystal structures. Additionally, the slip occurs in close-packed directions of the close-packed planes. These habit plane and direction couples are further called as *slip systems*. The number of slip systems in Bravais lattices can be calculated from the product of the number of slip planes and the number of slip directions in each plane. A high number of available slip systems imply that the microstructure provides a high number of pathways for deformation to happen. The number of slip systems is a strong function of symmetry and temperature. Therefore, we can say that crystal structures of high symmetry and/or at high temperature are known to be more malleable than their low symmetry and/or low temperature counterparts. Slip systems for common fcc and bcc Bravais lattices are given in Table 2.1.

As being disturbances of the lattice, dislocations pose a stress fields to their vicinity.The stress distribution around the dislocation can be qualitatively explained as the following. Considering an edge dislocation (Figure 2.1(a)), the part of the dislocation above the glide plane pushes its neighboring atoms in outward direction, thus posing a compressive stress to its surrounding lattice. Conversely, in the lower part of the dislocation on the glide plane, the neighboring atoms are pulled towards the dislocation line, thus creating tensile stresses to its surroundings. To the left and right of the dislocation line shear stresses are found. Screw dislocations only give rise to shear stresses.

In a completely relaxed lattice, the presence of a single dislocation creates a long range

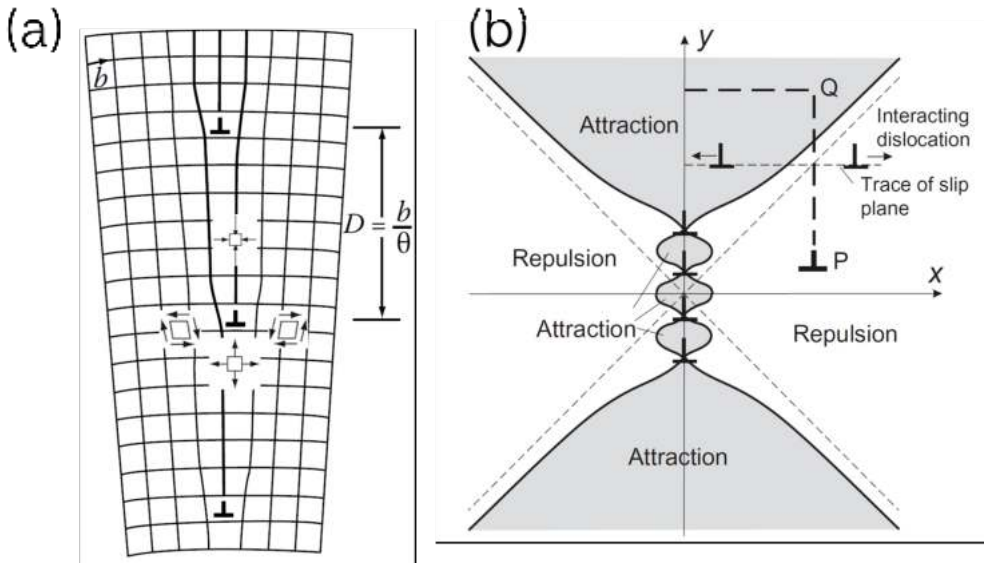

Figure 2.3: Illustration of (a) a tilt boundary, composed of edge dislocations and (b) the stress distribution around a tilt boundary of four edge dislocations. In (a), the stress components are indicated around the central dislocation. Figures (a) and (b) are retrieved from [15] and [13], respectively.

stress field around its surrounding lattice. Structurally, the introduction of a lone dislocation would expected to increase the total free energy of the material. In the presence of multiple dislocations, the excess free energy of the system can be partially relaxed due to special configurations of dislocations. This configuration can be illustrated via the formation of "tilt boundaries" (Figure 2.3): mobile dislocations in the microstructure can migrate close to each other, forming an extended planar boundary with linear cross-section. Through such formation, lone dislocations can relieve their accompanying stress fields by aligning ones compressive field to the tensile field of another and ones tensile field to its neighbors compressive field. Furthermore, the cross interaction between shear stress components create vanishing stress field around the tilt boundary. Figure 2.3(b) shows that along the tilt boundary, the dislocations chain their normal stress fields for acquiring a low-energy configuration along the boundary.

The disturbance at these points may attract the mobile dislocations that are moving under the influence of the applied shear stress. At the immediate vicinity of the boundary, the vanishing field due to stress interaction creates a local shear stresses that attracts the gliding dislocations of the same sign and repels the opposite sign [13]. Further away, dislocations of the same sign will be repelled. This implies that that an incoming mobile dislocation would be influenced with respect to its sign. The termination points of the boundary do not benefit from the stress relief, therefore, they retain their stress influence over their neighbourhood. A mobile dislocation that would have the same sign as those within the boundary would either get attracted or repelled to the boundary terminations, depending on its position. Whereas, a mobile dislocation with an opposite sign would either get repelled or it can find a minimum energy position at 45 degrees to a constituent of the boundary [13].

2.1.2 Structural hierarchy in deformation microstructures

Deformation of medium-to-high γ_{SFE} metals is mediated by slip. Usually, the deformation is accounted heterogeneously in the microstructure, as behavior of different regions vary

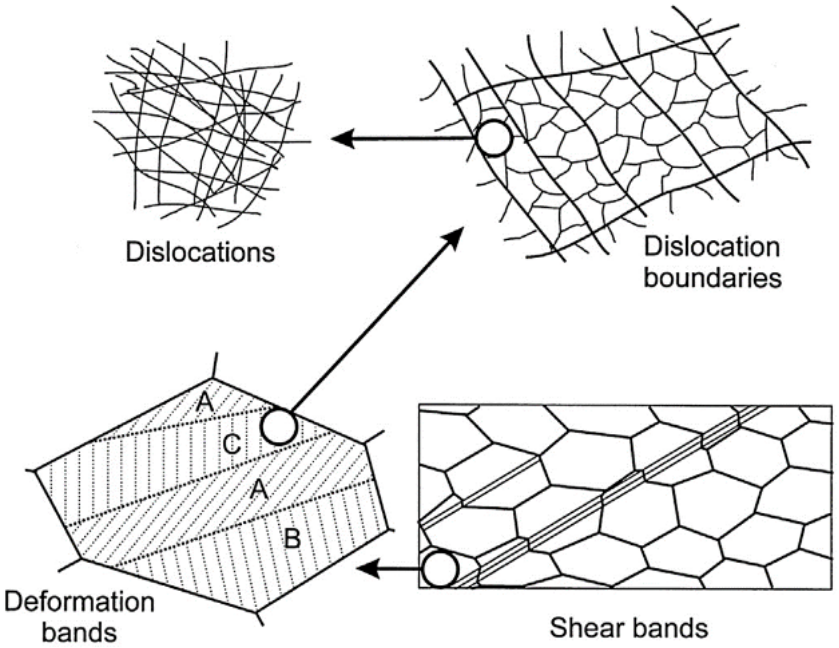

Figure 2.4: Hierarchical organization of deformation microstructure. The arrangement of dislocation tangles form dislocation boundaries. These boundaries form extended deformation bands inside a deforming grain. The deformation bands are created due to emergence of non-crystallographic intergranular shear bands. Figure retrieved from [14].

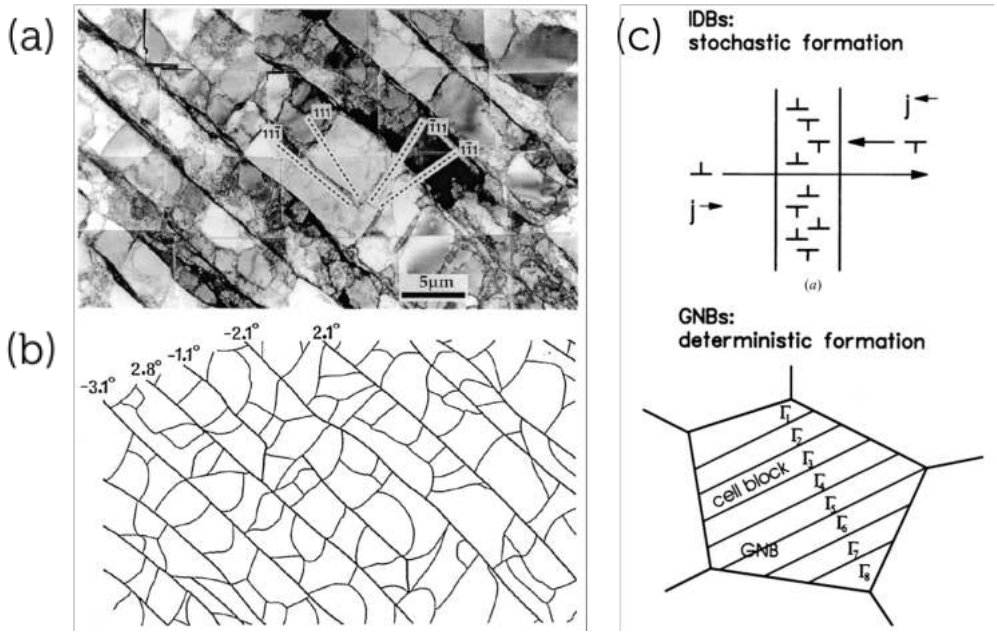

Figure 2.5: (a) TEM image of subgrain (also called as “cells”) blocks consisting of IDBs and GNBs in 10% cold rolled aluminum. (b) Sketch of boundaries and determined misorientation angles between bands from the same micrograph. (c) Formation mechanisms of IDB and GNBs: IDBs are formed by statistical entrapment of present dislocation flux, whereas GNBs are formation is assumed to be the result of a systematic difference in the active slip systems in the domains separated by the boundaries. Figure retrieved from [16].

within a single grain. Upon deformation, the microstructure develops regions of varying misorientations with respect to the initial grain structure. Considering a single deforming grain, the continuous microstructure with equilibrium defects starts to alter with generation of new dislocations. These dislocations form tangles to extended structures of bands of higher hierarchy. In this section, we will focus on the hierarchical structuring of deformation microstructures. The section will have an emphasis on dislocation bands, in regard to visualization of deformation microstructures.

Figure 2.4 shows the four levels of patterning observed during deformation. These patterns are listed below in decreasing length-scales [14]:

- **Shear bands**
  Shear bands are a common feature in rolling microstructures of polycrystals and they form because of plastic instabilities suffered during the rolling process. Simply, shear bands can be seen as rolling counterpart of neck formation in uniaxial tensile loading.

- **Deformation bands**
  During deformation, grains may subdivide into regions of differing orientation as a result of innate plastic instabilities of the grain or due to heterogeneous constrains from neighbouring grains. These bands may divide the grains in several bands of large misorientation angles. As a result, neighboring bands may deform on substantially different slip systems.

- **Dislocation boundaries**
  Cells (or “subgrains”) are the smallest building blocks of the mosaic deformed microstructure. Dislocations generated upon deformation accumulate on dense walls, forming dislocation free crystallites. These crystallites are often delineated by extended planar dislocation boundaries within deformation bands of a deformed grain.

- **Dislocation tangles**
  As mentioned earlier dislocations are generated and accumulated with the commencement of deformation. The accumulated dislocations then form randomized structures, e.g. dislocation tangles. Such structures are widely observed for lightly deformed materials (i.e. at low strain values, $\varepsilon < 0.05$).

Shear bands and deformation bands are relatively large microstructural features that can be visualized with readily available microscopy techniques, such as optical microscopy or electron microscopy. Visualization of dislocation boundary structures are currently performed with electron microscopy techniques with orientation imaging microscopy capabilities. However, these techniques provide surface-limited information. Lastly, low density dislocation structures such as tangles can be visualized with transmission electron microscopy studies, owing to its superior resolution.

The HR-3DXRD technique aims at an angular and spatial resolution enabling 3D mapping of the mosaic structure formed by GNBs and IDBs. Therefore, the current section will narrow its coverage to the 3D structuring of dislocation boundaries and thereof. These structures will be further narrowed down to the cell-forming metals and alloys, with medium-to-high γ_{SFE}, at strains above $\varepsilon = 5\%$.

Figure 2.5(a) and (b) shows a typical dislocation boundary structure composed of cells and planar dislocation boundaries. The shown microstructure consists of two main elements: near-planar dislocation boundaries delineating domains subdivided into individual cells of varying size and misorientation. The boundaries that separate individual cells are

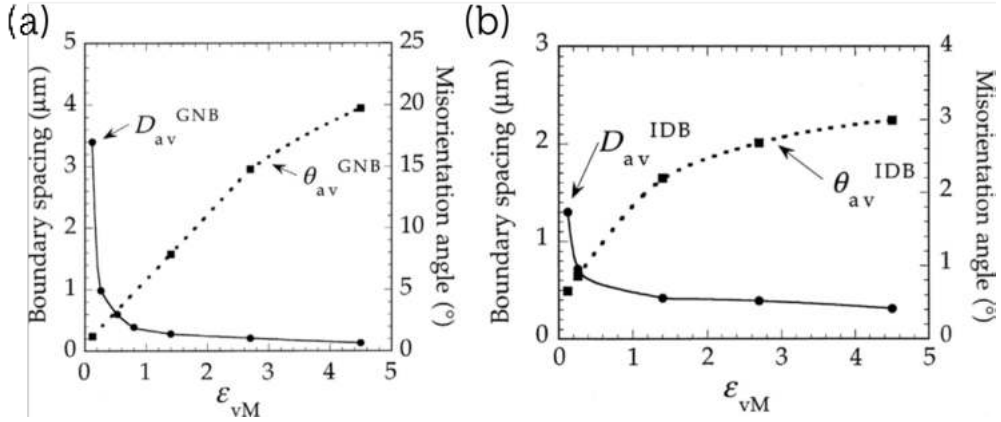

Figure 2.6: Boundary spacing and misorientation angle change of IDB and GNBs with respect to strain. Figure retrieved from [16].

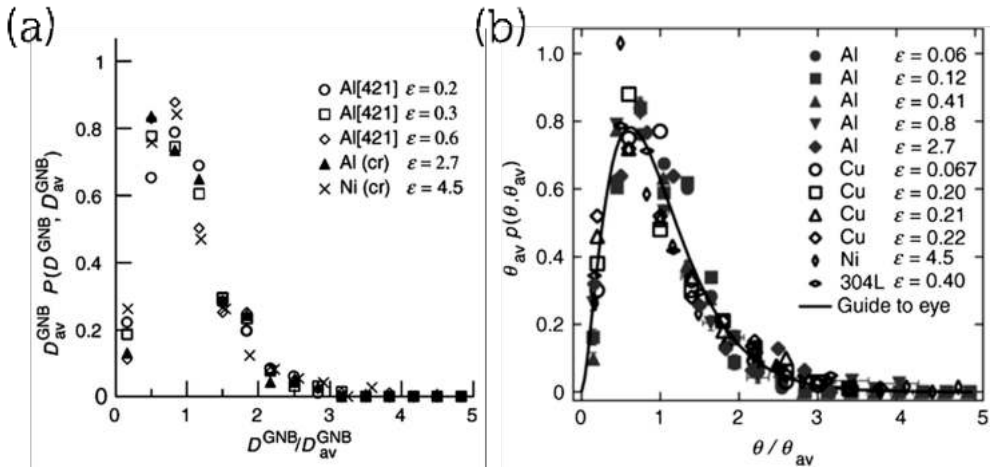

Figure 2.7: (a) Distribution of boundary spacing of GNBs scaled to mean boundary spacing for each strain. (b) Distribution of misorientation angles of IDBs scaled to mean misorientation for each strain. Figure retrieved from [16].

called as "*incidental dislocation boundaries*" (IDB) and the planar boundaries are called "*geometrically necessary dislocation boundaries*" (GNBs).

Owing to their formation processes, IDBs and GNBs are regarded as different boundary classes (Figure 2.5(c)). IDBs are classified to be composed of entrapment of the statistically stored dislocations to the formed boundary through a stochastic process. This implies that the net Burger's vector on IDBs is quite small, leading to minimal lattice rotations. Beside its statistical aspect, GNB formation is necessitated by the strain accommodation of the microstructure [10]. Neighboring volumes separated by GNBs may operate at varying slip systems, in which one neighbor may have e.g. a favorable orientation to promote generation and mobility of dislocations. The activity difference between the two neighboring domains is remedied by the separating GNB, by storing the "geometrically necessary dislocations" emitted from the active band. Therefore, GNBs are assumed to have a distinct Burger's vector, in accordance with the misorientation angle and axis across the boundary.

Upon commencement of deformation, large amounts of dislocations are generated on

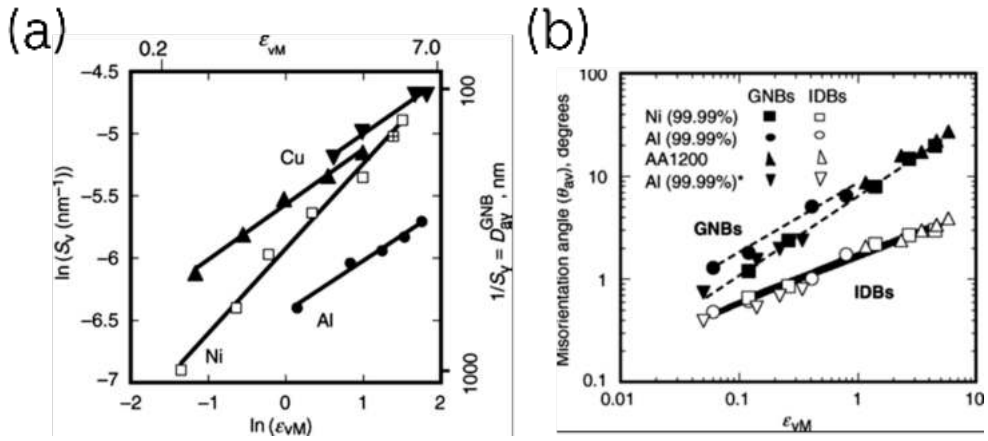

Figure 2.8: (a) Plot of strain against GNB boundary area per volume for Al, Cu and Ni. (b) Plot of strain against misorientation angle for IDB and GNBs for Al and Ni of differing purities. Figure retrieved from [16].

the active slip systems inside the grain in a spatially random fashion. The generated mobile dislocations start to self-organize into cellular structures for reaching a low energy configuration. The rate difference between these two processes determine the boundary characteristics of cellular structures; “cells” are defined as crystallites with diffuse boundaries, whereas “subgrains” are defined as crystallites with sharp boundaries [14].

The cellular structure can be regarded as a mixture of hard cell walls and soft cell interiors.

The later evolution of the deformed microstructure with increasing strain can be observed through the transformation of the IDB and GNB structures. The strain evolution of these can be characterized with the following parameters [10]:

- Spacing and width of boundaries,
- Misorientation angle over the boundaries,
- Crystallographic habit plane for planar boundaries.

The evolution these parameters is given in Figure 2.6.It can be seen that with increasing strain, the mean misorientation angle of IDB and GNBs increases, whereas the mean boundary spacing of both decreases. The misorientation increase and spatial refinement are observed to saturate, e.g. for pure-Ni around $40\,^{\circ}$ and $60\,\mathrm{nm}$, respectively [10]. This implies that at large strain values, the misorientation angle of GNBs may lose its low angle character and evolve into high angle boundaries.

The observed boundary spacing and misorientation angles of IDB and GNBs show a scaling behavior at different strain values. This behavior is illustrated in Figure 2.7. The normalization of observed GNB boundary spacings with the observed mean boundary spacing, the distributions of spacings for different straining conditions and extents show a similar behavior. A similar scaling can be seen for misorientation angle evolution of IDBs with mean misorientation angle (Figure 2.7(b)). Therefore, the distribution of boundary spacing and misorientation angles show a strain-independent behavior.

The evolution of boundary spacing and misorientation angles of IDB and GNBs show a power-law relationship with respect to strain. Figure 2.8(a) shows the power-law relationship between the mean GNB boundary area per volume and strain, i.e. a measure of

the boundary spacing. It can be seen that the power-law exponent has a dependence on the chemistry of the microstructure. Figure 2.8(b) shows the power-law behavior of misorientation angle evolution for IDB and GNBs. The figure reveals that IDBs and GNBs show differing exponents [10]. IDB misorientation show a steeper change with increasing strain. In comparison, GNB misorientation increases with a relatively higher power-law exponent than IDBs. Furthermore, the power-law behavior of IDBs shows no chemistry dependence, whereas misorientation evolution in GNBs of Al and Ni of differing chemical purities show slightly differing power-law exponents[10].

The stress resolved on the slip systems of a deforming grain is known to be a function of the grain's crystallographic orientation. Deformation of single crystals have shown that the resolved shear stress on some arbitrary slip system is given as,

$$\tau_{RSS} = \sigma \cos\phi \cos\lambda \tag{2.2}$$

where τ_{RSS} is the resolved shear stress, ϕ is the angle between the slip direction and the axis of deformation and λ is the angle between the slip plane normal and the axis of deformation [17]. The relation can be projected to the deformation of a polycrystal, suggesting that grains of varying orientations in the sample activate different sets of slip systems, and thus the nature of the interacting dislocations. Therefore, the substructure formed by the subdivision of a deforming grain can be expected to be affected by its crystallographic orientation with respect to the deformation axes, as well. Analysis of a large number of grains deformed in tension revealed three distinct structures. The occurrence of these depends on the crystallographic orientation of the grain with respect to the tensile axis [18]:

- **Type I** is a cell/subgrain structure with straight and parallel GNB boundaries (Figure 2.9(b)). These boundaries are found to be aligned within $10\,^\circ$ of slip planes, with a distinct crystallographic orientation. Type I grains are found have orientations around the medium section in the inverse pole figure in tensile deformation.
- **Type II** is a cell/subgrain structure with no GNB boundaries (Figure 2.9(c)). These grains show either equiaxed shapes or a tubular cell structure with a long-axis aligned with the axis of deformation [10]. Type II grains are found to have orientations condensed around the 100 corner of the inverse pole figure in tensile deformation.
- **Type III** is a cell/subgrain structure with GNB boundaries similar to Type I (Figure 2.9(d)). However, GNBs in Type III structure deviate significantly from the slip planes ($> 10\,^\circ$). GNBs comprise of short and long portions, that mostly show similar inclination with respect to the axis of deformation. Portions of high inclination ($> 20\,^\circ$ are observed, as well. Type III grains are found to have orientations around the 111 corner of the inverse pole figure in tensile deformation.

2.2 X-ray microscopy techniques

Ever since the discovery of X-rays by Röntgen, X-ray imaging methods are used as powerful tools for non-destructive investigation for materials of all kinds. Over the years, novel microscopy methods enabled multidimensional mapping studies of a wide range of materials, ranging from chemical mapping of nanometer-sized crystals to mapping of microstructural defects in cm-to-mm sized crystals. Each method utilizes at least one interaction between the materials and X-rays for obtaining detectable contrast related to the studied microstructure. E.g. X-ray topography makes use of the variation in diffraction signal (i.e. interplanar spacing) for imaging crystalline defects in single crystals [19–22];

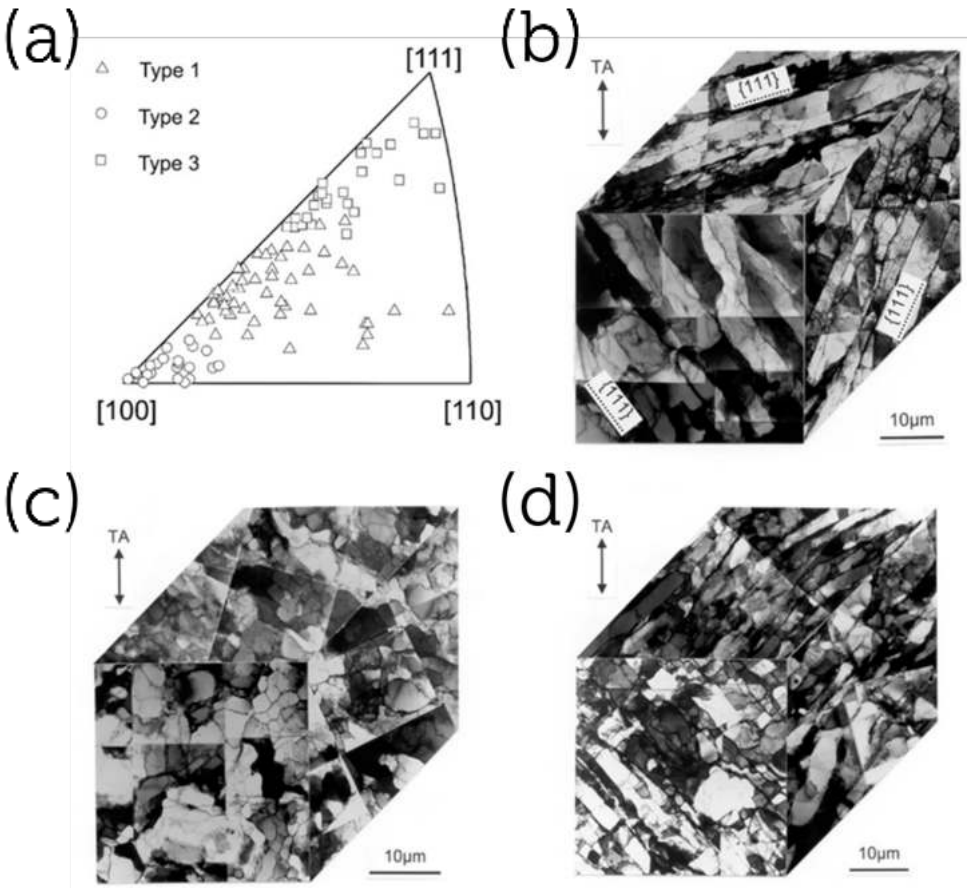

Figure 2.9: Orientation dependence of the microstructure of deformed grains in aluminum under tensile deformation. 3D illustration of (b) type I, (c) type II and (d) type III. The orientations of the grains with the three types of structures are given in the inverse pole figure in (a). Figure retrieved from [18].

whereas scanning X-ray microscopy methods makes use of the X-ray fluorescence signal for three dimensional chemical mapping of biological cells [23, 24].

Considering their acquisition strategies, X-ray microscopy techniques can be classified into two main classes: Scanning and full-field microscopy techniques (Figure 2.10). In scanning microscopy, the incoming X-ray beam is collimated with a condenser unit, forming a point-shaped incident spot on the sample. The focused probe is raster scanned across the sample, collecting signal from the corresponding volume in the detector. The acquired data is then analyzed (e.g. with a tomographic approach) providing a 2D or 3D map of the analyzed microstructure. In full-field microscopy, a large volume of the sample is simultaneously illuminated by collimating the incoming X-ray beam to have a box beam. A variation is section topography, where the sample is illuminated with a line beam and imaged at an oblique angle. Comparing to the scanning method, the full-field microscopy approach illuminates the user specified region-of-interest on the sample continuously throughout the microscopy scan. This allows the microscopy scan to determine information on a large portion of the sample volume, enabling full volumetric scanning with reasonable scanning times. The following text will focus on full-field X-ray microscopy techniques due their relevance regarding deformation microstructure imaging.

The full-field X-ray microscopy techniques can be further classified into three main classes, with respect to their main contrast mechanisms: absorption-based microscopy, phase contrast-based microscopy and diffraction-based microscopy. Absorption-based microscopy can be exemplified via bright-field microscopy[1]: assuming a sample with adequate X-ray absorption and no discernible refractive index variation (i.e. an “absorption object”), one can obtain the absorption tomogram of the specimen by placing a detector at in the image plane of the objective lens. Phase contrast-based microscopy can also be generalized through the same example with a sample with adequate refractive index variation and no discernible absorption variation (i.e. a “phase object”). In this case, the microscopy scan would end up with a phase contrast tomogram of the specimen at the chosen camera length, or propagation distance. For these two cases, the tomograms contain information of how absorption or phase contrast varies in the specimens. These variations are then analyzed in detail through segmentation of different regions and then quantified with tomographic analysis. Diffraction-based microscopy can be exemplified with the simplest case of topography or with so-called Rocking Curve Imaging of a single crystal, in which the illuminated specimen is rotated to satisfy one of it’s Bragg angles and the diffracted beam is imaged whist the sample is rocked around its Bragg angle. Topography scans can reveal the presence and distribution of defects with crystallographic manifestations, such as line defects like dislocation arrangements or planar defects like anti-phase boundaries. The following text will further focus on diffraction-based full-field X-ray microscopy techniques because of the significant and usable diffraction contrast emerging deformation microstructure.

The diffraction-based microscopy techniques are further classified into direct and indirect microscopy classes, with respect to their detection mechanisms. The direct microscopy utilizes a (semi-)Galilean approach, such that the image of the specimen is formed by illuminating the sample with a collimated beam and detecting the diffraction signal (optionally through an objective lens) on the detector. Near-field X-ray topography, magnified X-ray topography, near and far-field topo-tomography and dark field X-ray microscopy can be given as examples for direct diffraction-based microscopy techniques. Whereas, indirect

[1] Here, bright-field microscopy is defined as observation of the scattered signal that is following the same path of the incident beam after interacting with the sample. For introductory information on bright-field microscopy and tomography methods, please refer to [8] and [25].

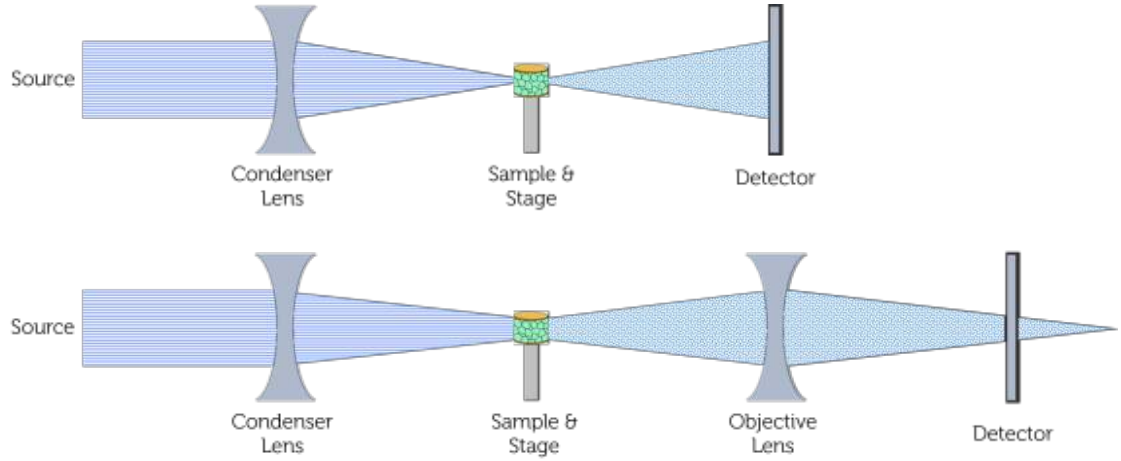

Figure 2.10: Generic setups for (top) scanning and (bottom) full-field X-ray microscopy techniques.

microscopy utilizes the scattering patterns from the specimen on detector frames and then, the microscopy results are reconstructed from these patterns. Three-dimensional X-ray diffraction microscopy techniques, differential aperture X-ray microscopy and Bragg coherent diffraction microscopy can be given as examples for indirect diffraction-based microscopy techniques.

In the following subsections, we will present the current diffraction-based X-ray microscopy methods used for 3D visualization of the deformation microstructures, with an extensive focus on three-dimensional X-ray diffraction microscopy, 3DXRD, methods. Then, we will briefly introduce two other diffraction-based microscopy techniques, dark field X-ray microscopy (DFXM) and differential aperture X-ray microscopy (DAXM) with a highlight on comparison and complementarity to 3DXRD microscopy.

2.2.1 3DXRD and its modalities

Three-dimensional X-ray diffraction microscopy (3DXRD), also referred to as high energy diffraction microscopy (HEDM), is a diffraction-based microscopy technique dedicated to orientation mapping of polycrystalline materials in 3D real space [3, 27, 28]. The methodology of 3DXRD can be said to be an polycrystalline extension of the to rotating crystal method for single crystal diffraction. In other words, 3DXRD treats the constituent grains in a microstructure as pseudo-single crystals (with or without having a substructure). Therefore, 3DXRD provides *grain resolved* information about the microstructure by mapping the orientation and lattice parameters of a polycrystalline lattice. A first step in this type of data analysis is often a simultaneous indexing of all grains. The analysis of the diffraction signals associated with each grain then provides three-dimensional information of the constituent grains of the gauge volume studied in an experiment.

The general experimental setup for 3DXRD is shown in Figure 2.11. The experiment is realized by illuminating a sample with monochromatic high energy X-rays and then collecting 2-dimensional diffraction patterns whilst a sample is rotated around the axis that it perpendicular to the incident beam. During the sample's rotation, the grains with the adequate orientation satisfy the Laue equation and thus cast diffraction spots on the detector frame. Unlike powder diffraction, 3DXRD requires the diffraction signal to be discrete and discontinuous, such that the diffraction spots are detected in a well-separated manner in the detector frames.

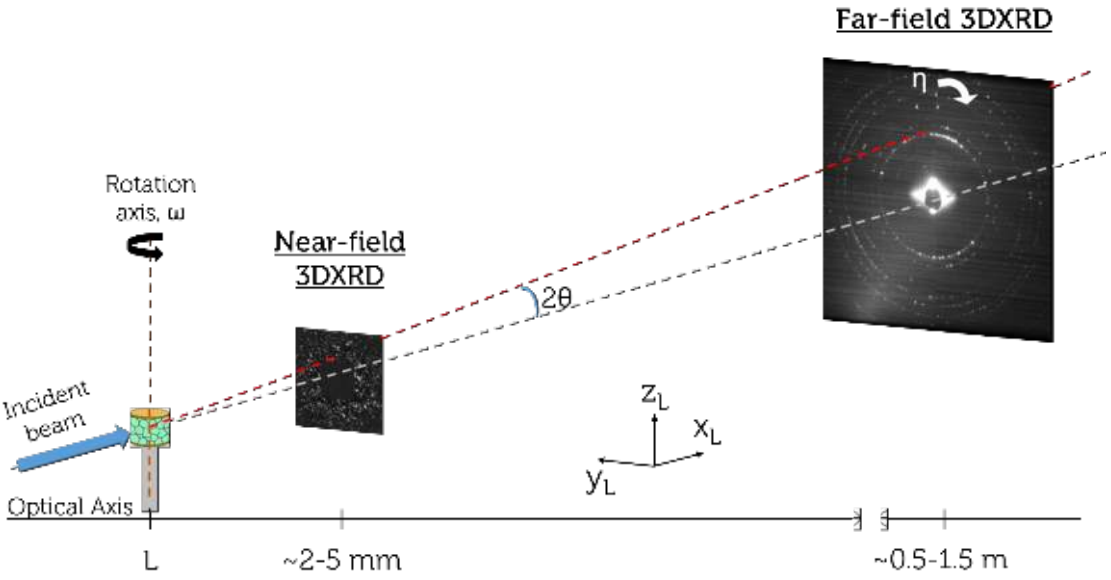

Figure 2.11: Schematic representation of 3DXRD microscopy setup for near and far-field configurations. 2θ, η and ω angles, and the laboratory coordinate system follow the conventions in [26] and [27], and they are given on the figure.

The scattering angles, 2θ, η and ω, and the position of the grain, $CoM = (x, y, z)$, are manifested in individual diffraction spots with the following relation [27];

$$y_{\text{det}} = -(\boldsymbol{L} - x_{\text{L}}) \tan(2\theta) \sin(\eta) + y_{\text{L}} \tag{2.3}$$

$$z_{\text{det}} = (\boldsymbol{L} - x_{\text{L}}) \tan(2\theta) \cos(\eta) + z_{\text{L}} \tag{2.4}$$

in which the real space position of the grain, $CoM = (x, y, z)$, is rotated to the laboratory coordinate axes, $CoM_{\text{L}} = (x_{\text{L}}, y_{\text{L}}, z_{\text{L}})$ with the following relation,

$$\begin{pmatrix} x_{\text{L}} \\ y_{\text{L}} \\ z_{\text{L}} \end{pmatrix} = \boldsymbol{\Omega} \begin{pmatrix} x \\ y \\ z \end{pmatrix} = \begin{pmatrix} \cos(\omega) & -\sin(\omega) & 0 \\ \sin(\omega) & \cos(\omega) & 0 \\ 0 & 0 & 1 \end{pmatrix} \begin{pmatrix} x \\ y \\ z \end{pmatrix}. \tag{2.5}$$

In the given equations above, y_{det} and z_{det} represents the position of the diffraction spot on the detector frame, $\boldsymbol{L}$ represents the distance between the center-of-rotation of the rotation stage and the detector frame (also called as *sample-to-detector distance*, see Section 2.2.1.1) and 2θ, η and ω are the scattering angles defined in Figure 2.11.

The normalized scattering vector expression, $\frac{G_l}{\|G_l\|}$, are defined via the convention in [27];

$$\frac{G_l}{\|G_l\|} = \frac{\lambda}{4\pi \sin\theta} \boldsymbol{\Omega}\mathbf{S}\mathbf{U}\mathbf{B} \begin{pmatrix} h \\ k \\ l \end{pmatrix}, \tag{2.6}$$

where θ is the Bragg angle, λ is the incident wavelength, $\boldsymbol{\Omega}(\omega)$ is the rotation matrix, **S** is the coordinate transformation operator, **U** is the orientation matrix of the subgrain, **B** is the so-called *B matrix* expressing the reciprocal lattice parameters and h, k, and l are the Miller indices. It should be noted that in the presented calculations, **S** is ignored as all constituents of the experimental geometry are defined in a single coordinate axes [27]. For example, considering a case of deformation, one may want to redefine the coordinate

frame in terms of rolling, normal and transverse directions [29]. Then, one shall utilize the S term for performing transformations from laboratory coordinate frame to the deformation coordinate frame.

The observed diffraction spots are converted to normalized scattering vectors through the relation obtained by introducing Equation (2.3) into Equation (2.6),

$$\begin{pmatrix} \mathsf{c}\,\boldsymbol{L} \\ y_{\mathsf{det}} \\ z_{\mathsf{det}} \end{pmatrix} = \begin{pmatrix} \mathsf{c}x_{\mathsf{L}} \\ y_{\mathsf{L}} \\ z_{\mathsf{L}} \end{pmatrix} + \frac{(\boldsymbol{L} - x_{\mathsf{L}})\tan(2\theta)}{\cos(\theta)}\,\boldsymbol{\Omega}\,\mathbf{S}\,\mathbf{U}\begin{pmatrix} h_1 \\ h_2 \\ h_3 \end{pmatrix} \tag{2.7}$$

in which c is a constant defined as,

$$\mathsf{c} = 1 - \frac{1}{\cos(2\theta)}, \tag{2.8}$$

and h is the unit vector in the Bragg relation,

$$\begin{pmatrix} h_1 \\ h_2 \\ h_3 \end{pmatrix} = \frac{\lambda}{4\pi\sin(\theta)}\,\mathbf{B}\begin{pmatrix} h \\ k \\ l \end{pmatrix}. \tag{2.9}$$

The indexing of the observed normalized scattering vectors enables 3DXRD to identify each grain with its orientation, **U**, center-of-mass (CoM) position in real space, $CoM = (x, y, z)$, and its lattice parameters. In order to calculate the elastic strain tensor from the determined lattice parameters, the found reciprocal space lattice parameters contained in the **B** matrix is first converted to its real space called the **A** matrix. Moreover, a **T** matrix is defined as [27],

$$\mathbf{T} = \mathbf{A}\mathbf{A}_0^{-1} \tag{2.10}$$

where $\mathbf{A}_0$ denotes the unstained equilibrium lattice parameters of the crystalline phase of concern. Then, the elastic strain tensor ε_{ij} is defined as,

$$\varepsilon_{\mathsf{ij}} = \frac{1}{2}\left(\mathbf{T}_{ij}\mathbf{T}_{ji}\right) - \mathbf{I}_{ij}, \tag{2.11}$$

where $\mathbf{I}_{ij}$ represents the identity matrix.

2.2.1.1 3DXRD geometry

Performing the mentioned conversion of diffraction spots to normalized scattering vector form requires the observed diffraction spots to be transformed from pixel coordinates of the detector frame of reference to the laboratory frame of reference [30]. This further requires the need for parameterization of the attained geometry given in Figure 2.11.

The experimental setup of 3DXRD is defined with a set of experimental global parameters. These can be listed as:

- Sample-to-detector distance, $\boldsymbol{L}$,
- Wedge angle,
- Detector rotations (or tilts) around x, y and z axes,
- Detector's center with respect to optical axis (also known as "point of normal incidence" or "PONI" [31]),
- Detector's pixel size in y and z axes, and

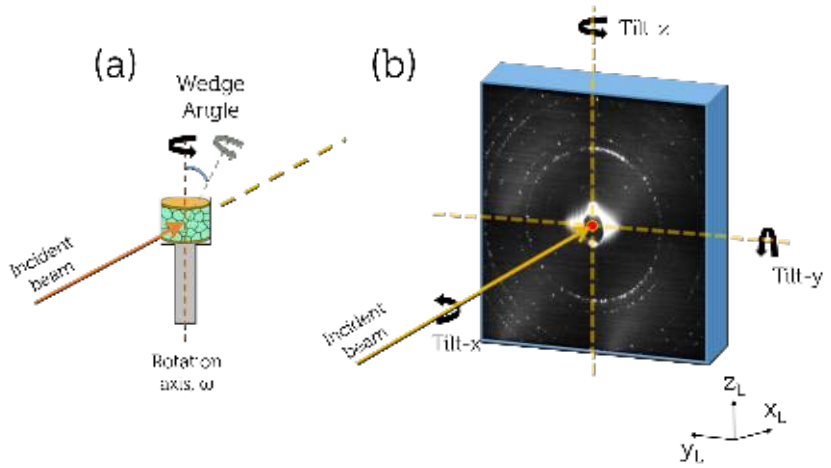

Figure 2.12: Sketches of experimental global parameters: (a) the wedge angle (b) detector rotations in x, y and z, and the detector center point (indicated by the red dot). Sample-to-detector distance, $\boldsymbol{L}$, is not shown for clarity.

- Wavelength of incident X-rays

The sample-to-detector distance, $\boldsymbol{L}$, is defined as the absolute distance along x_L axis between the sample position located at center-of-rotation (CoR) of the rotation axis, to the front face of the detector frame (Figure 2.11). The wedge angle is defined as the angle between the rotation axis and the vertical normal of the incident beam. Schematic description of the wedge angle is given in Figure 2.12(a). The detector rotations are defined as small inclinations of the detector frame with respect to the axes originated at center of the detector frame (2.12(b). The mentioned axis is defined to be parallel to the laboratory coordinate axes. The detector's center is defined as the point of normal incidence of the X-ray beam (or the optical axis) on the detector frame [31]. The pixel size of the detector and the incident wavelength are experimentally independent variables. Both of these parameters can be experimentally determined by calibration measurements[2].

With respect to the sample-to-detector distance, $\boldsymbol{L}$, 3DXRD experiments can realize differing sensitivities for short and long distances. These regimes can be described through a dimensionless parameter from classical optics, the Fresnel number [32],

$$N_{\mathrm{F}} = \frac{\mathrm{b}^2}{\lambda \boldsymbol{L}} \tag{2.12}$$

where b is the mean diameter of the diffracting units (i.e. average grain size of the microstructure), λ is the incident wavelength and $\boldsymbol{L}$ is the sample to detector distance. (To avoid misunderstanding: in X-rays the Fresnel number is often used in the context of phase contrast or coherence. These are not relevant here: 3DXRD builds on geometrical optics and does not utilize the coherence of the illuminated X-rays. Instead the Fresnel number is here used in its meaning from the classical optics context.) The Fresnel number acts as a convenient tool for describing the optical behavior of the scattered X-rays whilst their propagation along $\boldsymbol{L}$. Hence, when $N_{\mathrm{F}} \gg 1$, the optical configuration is said to be on *near-field* regime; whereas for $N_{\mathrm{F}} \ll 1$ the configuration is said to be in *far-field* regime.

[2] An example of determining pixel size from a measurement can be referred from https://pyfai.readthedocs.io/en/latest/usage/tutorial/CCD_Calibration/CCD_calibration.html

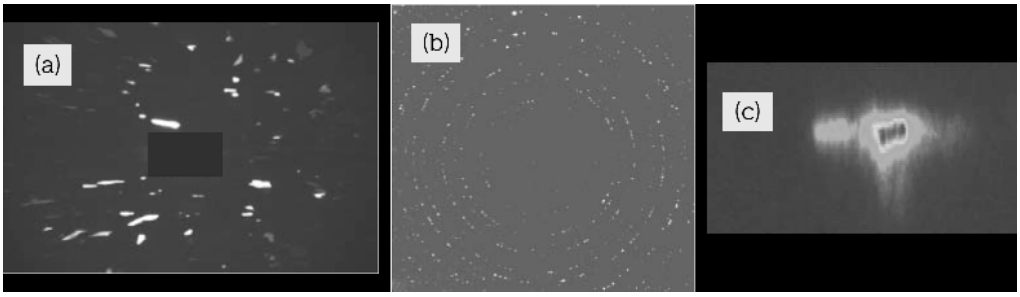

Figure 2.13: Typical diffraction patterns from an arbitrary coarse grained polycrystalline microstructure in (a) NF, (b) FF-3DXRD and from a single reflection of an arbitrary grain in (c) RSM (or very-far-field) techniques. The images were acquired at ample-to-detector distances, $\boldsymbol{L}$, of 4 mm, 400 mm and $3,000$ mm, respectively. The figure is adopted from [27].

In near-field (NF) configuration, a 2D high resolution imaging detector is placed at some $\boldsymbol{L}$, that is sufficiently small —on the order of few millimeters. In this regime, the individual diffraction spots retain its originating grain's shape with respect to their Miller indices. Furthermore, the near-field regime is known to have higher sensitivity regarding to spatial correlations, but depressed sensitivity in angular determination.

In contrast, in far-field (FF) configuration, a 2D detector with large pixels is placed at a sufficiently large $\boldsymbol{L}$, on the order of few centimeters to meters. In far-field, the individual diffraction spots lose their shape related information with increasing propagation distance through a phenomenon called *far-field blurring*. Thus, propagating through $\boldsymbol{L}$, diffraction spots start to suffer from an incremental Gaussian blurring. For sufficiently large distances, i.e. in the far-field regime, the diffraction spots attain a Gaussian-like shape and become more sensitive to changes in orientation and lattice parameter (or strain). Furthermore, the use of large pixel detectors hinder the observation of possible variations in the spot shapes.

The near and far-field configurations in 3DXRD are illustrated in Figure 2.11, as near-field and far-field variants for 3DXRD microscopy. The example diffraction patterns of NF and FF regimes are given in Figure 2.13. These two configuration will be presented in detail in upcoming sections of 2.2.1.3 and 2.2.1.4.

2.2.1.2 Operation modes

The 3DXRD experiment can be done in different modes of operation with respect to the desired temporal, spatial and orientation resolutions. These operation modes are illustrated in Figure 2.14 and they can be listed as,

- **Mode I** - the fast acquisition mode,
- **Mode II** - the CoM mapping mode,
- **Mode III** - 3D volumetric mapping of grains with no substructure,
- **Mode IV** - 3D volumetric mapping of grains with detectable substructure.

Mode I

Mode I is a far-field based operation, in which a short ω-range is scanned for a certain number of illuminated grains. These short scans can be repeated in a continuous manner over an in situ testing of a sample, e.g. continuous scanning during isothermal phase transformations, uniaxial loading etc.. Thus, Mode I provides valuable statistical informa-

tion on intensities, shapes and positions of individual diffraction spots with short time-scale bins over the tracked temporal evolution of the sample.

Mode I experiments cover only a certain fraction of 2θ, η and ω ranges, therefore, it does not provide any information about the spatial position of the grains nor the complete orientation and strain tensors. However, the temporal evolution of the diffraction angles can be used for quantitative interpretation of the angular shifts experienced by each grain.

Mode II

Mode II scanning aims to produce three-dimensional CoM maps of grains (also called "grain-center" maps) of the analyzed microstructure. This type of scanning can be done in both near and far-field regimes. However, Mode II-type scans are generally adopted in far-field 3DXRD experiments, as its near-field counterpart's innate sensitivity for grain volumes in 3D. In contrast to Mode I, this type of experiments are usually conducted in an ω-range of π or 2π. Therefore, the analysis of Mode II data is done through indexing and subsequent refinement of the observed orientations. The optimal analysis of Mode II provides highly accurate information on orientations, CoM positions, volumes and elastic strain tensors of individual grains in the field of view (FoV).

The Mode II analysis assumes that the observed diffraction spots are detected in a well-separated manner on the detector frame. This assumption is known to be valid for well-annealed samples that are free of internal strain variations. However, such assumption tends to breaks down with increasing deformation levels [3, 33]. Therefore, Mode II-type experiments can be applicable to materials with low levels of deformation.

Mode III

Mode III scanning is targeted for producing a complete grain map of the analyzed gauge volume. Mode III operation assumes that the constituent grains in the microstructure to have no internal substructure, together with a defined orientation (and strain). Mode III scanning is capable of determining 3D maps of several thousand grains with spatial and orientation resolutions of $2\,\mu$m and 0.1 deg, respectively, with acquisition times less than ≈ 1 h. Mode III scanning can be exemplified with diffraction contrast tomography (DCT) technique and near-field HEDM measurements (see Section 2.2.1.3). This mode can be said to be out of the scope of deformation microstructure imaging.

Mode IV

Mode IV scanning is a variant of Mode III that accounts for the possibly present substructure in the analyzed constituent grains. In microscopy community, such type of operation is called as Orientation Imaging Microscopy (OIM) [34, 35]. OIM operation has an important implication for its analysis, such that each voxel inside the sample is reconstructed independently with respect to each other.

Mode IV can be said to be the extension of Mode III for specifically visualising the deformation or related microstructures. The analysis of Mode IV scans provide 3D grain maps of the microstructure with intragranular information. Therefore, Mode IV 3DXRD can provide non-destructive 3D orientation maps that are similar to EBSD-type 3D maps obtained with serial sectioning approaches.

2.2.1.3 Near-field 3DXRD

Near-field 3DXRD (NF-3DXRD) is a diffraction-based direct microscopy technique that utilizes the superior real space resolution offered by the near-field regime. The generalized geometry of NF-3DXRD is given in Figure 2.11; a high resolution imaging detector with $\approx 1-3\,\mu$m is placed few millimeters downstream of the sample position, such that three or more hkl rings are imaged in detector's FoV. In real life operation, $\boldsymbol{L}$ and detector's pixel

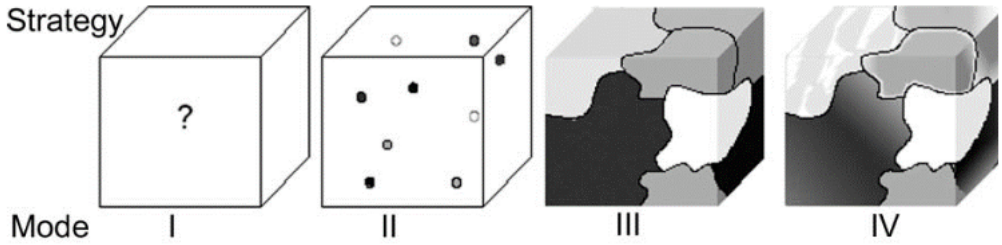

Figure 2.14: Illustration of 3DXRD modalities. Mode I presents rapidly acquired information, therefore is blind to grain CoM positions. Mode II determines the orientation, CoM position, volume and elastic strain matrices in 3D. Mode III and IV are grain-wise volumetric mapping operations, for which the former is suited for grains without substructure and the latter aims to provide non-destructive X-ray counterpart of 3D EBSD-type mapping. The figure is adopted from [33].

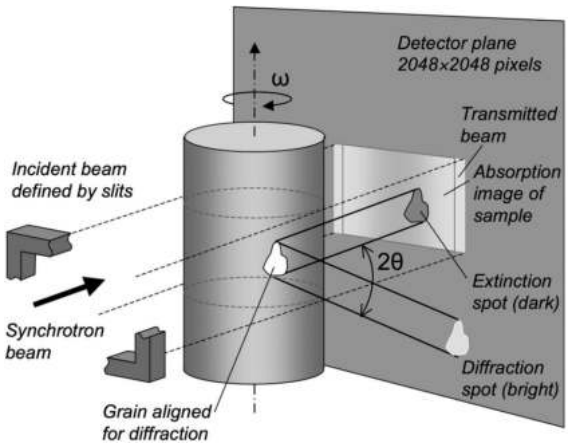

Figure 2.15: Schematic representation of DCT technique. The sample is illuminated with a box beam. The recorded images contain both the bright-field images of the sample with the extinction spot information, and the dark-field information of diffraction spots. The figure is adopted from [36].

size is usually optimized for satisfying $N_{\mathsf{F}} \gg 1$ condition, for attaining the highest possible sensitivity in real space.

As mentioned in Section 2.2.1.1, the shape of the observed diffraction spots in NF-3DXRD retains their originating grains' shape (Figure 2.13(a)). From a different perspective, we can say that each diffraction peak with certain Miller index shows the interaction cross-section of its originating grains. Owing to high resolution detectors and increased spatial sensitivity, such information can be gathered and used for reconstructing the 3D shape of the grains with tomographic approaches.

Over the years, NF-3DXRD can be realized through a selection of different techniques. Namely, diffraction contrast tomography (DCT) and NF-HEDM are the most popular tools for Mode III and IV type analyses, respectively. The difference between these two approaches lies on both the experimentation but also on the analysis side. NF-HEDM technique is usually realized through data acquisition with a line beam configuration. The volumetric mapping is then employed by scanning the line beam through the height of the specimen [28]. The reconstruction of NF-HEDM is conducted with a forward modelling approach [37], such that the experimental data is fitted and refined to a simulated

microstructure in an iterative manner.

DCT technique aims to collect the volumetric mapping information in a single scan. Thus, in comparison to NF-HEDM's line beam acquisition, DCT utilizes a box beam configuration for data collection [38]. Another difference can be sought in DCT's tomographic approach. In DCT experiments, diffraction spots are observed along side with the transmission image of the sample that is kept in the FoV (Figure 2.15). This strategy enables DCT to observe "extinction spots" and related diffraction spots of the diffracting grains at the same time [39]. Hence, DCT datasets will be composed of the absorption tomography data, bright-field imaging data from the observed extinction spots and dark-field imaging data from the observed diffraction spots. These three datasets are analyzed in tandem for reconstructing a 3D OIM map of the studied microstructure [36, 40].

The sensitivity of NF-HEDM and DCT in visualising a slightly deformed (uniaxial strain up to ≈ 1%) Al-0.3%Mn alloy was tested recently in [41]. Renversade and coworkers have shown that both NF-HEDM and DCT reconstructions are in good agreement with each other. It was shown that both reconstructions are spatially $4\,\mu$m and misorientation-wise ≈ 0.5 deg apart from each other [41].

In the last 10 years, the nondestructive visualization power of NF-HEDM and DCT methods paved their way to become daily used tools for Mode III and IV type grain-mapping experiments. Considering its relatively simple experimental configuration, NF-3DXRD techniques are offered as a default tool in many grain-mapping microscopy beamlines around the world. Mode III type near-field experiments are extended for differing probes and illumination, with laboratory sources for white-beam DCT [42–44], with monochromatic neutrons for nDCT [45] or with pulsed neutron sources for extinction spot indexing based time-of-flight 3D neutron diffraction microscopy (ToF-3DND) [46].

In the forward-modelling approach of NF-HEDM analysis, the intensity of each voxel in the FoV are individually fitted to the experimentally observed diffraction spots. This enables NF-HEDM to provide results that lie between Modes III and IV [33], implying NF-HEDM's importance for visualization of deformation microstructures. Li and co-workers have reported the NF-HEDM study of intragranular orientation evolution of pure copper grains up to 6% tensile strain [47]. Pokharel an co-workers have studied the same sample under in-situ uniaxial testing, by successfully tracking ≈ 5000 grains up to 12% tensile strain [48]. Similarly, DCT have found widespread use for deformation related studies. In [49] and [50], 3D growth behavior in magnesium under cyclic loading was studied by DCT and phase-contrast X-ray tomography, where DCT was used to probe the microstructure through EBSD-type Mode III and Mode IV scans. Furthermore, analysis of DCT reconstructions are fed to multiscale physics simulations, such as finite element modelling, crystal plasticity modelling, etc.. The tandem approach was shown for retrieving thermal lattice strains in polycrystalline alumina [51] and modelling grain growth in BCC-iron [52].

In general, spatial resolution of NF methods are limited by the employed detector's pixel size [40, 53]. In other words, it can be said that the detector's pixel size poses a lower limit for detecting spatial variations. This implies that the pixel size used determines the size of the minimum detectable grains. The high resolution detector configuration in ND-3DXRD experiments are usually done with pixel sizes of $\approx 0.75 - 5\,\mu$m [36, 40, 41, 47, 53–56]. Hence, the minimum detectable grain size with near-field methods can be inferred to be on the same extent. Furthermore, together with the aforementioned $\boldsymbol{L}$ of few millimeters, the number of hkl rings covered in the FoV is $\approx 2 - 4$.

From a deformation microstructure perspective, the mentioned experimental configura-

tion have critical implications. As mentioned in Section 2.1, intragranular misorientation of deformed grains increases with increasing levels of deformation. On diffraction spot level, such misorientation increase is manifested as a spread in η and ω directions [3, 27]. Considering the box beam approach of DCT for illuminating a large number of grains, the diffraction spots are expected to overlap in the acquired detector frames.

The overlap problem could be partially remedied in NF-HEDM method, as its line-beam collection strategy limits the number of illuminated grains with respect to the box beam configuration of DCT. However, in Section 2.1 we further mention the grain size refinement with increasing levels of deformation. Such increase in the number density of grains will pose an increased diffraction signal density on the detector frame. Considering the reciprocal relationship between $\boldsymbol{L}$ and diffraction spot separation [34], we can expect to observe further overlap of diffraction spots in the η and ω directions. Therefore, we can say that application of NF-3DXRD methods for visualizing deformation microstructures is limited to materials with low deformation levels of $\approx 1-2$% strain.

2.2.1.4 Far-field 3DXRD

Far-field 3DXRD (FF-3DXRD) is an diffraction-based indirect microscopy technique that utilizes the superior orientation and lattice parameter resolution offered by the far-field regime. The generalized geometry of FF-3DXRD is given in Figure 2.11; a 2D detector with pixel size of $\approx 50-300\,\mu$m is placed $\approx 0.5-1.5$ m downstream of the sample position, such that multiple hkl rings are imaged in detector's FoV. In real life operation, $\boldsymbol{L}$ and detector's pixel size is usually optimized for satisfying $N_{\mathsf{F}} \ll 1$ condition, for attaining the highest possible sensitivity in orientation and lattice parameter resolutions.

As mentioned in Section 2.2.1.1, the shape of the observed diffraction spots in FF-3DXRD show Gaussian-esque behavior and they retain no information about their originating grains' shape (Figure 2.13(b)). Yet, the CoM position of the grains are embedded in the diffraction signal, such that it can be inferred as correction terms on diffraction angle positions of each grain (see Equation (2.3)). In a similar perspective, it's known that elastic strain alters the local lattice parameters of each grain, thus altering 2θ, η and ω positions of diffraction spots [6, 7]. The elastic strain matrix can be determined for each grain by subjecting the indexed/found grains to an extensive refinement procedure [2, 57]. Through analysis of FF-3DXRD is capable of determining the orientations, CoM positions and elastic strain tensors of the grains with an accuracy of $2-5\,\mu$m, $0.01\,^\circ$ and $\approx 10^{-3}-10^{-4}$, respectively [27, 28, 33, 58].

Over the years, FF-3DXRD was realized through two main techniques: namely, FF-3DXRD and FF-HEDM. Unlike their near-field counterparts, the difference between these two approaches lies only on the analysis side. Both techniques are performed with either of line and box beams. In the line beam configuration, the volumetric mapping is achieved by scanning the line beam through the height of the specimen [28]. In the box beam configuration, the sample is illuminated with a large beam with rectangular cross-section, enabling the simultaneous acquisition of information from the complete illuminated volume.

The analysis of FF-3DXRD pursues to index the observed scattering vectors for identifying the illuminated grains [59, 60]. The identified orientations are then subjected to an extensive outlier rejection and refinement procedures for determining the orientation, CoM position, integrated intensities and local lattice parameters of each grain. Further simultaneous refinement of the whole dataset allows the deduction of the volume and the elastic strain tensor of the found grains [57]. In comparison, the analysis of FF-HEDM is conducted with a forward modelling approach [30, 61, 62], such that the candidate orienta-

tions are guessed from the experimental data. Then, the simulated microstructure is fitted and refined to the experimental data in an iterative manner. The final model provides a 3D map of the studied microstructure with determined orientation and refined elastic strain tensors of constituent grains.

FF-3DXRD approach can be utilized for various experiments through application of different modalities (see Section 2.2.1). For example, Mode I approach was widely utilized for studies of in situ mechanical testing [1] and recovery/recrystallization transformations [4, 63, 64]. Similarly, Mode II type approach was adopted in studies of microstructural evolution during deformation processing [2, 57, 65, 66]. Mode II type experiments can be further extended to Mode III type volumetric maps of the analyzed microstructure via tessellation approaches, such as Voronoi, Laguerre tessellations [67] and generalized balanced power diagram approach [68]. Lastly, Mode IV type can be applied for studying low-to-moderately deformed samples with coarse spatial resolution of $\approx 10\,\mu$m [69, 70].

Similar to NF approaches, application of FF-3DXRD on moderate-to-highly deformed samples is also limited by spot overlap. In Section 2.1, we mention the decrease in subgrain size, which lets the formation of neighboring subgrains with misorientations lower than $0.1\,^{\circ}$. These neighboring subgrains are expected to fall on similar diffraction angles on the detector frame - especially in radial direction, η [3]. Owing to depressed sensitivity of the FF configuration and its large choice of pixel size, these neighboring subgrains would be detected as overlapping spots. Hence, sole FF-3DXRD experimentation for tracking the microstructural evolution during deformation would provide incomplete information because of spot overlap issues.

2.2.1.5 Reciprocal space mapping

Reciprocal space mapping (RSM), also called as very-far-field 3DXRD/HEDM (vff-3DXRD/HEDM), is a grain-specific diffraction technique, in which a single diffraction spot originating of a bulk grain is analyzed at far-field regime [3, 27, 71]. RSM measurements are performed by placing a detector of moderate spatial resolution ($\approx 50\,\mu$m) at further downstream of FF-3DXRD detector, $\boldsymbol{L} = 3-5$ m. At mentioned detector distances, the detector configuration of RSM would attain a high angular resolution, enabling a strain resolution of 1×10^{-5} [27]. A typical detector image of RSM is given in Figure 2.13(c).

From a deformation perspective, the attained high resolution can be leveraged for resolving individual diffraction manifestations of subgrains, thus enabling studies of the intragranular dynamics during in situ testing. Therefore, RSM can be deemed as a Mode I technique by nature [71]. Jakobsen and co-workers have studied the evolution deeply embedded subgrains in OFHC copper under in situ tensile loading experiments [72]. The study was further extended to resolve the partial strain contributions in dislocation walls and individual subgrains [73] and determination of dislocation densities [74]. In a recent example, Diederichs and co-workers have studied recrystallized AA1050 alloy subjected to cyclic deformation, and resolved the evolution and interaction of subgrains with increasing loading cycles [75].

RSM-type experiments are shown to be useful for tracking the substructure evolution in metals during deformation processing. Observations from such experiments provide a high angular resolution picture of the individual subgrains within a deformed grain. However, RSM experiments fail to provide a real space information about the distribution and position of individual subgrains due to maximization of the angular sensitivity with the choice of relatively long $\boldsymbol{L}$. Furthermore, such analysis is limited to crystallites of defined boundaries (i.e. subgrains), due to diffuse diffraction signal originating from loose dislocation boundaries. This behavior is illustrated in Figure 2.16; with further deformation

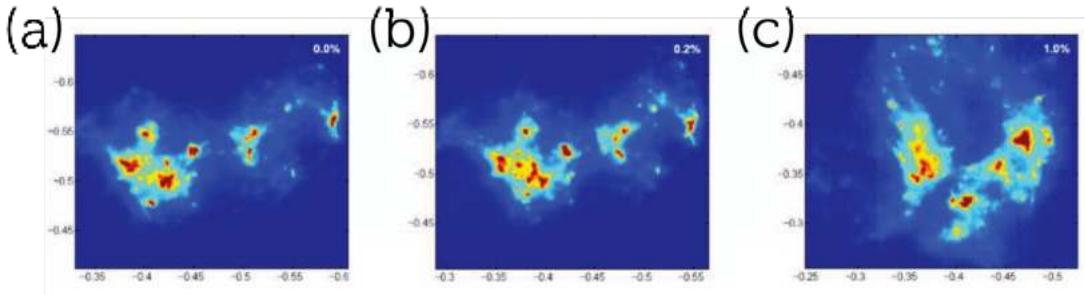

Figure 2.16: RSM azimuthal maps of a 400 reflection from a Cu grain in deformation levels of (a) 0.03%, (b) 0.2% and (c) 1.0% strain. The diffraction signal from subgrains are progressively obscured by the stray signal from loose dislocation boundaries. The figure is adopted from [71].

levels, the creation and accumulation of loosely packed dislocation boundaries form and cause unwanted diffraction signals. These stray signals may block the diffraction signal emanated from individual subgrains, thus hindering the tracking of subgrains-of-interest.

2.2.2 Emerging 3DXRD methods

NF & FF-3DXRD and RSM techniques have shown a potential for visualizing the deformation microstructures with differing methodologies. As described in the previous sections, each of these techniques are capable of imaging microstructures that undergone low extents of deformation. However, NF and FF techniques are not capable of resolving the deformation substructure of medium-to-high deformation levels. Whereas, RSM can detected the substructure through individual subgrains, however, it provides limited statistics about the studied deformed grain.

In recent years, new experimental and analysis concepts are introduced as remedy of this problem. These concepts all aim to resolve intragranular variations of polycrystals. In the following section, these concepts of scanning FF-3DXRD, intragranular analysis of NF and FF-HEDM and subgrain resolution DCT methods will be introduced.

2.2.2.1 Scanning far-field 3DXRD

Scanning 3DXRD is a far-field microscopy method realized by performing a two-dimensional raster 3DXRD scan with a point (or ”pencil”) beam. The raster scanning approach remedies the diffraction spot overlap problem by reducing the gauge volume to minimize the overlapping diffraction signal. The analysis of the acquired voxellated diffraction signal provides 3D grain maps with intragranular orientation and elastic strain tensor variations [76, 77]. This provides scanning 3DXRD to be a dedicated Mode IV method.

The scanning 3DXRD experiments is performed by raster scanning a collimated point beam over a user defined FoV on the sample surface. The point beam is collimated to be sufficiently smaller than the nominal grain size. The rastering is done in y_L and z_L directions, providing grains to be detected in multiple sample positions. Step size of the raster scan dictates the voxel size of the obtained 3D grain map [76, 78]. The diffraction patterns are collected in a FF-3DXRD fashion, with a large pixel detectors at long $\boldsymbol{L}$. The rastering approach enables scanning 3DXRD to provide a unique feature of determining the detected grains' shapes. The grain shapes are retrieved with filtered back projection reconstruction of the indexed diffraction spots over the rastering axes [77].

The analysis of the voxellated data is shown to be analyzed through different refinement methods [79]. Hayashi and co-workers adopted a single crystal refinement scheme, in

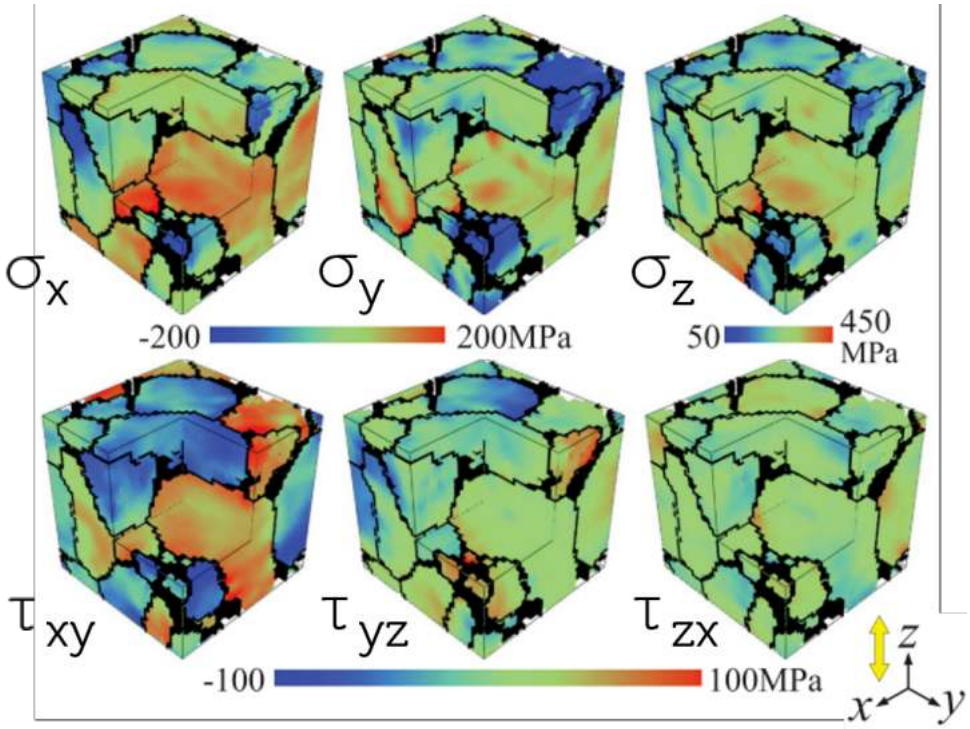

Figure 2.17: Intragranular stress components of a low carbon steel alloy developed after 5.1% elongation measured with scanning 3DXRD. The top row shows the principle components and the bottom row shows the deviatoric components. A volume of $87,500\,\mu\text{m}^3$ was studied with a voxel size $1.2\,\mu$m. The figure is adopted from [78].

which the individual voxels are assumed to have an average orientation and strain [76, 78, 79]. Henningsson and co-workers have proposed two different analysis routes, via iterative fitting and refinement of a voxellized polycrystalline forward model or algebraic refinement of the strain through the indexed diffraction spots at each voxel position [79].

Scanning 3DXRD is shown to be applicable for visualising intragranular variations in deformed microstructures. Hayashi and co-workers have studied the evolution of both grain averaged and intragranular stresses with scanning 3DXRD during in situ tensile testing [78]. The study revealed the stress variations of a volume of $44.4 \times 44.4 \times 44.4\,\mu\text{m}^3$ with a voxel size $1.2\,\mu$m (Figure 2.17). The technique can be performed with much smaller beam sizes; Hektor and co-workers have mapped the grain growth of Cu_6Sn_5 in a lead-free solder alloy from a volume of $16 \times 16 \times 16\,\mu\text{m}^3$ with a voxel size $0.25\,\mu$m [77].

Scanning 3DXRD provides a useful method for imaging deformation microstructures by visualizing the intragranular strain variation. However, the technique possess few intrinsic pitfalls. Strain sensitivity of scanning 3DXRD is discussed to get affected by the choice of analysis approach [79]. It is further discussed that, the analysis is prone to suffer from smoothing of the microstructural information as a reconstruction artifact. Secondly, the rastering 3DXRD scans over statistically significant volumes with adequate voxel sizes require long acquisition times. This defines scanning 3DXRD as a slow technique. Lastly, the rastering of the sample with fine voxel sizes require special sample stages (e.g. Nanoscope endstation of ESRF ID11 [80]) with fine step resolutions ($100 - 500\,$nm) of high reproducibility. Therefore, further considering the need of nano-sized collimation of the point beam, these requirements pose great experimental limitations for conducting scanning 3DXRD scans.

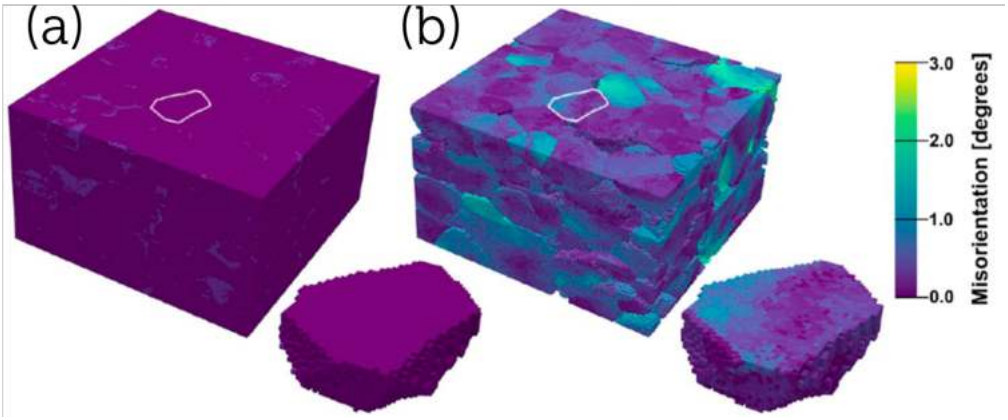

Figure 2.18: 3D Intragranular orientation maps of Ti-7%Al alloy in (a) undeformed state and (b) for 3% strained state, calculated with the Nygren method. The dimensions of the maps are given as $1 \times 1 \times 0.6\,\text{mm}^3$, with voxel size of $\approx 1.48\,\mu$m The figure is adopted from [84].

2.2.2.2 Intragranular analysis of NF and FF-HEDM

A combined analysis of simultaneously acquired NF and FF-3DXRD data are previously adopted in several studies for extending the observed information to intragranular level [81–83]. These approaches allowed reconstruction of Mode IV type intragranular property variations for a certain number of grains in the analyzed microstructure.

Nygren and co-workers have adopted and extended this approach for obtaining complete Mode IV type grain maps through a novel data analysis scheme [84, 85]. The Nygren method is devised for the analysis of NF and FF-HEDM data taken either simultaneously with a 3D detector approach [27] or with consecutive NF and FF scans. The analysis commences with the initial indexing of the FF dataset, in which the grains available in FoV are identified with their grain average properties, similar to Mode II approach. In this step, the orientations with extended features in η and ω directions (e.g. deformed grains) are treated to have a single orientation. The angular spreads are used for predicting the misorientation extent of the grain. In the next FF-analysis step, the observed orientations are further refined by determining an envelope function for each analyzed grains' orientation distribution function (ODF). These envelope functions are referred as a "grain orientation envelope" (GOE) [85], comprising of intragranular orientation distribution information. The determined GOE's represent sole orientation information; therefore, GOE's do not present the spatial distribution of contained orientations.

In the second step of the method, NF-HEDM data is indexed via utilizing the identified GOE's from FF analysis [84]. The analysis is performed by discretizing the NF gauge volume and performing a forward model fitting/refinement of all identified GOE's throughout each volume element. The resulting NF-HEDM grain map is further analyzed for missing grains. The missed grains are found by iterating the explained FF and NF analyses by using the initial grain map as an input. The obtained grain map will comprise Mode III type information.

The obtained space filling grain map is then subjected to a final analysis for extending the Mode III map into a Mode IV nature. This conversion enables determination of the spatial distribution of contained orientations with the following procedure [84]:

1. Discretizing the determined grain volumes of the Mode III grain map,

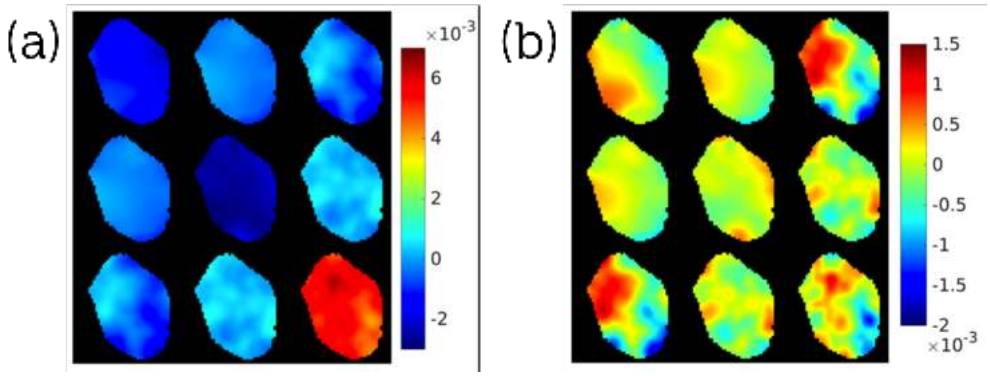

Figure 2.19: (a) Resolved strain components and (b) intragranular stress components of an example grain detected by DCT with subgrain resolution. The voxel size is $2.5\,\mu$m. The figure is adopted from [86].

2. For each grain, its FF determined GOE is used for forward modelling (i.e. a virtual diffraction experiment) for each discrete volume element,

3. The forward model predictions satisfying a figure of merit (e.g. completeness, see Section 4.2) are accepted, thus revealing the intragranular orientation distributions.

The resulting grain maps are presented in Figure 2.18. The figure shows that Nygren method is capable of identifying intragranular orientation distributions for deeply embedded grains during a in situ tensile testing experiment with a spatial resolution of $\approx 1.5\,\mu$m.

The Nygren method provides a novel data analysis tool for extracting the intragranular information from NF and FF-HEDM datasets of deformed microstructures with a unique approach. The method is adopted for commonly used NF and FF geometries. With current synchrotron light sources, the complete “classical” NF and FF-3DXRD techniques are performed within the range of few tens of minutes. Furthermore, Nygren and coworkers have reported that the analysis method can be performed within $3-4\,$h [84]. These timescale implies that the Nygren method can be adopted as on-line analysis tool during synchrotron experiments.

The explained methodology assumes the observed diffraction spots to be well separated in obtained NF and FF diffraction patterns [84, 85]. Similar to its sole NF and FF counterparts, we can comment that the Nygren method is limited by the spatial resolution and overlapping of observed diffraction spots. As stated in Section 2.2.1.3, the voxel size of a NF-3DXRD/HEDM reconstruction is dictated by the employed effective pixel size of the detector. Considering the $\approx 1.5\,\mu$m voxel size of the obtained 3D maps, we can discuss that Nygren method is not capable of resolving the individual subgrains in the deformation microstructure. The spot overlap limitation further implies a limit on resolvable deformation level (see Section 2.2.1.3). At moderete-to-high deformations, the smearing of the diffraction signal is expected to obstruct the intragranular resolution capabilities of the method. Lastly, the explained method is reported to assumes that the intragranular orientations of a single grain is contained in a single GOE blob [84]. This assumption may break down with the formation of crystallographically heterogeneous microstructural features, such as deformation twins or with formation of GNB bands comprising distinct subgrains. Therefore, we can conclude that the Nygren method can be applicable only for studies of low deformation levels.

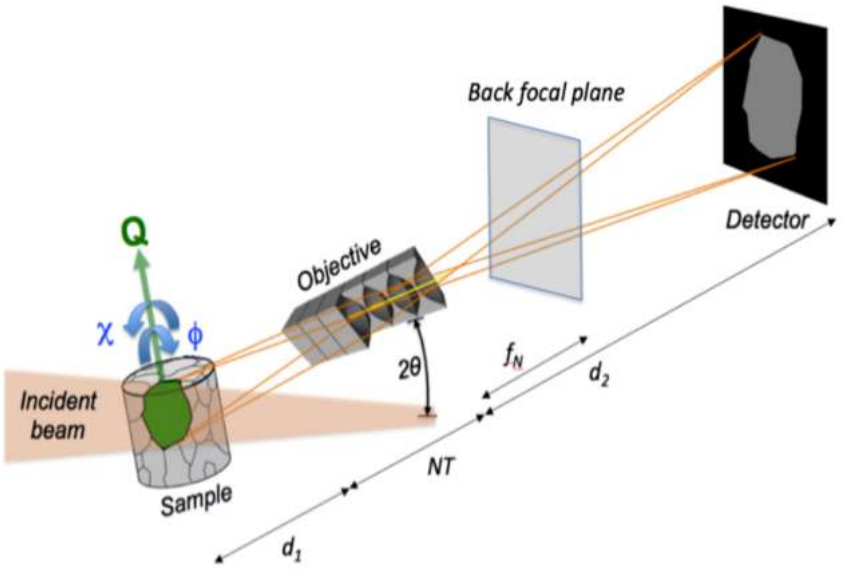

Figure 2.20: The schematic geometry of DFXM. A diffraction spot of a grain-of-interest is imaged in real space by placing an X-ray objective along its path. The figure is adopted from [88].

2.2.2.3 DCT with subgrain resolution

In Section 2.2.1.3, we have mentioned that the spatial resolution of NF-3DXRD techniques are determined by the employed detector pixel size. Recently, usage of high resolution detector configurations are shown to map $2-5\,\mu$m recrystallized grains in AA1050 [87]. Reflecting on the mean subgrain size of $\approx 1\,\mu$m, similar detection strategies may be leveraged for studying deformation microstructures.

Reischig and Ludwig have recently reported a Mode IV extension of the DCT technique [86]. The technique adopts the readily used DCT experimental configuration. The intragranular strain distribution of grains in FoV are calculated through a forward modelling approach, in which the shape and the in-grain deformation field of each grain is fitted and refined to the experimental diffraction frames iteratively. A exemplary reconstructed grain of a gum metal alloy with the new DCT analysis is given in Figure 2.19. The figure reveals that the new DCT analysis is capable of resolving intragranular strain variations with a spatial resolution of $2.5\,\mu$m [86].

The recent Mode IV extension of DCT offers a relatively fast tool for in situ studies, as it requires a single acquisition scan. It was shown to resolve intragranular strain variations in deformed microstructures. Yet, similar to other NF methods, this technique is expect to have a limited lightly deformed microstructures, as further deformation levels would obscure the diffraction signal by smearing out in η and ω directions. Also, similar to the Nygren method described in Section 2.2.2.2, we can discuss that this novel DCT method would not be capable of resolving the individual subgrains in a deformation substructure, due to its enlarged voxel size with respect to the mean subgrain size of $\approx 1\,\mu$m.

2.2.3 Dark field X-ray microscopy

Dark field X-ray microscopy, DFXM, is a diffraction-based full-field direct microscopy technique for visualising intragranular orientation and strain fields of bulk deeply embedded grains in 3D [89]. The technique can be seen as the X-ray counterpart of dark field operation in TEM, such that a magnified real space image of a crystal/grain is formed by placing an X-ray objective along one of its diffraction spots Figure 2.20. The X-ray objective has two main use: firstly, it acts as a high-pass spatial and angular filter, providing analysis of a crystalline sub-volume in the sample; secondly, and most importantly, it magnifies the

Figure 2.21: A room temperature DFXM mosaicity map and its corresponding pole figure of a deformed grain in highly deformed Fe-Si alloy ($\varepsilon = 2.0$). The grain slice is illuminated with line beam. The mosaicity scanning is done over $10\,^{\circ}$ in μ and χ angles with a step size of $0.5\,^{\circ}$. Effective pixel size of the map is $400\,$nm. Courtesy of Can Yıldırım.

image, thereby overcoming the spatial resolution limitation of 3DXRD.

DFXM can be seen as a combination of two well-known imaging techniques: magnified X-ray topography and RSM/vff-3DXRD (2.2.1.5). The former technique utilizes the same experimental geometry of placing an X-ray objective for forming real space image of the microstructure. In magnified X-ray topography, the microscopy scans are done by performing a rocking curve of the analyzed diffraction spot. Similarly, RSM experimentation can be seen as the reciprocal space counterpart of DFXM. In RSM, a diffraction spot is studied by careful mapping of its pole figure in reciprocal space. In a simple case, DFXM combines the RSM's pole figure determination methodology and magnified X-ray topography's real space resolution. This enables DFXM to obtain detailed intragranular orientation and/or strain maps with a spatial and angular resolutions of $150\,\mu$m and $10^{-4\,\circ}$, respectively[3]. We should point out that attained FoV and magnification can be tailored by adjusting the focal power of the X-ray objective [91].

The standard operation of DFXM consists of two main microscopy scans [92–95]. In *mosaicity mapping*, the pole figure of the magnified diffraction spot is determined with a 2D scan of μ [4] and χ angles. Whereas, in *strain mapping*, axial lattice strain of the microstructure through a 2D scan of θ and 2θ. These two scans can be performed in combination, i.e. a 3D μ-χ-2θ scan, enabling multi-axes real space characterization of pole figures. The modalities can be further expanded to differing sensitivities. For example, an aperture-limited X-ray topography approach can be adopted in the back focal plane of the X-ray objective, enabling high resolution 3D mapping of dislocations [96].

In the time of writing, DFXM technique is offered only in a dedicated instrument at the Hard X-ray Microscopy endstation of ESRF ID06 beamline [88]. The ID06 DFXM instrument has started its user operation in August 2020.

DFXM shows an unprecedented potential for 3D mapping of deformation microstructures with the utmost spatial and angular resolution. Aforementioned above, the X-ray objective suppresses the stray (and optionally, overlapping) diffraction signals. Recently, such filtering and high resolving power of DFXM has been demonstrated to map out deeply embedded subgrains in a binary Fe-Si alloy deformed to true strain of $\varepsilon_{vonMises} = 2$ [97]. Figure 2.21 shows a detailed view of the intragranular substructure field, by revealing the subgrains through its superior spatial and angular accuracy. We should point out that the given mosaicity map is in fact incomplete due to insufficient sampling of the pole fig-

[3] The figures are given considering the use of compound refractive lenses, CRLs, as X-ray optical elements. The spatial resolution can be improved with the use of multilayer Laue lenses [88, 90] in expense of attained field of view.

[4] In the time of writing, DFXM experiments in ESRF ID06-HXRM are performed in vertical geometry, in which μ = θ [88].

ure. This can be observed in the pole figure given in Figure 2.21, such that the scattering features in the lower left-hand-side of the pole extends out of the investigated angular range.

As a standalone technique, DFXM provides detailed information about the hierarchical structuring of multi-scale materials, such as deformation microstructures. However, we should note that mentioned DFXM operation is quite tedious and, currently, provides incomplete maps for the microstructures. As seen in Figure 2.20, the experimental setup of DFXM relies on combined movement of a multitude of stepper motors with sub-μm accuracy. This requirement is satisfied through the design of the ESRF ID06 instrument, through careful feedback of the encoded stepper motors. Secondly, we should point out that reconstructions strain maps from a single diffraction spot provides only 3 components of the orientation and elastic strain tensors [98]. Theoretically, the complete characterization of the elastic strain tensor can be obtained through collection of strain maps from two non-orthogonal diffraction spots from the same hkl family. Lastly, we have mentioned that the pole figure given in Figure 2.21 is incomplete. The main reason for the incomplete mapping can be attributed to the finite numerical aperture of the utilized X-ray objective lens. The numerical aperture of the lens defines the accepted diffraction signal to the objective [89, 99]. In the case of Figure 2.21, the angular extent of the studied reflection was larger than the numerical aperture of the lens. Therefore, a complete space-filling map of the analyzed grain can be obtained in expense of experimentation time by sampling the pole figure in larger ranges —for covering the entire scattering information- and with finer step sizes.

Similar to dark field TEM, DFXM offers a novel tool for detailed analysis of deformation microstructures. However, DFXM provides limited statistics on the microstructure, due its spot-by-spot (or grain-by-grain) measurement approach. From an experimental perspective, DFXM can be used as a complimentary tool for visualising deformation microstructures. Considering a deformation processing example, one may use 3DXRD modalities to track the compound evolution of the grain ensemble, and use DFXM for performing "zoom-in" high resolution mapping of a particular grain-of-interest (e.g. with low or high misorientation, or with certain strain/stress state).

Currently, DFXM is known to produce the most detailed 3D orientation and strain maps of the crystalline grains, in general. Specifically, the study shown in Figure 2.21 suggest that DFXM is also capable of providing detailed 3D orientation maps of the deformed microstructures. The mentioned 3D DFXM maps offer new opportunities for multi-scale modelling studies. The detailed reconstructions of the deformed grains can be used as experimental constrains for driving multi-scale models of deformation studies.

2.2.4 Differential aperture X-ray microscopy

Differential aperture X-ray microscopy (DAXM) is a scanning indirect microscopy method for 3D microstructural mapping that utilizes polychromatic microbeam X-ray diffraction. DAXM mapping is realized through raster scanning of a polychromatic point beam on the sample surface. For each rastering point, Laue patterns are acquired while the sample surface is scanned with a knife edge (Figure 2.22). During the scan of this "differential aperture", the diffraction spots get blocked by the knife edge, thus providing the depth position of the diffracting voxel. The analysis yields a voxellated 3D orientation and strain map of the studied microstructure with spatial and angular resolutions of $1.5\,\mu$m and $0.01\,^\circ$, respectively [101]. Owing to its high bandpass probe, DAXM mapping is not flux limited, but slow scanning of the differential aperture sets as the rate determining step.

DAXM has becoming to address to a wider audience, especially in metallurgical commu-

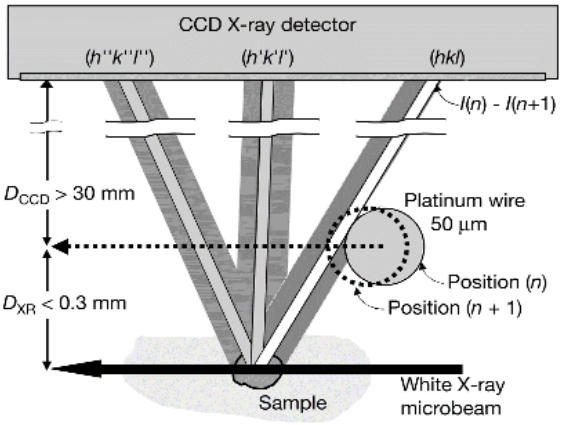

Figure 2.22: The detection geometry of DAXM. For each rastering point, a knife-edge — preferably a high-Z wire- is scanned over the sample surface, enabling the depth profiling of the observed diffraction spots. The figure is adopted from [100].

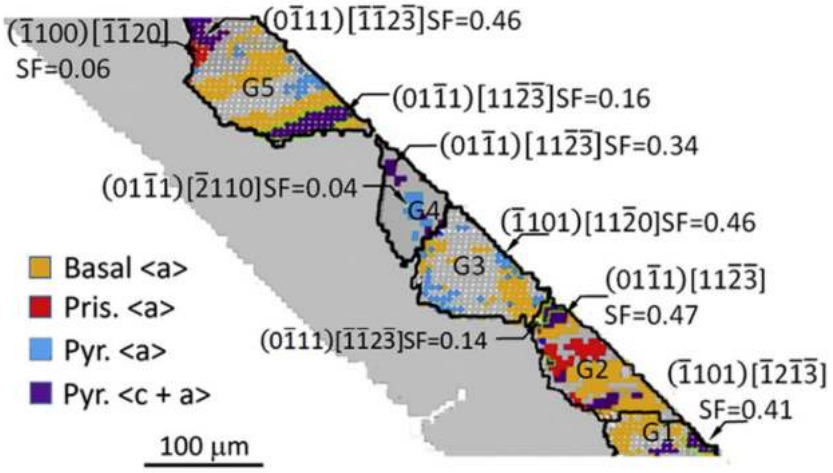

Figure 2.23: Characterization of GNB bands in Mg-Y alloys with DAXM through diffraction peak streak analysis. The figure is adopted from [102].

nity. Figure 2.23 shows a deformation processing related example use of DAXM. It can be seen from the figure that DAXM mapping is capable of characterizing the crystallography and spatial distribution of GNB bands in deformed microstructures. However, the constitution of such bands fall below the resolution limits of DAXM technique.

3 High Resolution 3DXRD

In this chapter, the description of deformed microstructures and the 3DXRD methodology given in Chapter 2 will be used as a starting point to derive a new 3DXRD modality, called *High Resolution-3DXRD* microscopy. Notably the aim is to simultaneously improve both the spatial and angular resolution in comparison to existing 3DXRD modes - and this without reverting to a (slow) scanning modality, as emphasis is on mapping the microstructure evolution. To facilitate this I will use *a priori* knowledge of deformation microstructures, as presented in section 2.1.

The chapter will start by introduction of the *high resolution* concept for the 3DXRD technique, by considering the scattering properties of deformation microstructures, together with the current methodology of 3DXRD modalities. Then, the proposed experimental geometry of *HR-3DXRD* will be presented for both numerical simulations and for actual experiments by discussing its experimental geometry with respect to the experimental global parameters. The chapter will conclude by comparing the *HR-3DXRD* methodology to the well established NF and FF 3DXRD approaches, and their emerging modalities.

3.1 The high resolution concept

In Section 2.2.1, different 3DXRD methods are compared with respect to their sensitivity for observing spatial and angular degrees of freedom. Near-field and far-field approaches are presented, corresponding to a Fresnel number substantially higher than 1, and substantially lower than 1, respectively. As stated in Section 2.2.1, these approaches will result in a maximized sensitivity of spatial variations for NF-3DXRD and conversely a maximized sensitivity in orientation and strain for FF-3DXRD. To our knowledge„ the mid-field regime having a Fresnel number of ≈ 1 has never been studied before within the context of 3DXRD microscopy.

The work presented in this Thesis is inspired by report by Ahl, Poulsen, Detlefs et al. [5]. In this study, a set of distinct diffraction spots from a recovered deformed grain in AA1050 alloy is observed through placing a high resolution imaging detector approximately in the mid-field regime. From this, it became clear that the subgrains are near perfect single crystals and that the associated diffraction spots are sufficiently intense to be observed, if they can be separated. In this experiment, it was reported that the observed diffraction peaks possessed no information about the shape of the subgrains. Furthermore, the authors state that they had not observed any further intensity or scattering features related to internal structure of the (sub)grains. As only a very small portion of the reciprocal space information was observed, *the analysis given in [5] was strictly limited to the statistical study of the observed diffraction spots*. The details of this study will be further discussed below.

As 3DXRD in the mid-field range was unknown territory, before we explain the details of the proposed *high-resolution modality*, we emphasize the list of theoretical and practical questions that arose at the very beginning of the presented work. These questions include:

- What are the experimental requirements for performing a mid-field 3DXRD experiment? What are the required experimental parameters (e.g. detector resolution, detector's positioning accuracy, long-term stability of the experimental setup, etc.) for resolving subgrains with $\approx 1\,\mu$m fidelity?

- Are the required experimental hardware available in grain-mapping and/or materials science beamlines? Can a demonstration experiment be performed with existing, sub-optimal instrumentation?
- What method of analysis and/or reconstruction is appropriate for such datasets? Can the existing codes be used, or does the technique demands new software to be developed? A particular concern here was the indexing algorithm: existing algorithms were not developed with this case in mind.
- What method of simulation is appropriate for modelling such technique? Can the existing codes be used, or does the technique demands new software to be developed?
- How can we quantify the experimental inaccuracies due to the attained setup (e.g. alignment errors, mechanical vibrations, etc.)?

In this thesis I will discuss these questions by means of theoretical explanations, numerical simulations and experimental realizations of the proposed mid-field HR-3DXRD technique.

The fundamental aim of HR-3DXRD is to visualize the microstructural details of moderate-to-highly deformed metals and alloys. Therefore, in order to derive the concept of *high resolution*, one needs to make use of the information from the extensive literature on electron microscopy studies of deformed metal microstructures and the scattering properties of their building blocks, namely subgrains (or cells). Referring to Section 2.1, it is well known that subgrains are near perfect crystals of $\approx 1\,\mu$m size, having a well defined orientation with a homogeneously defined elastic strain [4, 14, 16]. Scattering-wise, in a diffraction experiment that assumes to be free of instrumental broadening, the width of a diffraction spots can be expressed as

$$\text{FWHM} \approx D + \boldsymbol{L}\alpha, \tag{3.1}$$

where FWHM is the full width at half maximum of the diffraction spot, D is the size of the diffracting unit (in this case size of a subgrain), $\boldsymbol{L}$ is the sample-to-detector distance and α is the angular divergence due to diffracting from a lattice. The mentioned fundamental properties of subgrains imply that in a diffraction experiment, the angular divergence, α, of diffraction spots emanated from subgrain lattice will be close to the Abbe diffraction limit λ/D. This leads to the width of a diffraction spot to be a weak function of the sample-to-detector distance, $\boldsymbol{L}$ until the distance where the real space dimension of the diffracting unit is the same as the size broadening: that distance corresponds to a Fresnel number of 1. . In other words, the diffraction spots are expected to have a rather constant width, regardless of the sample-to-detector distance. Thus, considering a detector with a constant and finite resolution, increasing $\boldsymbol{L}$ would provide two improvements:

- The angular resolution of the experimental setup will improve due to better sampling on the detector frame, and
- The distance on the detector of neighboring diffraction spots will increase, and hence the likelihood of overlapping diffraction spots will decrease.

It should be noted that, due their reciprocal relationship, the former improvement of angular resolution is achieved at the cost of reduced detector field of view (FoV) in both direct and reciprocal space.

From a crystallographic perspective, diffraction peak shapes emerging from subgrains are expected to be composed of the broadening due to mentioned relation of beam divergence

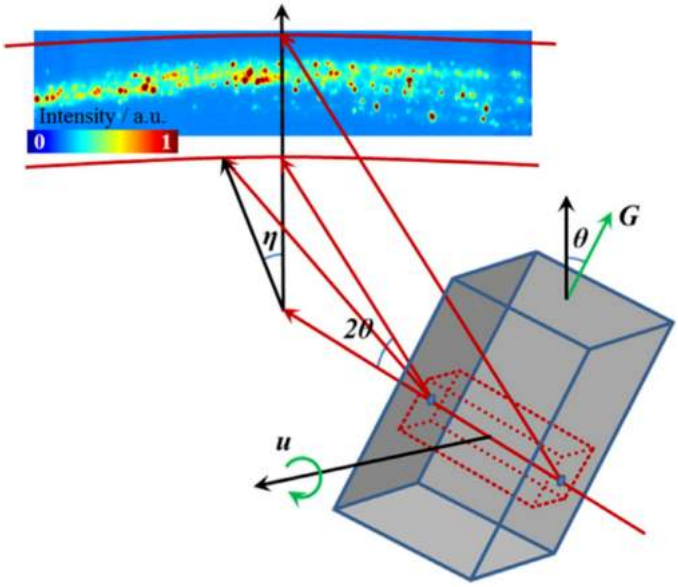

Figure 3.1: Schematics representation of the experimental setup in Ahl et al. [5]. In this study, a high resolution imaging detector was placed at mid-field regime, for observing the individual diffraction spots emanated from subgrains during the late recovery stage of 50% recrystallized AA1050. Considering the definitions given in this thesis, we can retrospectively regard the Ahl et al.'s report as an **Mode-I** implementation of HR-3DXRD method. Please note that, unlike the presented Mode-II HR-3DXRD method in this thesis, the report by Ahl et al. comprises **no information** about the position of the subgrains within the analyzed sample volume, since indexing of the diffraction peaks was not possible due to limited azimuthal coverage of the employed detector. Figure adopted from [5].

and Abbe diffraction limit, and the bandwidth of the incident beam. The former component is a weak function of the Bragg angle, 2θ, whereas the latter is a user-defined experimental parameter. Hence, the diffraction spot shapes for HR-3DXRD will be a dominated by the bandwidth of the incident beam, with comparable shapes for all hkl values with weak 2θ dependence. For sufficiently high incident beam flux, it is known that the center-of-mass (CoM) position of diffraction spots can be determined with an accuracy better than 10% of its size with the currently available analysis tools [103]. It is further known that the real space position of (sub)grains is calculated from the cumulative collection of its indexed peaks. The accuracy of this calculation is known to vary as $\sqrt{N}$ [104].

As explained in Section 2.1.2, the nature of a deformation microstructure is inherently multiscale; a collection of subgrains form GNB bands, a number of these bands form grains, and an ensemble of grains form the microstructure. The misorientation relationship between these hierarchical levels are on the order of a degrees, to few degrees and few tens of degrees, respectively. A diffraction pattern obtained from a deformed sample is also expected reflect this *multiscale* behaviour. Such misorientation relations can be utilized for selecting diffraction signals from different deformed grains. Then, using the same strategy, the diffraction signal from individual bands can also be separated. This will allow the study of different orientation fibres, even on intragranular level. Separation of diffraction signals will in turn decrease the number of observed diffraction spots, hence, decreasing the probability of spot overlap.

Within the light of these information, we can formalize the *high resolution* concept as the following:

- Deformed microstructures and their diffraction patterns show a structural hierarchy, from grains measuring of tens of micrometers to subgrains of $\approx 1\,\mu$m. Observation of this multiscale structure requires a high resolution in both real space and in reciprocal space,
- Experimentally, a setup with Fresnel number of ≈ 1 can provide increased sensitivity for both real space and reciprocal space,
- The angular resolution can be enhanced by using a high resolution detector with adequately small pixel size,
- The sample-to-detector distance, $\boldsymbol{L}$ should be optimized for both angular resolution and diffraction spot separation,
- After these optimisations, the diffraction spots shall be detected with an superior accuracy,
- Volume of subgrains can be deduced from integrated intensity of diffraction spots [63].

This approach was first demonstrated by [5] for a 3DXRD **Mode-I type** experiment for following the late recovery behavior of 50% recrystallized AA1050 alloy under *in situ* heating conditions. Figure 3.1 shows the experimental configuration. A high resolution detector with $0.625\,\mu$m effective pixel size was placed off of the optical axis, to cover 9.5° azimuthal portion of (111) rings ($2\theta = 19.1^\circ$). The experiment was performed at 16 keV, by placing the high resolution detector $\boldsymbol{L} = 22$ mm away from the sample. As the average grain size of the subgrains are approximately $1\,\mu$m, the calculated Fresnel number (see Equation (2.12)) of this setting is 0.59. Here, subgrain reflections were quickly tracked in interrupted annealing steps, by performing a narrow ω-scan in 2° range with steps of 0.05° [5].

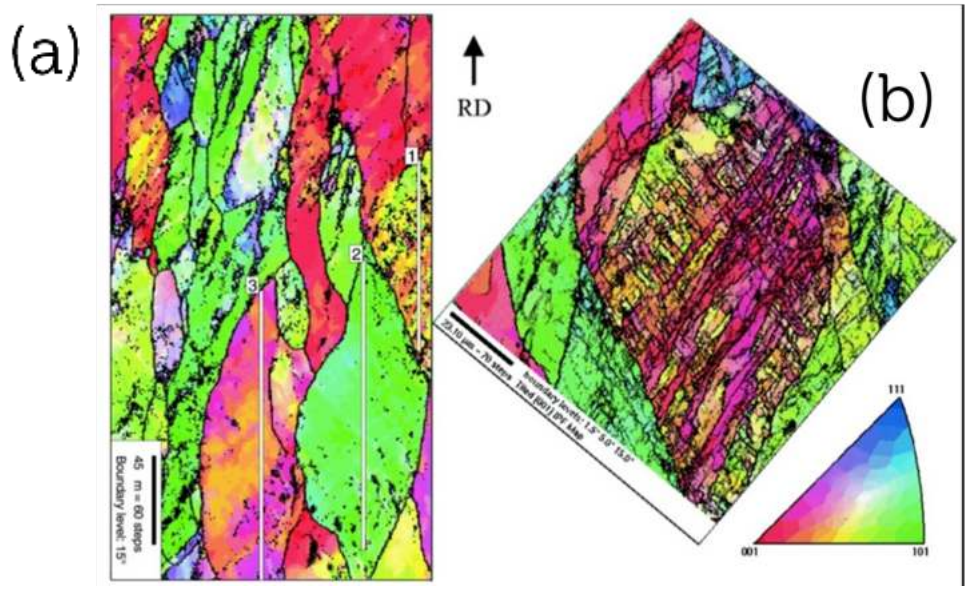

Figure 3.2: EBSD maps of 40% cold-rolled AA1050. (a) A map of 30 grains with a step size of $0.75\,\mu$m. Black regions show misorientations larger than $15\,^\circ$. (b) A detailed map of a highly subdivided grain with a step size of $0.3\,\mu$m. Black regions show misorientations larger than $1.5\,^\circ$. Figure retrieved from [105].

The authors have reported the evolution of ≈ 500 individual subgrain during the late stage of recovery.

Regarding the discussed Ahl study [5], we would like to remind the reader that the mentioned paper does not entitle itself as neither a high resolution modality of 3DXRD microscopy technique, nor regards itself as a Mode-I microscopy modality. The reported analysis by Ahl et al. comprises **no information** about the position of the subgrains within the analyzed sample volume, and indexing of the diffraction peaks was not possible due to limited azimuthal coverage of the employed detector.

As mentioned in Section 2.2.1, Mode-I scans are targeted for fast acquisition schemes for tracking the dynamics of structural changes. Thus, we can ***retrospectively*** regard the described experiment in [5] as the *high resolution* extension of Mode-I 3DXRD microscopy [4, 63, 64]. These Mode-I type experiments provide no information about the spatial position of the (sub)grains, due to detection of low number of diffraction peaks originating from the same diffracting unit.

In this study, I generalize the mid-field setup to *high resolution* 3DXRD microscopy, a strategy for ***Mode-II type CoM mapping experiments***. If one can observe the complete diffraction pattern of 2π range in azimuth for a set of Debye-Scherrer rings, this would enable determination of the observed subgrains in the analyzed volume through indexing. The indexed grains are then can be refined for creating a 3D center-of-mass map of the subgrains by utilizing the center-of-mass mapping reconstruction (for example as in [57]). Such analysis would provide detailed orientation maps of deformed microstructures. Furthermore, within the same procedure, the volume of subgrains can be determined from the cumulative of integrated intensities of its assigned reflections. This information can be used for creating 3D volumetric maps by Laguerre tessellation (The mentioned analysis procedure for HR-3DXRD will be presented in Section 4.1).

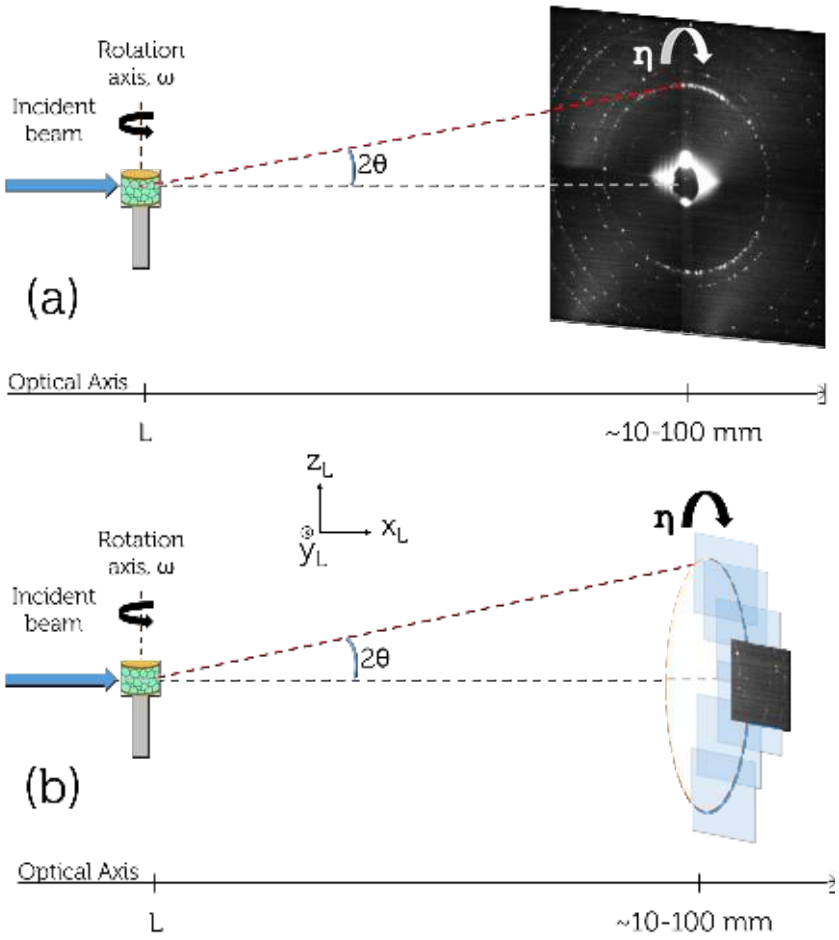

Figure 3.3: The proposed experimental setups for High Resolution 3DXRD microscopy. Depending on available detector FoV, HR-3DXRD experiments can be done with (a) a large detector or with (b) patches of low FoV detector images. Laboratory coordinate system is given for both configurations.

The characteristics of the deformation microstructure require HR-3DXRD to satisfy certain spatial and angular resolution. Figure 3.2 shows two EBDS maps of a 40% cold-rolled AA1050 alloy with two different resolution settings. It can be seen that the low resolution setting provides limited information about the intragranular orientation variations in the deformed grains. In comparison, the high resolution setting (rastering step size of $0.3\,\mu$m, black regions having misorientations smaller than $1.5\,^\circ$) resolves the GNB band structure inside a highly deformed grain. These resolution constrains can be further narrowed down considering the boundary spacings and misorientations of the IDB and GNBs. The spacing and misorientation values of IDB and GNBs in the medium-to-high deformation regime ($0.3 < \varepsilon < 1.0$) reach as low as $\approx 0.5\,\mu$m and $\approx 0.1\,^\circ$ (see Figure 2.6). Therefore, HR-3DXRD needs to determine the grain center positions with an accuracy of $\approx 0.3\,\mu$m and misorientations with an accuracy of $\approx 0.01\,^\circ$.

One may argue that the intensity profiles of the diffraction spots in the mid-field will be complicated to describe - as they are in the Fresnel regime - and may be influenced by a range of instrumental artefacts, related to e.g. partial coherence and reciprocal space resolution. In addition comes blurring caused by the sample itself, such as the diffraction due to the limited size of the subgrains and broadening due to isolated dislocations within

the interior of a given subgrain.

In that respect, I note that a center-of-mass type of analysis is a very robust approach.A basic principle of optics going back to [106], is that the CoM position of a propagating X-ray beam will always follow a straight line, irrespective of coherence etc (for the proof of this statement, please refer also to Appendix A [107].) Therefore, the CoM position of an isolated diffraction spot in a HR 3DXRD experiment will follow a linear path with respect to the propagation distance. This linearity is underlying existing Mode-II analysis and simulation algorithms dedicated for far-field 3DXRD. Hence, due to this general optics property related to the CoM of beams, I argue that the readily available forward projection programs for far field 3DXRD simulation are suitable also for the forward simulation of Mode-II HR-3DXRD datasets.

This still leaves the question of spot overlap, where the diffraction profile evidently matters. But experimental evidence points towards the spot dimension being dominated by the instrumental resolution function, which can be represented well by the forward models.

3.2 Experimental setup

Figure 3.3 shows the proposed experimental setups for implementing the *high resolution* methodology, presented above. As seen from the figure, the setup consists of two main components: a sample stage with a tomographic rotation table — for ω-scanning — and a detector stage holding the high resolution detector. There are no special requirements for the sample stage. However, its rotation axis is expected to be aligned perpendicularly to the optical axis. For the detector stage, two different configurations are proposed:

1. A single high resolution imaging detector with a large number of pixels, e.g. $\approx 15,000$ by $15,000$ pixels (Figure 3.3(a)), sufficient to cover the whole azimuthal range in a single ω-scan, for a relevant number of $(hk\ell)$ rings.

2. A single high resolution imaging imaging detector with a small FoV, e.g. ≈ 2048 by 2048 pixels (Figure 3.3(b)) can be used to cover a portion of azimuthal range in single detector frames. The full azimuth range can be covered by translating the small FoV detector around the Debye-Scherrer rings (within the plane defined by y_L and z_L axes) and repeating the ω-scan.

The first approach (Figure 3.3(a)) can be seen as a mid-field variant of classical FF-3DXRD with a much higher ratio of FOV to spatial resolution. The detector's center is placed to coincide with the optical axis. Depending on the sample-to-detector distance, the detector's extent of FoV defines the observed 2θ range. For each ω-step, all sub-grain reflections within the 2θ range are captured regardless of their azimuthal angle η on the detector frame. At the time of writing this text, it is known that high resolution imaging cameras with large number of pixels are being developed, yet currently, they are not commercially available. In this respect, the former configuration is therefore only used in numerical simulations of HR-3DXRD experiments.

The second approach relies on patching partially observed η ranges of Debye-Scherrer rings. As in the case of [5], the small FoV would only cover a limited portion of the 2π azimuthal range. For a certain hkl ring, such coverage, $\Delta\eta$ can be determined with respect to sample-to-detector distance and pixel size. Then, the number of detector positions can be calculated by,

$$\mathsf{N}_{\text{detector}} \geq 2\pi/\Delta\eta. \tag{3.2}$$

In order to cover the full azimuthal range, the detector should be translated along its plane (i.e. plane defined by y_L and z_L axes) to the predetermined detector positions and perform an identical ω-scan at each position. In the end, one would end up with patches of 3DXRD scans for the number of measured detector positions. These images could be merged with various methods for obtaining the large FoV detector images. Strategies for such operations will be discussed in Section 5.3.

3.3 HR-3DXRD vs. present approaches

If we compare the explained high resolution approach to the classical 3DXRD methods, one can realize that HR-3DXRD offers interesting attributes with respect to its predecessors. In this section, we will qualitatively discuss HR-3DXRD's capabilities with respect to classical and emerging 3DXRD methods.

As described in Section 2.2.1.3, NF-3DXRD and its sister methods (NF-HEDM, DCT, etc.) have a superior sensitivity for spatial variations due to exploiting the near-field regime. These properties enable near-field methods to be capable of retaining the shape of grains and thus the grain boundary structures. To a first approximation, the spatial resolution of near-field reconstructions is determined by the effective pixel size of the detector. Whereas in HR-3DXRD, the spatial resolution is dictated by the accuracy of the determined CoM positions of individual subgrains via indexing and refinement of multiple diffraction spots of regular shapes and adequate intensity. Therefore, we can say that although HR-3DXRD offers a comparably worse spatial sensitivity, for an optimized setup, the detailed sampling of each subgrains' pole figure enables HR-3DXRD to provide better spatial resolution for determining grains' CoM position than NF-3DXRD. However, HR-3DXRD provides no information on the subgrain boundaries due to progressive blurring of the diffraction spots with increasing $\boldsymbol{L}$. The subgrain boundary structure has to be inferred from HR-3DXRD data by tessellation methods. It was previously reported that such methods enable retrieving the boundary microstructure with high confidence [67] for Mode-II far-field 3DXRD technique. From volume determination perspective, it was shown that tessellations lead to slightly worse definition of the boundary structure than NF methods due to inaccurate determination of grain volumes [41]. Nevertheless, HR-3DXRD can leverage its Mode-II type CoM maps through tessellations within reasonable confidence. This enables HR-3DXRD to produce NF-3DXRD type 3D maps composed of submicron sized grains with superior angular resolution.

Hypothetically, supposing a HR-3DXRD experiment at 52 keV with a detector (with pixel size of $2.93\,\mu$m) placed 70 mm behind the sample, the angular coverage of a single pixel would be 0.0024° in 2θ direction. In order to understand the extent of this, we will propagate this parameter to NF and FF-3DXRD configurations. In order to achieve the same angular coverage for a NF-3DXRD experiment at the same energy and placing the detector 7 mm behind the sample, the required pixel size should be $0.3\,\mu$m. Although such small pixel sizes can be achieved with some considerable effort with the current indirect X-ray imaging detectors, the exemplified NF-3DXRD configuration would be prone to spot overlap. This, in turn, would limit its usage for imaging microstructures of low end of the deformation spectrum. In comparison, HR-3DXRD offers a versatile configuration gamut via optimization of its global parameters and detector configuration.

In the other end of the optical spectrum, FF-3DXRD and related methods (FF-HEDM, etc.) present a superior sensitivity for variations of orientation and strain. This sensitivity is exploited by placing the detector quite far away from the sample stage, $0.5-1.5$ m depending on the pixel size. Albeit its great reciprocal space resolution, the far-field methods are less sensitive to real space variations. The center-of-mass position of grains are calculated

as a correction term on the determined orientation. Far-field experiments most usually employ detectors with large pixel sizes, ranging from approximately 50 to $200\,\mu$m. For example, Oddershede and coworkers have reported $10\,\mu$m CoM position accuracy with a detector of $50\,\mu$m pixel size [66]. Supposing the ratio between the detector's pixel size and attained spatial resolution is constant for Mode-II 3DXRD experiments, the spatial resolution of a HR-3DXRD experiment with $2.93\,\mu$m pixels can be estimated as $\approx 0.1\,\mu$m. In the Section 4.7, we will show via numerical simulations that such spatial resolutions can be achieved with HR-3DXRD methodology. Hence, the overall accuracy of determining CoM positions from FF-3DXRD and HR-3DXRD is expected to show a similar performance.

From an angular resolution perspective, HR-3DXRD's small pixels approach offers a better resolution with respect to FF-3DXRD. In a usual FF-3DXRD setup, an angular resolution of $10^{-2}\,^{\circ} - 10^{-3}\,^{\circ}$ can be easily achieved [33]. In Section 4.4, we will show that angular resolution of $10^{-4}\,^{\circ}$ or better can be achieved with HR-3DXRD due to its small pixel size and large FoV. Supposing the hypothetical HR-3DXRD setup given above, the angular coverage of a single pixel would be 0.0024° in 2θ direction and 0.02° in the horizontal section of η direction. Furthermore, suppose that the ω-width of the diffraction spots are equivalent to the ω step size, and the spots are detected in multiple ω-steps. Then, we can deduce that the angular resolution for position of diffraction peaks will depend on the fitting quality of the 3D diffraction peak in 2θ, η and ω directions. The small pixel size of HR-3DXRD assures a better angular sampling of the 3D diffraction peak than FF-3DXRD. Hence, HR-3DXRD is expected to attain a substantially better angular resolution to its far-field counterparts.

Apart from the classical 3DXRD techniques, we shall briefly compare HR-3DXRD to the emerging 3DXRD techniques with intragranular resolution (Section 2.2.2). The comparison of HR-3DXRD to scanning FF-3DXRD would be similar to the presented analysis to the far-field methods. Accordingly, we expect that the angular resolution capability of HR-3DXRD to be substantially better than scanning FF-3DXRD. Nevertheless, the marked difference between these methods reside in their experimental strategies. As mentioned in 2.2.2.1, the scanning method utilize a raster-scanning approach with a pencil beam. The rastering is performed with the use of a sample translation stage with $\approx 100\,$nm resolution [80]. In comparison, HR-3DXRD proposes to a well-known line beam approach. Therefore, it can be said that raster-scanning of a pencil beam to be an inherently slow approach. Considering the multi-panel acquisition approach presented in Section 3.1, HR-3DXRD could also be deemed as a slow method, as well. However, this can be remedied by considering the angular extends of the studied microstructure and accordingly optimizing the experimental parameters of HR-3DXRD, such as decreasing the number of panels via optimization of $\boldsymbol{L}$ and detector's effective pixel size.

In the approach combining near and far-field HEDM analysis [84], the deformation microstructure is first observed by precise determination of the angular spread of orientations from FF-HEDM, then these so-called "orientation envelopes" are used for voxel-by-voxel refinement of intragranular orientation and strain variations through NF-HEDM analysis. The mentioned method retrieves its intragranular resolution in the data analysis step and it requires only two scans. Thus, comparing to the currently available multi-panel HR-3DXRD, this method is experimentally much faster. However, it should be stated that the [84] approach has a limit in deformation scale. As mentioned in 2.2.2.2, the method combines the observed orientations with low misorientation together into "orientation envelopes" in the far-field. The resulting orientation envelopes are refined over the observed area of each near-field diffraction spots. It is known that with increasing deformation levels, the diffraction spots start to smear out in the azimuthal direction, increasing the prob-

ability of diffraction spot overlap [3, 28]. Thus, for medium-to-high deformation levels, the spot overlap would be highly expected in the NF-HEDM scans. In comparison, HR-3DXRD probes a single deformed grain and also makes use of the sharp boundaries (i.e. IDBs and GNBs) of medium-to-high deformation deformation levels. Hence, considering an in situ deformation experiment, one can use the same experimental setup for using two techniques in tandem: one may use the [84] approach for imaging low deformation microstructures and with increasing deformation levels, the selected deformed grain can be imaged in a zoom-in manner with HR-3DXRD.

The approach of [86] (Section 2.2.2.3) has similar limitations to the previous example. Compared to the approach of [84] using a line beam, the novel DCT analysis is more prone to spot overlap due to its box beam collection strategy. In this case, the optimization of $\boldsymbol{L}$ for reducing the spot overlap is not trivial. One can increase the $\boldsymbol{L}$, in expense of 2θ range. However, the depressed $\boldsymbol{Q}$-range will cause a decrease in the reconstruction accuracy.

Lastly, we should emphasize that the use of novel methods involving NF-3DXRD (i.e. Nygren and Reischig-Ludwig methods) for visualization of the deformation microstructures are essentially limited by their spatial resolution. In contrast, HR-3DXRD remedies the spatial resolution problem through its novel experimental configuration and consequent Mode II analysis by providing sub-micrometer spatial resolution.

3.4 Aim

The discussion given above shows a potential such that a mid-field technique could offer superior spatial and angular resolution over currently available 3DXRD (or HEDM) methods. Reaching such resolutions will in turn provide a detailed information about the deformation microstructures of medium-to-high strain with adequate real and reciprocal space resolutions. As discussed above, by considering the a priori knowledge on deformation microstructures and employing them as the outlined *high resolution* strategy, one can enable EBSD-type yet non-destructive characterization of the deformation microstructures with the HR-3DXRD technique. Thus, this thesis aims to present and develop the *high resolution* strategy for 3DXRD microscopy.

In the following chapters, we are going to explore the proposed new *high resolution* paradigm for 3DXRD microscopy. In Chapter 4, the limitations and applicability of HR-3DXRD will be discussed in the light of numerical simulations. Then, in Chapter 5, efforts for experimental realization of HR-3DXRD will be discussed. The thesis will end with Chapter 8, by presenting the conclusions and recommendations for future experiments.

4 Simulations of HR-3DXRD

In Chapter 3, the *high resolution* concept for 3DXRD microscopy is derived by combining *a priori* knowledge on deformation microstructures and their scattering properties. In this chapter, I will present extensive full scale numerical simulation studies of the HR-3DXRD technique. These will address two fundamental challenges:

- The feasibility of indexing HR-3DXRD type data sets. Existing far-field indexing algorithms are developed for cases where the spot density is much lower and the ratio between diffraction spot translations due to orientation and spatial degrees of freedom is very different from than in HR-3DXRD.
- The increased ratio between FoV and pixel size as well as a need for smaller ω-steps implies that HR-3DXRD data sets are an order of magnitude larger in size than conventional 3DXRD. Memory and data handling issues implies that the entire data analysis chain must be reconsidered.

The chapter will first present the simulation and analysis tools and analysis methods in Sections 4.1 and 4.2. In Section 4.3, we will do an initial validation of the analysis pipeline with a short study on the effect of ω-step size. Then, in Section 4.4, HR-3DXRD technique will be validated with randomly oriented grain ensembles of various population, for observing the extent of the presented method. Beside the ω-step size effect, the chapter will continue by presenting limitations of the technique through two more cases: the study of systematic error in the detector frame in Section 4.5 and the effect of signal-to-noise response in Section 4.6. Lastly, the chapter will finish with presenting a numerical proof-of-concept study with physically representative phantoms in Section 4.7.

4.1 Software pipeline

In Section 3.1, it is indicated that HR-3DXRD can be seen as a high resolution modality of the well-established Mode-II CoM mapping measurements [33, 57]. As explained in Section 2.2.1, CoM mapping is a branch of classical far-field 3DXRD. Hence, it seems a natural choice to attempt to pursue the simulations with the tools of FF-3DXRD to the extent possible. The applicability of a FF forward simulator was argued to be fully adequate previously, while the applicability of FF-3DXRD data analysis algorithms [30, 37, 59, 108, 109], in particular for indexing, is unknown.

With these comments in mind, the proposed data analysis pipeline is shown in Figure 4.1. The pipeline commences with the generation of synthetic data based on a used-supplied phantom. Synthetic data are generated with the far-field PolyXSim software of the FABLE package [110]. The phantom is composed of a number of grains. Each grain is described in terms of its CoM position in 3D, its orientation matrix and its volume. PolyXSim simulates a virtual diffraction experiment for the given experimental settings, by calculating the scattering vectors of the supplied phantom. From the calculated scattering vectors, synthetic diffraction images are generated. The diffraction spots are harvested from these images, and are then subjected to indexing and refinement steps. Optionally, the refined grain ensembles are tessellated for obtaining ESBD-type three dimensional maps.

The analysis operates on two different analysis routes:

Table 4.1: List of global parameters used in the numerical simulations.

Global parameters for simulations	
Energy (wavelength)	52 keV (0.23843 Å)
Sample-to-detector distance, $\boldsymbol{L}$	70 mm
Field of view	15,000 pixel x 15,000 pixel
Pixel size	2.93 μm
Detector y-center	7,500 px
Detector z-center	7,500 px
Detector $tilt_x$	0 °
Detector $tilt_y$	0 °
Detector $tilt_z$	0 °
Wedge angle	0 °

- The *direct route* takes the simulated diffraction peaks and global parameters as outputted by PolyXSim. This route by-passes the synthetic diffraction images, thus, it serves to illustrate the ideal experimental conditions, without degradation from detection noise, spot overlap, etc.
- The *harvested route* takes the simulated synthetic diffraction images as its input. Diffraction spots are then harvested from these images to be used in indexing. The harvested route represents the actual experimental conditions, as synthetic images are subject to finite detector resolution, noise and spot overlap.

The reader should bear in mind that the mentioned analysis routes only differentiate with respect to their inputs for the indexing stage. Starting from the indexing step, both routes will follow the remainder of the pipeline identically. In this chapter, all of the presented simulations studies follow the presented pipeline. Any deviation from the presented procedure will be indicated in the respective sections, individually. In the following sections, Figure 4.1 will be presented in a step-wise manner.

4.1.1 Synthetic Data Generation

In this study, I use the PolyXSim software of the FABLE software package [110]. PolyXSim is a classical FF-3DXRD simulation software, that is capable of producing randomly oriented polycrystalline phantoms with defined size, orientation and CoM positions. It allows taking into account the instrumental resolution. Regarding the similarities between FF-3DXRD and HR-3DXRD, PolyXSim was utilized for the current study by choosing the appropriate detector and experimental global parameters.

Synthetic data was produced with PolyXSim [110] from a user-provided phantom. The phantoms are provided to PolyXSim by specifying the CoM position, orientation and volume of the constituent (sub)grains. The experimental geometry is specified through global parameters, given in Table 4.1. The incident beam was assumed to be ideally parallel and monochromatic with a given bandwidth. The virtual two-dimensional detector frame is assumed to be free of distortions, and its center is positioned to coincide with the optical axis. The detector rotations around three possible axes are set to zero. Omega scans are done according to the specifications given in Table 4.2. The phantom is chosen to be pure α Iron (space group # 229, $Im\bar{3}m$) with lattice parameter of 2.856 Å. Following the discussion presented in Section 3.1, in all of the presented phantoms, constituent subgrains are assumed to have a homogeneous elastic strain. For purposes of simplicity, the presented simulations will assume that such homogeneous elastic strain are zero for all constituent subgrains.

Table 4.2: ω-scan specifications used in the numerical simulations.

ω-scan	
Range	$[0^\circ, 360^\circ]$
Step size	0.1°

PolyXSim generates the synthetic data by calculating the normalized scattering vectors from the user-specified phantom with respect to the specified global parameters. The calculated normalized scattering vectors are outputted as a list in ASCII format (i.e. ".gve" file, column-file format of ImageD11 [111]) and synthetic diffraction image frames in ".tiff" format. The normalized scattering vectors follow the definition given in Equation (2.6).

The generated synthetic diffraction frames do not constitute any fluctuating background nor noise. Furthermore, the point spread function of the pixels are assumed to be 0. According to the assumed global parameters, synthetic detector frames cover 6 full and 6 partial hkl-rings. The angular coverage of each pixel is $0.0024\,^\circ$ in 2θ and $0.02\,^\circ$ in the horizontal axis of η direction. The size of a single synthetic frame is $450\,$MB and the cumulative size of a full ω-scan is $1.6\,$TB.

For the latter, the synthetic images are needed to go through image pre-processing (optional), followed by the peak harvesting processes. The input is derived via converting the harvested diffraction spots to normalized scattering vectors through the defined global parameters.

4.1.2 Image Processing and Peak Harvesting

This stage is only applicable to the harvested analysis route. Before the peak harvesting stage, the synthetic diffraction images are first preprocessed for background subtraction, if they comprise any fluctuating background. The processed images are then fed to the *peaksearch* module of the FABLE package [111] for determining the position and intensity of the diffraction peaks. In the case of no background images, the watershed threshold of peak-searching algorithm is set to zero. For images having a fluctuating background, the watershed threshold was set as the corresponding mean value of the fluctuating background. The harvested diffraction peaks are converted to normalized scattering vectors through the defined global parameters.

4.1.3 Indexing

Identifying a suitable approach for indexing was a major time-consuming part of the Thesis work. From the outset, it appeared that an entirely new algorithm may be the proper solution. To avoid this complication, it was decided to attempt using the existing FF-3DXRD algorithms available in the FABLE package. A number of adaptations and combinations of software were tested, until it was revealed that - at least for the phantoms used - it is possible to define tolerances etc. such that the indexing of the synthetic datasets could be performed with Grainspotter software [59]. This had the added benefit that the entire data analysis pipeline then could be made similar to FF-3DXRD, as illustrated in Fig Figure 4.1. However, the increased volume of the data sets required numerous parsers etc. to be made.

In the indexing step, the direct route uses the list of scattering vectors in ASCII format and the harvested route gets the harvested scattering vectors from generated synthetic diffraction frames as its sole input. Grainspotter is let to identify grains through indexing each grains orientation, together with refining its CoM position in real space. The indexing tolerances are varied for different simulation examples. Thus, in order to avoid confusion, the employed tolerances will be indicated in their respective sections.

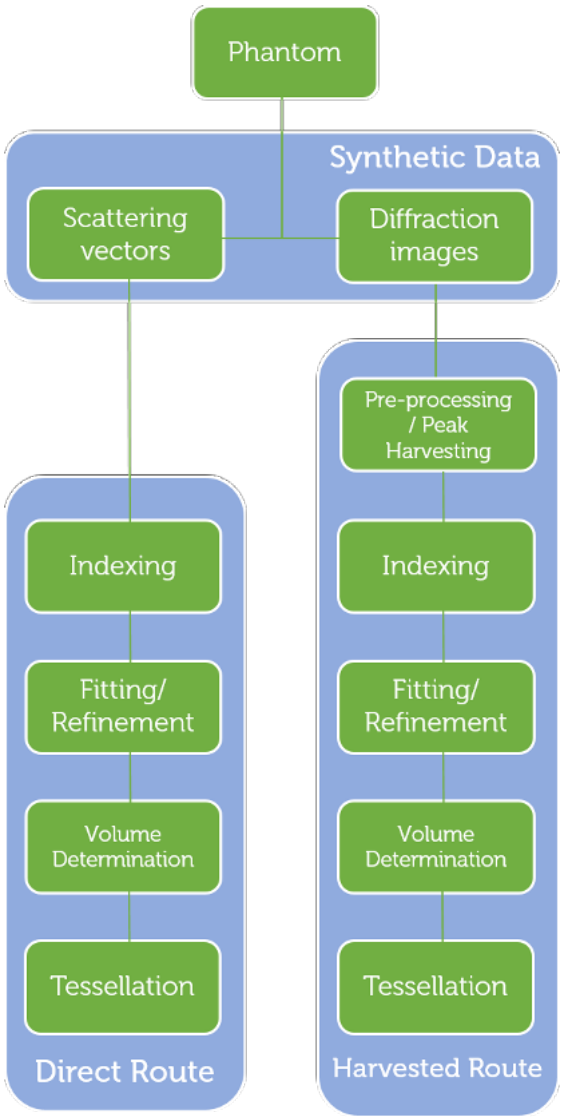

Figure 4.1: Flowchart of the software pipeline adopted for the numerical simulations, shown for direct and harvested analysis routes. Figure adopted from Paper 2 on the List of Publications.

The indexing scheme outputs a list of grains with their respective CoM positions and UBI matrix [26, 27] and a list of assigned reflections.

4.1.4 Fitting and Refinement

In a far-field 3DXRD analysis for obtaining Mode-II type CoM maps, the indexing is usually done by assuming the grain CoM is positioned at the CoR [57]. After the indexing step, the found orientations are subjected to refinement. In the refinement stage, the UBI matrices of the indexed orientations are refined by fitting the CoM position and by further re-assignment of the scattering vectors[1]. The assigned scattering vectors were re-assigned to indexed grains by successively decreasing a hkl tolerance of assigned peaks. The hkl tolerance is defined as

$$hkl_{\text{tol}} = \sqrt{(h_{\text{obs}} - h_{\text{theory}})^2 + (k_{\text{obs}} - k_{\text{theory}})^2 + (l_{\text{obs}} - l_{\text{theory}})^2}, \tag{4.1}$$

where "obs" stands for the observed hkl values and "theory" stands for the theoretically calculated hkl values from grain's found[2] orientation.

For HR-3DXRD case, we let the indexing program to find grains, together with refining its CoM position. These assignments are found to be *complete* but not *pure* (see Section 4.2), thus requiring a refinement stage. The found grains are subjected to refinement by using the *makemap* module of ImageD11 [111]. For all of the presented analysis, the refinement is commence with a relatively high hkl tolerance, and it is successively decreased until both orientation and CoM position errors of the entire grain ensemble reaches a saturation.

The refinement output is similar to the indexing step. It consists of a list of grains with their respective CoM positions and UBI matrix [26, 27] and a list of assigned reflections.

4.1.5 Volume Determination

The volume of a diffracting grain can be approximated as the ratio of the integrated intensity of its diffraction spots and the Lorentz factor [27],

$$\mathsf{V}_{\text{subgrain}} = \frac{\mathsf{I}_{\text{integrated}}}{\mathsf{c} \cdot \mathsf{Lorentz}}, \tag{4.2}$$

where c is an experiment specific global normalization parameter and Lorentz factor is defined as

$$\mathsf{Lorentz}(2\theta, \eta) = \frac{1}{\mathsf{sin}(2\theta)\,|\mathsf{sin}(\eta)|}. \tag{4.3}$$

Thus, if the gauge volume of the sample is known, then one can infer the volume of a diffracting grain through determining global normalization parameter, c of the diffraction experiment[60, 112]. In the next stage of the pipeline, c-parameter could also be used as a global fitting parameter during the tessellation step (Section 4.1.6).

[1] In Section 4.1.1, we mention that the simulated grains are assumed to have zero elastic strain. Here, also we mention that the refinement procedure considers the refinement of UBI matrices with redistribution of the assigned scattering vectors. Referring to Equations 2.7 to 2.11, the elastic strain matrix can be calculated from the decomposed B-matrix part of the UBI matrix [27]. Therefore, considering a hypothetical re-run of the simulations with the further assumption of finite constant elastic strain for each grain, we argue that the explained refinement would provide a first approximation of such constant strain for each indexed grain. The determination of elastic strains will be further discussed in the upcoming Section 5.4.

[2] In the following text, the terms "found" and "indexed" will be used in interchangeably.

4.1.6 Volumetric Mapping by Tessellation

In order to obtain EBSD-type 3D grain maps, the resulting refined grain ensemble is tessellated using a weighted Voronoi tesellation scheme, called Laguerre tessellation [67]. In comparison to a regular Voronoi tessellation, Laguerre tessellation uses the determined volumes as a weighting scale for each tessellated grain in the ensemble. [67] has shown that such tessellation strategies represent the local organizations inside the ensemble with great accuracy, with 0.7 missing neighbours and 0.9 wrong neighbour was observed per tessellated grain. Furthermore, the tessellation results were found to be tolerant with regard to relative errors in CoM position and volume of 20%.

Another tessellation approach is presented by [68], called generalized balanced power diagrams (GBPDs) approach. Here, the determined CoM and position and volume are optimized via a general linear programming model by decreasing the total energy of the tessellation. Compared to Laguerre tessellations, the GBPD approach produces better 3D maps. However, GBPD approach is known to be a computationally intensive process. Thus, in the presented study, tessellations are performed using the Laguerre tessellation module of the open-source Neper software package [113]. Neper allows simultaneous specification of the orientations, centroids and volumes of identified (sub)grains as input to the tessellation algorithm, a feature developed for tessellating 3DXRD data. It was shown that the mentioned module is capable of correctly identifying $\approx 90\%$ of voxels in a DCT dataset [114]. Neper allows simultaneous specification of the orientations, centroids and volumes as input to the tessellation algorithm, a feature developed for tessellation of 3DXRD data.

4.2 Analysis methods

The resulting indexed grain ensembles are analyzed with respect to the ground truth grain ensemble (i.e. phantom). In order to analyze the errors in a grain-wise fashion, the indexed grains are matched to its ground truth counterpart by minimising a figure of merit, consisting of respective orientation and CoM position differences. For orientation difference calculation, the orientation pair is first rotated to the fundamental zone, and then the angle between the two poles is measured. During the matching process, the candidate pairs showing orientation and CoM errors less than $0.1\,^\circ$ and $0.5\,\mu$m, respectively, are considered. After the grain-matching routine, the diffraction spots of the paired grains are matched by minimising the distance between the normalized scattering vectors. In the minimisation process, candidate pairs are considered, if only their relative distance is below $0.1\,\text{Å}^{-1}$ in reciprocal space.

The quality of the analyses are calculated on both the grain level and diffraction peaks level. The errors of resulting matched grains and their reflections are quantified with the following figures-of-merit:

- The *number of grains indexed*, to be compared to the number of simulated grains.
- The *number of input reflections* for indexing, to be compared to the number of simulated reflections.
- The *completeness* is defined as the grain average of the ratio of the number of assigned reflections (either correct or not) to a grain by the indexing algorithm and the number of diffraction spots available in FoV for that grain.
- *Purity* defined as the grain average of the ratio between the number of reflections correctly assigned to a grain by the indexing algorithm and the number of simulated diffraction spots for the grain [59].

- The grain average of the *accuracy of the CoM positions* of the grains indexed, calculated with respect to their ground truth matches.
- The grain average of the *accuracy of the orientations* of the grains indexed, calculated with respect to their ground truth matches.
- The grain average of the θ, η *and* ω *errors* of the assigned reflections, calculated with respect to their ground truth matches.

The presented figures-of-merit can be used for quantifying both indexing and refinement steps. It should be noted that for experimental studies, *completeness* is presented as a key figure-of-merit for expressing the performance of the indexing step. For the presented results in this chapter, it was found that the refined grain ensembles show no incorrect reflection assignments. Because of this, due their definition, both *completeness* and *purity* values are calculated as the same. Hence, in order to avoid repetition, we shall only report the *purity* values. For special cases, this equality breaks down, and thus, *completeness* values will be reported alongside with *purity*.

4.3 Effect of omega-step size

It is known that angular resolution of 3DXRD-type experiments depends on the tomographic rotation angle step size, $\Delta\omega$ [27, 53]. As the diffraction peaks are defined to lie between 2θ, η and ω angles, the proposed *high resolution* scheme is expected to determine the 2θ and η angles with superior sensitivity due to fine sampling of small pixels. Therefore, we can say that the rotation step size determines the extent of how fine the diffraction peaks are sampled during an experiment. In other words, for a diffraction peak that lies in an arbitrary 2θ and η angle, the accuracy for determining its reciprocal space position of is inversely related to rotation step size, $\Delta\omega$. In order to extent this observation to determination of the real space position of (sub)grains with HR-3DXRD, this section will present a short study on the effect of $\Delta\omega$ on CoM position and orientation determination.

The current study is devised to be conducted with a simple single crystalline phantom, a lone $1\,\mu$m-sized subgrain. Thus, in addition to the effect of $\Delta\omega$, the study further aims to perform the initial validation of HR-3DXRD with the simplest case of a single crystal. This example will show the limits of the technique and it will be free of any possible collective movement and rotation of the grain ensemble. The lone $1\,\mu$m-sized subgrains placed in an arbitrary position in a large simulation box of $100\,\mu$m with a randomly generated orientation. The synthetic datasets and diffraction images are generated according to the methodology presented in Section 4.1.1.

The current simulations are produced with slight deviations from the proposed experimental configuration given in Tables 4.1 and 4.2. These simulations utilize a synthetic detector with a FoV of $12,000$ x $12,000$ pixels for which both of its y and z-centers are placed in the middle of the FoV at 6000 px. Secondly, ω-scan is done on the half range of $[0\,^\circ, 180\,^\circ]$. The rest of the global parameters are used follows the specifications given in Tables 4.1 and 4.2. The study is conducted on three commonly used cases of $\Delta\omega$: $0.05\,^\circ$, $0.1\,^\circ$ and $0.25\,^\circ$. Analyses of the produced synthetic data are according to Section 4.1.

Table 4.3 shows the results for direct and harvested analysis of the lone subgrain with different $\Delta\omega$ steps. The analysis of both routes lead to similar results with some observable discrepancies. In the direct analysis have shown that decreasing $\Delta\omega$ effectively increases the determined CoM position accuracy by several tens of nanometers. Conversely, such refinement is not observed for the harvested analysis. It can be seen that determined CoM positions from harvested analysis vary in an non-systematic fashion. The determined ori-

Table 4.3: Summary of results for direct and harvested routes of the lone subgrain phantoms with varying rotation step size. Purity and errors are calculated by matching analyzed subgrain to its ground truth.

Direct $\delta\omega$ ($^\circ$)	CoM error (μm)	Orientation error ($^\circ$)	Purity (%)	2θ error ($^\circ$)		η error ($^\circ$)		ω error ($^\circ$)	
				Mean	St.dev.	Mean	St.dev.	Mean	St.dev.
0.25	0.09	0.00005	100	0	0	0	0	0	0
0.1	0.07	0.00000	100	0	0	0	0	0	0
0.05	0.03	0.00000	100	0	0	0	0	0	0
Harvested $\delta\omega$ ($^\circ$)	CoM error (μm)	Orientation error ($^\circ$)	Purity (%)	2θ error ($^\circ$)		η error ($^\circ$)		ω error ($^\circ$)	
				Mean	St.dev.	Mean	St.dev.	Mean	St.dev.
0.25	0.06	0.00000	98.57	0.000000	0.000000	0.000000	0.000000	-0.000023	0.000171
0.1	0.12	0.00000	98.57	0.000000	0.000000	0.000000	0.000000	-0.000022	0.000160
0.05	0.10	0.00000	98.57	0.000000	0.000000	0.000001	0.000012	-0.000016	0.000128

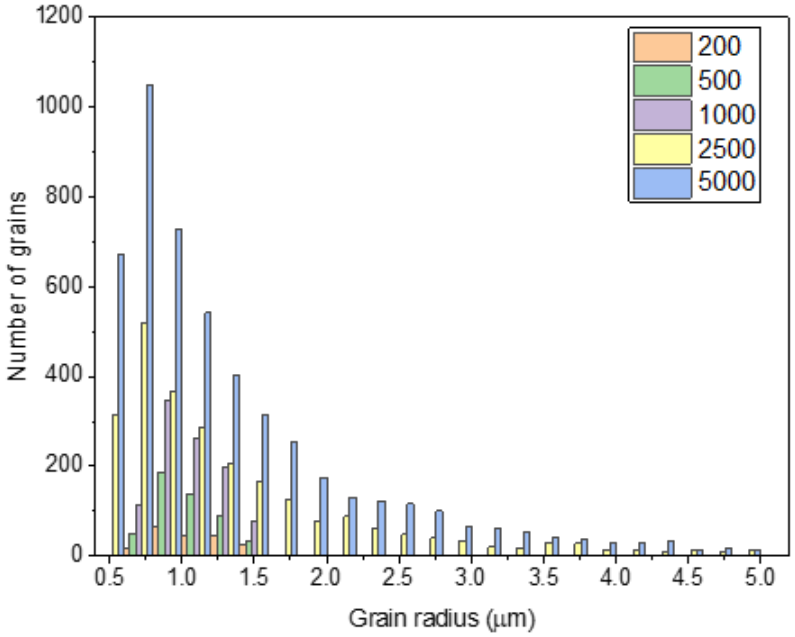

Figure 4.2: Grain size distribution of randomly oriented validation phantoms. The grain radii are calculated by approximating grain volumes to have a spherical shape.

entations are quantified by calculating the angle between the indexed subgrain and the ground truth. It can be seen that both analysis routes successfully finds the orientation of the lone subgrain with utmost accuracy, better than 10^{-5} degrees. Further inspection of Table 4.3 reveals that direct analysis route has identified the subgrain by assigning all of the available diffraction peaks correctly. Harvested analysis has rejected only a single diffraction peak, thus attaining 99% purity. Furthermore, it can be seen that both analysis routes have correctly identified grains in 2θ and η directions. For the harvested analysis, it can be seen that with decreasing $\Delta\omega$ enabled better fitting of the ω angle, as seen from the improvement of the mean and standard deviation values.

The observed results follow the reports from literature. A previous numerical analysis on NF-HEDM technique have shown that decreasing $\Delta\omega$ cause no apparent improvement on determined CoM position, yet the orientation determination improves drastically [53]. The current results for HR-3DXRD show that the determined orientation is already of high precision better than 10^{-5} degrees due to its experimental configuration. However, one can conclude that in the need of better orientation determination, in expense of longer scanning or simulation times, the attained precision can be further improved beyond 10^{-5} degrees by decreasing $\Delta\omega$. Hence, depending on the ω-width of subgrain's rocking curve, $\Delta\omega$ should be optimized for acquiring datasets with better angular resolution in reasonable acquisition times. We should lastly mention that, $\Delta\omega$ may also be dictated by the analyzed microstructure. In case of a deformation substructure, increasing deformation levels may require acquisitions with finer ω-steps for resolving overlapping diffraction spots.

4.4 Validation with randomly oriented grains

In order to validate the presented data generation and analysis pipeline, a number of randomly orientated phantoms are generated with varying subgrain populations of 200, 500, 1000, 2500 and 5000 subgrains. The validation simulations follow the procedure described in 4.1, for both direct and harvested analysis routes.

The phantoms are generated with the built-in grain ensemble generator of PolyXSim [110].

Table 4.4: List of angular tolerances used for indexing of validation datasets.

	2θ		η		ω	
Number of subgrains	Direct	Harvested	Direct	Harvested	Direct	Harvested
200	0.01	0.01	0.2	0.2	0.05	0.05
500	0.01	0.01	0.2	0.2	0.05	0.05
1000	0.01	0.01	0.2	0.2	0.05	0.05
2500	0.005	0.015	0.1	0.1	0.05	0.05
5000	0.005	0.0185	0.1	0.1	0.05	0.05

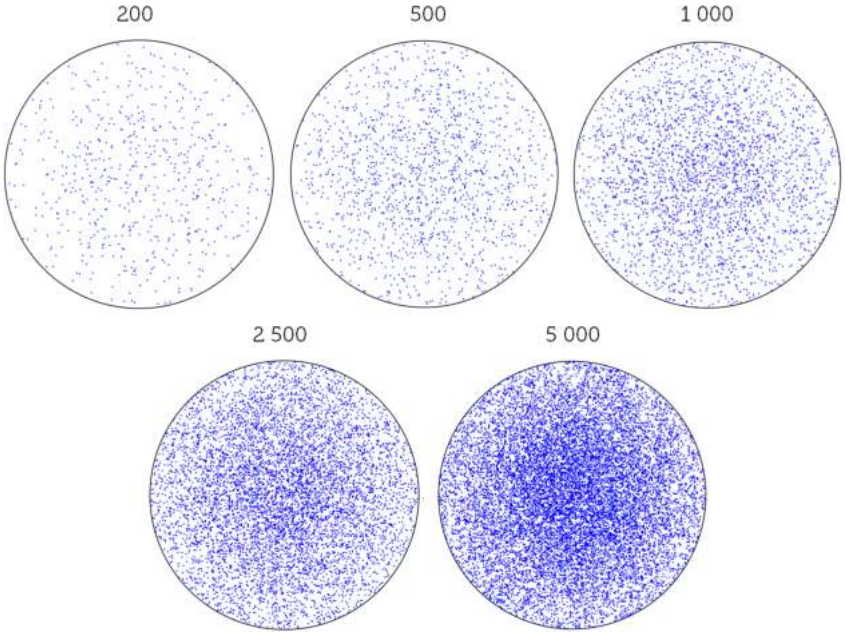

Figure 4.3: (100) pole figures of randomly oriented validation phantoms.

The produced synthetic data of normalized scattering vectors and synthetic diffraction images are analyzed as described in Section 4.1. The tolerances adopted for indexing step are given in Table 4.4. The resulting grain ensembles are analyzed as described in Section 4.2.

The properties of the randomly oriented phantoms are analysed by means of subgrain size distribution and their respective pole figures. Figure 4.2 shows the subgrain size distribution of the phantoms. For phantoms having 200, 500 and $1,000$ subgrains, the bounds of the grain size distribution is set as $0.75\,\mu$m and $1.5\,\mu$m. Whereas for phantoms having $2,500$ and $5,000$ subgrains, the upper bound of the distribution is set as $5\,\mu$m. It can be seen that the mean size of subgrains in all phantoms are below $1\,\mu$m. Figure 4.3 shows the (100) pole figure of the phantoms, confirming the random nature of the generated orientations.

The results are presented in Table 4.5 for the direct analysis and in Table 4.6 for the harvested analysis route. The direct analysis have identified all available subgrains for all phantoms with a CoM position and orientation error of $0.09 \pm 0.03\,\mu$m and $2 \times 10^{-5} \pm 2 \times 10^{-5}$ degrees, respectively. The pipeline have indexed the grains with 100% purity,

Table 4.5: Summary of results for direct route of validation phantoms. Purity and errors are calculated by matching analyzed subgrains to their ground truth counterparts.

Phantom	Num. of sub-grains	Num. of peaks	Purity (%)	2θ error (degrees)	η error (degrees)	ω error (degrees)	Position error (μm)	Orientation error (degrees)	Volume error (%)
200	200	$56,283$	100 ± 0	$0 \pm 2 \times 10^{-6}$	$0 \pm 4 \times 10^{-6}$	0 ± 0	0.09 ± 0.03	$2 \times 10^{-5} \pm 2 \times 10^{-5}$	0.0 ± 0.0
500	500	$140,431$	100 ± 0	$0 \pm 2 \times 10^{-6}$	$0 \pm 5 \times 10^{-6}$	0 ± 0	0.09 ± 0.03	$2 \times 10^{-5} \pm 2 \times 10^{-5}$	0.0 ± 0.0
1000	1000	$221,340$	100 ± 0	$0 \pm 2 \times 10^{-6}$	$0 \pm 5 \times 10^{-6}$	0 ± 0	0.09 ± 0.03	$2 \times 10^{-5} \pm 2 \times 10^{-5}$	0.0 ± 0.0
2500	2500	$702,706$	100 ± 0	$0 \pm 2 \times 10^{-6}$	$0 \pm 5 \times 10^{-6}$	0 ± 0	0.09 ± 0.03	$2 \times 10^{-5} \pm 2 \times 10^{-5}$	0.0 ± 0.0
5000	5000	$1,404,501$	100 ± 0	$0 \pm 2 \times 10^{-6}$	$0 \pm 5 \times 10^{-6}$	0 ± 0	0.09 ± 0.03	$2 \times 10^{-5} \pm 2 \times 10^{-5}$	0.0 ± 0.0

Table 4.6: Summary of results for harvested route of validation phantoms. Purity and errors are calculated by matching analyzed subgrains to their ground truth counterparts.

Phantom	Num. of sub-grains	Num. of peaks	Purity (%)	2θ error (degrees)	η error (degrees)	ω error (degrees)	Position error (μm)	Orientation error (degrees)	Volume error (%)
200	200	$56,015$	99 ± 1.2	$0 \pm 3 \times 10^{-5}$	$0 \pm 1 \times 10^{-4}$	$0 \pm 4 \times 10^{-4}$	0.09 ± 0.03	$3 \times 10^{-5} \pm 3 \times 10^{-5}$	0.0 ± 0.0
500	500	$97,300$	93.6 ± 3.1	$0 \pm 5 \times 10^{-5}$	$0 \pm 2 \times 10^{-4}$	$0 \pm 1 \times 10^{-3}$	0.09 ± 0.03	$1 \times 10^{-4} \pm 7 \times 10^{-5}$	0.0 ± 0.0
1000	1000	$235,898$	82.4 ± 11	$0 \pm 2 \times 10^{-4}$	$0 \pm 4 \times 10^{-3}$	$0 \pm 4 \times 10^{-3}$	0.09 ± 0.04	$5 \times 10^{-4} \pm 5 \times 10^{-4}$	0.0 ± 0.2
2500	2500	$670,695$	86.6 ± 8.9	$0 \pm 3 \times 10^{-5}$	$0 \pm 8 \times 10^{-5}$	$0 \pm 5 \times 10^{-4}$	0.09 ± 0.03	$3 \times 10^{-5} \pm 3 \times 10^{-5}$	0.0 ± 0.0
5000	5000	$1,291,942$	87.4 ± 4.1	$0 \pm 8 \times 10^{-5}$	$0 \pm 5 \times 10^{-4}$	$0 \pm 1 \times 10^{-3}$	0.09 ± 0.03	$1 \times 10^{-4} \pm 9 \times 10^{-5}$	0.02 ± 1.40

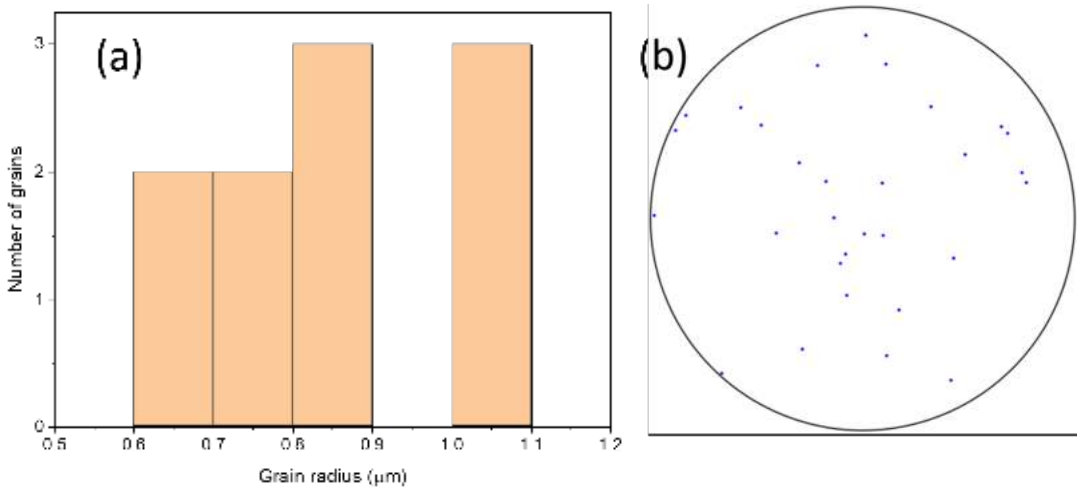

Figure 4.4: (a) Grain size distribution and (b) 100 pole figure of the 10-grained phantom.

indicating that all diffraction peaks are correctly assigned to its parent orientation. The angular position of diffraction peaks are determined 10^{-5} degrees in 2θ, η and ω.

In the case of harvested analysis, it can be seen that with increasing subgrain population, harvested route has fails to identify available diffraction peaks. For the $5,000$-grains-phantom, harvested analysis misses 8% of the ground truth peaks. Nevertheless, all available subgrains for all phantoms are identified with a CoM position error of 0.09 ± 0.03 μm. The calculated orientation errors is also found to vary with the subgrain population. The attained orientation error for 200-grains-phantom of $3 \times 10^{-5} \pm 3 \times 10^{-5}$ degrees is found to decrease to $1 \times 10^{-4} \pm 9 \times 10^{-5}$ degrees for the $5,000$-grains-phantom. The effect of missed diffraction peaks can be seen in the purity values, as well. The analysis on assigned peaks show that peaks are determined with an accuracy of 10^{-5}, $\approx 10^{-4}$ and $\approx 10^{-3}$ in 2θ, η and ω, respectively. Hence, this study shows that in absence of localized texture, the proposed analysis pipeline for HR-3DXRD is capable of identifying up to $5,000$ subgrains of 1 μm size.

4.5 Study of systematic errors

3DXRD is a diffraction-based indirect microscopy technique based on determination of scattering vectors from two dimensional detector frames. The conversion from the diffraction spot position on the detector to scattering vectors are calculated by utilizing the measured experimental geometry parameters. Therefore, the precision of the determined scattering vectors are directly correlated with the precision of the experimental global parameters. In the analysis of diffraction patterns acquired with 2D detectors, global parameters are needed to be determined and refined prior to scattering vector calculation. For such refinement, diffraction patterns from calibration samples (for example LaB_6, polycrystalline Si, CeO_2, etc.) are utilized. Then, global parameters are determined and refined from these diffraction images via iterative forward modelling and fitting [31].

The effect of global parameters precision for 3DXRD analysis is previously reported by [115] for a near-field configuration. In this study, all global parameters are varied in parallel with respect to each other, and their affect on determined grain boundary position and its curvature is calculated. It was found that, beam center-z (detector-z center) position and detector rotation around z-axis (detector tilt-z) were susceptible to systematic errors with respect to all global parameters. Moreover, errors in sample-to-detector distance and

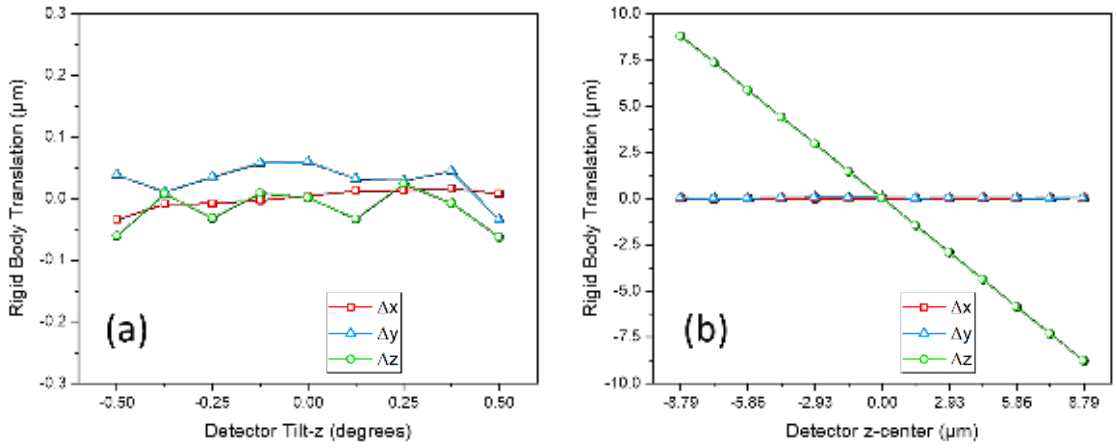

Figure 4.5: Effect of inaccurately determined geometry on the determined CoM positions with HR-3DXRD. Shown are the RBT vector components of the harvested analysis of a 10 grains phantom for (a) variation in detector tilt-z and (b) variation in detector z-center. Figure adopted from Paper 2 on the List of Publications.

beam center-y position were observed to cause rigid body translation of the analyzed grain ensemble [115].

The work of [115] shows that errors in the geometrical parameters have a direct effect on the reconstruction that is comparable to the CoM precision were attempt to achieve. Our investigation differs from that of [115] such that we have chosen geometrical parameter that are characteristic of HR-3DXRD, situated in between the near- and far-field limits (Section 3.1). In the following, we present two examples for the effect of the geometrical parameters on the refined microstructure: detector tilt-z and detector z-center. Following the procedure in 4.1, a small phantom of 10 subgrains of random orientation with $\approx 1\,\mu$m average grain size is generated by PolyXSim [110] and used for the following simulations. The grain size distribution and (100) pole figure of the used phantom is given in Figure 4.4.

The effect of offset in detector z-center position is studied within a range of 6 pixels in steps of half of pixel size, corresponding to a range of $[-8.79, 8.79]\,\mu$m. The effect of offsets in detector tilt-z is studied within a detector tilt range of $1\,^\circ$, corresponding to a scan of $[-0.5\,^\circ, 0.5\,^\circ]$ with steps of $0.125\,^\circ$. The rest of the global parameters are set as zero. The analysis of the synthetic data is performed as explained in Section 4.1. For all of the analyses, the indexing tolerances in 2θ, η and ω angles are set as 0.05°, 0.075° and 0.05°, respectively.

The determined CoM positions of the found grains are separated into rigid-body translation (RBT) motion of the entire grain ensemble, $\vec{t}_{\text{rigid body}}$ and individual subgrain motions, $\vec{t}_i$ with the following formulation:

- First the global CoM of the entire grain ensemble is determined by:

$$\vec{\text{CoM}}_{\text{global}} = \frac{\sum_i V_i \vec{r}_i}{\sum_i V_i}, \tag{4.4}$$

  where i accounts for all subgrains in the sample/phantom, and V_i and $\vec{r}_i$ are the volume and CoM position of subgrain i.

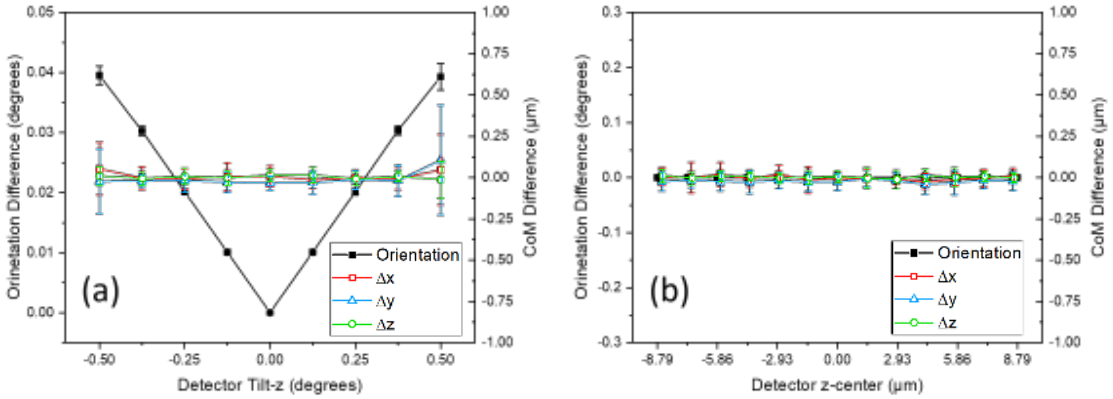

Figure 4.6: Orientation error and residual CoM motion of subgrains after the removal of RBT for (a) detector z-center and (b) in detector z-tilt position. The results are given for the harvested analysis route. Figure adopted from Paper 2 on the List of Publications.

Assuming the grain ensemble to have a homogeneous density, the volume of each subgrain is used as a weighting factor for determining the global CoM of the grain ensemble.

- Then, the rigid body translation is calculated by subtracting in global CoM positions of the ground truth and the analyzed grain ensemble;

$$\vec{t}_{\text{rigid body}} = \vec{\text{CoM}}_{\text{global}}^{\text{reconstructed}} - \vec{\text{CoM}}_{\text{global}}^{\text{ground truth}}. \tag{4.5}$$

- Lastly, the residual motion of individual subgrain i is calculated as the difference of the found CoM position and the sum of ground truth CoM position and the rigid body translation;

$$\vec{t}_i = \vec{r}_i^{\,\text{reconstructed}} - \vec{r}_i^{\,\text{ground truth}} - \vec{t}_{\text{rigid body}}. \tag{4.6}$$

The orientation errors are calculated by with the same procedure for grain matching mentioned in Section 4.2. This approach assumes that the motion of subgrains is independent of its rotational movement. In other words, the adopted analysis disregards the coupling between the rigid body rotation and the linear translation of the grains. Such analysis would first calculate the rotational movement of each subgrain and then its coupled linear motion could be determined. The validation efforts in Section 4.4 have shown that the orientation error of each subgrain is substantially low, $\approx 5 \times 10^{-4}$ degrees. Thus, one can expect the impact of orientation errors on the linear motion of the subgrains to be substantially low, as well.

The resulting direct and harvested grain ensembles are analyzed with respect to the ground truth grain ensemble, according to Section 4.2. As stated in Section 4.1, the direct analysis serves as a validation tool. The analysis have shown that the results of both direct and harvested routes are found to be identical.Thus, in order to avoid repetition, the following text presents the results for harvested route only. Figure 4.5 shows the components of the calculated RBT vector of the analyzed volumes as function of the detector-z center and detector tilt-z misalignment. It can be clearly seen that both cases cause distinctly different motions. Detector tilt-z misalignment is found to cause the found subgrains to suffer a non-systematic rigid body translation in three dimensions. It was

found that the magnitude of such shifts to be below $0.2\,\mu$m. Whereas, detector z-center misalignment have caused the found grains to undergo a rigid body translation in negative z_L direction by the amount misalignment. Such behaviour is observed only in z_L axis, as for all found grains, the x and y components of the rigid body translation vectors shown variations below $0.1\,\mu$m.

Figure 4.6 shows the calculated single grain motions and orientation errors of the resulting grain ensembles for both detector-z center and detector tilt-z misalignment cases. Within the investigated misalignment ranges, it was found that posed misalignments have negligible influence on single grain motions. For both cases, all three components of calculated single grain motions were found to be below $0.1\,\mu$m. It should be noted that for the detector tilt-z case, the standard deviation of x and y component of the motion have shown a substantial increase at the extremities of the studied range. For the detector$z$ center case, such variation was not observed for all three components of the motion. The studied misalignments manifest different behaviors for the orientation error. For the detector tilt-z case, the orientation error and its standard deviation increases linearly with the posed misalignment, $0.4 \pm 0.02\,^\circ$ for tilt$_z = \pm 0.5\,^\circ$ cases. conversely, orientation errors resulting from the posed misalignment are below $0.001\,^\circ$ for all detector z-center cases.

The presented results have shown that inaccuracies in detector z-center and detector tilt-z parameters lead to different effect on the resulting grain ensembles. Misalignment in detector z-center only caused a linear rigid body translation of the resulting grain ensemble in the negative direction of the misalignment with no observable inaccuracies in determined orientation and CoM position. Whereas, in the detector tilt-z case, misalignment caused a non-systematic rigid body translation of the resulting grain ensemble with an increased tendency for inaccuracies in orientation determination. The found residual motions of subgrains are smaller than 10% of mean subgrain size, thus CoM errors are deemed to be negligible within the studied misalignment ranges. Furthermore, it should be noted that the calculated orientation errors are approximately ten times better than the accuracy of 3D maps obtained from conventional EBSD measurements [116–118], hence, in general it is negligible.

4.6 Effect of signal-to-noise

In section 4.1.1, it was mentioned that the calculated diffraction frames are free of fluctuating background and detector noise, for modelling ideal experimental conditions. Throughout this section, these images will be called as *"ideal images"*. However, experimentally acquired diffraction images show an innate noise due to various experimental factors. As a result, it may cause missing low intensity peaks, detection of false peaks [119] and errors in determined peak positions of diffraction peaks. Hence, noisy diffraction images may expect to cause inaccuracies on CoM positions and orientation determination of any type of 3DXRD experiment, including HR-3DXRD.

In general, sources of noise contribution in experimentally acquired 2D detector images can be classified into three main categories [120] :

- *Structured noise*, via parasitic scattering, detector saturation and detector's dark noise contribution,
- *Random noise*, via photon counting noise and detector readout noise,
- *Outlier noise sources*, dead pixels in FoV, stray signals from extraterrestrial rays, etc.

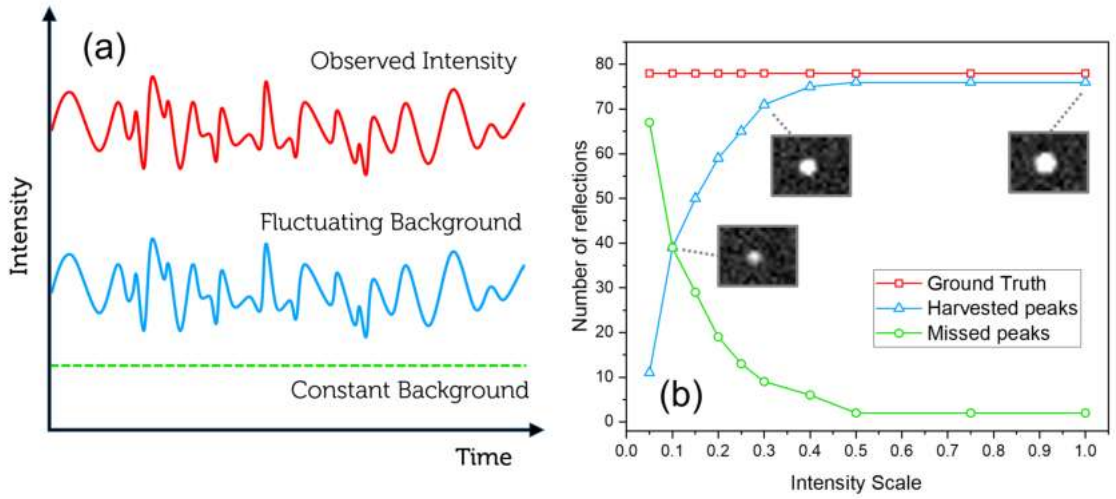

Figure 4.7: (a) Schematic representation of the assumed noise model. The observed intensity assumed to be comprise of a constant background, a fluctuating readout noise and the diffraction signal (omitted for clarity). (b) The effect of S/N variation on the number of harvested peaks. The insets show an arbitrarily chosen $(1\bar{1}2)$ peak for intensity scales of 0.1, 0.3 and 1.0. For ease of comparison, the contrast setting of the inset images are set as equal. Figure adopted from Paper 2 on the List of Publications.

In this section, the impact of noise on HR-3DXRD experiments will be presented. The study is done on the diffraction peaks level. The *ideal* synthetic images are processed with a noise model for attaining different signal-to-noise (S/N) levels. Then, the diffraction peaks and their attributes are determined by harvesting peaks from these noisy images. The adopted noise model assumes that the observed intensity consist of a constant background, a fluctuating readout noise and the diffraction signal. The model is schematically explained in Figure 4.7(a). To accommodate this noise model the ideal images, Im_{ideal}, generated by PolyXSim are modified as follows

- *Intensity adjustment* of the ideal synthetic image, for simulating the change of experimental exposure time,
- *Adding a constant background* image to the intensity adjusted ideal image,
- Dividing the background added ideal image to a *noise scaling* factor,
- Processing the resulting image with the *Poisson filter*, for noise introduction,
- Multiplying the noisy image with the previously used noise scaling.

This procedure is formalised as the following:

$$\mathrm{Im}_{\mathrm{noisy}} = \alpha\, \mathrm{Poisson}\left[\frac{\frac{\mathrm{Im}_{\mathrm{ideal}}}{\mathrm{I}_{\mathrm{scale}}} + \mathrm{bkg}}{\alpha}\right], \tag{4.7}$$

where $\mathrm{I}_{\mathrm{scale}}$ is an intensity scaling factor for varying the experimental exposure time, bkg is the constant-valued background image, α is the noise scaling factor, $Poisson$ is the Poisson filter operator and $\mathrm{Im}_{\mathrm{noisy}}$ is the noise introduced synthetic diffraction image. In this formulation, the constant background and the noise scaling factor are detector specific parameters. In order to mimic the actual experimental conditions, both of these parameters

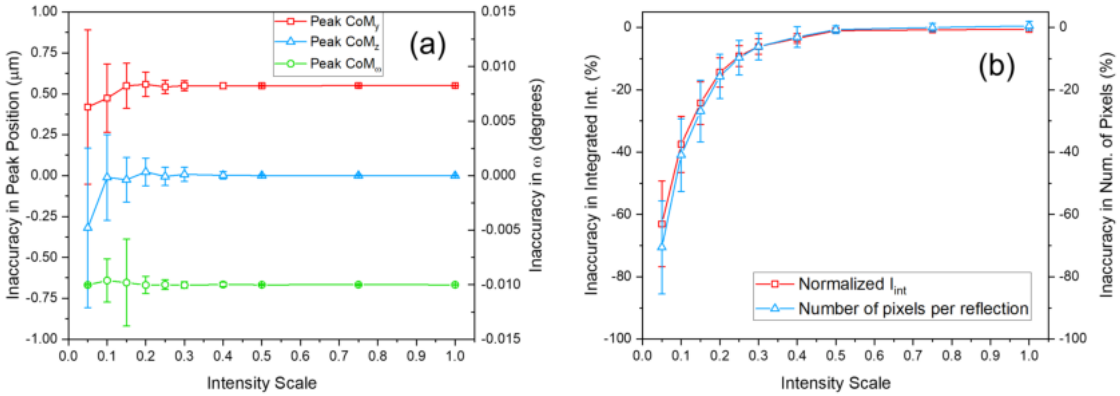

Figure 4.8: Plots of (a) error in CoM positions of diffraction peaks on the detector frame and corresponding error in rotation angle, ω assignment, and (b) percent error in the number of detector pixels per peak and in the integrated intensities of the harvested peaks with respect to signal-to-noise variation. Figure adopted from Paper 2 on the List of Publications.

are determined from twenty experimentally obtained diffraction images from a FReLoN camera [121]. These parameters are determined from regions of interest, RoIs, comprising no diffraction signal. The constant background is defined as the average intensity of the RoI, while the noise scaling factor is defined to be equal to the standard deviation of the RoI. The measured values of 108 and 0.2 are used as for representing the constant background and noise scaling, respectively.

The current study uses the same grain ensemble introduced in Section 4.5. Synthetic data and diffraction images are generated with PolyXSim (see Section 4.1) with the experimental setting defined in Table 4.1. The study is conducted on a 10° wedge from the full ω-scan, corresponding to 100 synthetic diffraction images. Exposure time was simulated by varying the intensity scaling from 1.0 (corresponding to the original intensity level of the ideal image) to 0.05. The peaks harvesting from the noisy images are done by following the procedure described in Section 4.1.2.

Figure 4.7(b) shows the impact of S/N on the number of harvested peaks. The results show that more than $\approx$95% of diffraction peaks are identified up to $I_{scale} = 0.4$. It was observed that further loss of S/N decreases the number of detected diffraction peaks exponentially. For the extreme case of $I_{scale} = 0.05$, only $\approx$ 13% of the ground truth diffraction peaks are detected.

Figure 4.8 shows the determined CoM position, spread and intensity change of the harvested diffraction peaks. Following a similar tendency to the number of harvested peaks, the precision of determined properties of the diffraction peaks starts to degrade for S/N values below $I_{scale} = 0.4$. Furthermore, it was observed that the standard deviation of the presented peak properties also degrades with decreasing S/N. Below $I_{scale} = 0.4$, the observed error in CoM position reaches to $\approx 1\,\mu$m in the extreme case of $I_{scale} = 0.05$. Peak shape parameters such as the number of pixels per reflection and the integrated intensity also shows a similar behavior. It can be seen that with decreasing S/N levels, the number of pixels per reflection and the integrated intensity show an error of 71 ± 15% and -63 ± 14%, respectively, for the extreme case.

Figure 4.9: The shape change of a randomly chosen $(1\bar{1}2)$ peak with respect to signal-to-noise variation under noise scaling $\alpha = 0.2$ condition. For ease of comparison, the contrast setting of all images are set as equal.

The degradation behavior can also be tracked qualitatively from the peak shape on the noisy detector frames. In Figure 4.9, the aforementioned behavior is clearly visible: The shape of the peak does not get effected with the decreasing S/N levels. However, by decreasing below $I_{scale} = 0.4$, the diffraction peak becomes gradually smaller and dimmer, reaching intensity values close to the fluctuating background. For low intensity levels, the distinction between the noisy background and the diffraction peak becomes more and more vague. Thus, in low S/n conditions, the used peak searching algorithm starts to fail determining ill-defined diffraction peaks.

The results given above focuses on the quality of determined diffraction peak shapes with respect to S/N. Next, the impact of S/N on a full CoM maps are studied for selected S/N settings of 0.1, 0.3 and 1.0, for reflecting a poor, moderate and good S/N ratio, respectively. The study utilizes the phantom presented in Figure 4.4. Synthetic diffraction images of the mentioned three cases are generated and analyzed according to the specifications given in Section 4.1. Noise introduction to the generated ideal images are held with the noise introduction scheme presented above.

The analysis results of full-scale noisy datasets are given in Section 4.6. From the table, it can be seen that peak harvesting have identified 34%, 89% and 99% of the ground truth peaks for $I_{scale} = 0.1$, 0.3 and 1.0 cases, respectively. The analysis of the noisy datasets have shown that $I_{scale} = 0.1$ case shown the worst performance, by finding 90% of the subgrains, whereas all subgrains are found for the moderate and good S/N ratio cases. On the diffraction peaks level, all error metrics are found to be inversely related to the S/N level. It should be pointed out that the number of input peaks from peak harvesting and the purity level subsequent to indexing are on the same order. This implies that the peak harvesting procedure have identified a very low number of false peaks.

On subgrain's level, determination of CoM positions and orientations show different behaviors. It can be seen that the CoM position error of all three cases are rather comparable. However, orientation error is found to degrade by an order of magnitude with decreasing S/N level. This observation can be traced back to the results given in Figure 4.8. With decreasing S/N levels, the CoM position of diffraction peaks become more and more ill-defined. Thus, the propagation of such errors throughout the analysis pipeline manifests itself as errors in the determined orientations.

The presented noise study reveal important implications for HR-3DXRD experiments. It can be clearly seen that the proposed experimental setup for HR-3DXRD is capable of determining the position and properties of diffraction peaks with an accuracy better than the pixel size. Furthermore, the mentioned accuracy is found to be a strong function of S/N level. It was seen that a large portion of diffraction peaks are detected until reaching a a well-defined S/N threshold. These arguments is shown to be applicable to full-scale noisy datasets, as well. It was seen that even though ≈ 85% of available diffraction peaks are missed by peak harvesting, the proposed analysis pipeline was found to be capable of

Table 4.7: Summary of results for the harvested analysis of noisy phantoms. Purity and errors are calculated by matching analyzed subgrains to their ground truth counterparts.

I_{scale}	Num. of sub-grains	Num. of peaks	Purity (%)	2θ error (degrees)	η error (degrees)	ω error (degrees)	Position error (μm)	Orientation error (degrees)	Volume error (%)
Ground truth	10	2,848	-	-	-	-	-	-	-
0.1	9	957	30.7 ± 18.2	$0 \pm 3 \times 10^{-4}$	$8 \times 10^{-5} \pm 2 \times 10^{-3}$	$1 \times 10^{-3} \pm 2 \times 10^{-2}$	0.16 ± 0.08	$5 \times 10^{-3} \pm 2 \times 10^{-3}$	0.0 ± 0.0
0.3	10	2,553	75.9 ± 20.8	$0 \pm 2 \times 10^{-4}$	$2 \times 10^{-5} \pm 9 \times 10^{-4}$	$1 \times 10^{-6} \pm 9 \times 10^{-3}$	0.10 ± 0.02	$3 \times 10^{-3} \pm 2 \times 10^{-3}$	0.0 ± 0.0
1.0	10	2,846	99.0 ± 2.7	$0 \pm 9 \times 10^{-5}$	$3 \times 10^{-6} \pm 4 \times 10^{-4}$	$0 \pm 3 \times 10^{-3}$	0.08 ± 0.01	$3 \times 10^{-4} \pm 2 \times 10^{-4}$	0.0 ± 0.0

determining 90% of the subgrains with a CoM accuracy of $0.16\,\mu$m. Experimentally, these results have two major implications:

- Considering a real-life HR-3DXRD experiment, one can use the mentioned threshold for on-line quality measure for data acquisition. This can be done via collecting consecutive ω scans on a narrow angular wedge with different exposure times, then performing peak harvesting on the acquired images. By plotting the number of harvested peaks with respect to the exposure times, one can assess the data quality. This fast procedure can be used for optimizing the acquisition speed and data quality.
- HR-3DXRD is capable of retrieving full to partial three-dimensional maps, due to its superior capability of determining well-defined peaks. This behavior is sustained for low S/N levels, without compromising from its high spatial and angular resolution.

4.7 Virtual experiments on deformed microstructures

Metals and alloys of medium-to-high stacking fault energy, Γ_{SFE}, are known to develop a multiscale microstructural hierarchy for deformation levels exceeding $\varepsilon_{vM} = 0.05$. As introduced in Section 2.1, the intragranular microstructure consists of extended planar GNBs delineating volumes containing cells made of IDBs. Such structural configurations are known to produce a localized texture with a small misorientation [14, 16]. Therefore, it can be argued that the presented validation efforts through randomly oriented phantoms (see Section 4.4) do not represent the applicability of HR-3DXRD on deformed microstructures.

In this section, we present two virtual experiments with phantoms with more realistic microstructures for assessing the resolution capabilities of the HR-3DXRD microscopy technique. The phantoms represent a cubical cross-section of a deformed grain with two different populations of 104 and 828 subgrains. The deformation-induced microstructure of iron, having the bcc crystal structure, is known to follow the same overall pattern as for fcc crystals [122, 123]. It has, however, not been characterized in the same detail with respect to the grain orientation dependence of the GNBs and the habit planes of these. In order to better compare the simulations for these phantoms with the phantoms with random texture it was decided to keep the same set-up of the virtual experiment with simulations for bcc. Switching to simulations for fcc would change both the diffraction angles and the multiplicity of the diffraction peaks. In lack of a really well-characterized bcc microstructure, inspiration was taken from a well-known fcc microstructure. Both phantoms therefore resemble a deformed grain with the so-called copper orientation, $\{111\}\langle 112\rangle$, in the fcc rolling texture. In this configuration, GNBs are oriented to be parallel to the (001) plane [18]. The reference orientation for both phantoms is given as

$$\mathsf{U}_{\text{seed}} = \begin{pmatrix} \frac{1}{\sqrt{3}} & \frac{1}{\sqrt{3}} & \frac{-1}{\sqrt{3}} \\ \frac{-1}{\sqrt{2}} & \frac{1}{\sqrt{2}} & 0 \\ \frac{1}{\sqrt{6}} & \frac{1}{\sqrt{6}} & \frac{2}{\sqrt{6}} \end{pmatrix}. \tag{4.8}$$

This mix of bcc and fcc has no consequences for the aim of these simulations of demonstrating a working simulation pipeline. Both phantoms show an average internal crystallographic misorientation of $\approx 7^\circ$ with mean IDB separations being less than half of the GNB separation. While these parameters vary somewhat with the material and strain level, they are in the right ball park and roughly correspond to experimentally observed values at $\varepsilon_{vM} = 1$ Figure 2.6. The misorientation angles across neighbouring GNBs exhibit alternating signs, in agreement with Figure 2.4(b). Both phantoms are generated

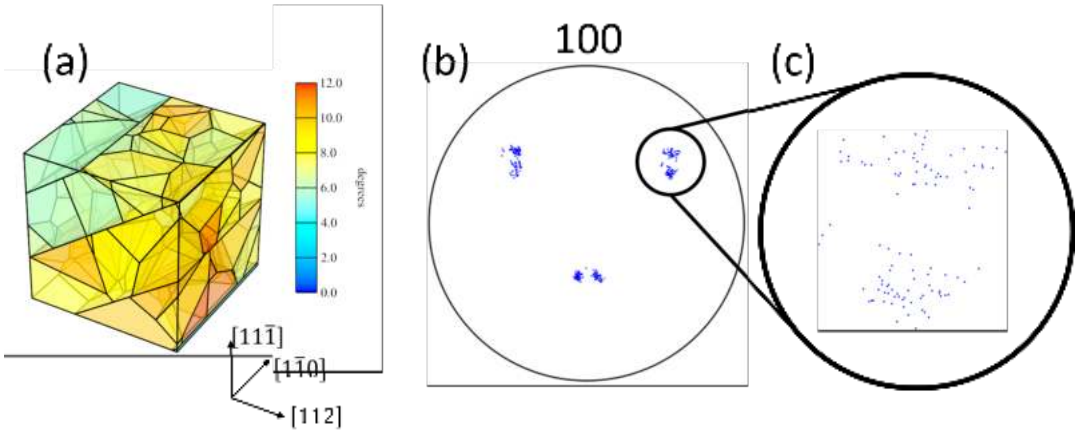

Figure 4.10: Ground truth representation of Phantom A (a) and its (100) pole figure (b). Crystal reference frame and legend for misorientation coloring of the phantom is given in (a). (c) A close-up of the orientation blob, encircled in the pole figure. The diameter of the circle is approximately $30\,^\circ$.

with the Neper software package [113, 124]. The following sections will first present the utilized phantoms and then continue with the results of the virtual experiments.

4.7.1 Phantom A

Figure 4.10 shows the 3D configuration and (100) pole figure of Phantom A. The phantom comprises 104 subgrains subdivided by 3 GNBs. The cube shaped simulation box has an edge length of $10\,\mu$m. i.e. a GNB spacing of about $4.7\,\mu$m . As seen from Figure 4.10(a), the misorientation between two neighboring GNBs is significantly higher than the internal misorientation difference in individual GNBs. This is in agreement with experimental observations [125].

The size and misorientation distribution of Phantom A is given in Figure 4.11. The mean subgrain size of Phantom A is calculated as $1.25 \pm 0.31\,\mu$m. Misorientations are calculated with respect to the reference orientation given in Equation (4.8). The mean misorientation of subgrains is calculated as $8.2\,^\circ \pm 1.6\,^\circ$. For technical reasons, no distinction is made between the misorientations of IDBs and GNBs.

The synthetic datasets and diffraction images are generated and analyzed, following the instructions presented in Figure 4.1. Indexing tolerances used for Phantom A are $0.005\,^\circ$ in 2θ, $0.025\,^\circ$ in η and $0.05\,^\circ$ in ω.

The analysis results of direct and harvested routes are presented in Table 4.8. The number of input peaks for the harvested route is found to miss 6% of the theoretically available diffraction peaks. It can be seen that both analysis routes have successfully identified 104 subgrains, finding all available subgrains present in the ground truth. The calculated CoM position and orientation errors for the harvested route are $0.09 \pm 0.04\,\mu$m and $5 \times 10^{-4}\,^\circ \pm 6 \times 10^{-4}\,^\circ$, respectively. The largest observed errors for CoM position and orientation are found as $0.242\,\mu$m and $0.002\,^\circ$, respectively.

The origin of the low CoM position and orientation errors can be traced back to the magnitude errors in the assigned diffraction spots. As shown in Table 4.8, the angular errors on assigned diffraction peaks are found to be below than the angular coverage of a single pixel of the synthetic diffraction images and also the rotation angle step, $\Delta\omega$. Furthermore,

Table 4.8: Summary of results for Phantom A. Purity and errors are calculated by matching analyzed subgrains to their ground truth counterparts.

	Num. of sub-grains	Num. of peaks	Purity (%)	2θ error (degrees)	η error (degrees)	ω error (degrees)	Position error (μm)	Orientation error (degrees)	Volume error (%)
Ground Truth	104	29,684	—	—	—	—	—	—	—
Direct Route	104	29,684	100 ± 0	$0 \pm 2 \times 10^{-6}$	$0 \pm 4 \times 10^{-6}$	0 ± 0	0.07 ± 0.02	$5 \times 10^{-4} \pm 6 \times 10^{-4}$	0.06 ± 0.73
Harvested Route	104	27,835	88.3 ± 0.1	$0 \pm 3 \times 10^{-5}$	$0 \pm 9 \times 10^{-5}$	$0 \pm 3 \times 10^{-4}$	0.09 ± 0.04	$5 \times 10^{-4} \pm 6 \times 10^{-4}$	-1.45 ± 3.63

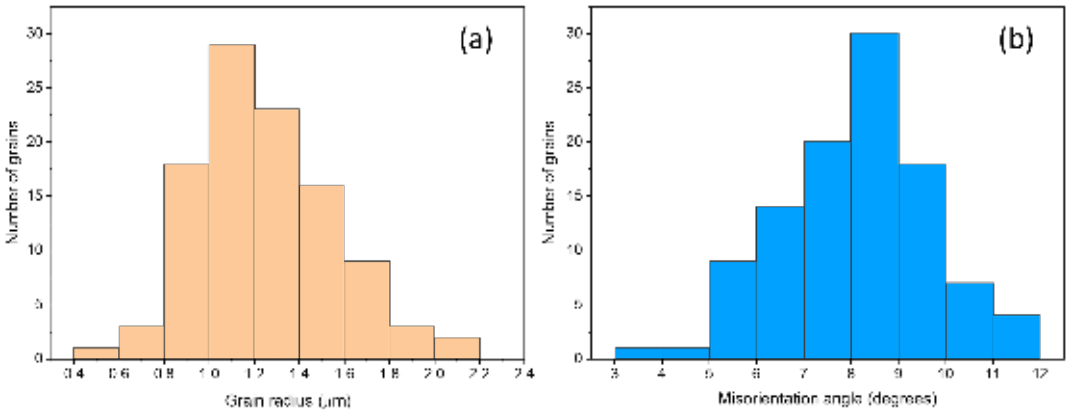

Figure 4.11: (a) Subgrain size distribution and (b) misorientation angle distribution of Phantom A. Misorientations are calculated with respect to the reference orientation given in Equation (4.8).

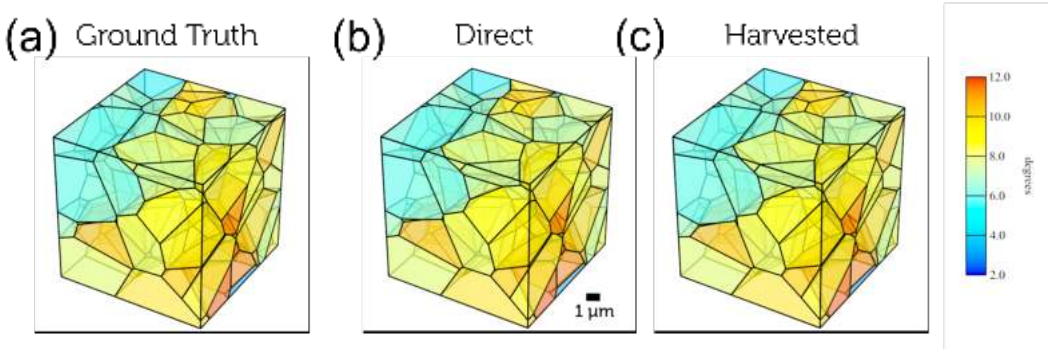

Figure 4.12: 3D tessellated volume maps of Phantom A for (a) ground truth, and (b) direct and (c) harvested analysis routes. Scale legends for length is given in (b) and misorientation is given in (c). The side length of the cube shaped simulation box is $10\,\mu$m. The shown misorientations are calculated with respect to the reference orientation given in Equation (4.8).

the indexed grains have a mean purity[3] of 88% with negligible variation. This implies that the diffraction peaks are assigned to its correct ground truth subgrain. The volume of each subgrain is calculated with respect to Section 4.1.5. It was found that the indexed subgrains have shown relative volume error of 2%.

Figure 4.12 shows 3D tessellations of ground truth, direct and harvested analysis grain ensembles of Phantom A are constructed following the description in Section 4.1.6. The planar character of the GNBs is as expected not directly reproduced in the tessellations. However, the larger misorientation angles and the alternating sign of across neighbouring GNBs clearly identifies their location with a colour scale based on the misorientation of each grain with respect to a new reference orientation, which lies in the outskirts of the

[3]Following the definition in Section 4.2, the reader should bare in mind that in the present context, *completeness* and *purity* have exactly the same value. Thus, they shall be interpreted interchangeably.

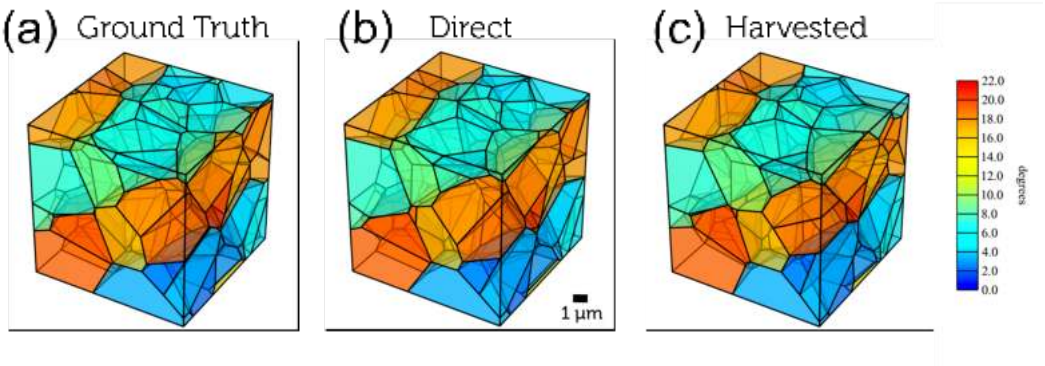

Figure 4.13: 3D tessellated volume maps of Phantom A for (a) ground truth, and (b) direct and (c) harvested analysis routes. Scale legends for length is given in (b) and misorientation is given in (c). The shown misorientations are calculated with respect to the reference orientation given in Equation (4.9) to clearly identify the location of the GNBs. Figure adopted from Paper 2 on the List of Publications.

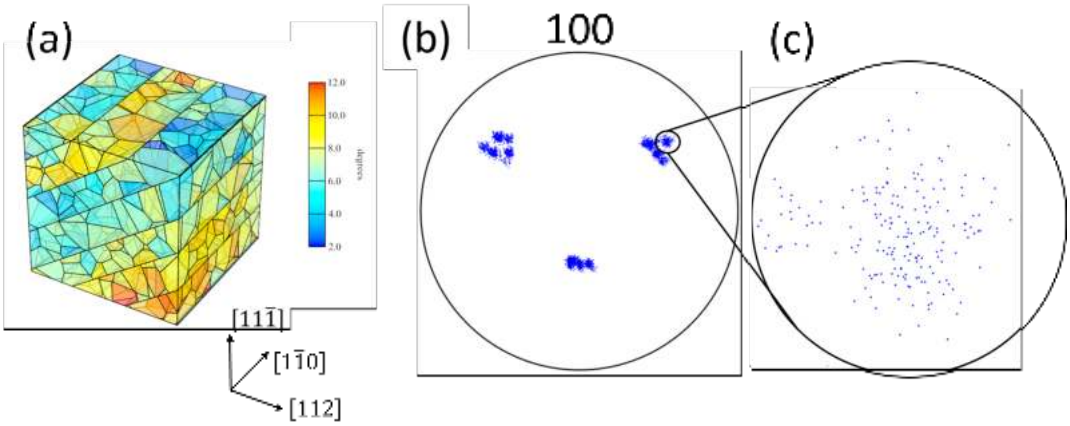

Figure 4.14: Ground truth representation of Phantom B (a) and its (100) pole figure (b). Crystal reference frame and legend for misorientation coloring of the phantom is given in (a). (c) A close-up of the orientation blob, encircled in the pole figure. The diameter of the circle is approximately $14\,^{\circ}$.

orientation distribution:

$$\mathsf{U}'_{\mathsf{seed}} = \begin{pmatrix} 0.4754 & 0.6250 & -0.6191 \\ -0.6770 & 0.7093 & 0.1962 \\ 0.5618 & 0.3259 & 0.7604 \end{pmatrix}. \tag{4.9}$$

The re-tessellation of the ground truth, direct and harvested analysis grain ensembles of Phantom A using the new colour scale are given in Figure 4.13.

4.7.2 Phantom B

Figure 4.14 shows the 3D configuration and (100) pole figure of Phantom B. The phantom comprises 828 subgrains and 6 GNBs. The cube shaped simulation box has an edge length of $20\,\mu$m. The size and misorientation distribution of Phantom B is given in Figure 4.15. The mean subgrain size of Phantom B is calculated as $1.25 \pm 0.30\,\mu$m. The spacing between GNBs is about $4\,\mu$m Misorientations are calculated with respect to the

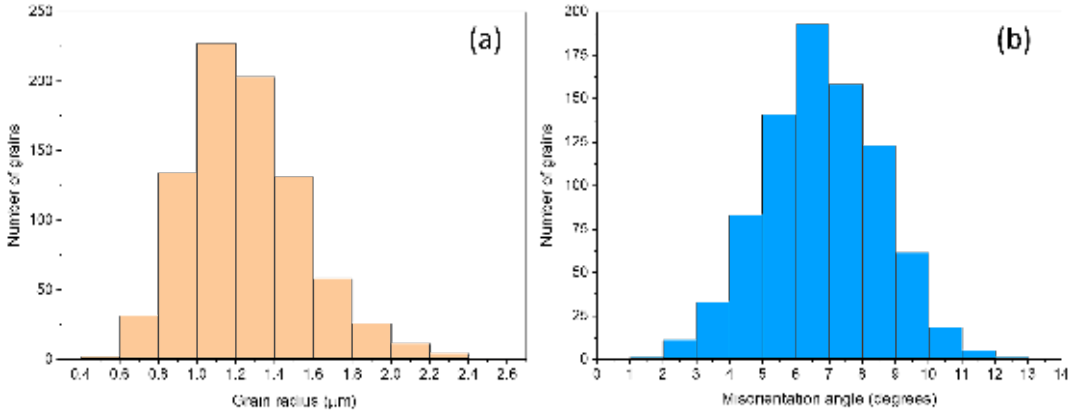

Figure 4.15: (a) Subgrain size distribution and (b) misorientation angle distribution of Phantom B. Misorientations are calculated with respect to the reference orientation given in Equation (4.8).

reference orientation given in Equation (4.8). The mean misorientation of subgrains is calculated as $6.8\,^{\circ} \pm 1.7\,^{\circ}$.

The given spatial and angular configuration of both Phantom A and B shows equivalent characteristics. However, the increased number of subgrains from Phantom A to B should imply that the number of slightly misoriented grains would also increase. Therefore, the latter phantom is expected to have a relatively denser pole figure than the former case. This can be observed by inspecting (100) pole figures of both phantoms, in Figures 4.10(c) and 4.14(c). Considering the latter RoI is $16\,^{\circ}$ larger than the former, the comparison of these two pole figure close-up clearly delineates Phantom B has a high number of orientations within a small slice of the pole figure due to the increased number of GNB bands.

The synthetic datasets and diffraction images are generated and analyzed, following the instructions presented in Figure 4.1. Indexing tolerances used for Phantom B are $0.013\,^{\circ}$ in 2θ, $0.025\,^{\circ}$ in η and $0.025\,^{\circ}$ in ω.

The analysis results of direct and harvested routes are presented in Table 4.9. The discussed increase in local density of orientations manifests itself as peak overlap in the diffraction images. The table shows that the number of input peaks for the harvested route is found to miss 28% of the theoretically available diffraction peaks. Meaning that Phantom B has missed 4.5 times more diffraction peaks in comparison to Phantom A.

The direct analysis route successfully indexed all 828 subgrains with 100% purity, whereas the harvested route indexed 772 subgrains with 59% purity. Both analyses have determined CoM positions and orientations with similar accuracy: $0.09 \pm 0.03\,\mu$m and $5 \times 10^{-4}\,^{\circ} \pm 6 \times 10^{-4}\,^{\circ}$, respectively. The largest observed errors for CoM position is found as $0.367\,\mu$m and for orientation $0.002\,^{\circ}$. Figures 4.16 and 4.17 show the 3D distribution, (100) pole figure, size and misorientation distribution of the missed ground truth subgrains. It can be seen that the missing subgrains are not agglomerated in certain GNBs but rather scattered homogeneously in both real space and in orientation space. The size distribution of the missing subgrains given in Figure 4.17(a) reveals a similar behavior to the overall ground truth size distribution. The mean size of the missing subgrains is calculated as $1.24 \pm 0.29\,\mu$m. Figure 4.17(b) shows the misorientation distribution of the missing sub-

Table 4.9: Summary of results for Phantom B. Purity and errors are calculated by matching analyzed subgrains to their ground truth counterparts.

	Num. of sub-grains	Num. of peaks	Purity (%)	2θ error (degrees)	η error (degrees)	ω error (degrees)	Position error (μm)	Orientation error (degrees)	Volume error (%)
Ground Truth	828	$235,898$	—	—	—	—	—	—	—
Direct Route	828	$235,898$	100 ± 0	$0 \pm 2 \times 10^{-6}$	$0 \pm 4 \times 10^{-6}$	0 ± 0	0.09 ± 0.03	$5 \times 10^{-4} \pm 6 \times 10^{-4}$	0.02 ± 0.86
Harvested Route	772	$169,652$	59.6 ± 15.6	$0 \pm 2 \times 10^{-5}$	$0 \pm 5 \times 10^{-5}$	$0 \pm 3 \times 10^{-4}$	0.09 ± 0.04	$5 \times 10^{-4} \pm 6 \times 10^{-4}$	5.12 ± 4.03

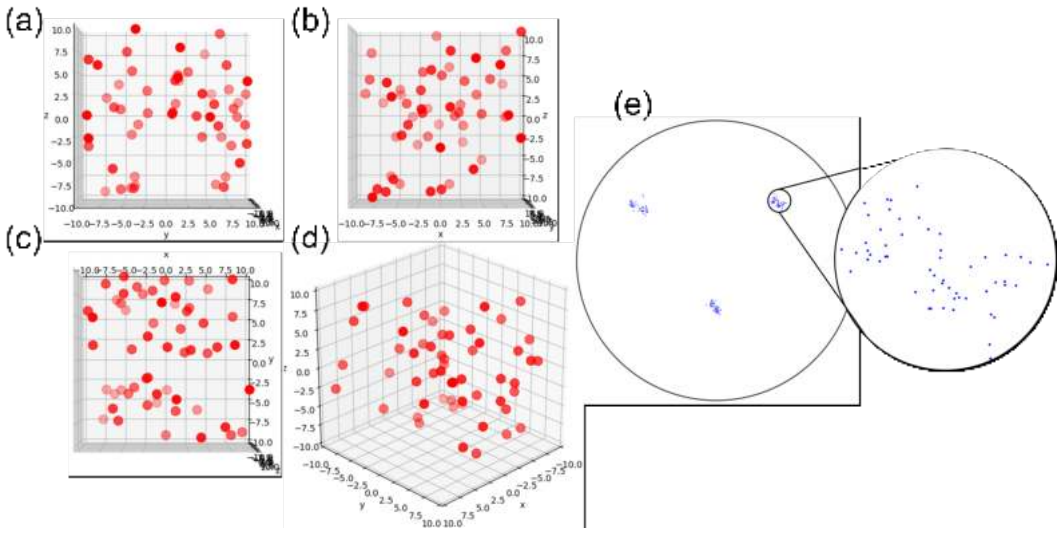

Figure 4.16: Missed grains in harvested analysis of Phantom B. CoM positions of the missed grains are shown from sides of (a-c) x_L, y_L anz z_L and (d) isometric point-of-view. (e) Orientation distribution of missed subgrains presented in 100 pole figure. Inset shows a close-up of the orientation cluster on the right-hand-side. The diameter of the circle is approximately $14\,^\circ$.

grains are calculated with respect to the reference orientation given in Equation (4.8). Similar to the ground truth values, the mean misorientation of missing subgrains is calculated as $6.4\,^\circ \pm 1.8\,^\circ$.

From an assigned diffraction spots point, Table 4.9 shows that Phantom B shows similar errors to Phantom A in 2θ, η and ω angles. The angular errors on assigned diffraction peaks are found to be below than the pixel size of synthetic diffraction images and also the rotation angle step, $\Delta\omega$. Mean purity of indexed subgrains is found as $\approx 60\%$ with considerable standard deviation. It was found that the indexed subgrains have shown relative volume error of 5%.

The performance of Phantom B's harvested analysis route shows that HR-3DXRD is capable of identifying a large portion of subgrains with relatively low CoM position and orientation errors. Yet, such results are obtained from a dataset that covers only 70% of the available diffraction peaks and furthermore calculated mean purity of indexed subgrains is of $\approx 60\%$. Such results seem to contradict with one of the main elements of HR-3DXRD conceptualization (see Section 3.1), stating that the precision of identifying CoM positions is proportional to the number of assigned peaks. This contradiction can be solved by considering the peak overlap caused by high local texture and the post-indexing refinement step: It's known that increasing local texture causes peaks originating from low misorientation subgrains to overlap in η-direction for any hkl ring. It can be argued that peaks having substantial overlap would have an imprecisely determined CoM position on the detector frame. Thus, such error can accumulate and manifest itself as detriment in determined CoM position. As stated in Section 4.1.4, refinement of an indexed grain ensemble is performed by successively decreasing the hkl_{tol}. In the analysis of harvested route, decreasing the tolerance to considerably low values lead to rejection of peaks that are assigned to a smeared overlapping peak. In other words, refinement with finer tolerances would successively increase the determined CoM position by rejecting "bad peaks" suffering from possible overlap. As Table 4.9 shows that CoM and orientation precision

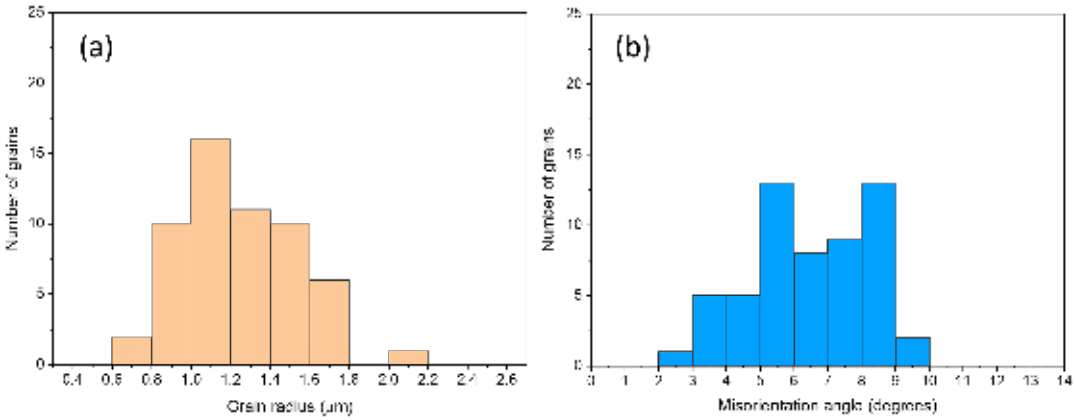

Figure 4.17: (a) Grain size and (b) misorientation distribution of the missed ground truth subgrains. The shown misorientations are calculated with respect to the reference orientation given in Equation (4.8).

of both direct and harvested route is *equivalent*, one can say that fine and through refinement eliminates most of the overlapping peaks. After such outlier rejection, HR-3DXRD retains its superior precision by indexing the rest of the available reflections.

Figure 4.18 shows 3D tessellations of ground truth, direct and harvested analysis grain ensembles of Phantom B are constructed following the description in Section 4.1.6. Here, the subgrains are colored with respect to their misorientation angle to the reference orientation of the deformed grain, given in Equation (4.8). Despite missing 7% of the available subgrains, the tessellated 3D map has identified most of the 6 GNBs and the internal IDBs with their misorientation angles. A qualitative comparison of the tessellated 3D maps of the ground truth and harvested route have shown clear topological similarities. The Laguerre tesellation work of [67] have shown that tessellations derived from datasets having ≈ 10% error in determined volume would lead to quite low errors on the local neighborhood of indexed subgrains: on average 0.6 additional neighbour per grain and 0.6 missing neighbors per grain. The results presented in Table 4.9 is parallel with the analysis of [67], hence, we can conclude that albeit missing 7%, the tessellated deformation microstructure in Figure 4.19 is of good quality with adequate definition of subgrains' local neighbourhood. From the point of view of metallurgical applications, it is of particular importance that the GNB structure is well-characterized in the tessellations and that the overall orientation and size distributions are also representative of the ground truth. This enables meaningful comparison with simulations of microstructural evolution as well as correlations with nucleation sites of recrystallisation or damage.

Similar to Phantom A, the tessellations given in Figure 4.18 are recalculated with a new reference orientation for highlighting the GNBs:

$$\mathsf{U}''_{\text{seed}} = \begin{pmatrix} 0.4360 & 0.6095 & -0.6622 \\ -0.6978 & 0.6936 & 0.1789 \\ 0.5683 & 0.3841 & 0.7277 \end{pmatrix}. \tag{4.10}$$

The re-tessellation of the ground truth, direct and harvested analysis grain ensembles of Phantom B are given in Figure 4.19. With this colour scheme all GNBs are revealed and the alternating colour bands further show that no cells erroneously appear on the wrong

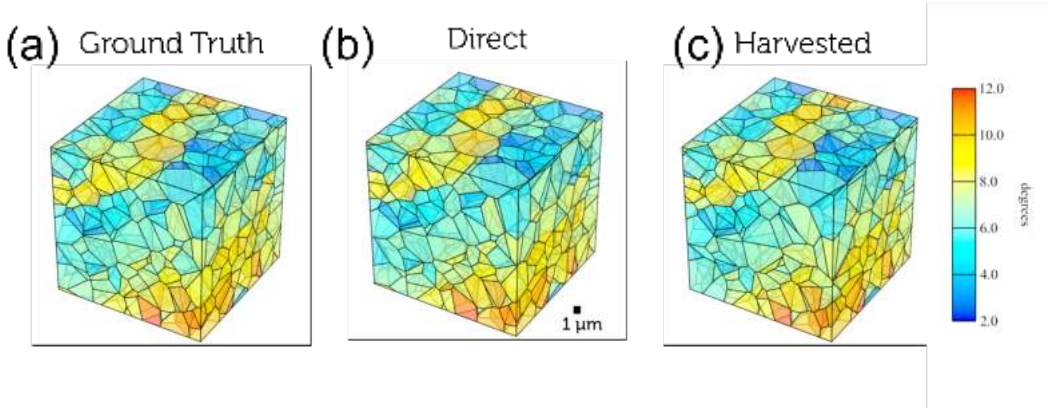

Figure 4.18: 3D tessellated volume maps of Phantom A for (a) ground truth, and (b) direct and (c) harvested analysis routes. Scale legends for length is given in (b) and misorientation is given in (c). The side length of the cube shaped simulation box is $10\,\mu$m. The shown misorientations are calculated with respect to the reference orientation given in Equation (4.8).

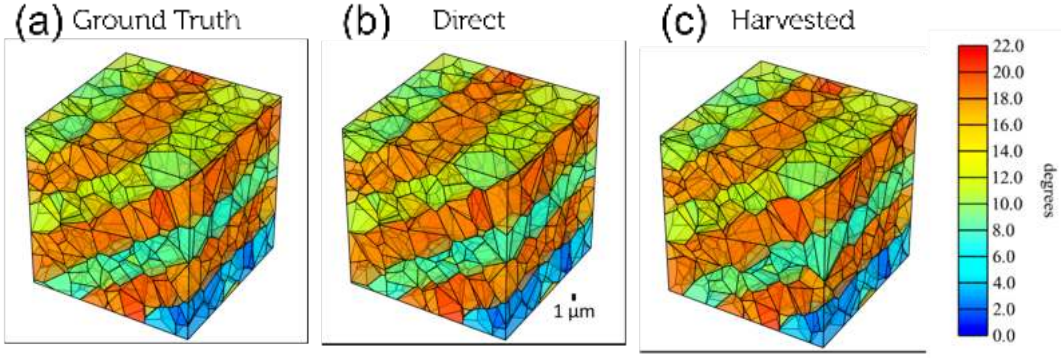

Figure 4.19: 3D tessellated volume maps of Phantom A for (a) ground truth, and (b) direct and (c) harvested analysis routes. Scale legends for length is given in (b) and misorientation is given in (c). The shown misorientations are calculated with respect to the reference orientation given in Equation (4.10). Figure adopted from Paper 2 on the List of Publications.

side of a GNB. The figure clearly shows the robustness of HR-3DXRD on identifying a multitude of GNBs simultaneously.

5 HR-3DXRD Experiments

In Chapter 3, I have derived the HR-3DXRD concept for observing (sub)grains of $1\ \mu$m size or below. In light of the presented numerical simulations, I have optimized the possible experimental parameters and validated HR-3DXRD technique with phantoms of varying complexity; from differing populations to local textures. In this chapter, similar information will be gathered for progress towards the real-life experimental demonstration of HR-3DXRD. In the course of this PhD study, HR-3DXRD has been applied in four X-ray microscopy beamlines with "grain-mapping" capabilities: ID11 and ID06-HXRM beamlines in European Synchrotron Radiation Facility, 1-ID-E beamline in Advance Photon Source and P21.2 beamline in DESY PETRA III. In these experimental demonstrations of HR-3DXRD, we have tried to study different experimental aspects of the technique with a variety of deformation microstructures. Please note that the main purpose of these experiments was to implement the technique in experimental setups that were not dedicated for the multi-panel acquisition HR-3DXRD scanning. Therefore, one of the main aspect of all mentioned experiments was to discover the unknown experimental limitations of the proposed HR-3DXRD technique.

At the time of writing, the complete analysis of an experimental dataset from any of these experiments has not been concluded. Thus, in this chapter, we shall provide the motivation for the different experiments – representing different materials microstructures, and present the experimental methodologies. Then, we will describe the possible data analysis pipeline in detail. Based on the results from the full scale numerical simulations, we will discuss the feasibility of using HR-3DXRD for the various microstructures. The primary difficulty with the experimental data analysis have been the registration of the position of a multitude of detector positions (see Section 3.2). Strategies for this multi-panel registration and an experimental demonstration of such a scheme will be presentend in Chapter 6.

This chapter will start by introducing the studied samples and their respective microstructure. Then, the experimental configuration in the mentioned four beamtimes will be explained in detail with regarding the studied samples. The chapter will continue by introducing the methodology for experimental data analysis. Lastly, the chapter will conclude by discussing the experimental challenges.

5.1 Studied samples and their preparation

In order to demonstrate HR-3DXRD in actual experimental conditions, a selection of samples with varying microstructural features are studied. In this section, the microstructural features and preparation methods of all studied samples will be given in detail. The section will introduce the samples in chronological order with respect to their respective experiments[1].

5.1.1 Eutectic High Entropy Alloy

High entropy alloy (HEA, also known as multi-principle element alloys — MPEA) are an emergent class of metallic alloys, which constitutes equiatomic or near-equiatomic chemical configurations of five or more elements [127]. Rapid solidification of such alloys results

[1] Due to ESRF being closed down for the last 1.5 years of the thesis period, experiments were performed prior to the establishment of the data analysis pipeline and the associated understanding of the tolerances.

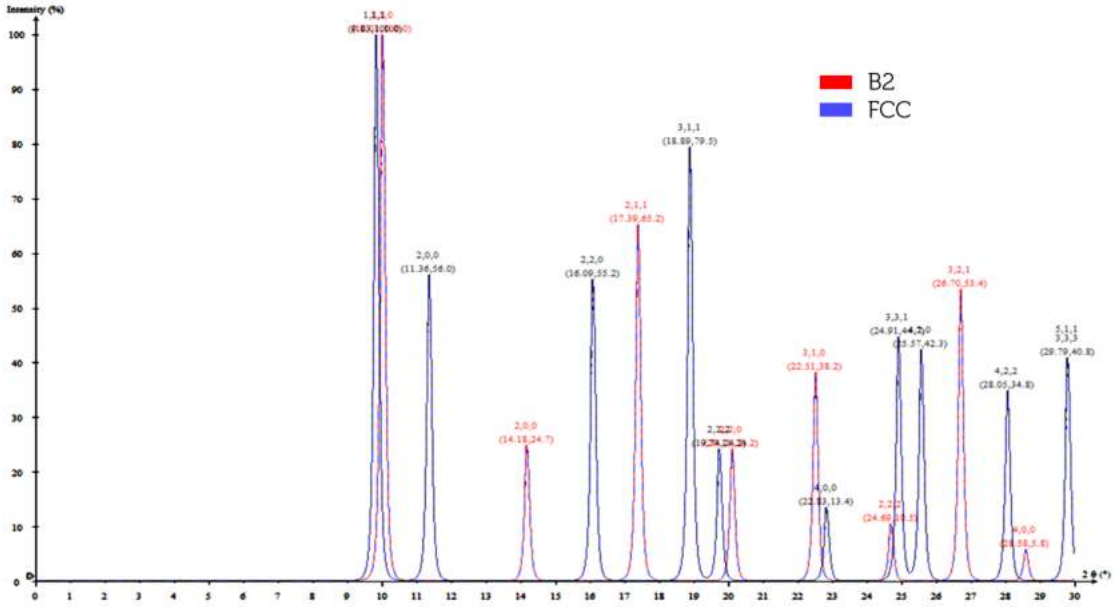

Figure 5.1: Theoretical 1D powder diffraction pattern of the HEA sample calculated with 35 keV X-rays.

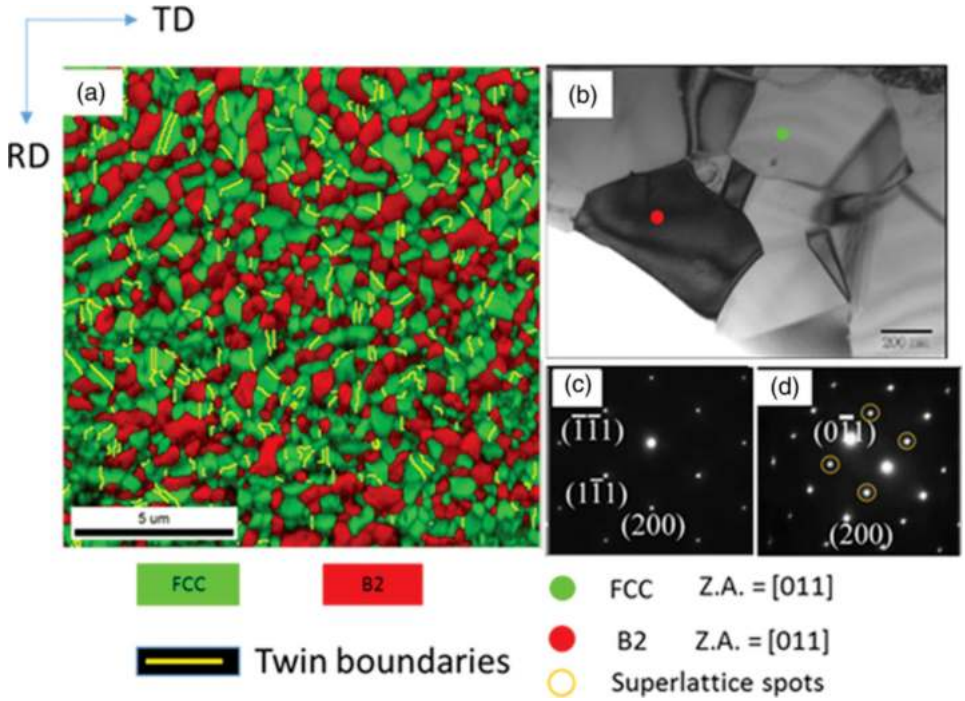

Figure 5.2: Microstructural characterization of 90% cold rolled eutectic AlCoCrFeNi$_{2.1}$ alloy heat treated for 1 hour at $800\,^{\circ}$C. (a) EBSD map revealing the eutectic microstructure of equiaxed grains. Color coding of microstructural features are given below. (b) Bright-field TEM micrograph of the specimen. (c-d) Selected area diffraction patterns of FCC and B2 phases collected from grains with color coding in (b). Zone axes of the micrograph and the diffraction patterns are given in the figure. Figures are adopted from [126].

in a special solid solution microstructure having topological arrangement of all alloying elements into a simple Bravais lattices of body-centered cubic (BCC), face-centered cubic (FCC) or hexagonal closed-packing (HCP). Due to sluggish kinetic restrictions of the rapid solidification processing, the constituent elements have inadequate kinetics for forming their equilibrium crystalline phases. Conversely, constituent elements form solid solution phases with simple Bravais lattices. These highly saturated solid solutions reaches a metastable equilibrium by decreasing their total free energy through their high configurational entropy. Depending on the alloy compositions, the microstructure can solidify either into a single phase solid solution or into a duplex eutectic microstructure of two solid solution phases with distinct crystal structures and compositions.

Thermo-mechanical processing of HEAs offer unique microstructures for engineering applications. A recent work by [126] have shown that thermo-mechanical treatment of eutectic AlCoCrFeNi$_{2.1}$ yielding an equiaxed microstructure to have an ultimate tensile strength of 1.2 GPa with 10% elongation. These mechanical properties were achieved by tailoring the microstructure by first cold rolling to $\approx$90% reduction in thickness, followed by a heat treatment of 1 hour at $800\,^{\circ}$C under controlled atmosphere. The resulting microstructure is shown in Figure 5.2. As seen from the figure, the eutectic microstructure is fully recrystallized to a FCC and a B2-type phases. The lattice parameters of these phases are given as 3.58 Å and 2.87 Å, respectively. Phase fractions were reported as 55% and 45%, respectively. The mean grain size of the whole microstructure was reported as $0.6\,\mu$m.

The explained microstructure presents interesting features and challenges to be studied with HR-3DXRD technique. The reported mean grain size is matches with the desired size regime to be exploited. Eutectic AlCoCrFeNi$_{2.1}$ alloy was produced by arc melting under Ti-gettered controlled atmosphere with high purity (better than 99.9%) starting materials. The master alloy was melted five times for constituting the chemical homogeneity of the sample. A rod-shaped specimen was formed from the master alloy with suction casting method. The surface of the as-cast alloy was polished for reducing the surface roughness and removing any possible contaminants. Then, the rod-shaped specimen was subjected cold rolling at ambient conditions to $\approx$90% reduction in thickness. The final thickness of the as-rolled specimens is measured as $300\,\mu$m. The as-rolled specimen was further heat treated for 1 hour at $800\,^{\circ}$C (1073 K). A needle shaped specimen was produced by chemical etching. The axis of the needle was adjusted to be parallel to the rolling direction. For further details of specimen preparation, please refer to [126] and [128]. A optical camera image of the specimen is given in Figure 5.3(a).

HEA specimen offers interesting microstructural features for demonstration of HR-3DXRD. The specimen's microstructure is composed of two distinct cubic phases with known lattice parameters. The theoretical 1D diffraction pattern of the microstructure is given in Figure 5.1. The figure reveals that the first Debye-Scherrer ring of both phases are overlapping in 2θ direction. This presence of such ring overlap is detrimental. However, the rest of the diffraction signal for both phases are expected to be well separated and well defined. Therefore, the analysis of this specimen should omit the overlapping rings and it shall be conducted through non-overlapping peaks. Secondly, comparing the EBSD map shown in Figure 5.2(a) to a hierarchically organized deformation microstructures, HEA specimen shows that the equiaxed grains of FCC and $B2$ phases are distributed rather homogeneously. The absence of a banded microstructure (as in the case of subgrains in GNB bands, Figure 4.14(a)) is expected to ease the 3D tessellation operation of these results.

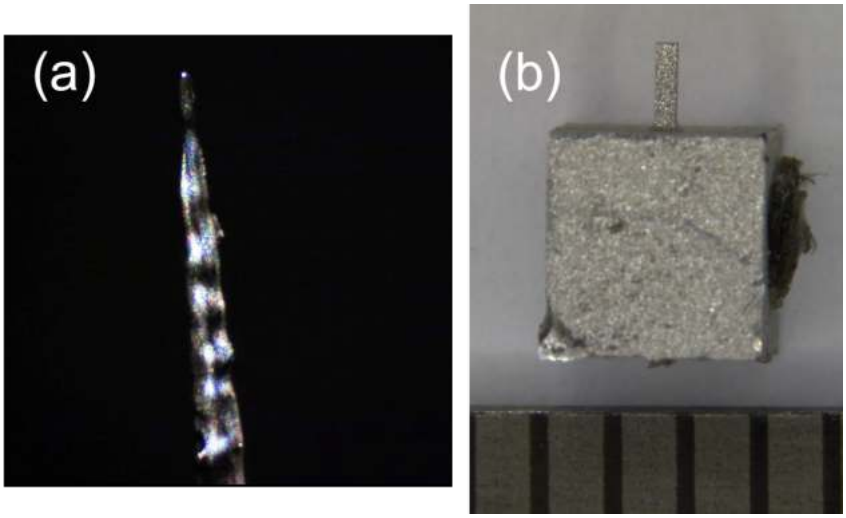

Figure 5.3: Images of (a) eutectic HEA and (b) partially recrystallized AA1050 specimens.

5.1.2 Commercially pure aluminum - AA1050

Aluminum and its alloys are widely used as structural materials in various industrial applications due their low density, high strength and high specific conductivity. From a large catalogue of chemical compositions, commercially pure aluminum alloy, designated as AA1050, have been used as a model alloy in literature for studying fundamental phenomena by offering a large selection of microstructure. Regarding 3DXRD literature, microstructures obtained from AA1050 has been used as models for demonstration of different modalities:

- Poulsen and coworkers have studied the rotation behavior of bulk grains of AA1050 under in situ tensile deformation with Mode I FF-3DXRD [1].
- Lauridsen and coworkers have studied the dynamics nucleation and growth behavior of recrystallized grains of AA1050 with Mode I FF-3DXRD [63].
- Schmidt and coworkers extended this study by following the 3D nucleation and growth behavior of a recrystallized grain from a single crystalline AA1050 by reconstructing its shape with back-projection methods [129].
- Gundlach and coworkers have studied the isothermal recovery of AA1050 with Mode I FF-3DXRD, tracking the growth behavior of 9 distinct subgrains [4].
- Ludwig and coworkers have showed the first experimental demonstration of DCT with a fully recrystallized AA1050 (with mean grain size of $\approx 200\,\mu$m [38].
- As previously mentioned in Chapter 3, Ahl and coworkers have shown the first experimental demonstration of Mode I HR-3DXRD by following the growth of ≈ 500 subgrains during the late stage recovery in AA1050 [5].

As seen from the examples above, AA1050 is a well-suited candidate that can be tailored to a multitude of desired microstructures for demonstration of emergent microscopy techniques. We have previously mentioned that HR-3DXRD is the Mode II extension of the technique shown in the [5] study. Hence, this study shall use samples of AA1050 alloy with equivalent microstructural features with respect to [5].

Purchased commercially pure AA1050 samples were subjected cold rolling at ambient conditions to ≈ 50% reduction in thickness. The as-rolled specimens were subjected

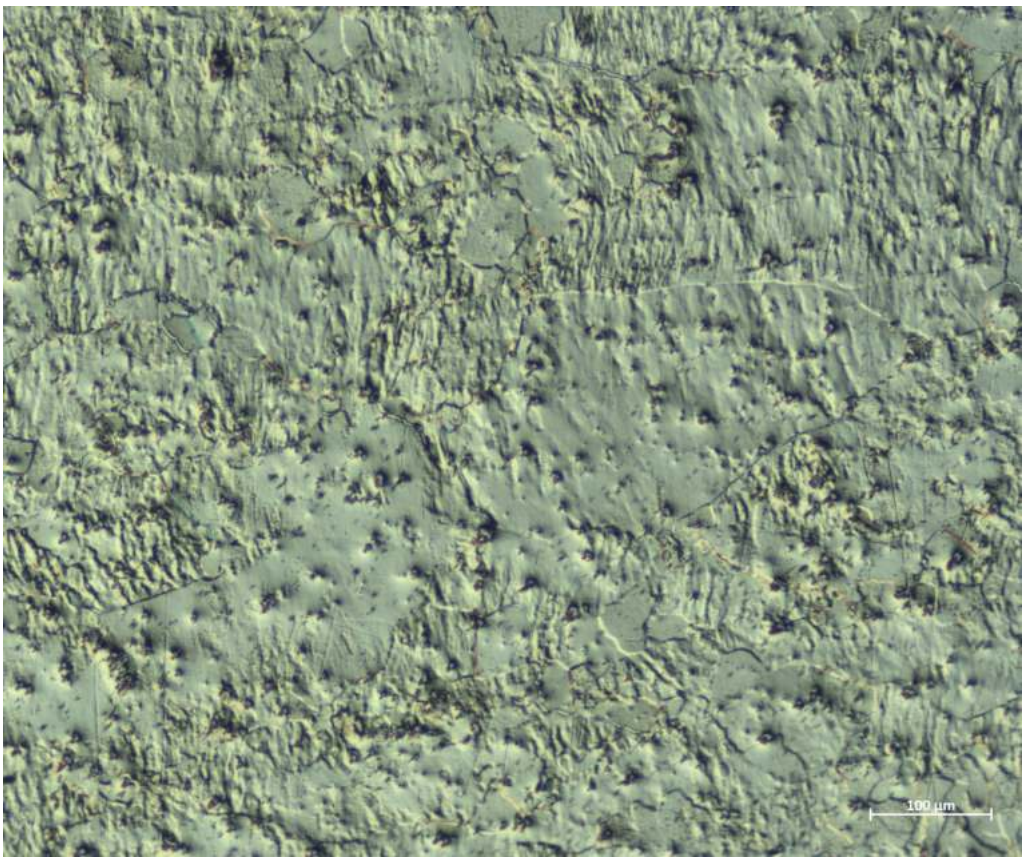

Figure 5.4: An optical microscopy image of the AA1050 sample. Courtesy of G. Winther.

to heat treatment in ambient atmosphere for 50 minutes at $325\,^{\circ}$C ($598\,$K). The resulting microstructure was characterized to be partially recrystallized. The volume fraction of the recrystallized grains was found as 50%. Specimens are prepared from the heat treated sample with electric discharge machining method by cutting rods of $1\,$mm height and cross-section of 300 by $300\,\mu$m^2. The long axis of the rod was cut to be parallel to the rolling direction. The final microstructure consists of large recrystallized grains and recovered grains with hierarchical organization (see Section 2.1). For further details of specimen preparation, please refer to [130] and [5]. An image of the specimen is given in Figure 5.3(b). The optical microscopy image of the sample's microstructure (after metallurgical sample preparation) is presented in Figure 5.4.

50% recrystallized AA1050 specimen has a highly heterogeneous microstructure, composed of large recrystallized grains of several tens of micrometers and "deformed grains" that undergo recovery [130]. In HR-3DXRD's regard, such heterogeneity can said to be advantageous. During recrystallization, the fresh recrystallized grains grow in expense of the remainder of the deformed (or recovered) microstructure [14]. As the static microstructure of the specimen is composed of both recrystallized and deformed (or recovered) grains, the diffraction patterns from AA1050 sample are expected show both type of grains separately. This information can be leveraged for finding regions with a low population of deformed grains inside, thus providing a valuable asset for overcoming the spot overlap.

5.1.3 Oligocrystalline gold

In a recent study by Shade and coworkers, oligocrystalline gold blocks of $50\,\mu$m size are adopted as spatial and chemical fiducial markers for in situ 3DXRD experimentation [131].

Table 5.1: Chemical composition of IF steel samples as mass fraction. Table adopted from [133].

C	N	Si	Mn	P	Cu	Ni	Ti	Fe
0.002	0.003	0.01	0.17	0.012	0.01	0.02	0.072	Balance

These markers are designed to be attach to sample surfaces, thus providing a spatial marker owing to gold's high X-ray attenuation in the relevant energy regimes (≤ 80 keV). The small blocks are cut from a well-annealed $50\,\mu$m gold foil with purity of $\approx 99.95\%$. The annealing procedure assures that cubes comprise of $1-3$ non-structured grains. The cut cubes are attached to specimen surfaces with a micro-manipulator assisted focused ion-beam SEM. For further details of preparation, please refer to [131].

Following the strategy taken in simulation studies, oligocrystalline gold cube is devised as the simplest proof-of-concept specimen for HR-3DXRD. The specimen was recycled from a previously purposed fiducial marker of an old sample, provided by APS 1-ID beamline. FF-3DXRD characterization of the sample revealed the presence of only 2 grains, both larger than $20\,\mu$m.

5.1.4 ARB-processed interstitial-free steel

In metals and their alloys, it is known that small interstitial atoms exert compressive forces on the surrounding solvent atoms in their local neighbourhood [17]. This high-energy state is relieved by migration of interstitial to the dislocation cores, which are know to create tensile forces within their local neighbourhood. Such placement of interstitials in dislocation cores greatly reduces the net force between the dislocation-interstitial pair, thus lowering its overall free energy [132]. However, such low-energy metastable structures give rise to adverse consequences in processing of metals and alloys. Interstitial-free (IF) steel is a special class of low-carbon iron alloys, in which the dislocation pinning of interstitial solute atoms is prevented via microstructural engineering. IF steel compositions contain a considerable amount of substitutional solute atoms having a high tendency of carbide and/or nitride formation. The presence of carbide formers attract the low concentration of interstitial atoms, thus exiling them from the matrix phase to low volume-fraction of carbide phases.

Severe plastic deformation (SPD) processing techniques are known to be capable of producing fine-to-ultra-fine grained microstructures [134]. Following the well-known Hall-Petch relation, SPD microstructures show high strength due to grain size refinement. Yet, deformation mechanism of these nanostructured materials exhibit a counter-intuitive behavior. In such materials, increasing deformation leads to softening of the material, whereas consequent annealing leads to hardening of the material [133]. The nature of such behavior was recently studied by Gao and coworkers of SPD processed IF steel by studying uniaxial tensile deformation behavior of SPD microstructures with varying thermal history, thus grain sizes [133, 135]. The study reports an abrupt loss of elongation for microstructures with grain sizes below $1.5\,\mu$m, which was attributed to the observed change from continuous to discontinuous yielding [133]. The explained microstructures in [133] are presented in Figure 5.7. We believe that such microstructures are good candidates for demonstration of HR-3DXRD, due to their adequately small grain sizes that can be tailored with heat treatment, and also due to their high misorientations.

Chemical composition of the IF steel samples are given in Table 5.1. The purchased IF steel samples of starting grain size of $20\,\mu$m was subjected to accumulative roll bonding (ARB) process for 7 cycles. All cycles are performed at $500\,^{\circ}$C (773 K) without applying

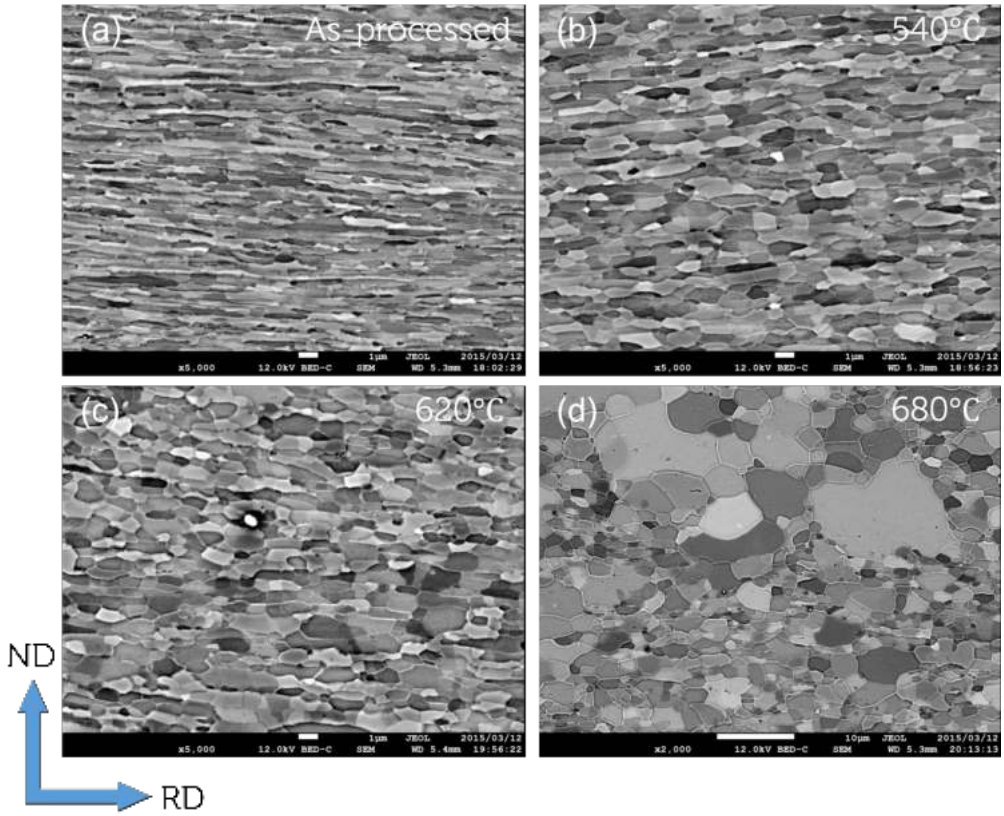

Figure 5.5: Secondary electron SEM micrographs of (a) as-processed and (b-d) 30 minute heat treated samples. Heat treatment temperatures, normal and rolling directions are indicated in the figure. Courtesy of S. Gao.

any lubrication. Each cycle corresponded to a 50% reduction in thickness, adding up to a total strain of 5.6 for the whole ARB process [133]. Heat treatment of the samples were conducted using salt baths at $540\,^{\circ}$C, $620\,^{\circ}$C and $680\,^{\circ}$C (813 K, 893 K and 953 K, respectively) for 30 minutes. The resulting microstructures are presented in Figure 5.5.

Two sets of pyramid-tipped needle-shaped specimens from the as-processed and three heat treated samples were prepared with electric discharge machining and electropolishing methods. The latter was done by using a solution of 63% H_3PO_4, 15% H_2SO_4, 10% CrO_3 and 12% water at $50\,^{\circ}$C (323 K) [136], with a current density of $2500\,\mathrm{A/m^2}$. The final thickness of the tip region of all specimens are approximately $40\,\mu$m. Example optical microscopy images of specimens are given in Figure 5.6.

ARB processed IF steel samples provide an adequate gamut of grain sizes with respect to its thermal processing history. The as-processed sample offers a highly strained microstructure, which is devised to test the resolution capabilities of the HR-3DXRD concept. As seen in Figure 5.5, the annealed samples are composed of subgrains with differing sizes. Furthermore, the figure shows that samples heat treated at $540\,^{\circ}$C and $620\,^{\circ}$C have relatively uniform grain size distributions. Whereas, the microstructure of $680\,^{\circ}$C heat treated sample is relatively more heterogeneous, owing to the presence of large grains of $> 5\,\mu$m. Lastly, the texture of all heat treated samples are expected to be weaker than their as-processed counterpart. Thus, we can expect the characteristics of the samples with $540\,^{\circ}$C and $620\,^{\circ}$C heat treatment to resemble the phantoms analyzed in Section 4.7.

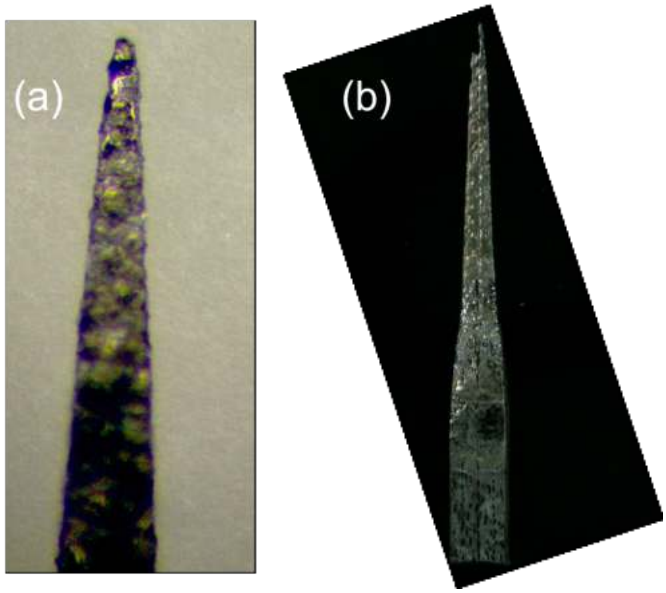

Figure 5.6: Optical microscopy images of (a) electric discharge machined and (b) electropolished ARB processed IF steel. Images are not to scale with respect to each other.

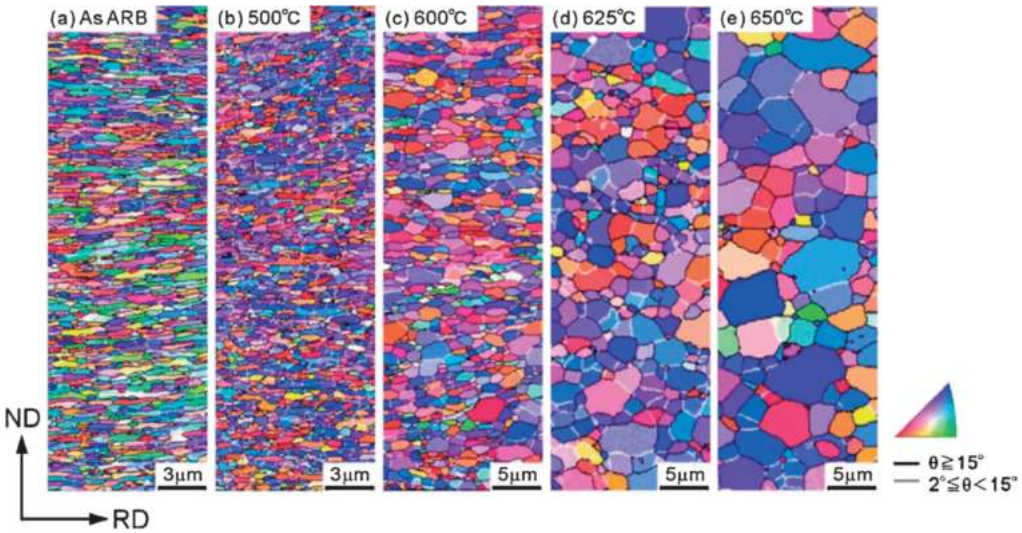

Figure 5.7: EBSD maps of (a) as-SPD processed and (b-e) 30 minutes heat treated IF steel. Heat treatment temperatures are indicated in the figure. Adopted from [133].

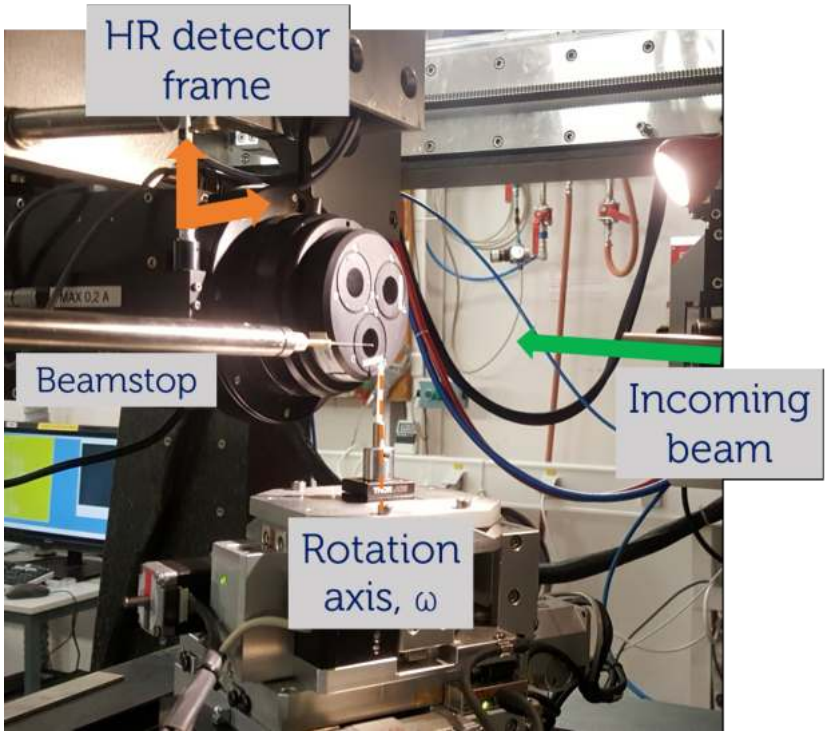

Figure 5.8: The experimental configuration of ESRF ID11 experiment. High resolution detector was translated on the plane defined by y and z axes (shown in orange).

5.2 Experimental setups

HR-3DXRD test experiments were pursued at four different grain mapping beamlines with the samples presented in Section 5.1. In this section, the experimental configurations relevant to each experiment will be presented.

5.2.1 ESRF ID11 beamline

In this experiment, eutectic HEA and AA1050 samples were studied by combining classical FF-3DXRD and HR-3DXRD scans.

Photon energy of 35 keV was selected with a Si(100) bent Laue double crystal monochromator that is 29.9 m away from the source. The bandwidth of the incident beam was estimated as $\frac{\Delta E}{E} = 2 \times 10^{-3}$. The monochromated primary beam was initially collimated with an in-vacuum transfocator system [137] located 31.5 m away from the source, comprising 8 2D Be compound refractive lenses (CRLs). For each individual lenslet, physical aperture was 1 mm, web thickness was $\approx 50\ \mu$m and radius of curvature was $200\ \mu$m. The transfocator collimated the incoming beam to the slit system located on entrance of the Kirkpatrick-Baez (KB) mirror system, located 31.5 m away from the source. The size of the slits were set as 1 mm in both directions. The size of the beam on the entrance of the KB mirror system was 0.5 mm in vertical and 0.9 mm in horizontal. The incident beam used for the experiments was defined with the KB mirror. The mirror was set for vertical focusing on the sample position and horizontal focusing after the sample position. An extra set of slits were placed after the KB mirrors with openings of 0.5 mm in vertical and 0.9 mm in horizontal, for cleaning purposes. The beam profile on the sample position was measured as $\approx 1.5\ \mu$m in vertical and $\approx 30\ \mu$m in horizontal directions.

The samples were place on the vertical rotation stage, shown in Figure 5.8. CoR of the rotation stage was aligned to coincide with the defined optical axis. The detector frame was

placed 7.3 mm downstream of the sample position. For both HR-3DXRD and FF-3DXRD scans, a FReLoN (Kodak F4M) CCD camera [138] was used with an visible light optics system. The native pixel size of the FReLoN camera was $24\,\mu$m in both vertical and horizontal directions. The optical system consisted of a scintillator screen, a static eyepiece with $3.1x$ magnification and a secondary objective. Both scans utilized a $22\,\mu$m thick Eu-doped gadolinium gallium garnet (GGG) scintillator screen. For HR-3DXRD scans, the secondary objective was chosen as $10x$ magnification, providing a $31x$ magnification with effective pixel size of $0.77\,\mu$m and FoV of 1.577 x $1.577\,\text{mm}^2$. For FF-3DXRD scans, the secondary objective was changed to $4x$ magnification, providing a $12.4x$ magnification with effective pixel size of $1.94\,\mu$m and FoV of 3.964 x $3.964\,\text{mm}^2$. A beamstop made from a 0.3 mm thick Ta wire and placed 2 mm upstream of the camera.

The employed detector configuration for HR-3DXRD scans is shown in Figure 5.9(a). The experiment was performed with 4 detector positions, covering $\approx 90\,^\circ$ in η direction. With this configuration, each panel contains 6 full rings of the FCC phase and 5 full rings of the B2 phase. Detector positions were adjusted such that each panel has $\approx 5\%$ overlap with its neighboring position. Considering the nominal grain size of the HEA sample, Fresnel number of the setup was calculated as 1.39. ω-scans were done on the half range of $[0\,^\circ, 180\,^\circ]$ with steps of $0.1\,^\circ$.

The ESRF ID11 experiment was the first experimental trial of the multi-panel acquisition HR-3DXRD technique. As mentioned above, the experiment utilized the eutectic HEA sample introduced in Section 5.1.1. The initial aims for the experiment can be explained as follows:

- Observation of individual diffraction spots: In Section 3.2, we mention the first report of observation of individual diffraction spots from micrometer- sized subgrains in AA1050. Thus, the first aim of this experiment was to determination and optimization of the experimental parameters, such as $\boldsymbol{L}$, effective pixel size and number of detector positions for HR-3DXRD scanning, with respect to the studied sample.
- Stability of the incident beam and of the mechanical construction: The attained experimental setup dictated the HR-3DXRD scans to take approximately $6-8$ hours with respect to incident flux and consequently the exposure time. Considering the tight positional accuracy requirement of HR-3DXRD, the extended scanning times implies the issue of incident beam stability, but also the stability of the mechanical construction of the experimental setup. We should note that decoupling of the mentioned two sources of instability is not trivially measured in a regular non-dedicated grain-mapping beamline. Therefore, the second aim of the experiment was to determine and remedy the stability issues in an *ad hoc* manner during the long HR-3DXRD scanning.

At the time of the experiment, the first aim was achieved with the parameters given in the beginning of this section. The optimized parameter were inspired from the mentioned Ahl work [5]; the reported experimental parameters of incident wavelength, $\boldsymbol{L}$, and the reported mean grain size of their sample was used for computing the dimensionless Fresnel number of the corresponding experimental setup. Then, the calculated Fresnel number was used as a starting point for determining the initial guesses for $\boldsymbol{L}$ with respect to the mean grain size of the analyzed HEA sample. The effective pixel size of the detector used for HR-3DXRD scans was selected from the visible light objectives available in the beamline. The number of multi-acquisition panels were then determined and optimized via the initial guess of $\boldsymbol{L}$ and the employed effective pixel size of the high-resolution imaging detector.

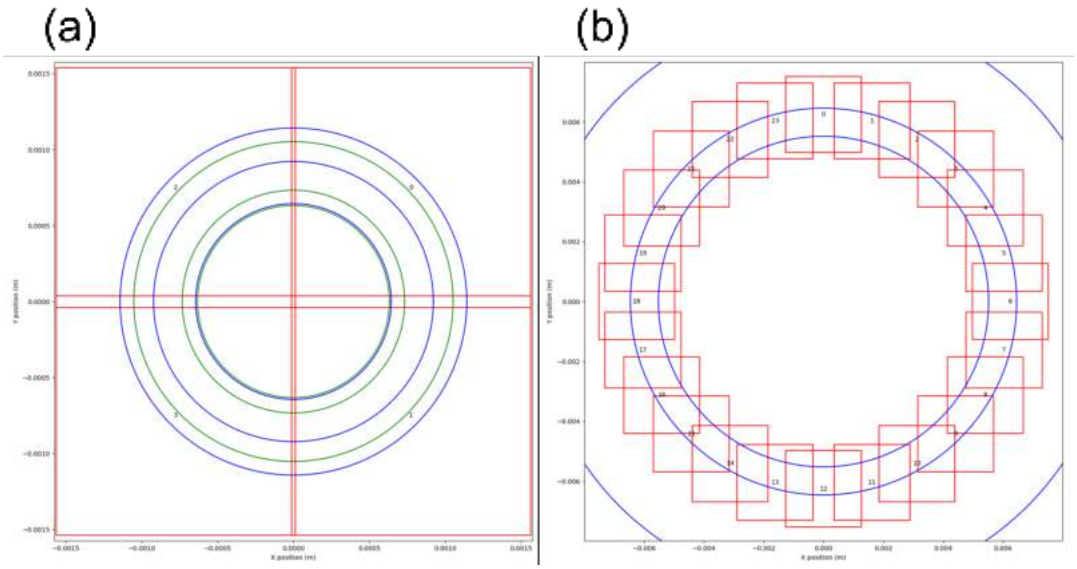

Figure 5.9: HR-3DXRD detector configurations utilized in (a) ESRF ID11 and (b) ESRF ID06-HXRM experiments. First three Debye-Scherrer ring positions of (a) HEA's FCC (blue) and B2 (green) phases, and (b) α-Al (blue) are given with respect to the employed X-ray energies.

In order to address the stability issue, the first 36 hours of the experiment was dedicated for optimization of the incident beam flux and also for extended stability tests. Firstly, the optical alignment of the beamline (e.g. mainly monochromator and collimation elements) was fine tuned for achieving the highest possible incident beam flux on the sample position. Then, the (attenuated and) collimated direct beam was tracked for ≈ 12 hours to observe the extent of experimental setup's stability. The on-line analysis had shown that the incident beam had drifted suffered from a stochastic drift in y_L and z_L directions by more than ≈ 5 pixels. Considering the attained effective pixel size, such a drift corresponds to $\approx 4\,\mu$m misplacement in the surface defined by y_L and z_L axes. In order to remedy the stability problem, the data acquisition at each detector position was divided into ≈ 30 minute steps, such that between each step the sample was re-aligned with a pre-determined diffraction spot in y_L and z_L directions.

Lastly, we should discuss that the stability issues regarding the incident beam may stem from the chosen incident beam energy. In this experiment, the energy of the incident beam was decided as 35 keV, that can be attributed to be on the lower-most side of the energy range offered by the ESRF ID11 beamline [80]. In fact, ESRF ID11 beamline is optimized for high energy (i.e. in the current context, the term "high energy" refers to X-rays energies $\gg 45-50$ keV.) diffraction studies. Therefore, one can expect the utilized optical elements of the experimental setup to perform sub-optimally in terms of obtained flux and also in terms of its thermo-mechanical response. Thus, the observed incident beam stability issues may have had arisen due to such sub-optimal low energy choice with respect to ESRF ID11 beamline specifications.

5.2.2 ESRF ID06 beamline

In this experiment, AA1050 sample was studied by combining HR-3DXRD and DFXM scans. The latter is out of the scope of this thesis, thus its configuration will not be presented.

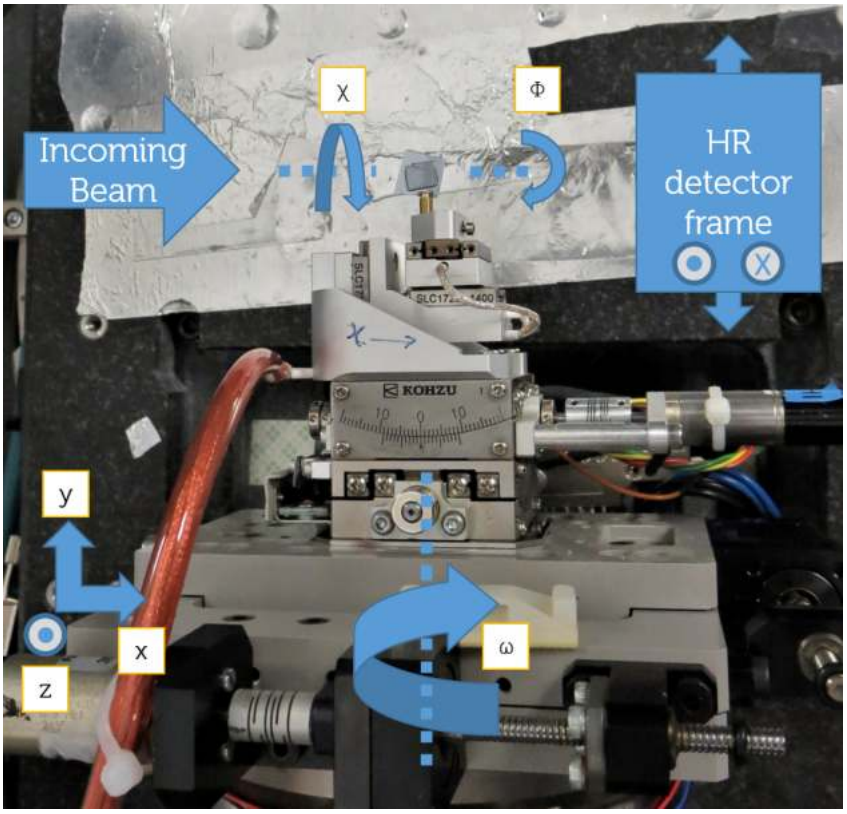

Figure 5.10: The experimental configuration of ESRF ID06-HXRM experiment. Detector was translated on the plane defined by y and z axes. Figure adopted from [88].

The experiment was held in the High Energy X-ray Microscopy (HXRM) hutch of the ID06 beamline. Photon energy of 17 keV was selected with a Si(111) Bragg-Bragg double crystal monochromator that is 35.8 m away from the source. The bandwidth of the incident beam was estimated as $\frac{\Delta E}{E} =\approx 1 \times 10^{-4}$. The monochromated primary beam was initially collimated with a UHV transfocator system [139] located 38.7 m away from the source, comprising 6 2D Be compound refractive lenses (CRLs). For each individual lenslet in the transfocator, physical aperture was 1 mm, web thickness was $\approx 50\,\mu$m and radius of curvature was $200\,\mu$m. The transfocator collimated the incoming beam to the slit system located on entrance of the condenser system, located ≈ 55 m away from the source. The size of the slits were set as $20\,\mu$m in both directions. The condenser system was composed of 58 1D Be CRLs. For each individual lenslet in the condenser system, physical aperture was 0.6 mm, web thickness was $\approx 50\,\mu$m and radius of curvature was $100\,\mu$m. The condenser was overfocused with respect to sample position. The height of the beam on the sample position was measured as $10\,\mu$m with a knife-edge scan.

The samples were place on the horizontal rotation stage. CoR of the rotation stage was aligned to coincide with the defined optical axis. The detector frame was placed 17 mm downstream of the sample position. HR-3DXRD scan was collected using a FReLoN (Atmel TH7899M) CCD camera [138] with a visible light optics system. The native pixel size of the FReLoN camera was $14\,\mu$m in both vertical and horizontal directions. The optical system consisted of a scintillator screen, a tube lens with $0.9x$ magnification, a static eyepiece with $2.5x$ magnification and a secondary objective. A free-standing $25\,\mu$m thick Eu-doped GGG crystal was used as a scintillator screen. The scintillator was screened by a thin optical cloth for reduction of noise from background radiation. The secondary

objective was chosen as $10x$ magnification, providing an effective pixel size of $0.62\,\mu$m and FoV of 1.24 x $1.24\,\text{mm}^2$. A beamstop made from a ≈ 1 mm thick W wire and placed 2 mm downstream of the sample. For further details about the equipment, please refer to [88].

The employed detector configuration for HR-3DXRD scans is shown in Figure 5.9(b). The experiment was performed with 24 detector positions, covering $\approx 15\,^\circ$ in η direction. Detector positions were adjusted such that each panel has $\approx 30\%$ overlap with its neighboring position. With this configuration, each panel contains 2 full rings of the α-Al phase. Considering a $1\,\mu$m subgrain size of the AA1050 sample, Fresnel number of the setup was calculated as 0.8. ω-scans were done on the half range of $[0\,^\circ, 180\,^\circ]$ with steps of $0.05\,^\circ$.

The ESRF ID06-HXRM experiment was the second experimental trial of the HR-3DXRD technique with multi-panel acquisition. As mentioned above, the experiment utilized the AA1050 sample introduced in Section 5.1.2. Our initial aim for the experiment can be explained as follows:

- Low incident X-ray energy configuration: In contrast to the previous ESRF ID11 experiment, the configuration was set up at a relatively low incident X-ray energy of 17 keV. According to beamline specifications, the chosen energy is one of the optimized energy options offered by ESRF ID06 beamline [88]. In turn, such choice required further optimization of the experimental setup with respect to $\boldsymbol{L}$ and number of detector positions for HR-3DXRD scan.
- Mode-I to Mode-II extension: Aforementioned work of Ahl and co-workers ([5]) was reported to be conducted in the same beamline with similar experimental specifications. Therefore, one aim of this experiment was to ***extend*** **what we attribute as a Mode-I HR-3DXRD work of Ahl and co-workers** to Mode-II CoM mapping work with a sample of equivalent microstructure.
- Incident X-ray energy bandwidth: The optical configuration of ESRF ID06 enabled us to conduct the experiment with the lowest incident X-ray bandwidth of $\frac{\Delta E}{E} \approx 1 \times 10^{-4}$ that had ever tried for HR-3DXRD. Therefore, the effect of bandwidth on the observed diffraction peaks was one of the main aims of this experiment.
- Alignment of a particular microstructural feature: As stated above, this experiment was designed to be a multi-modal X-ray microscopy experiment. One of the main aims of this experiment was to utilize the X-ray objective lens of the DFXM setup in ESRF ID06 for alignment of a particular microstructural feature for the HR-3DXRD (and consequently, DFXM) scanning of the analyzed sample volume.

The first aim of the optimization for the low energy configuration was achieved successfully in the first day of the experiment. The parameters found in the previous ESRF ID11 experiment was scaled down to the current choice of energy via the calculated Fresnel numbers of both experimental setups. The low energy choice led to a shorter $\boldsymbol{L}$ and for the HR-3DXRD scan, a total of 24 detector positions around the azimuthal direction. Therefore, the achieved experimental setup ensured the achievement of the second aim of the experiment, i.e. extending the mentioned Mode-I work to the Mode-II CoM mapping technique, with success. In comparison to the work of Ahl and co-workers [5], in this experiment we have successfully collected a complete Mode-II HR-3DXRD dataset comprising 24 detector positions around the azimuth with respect to the reported 1 detector position in [5]. Furthermore, the collected Mode-II HR-3DXRD dataset had acquired the diffraction signal for $\omega_{range} = \pi$, whereas the scans reported in Ahl work was only limited to $\omega_{range} = 0.011\pi$.

Considering the Bragg's Law and a finite interplanar spacing of a theoretical crystal, the bandwidth of the incident beam energy was expected to affect the radial spread of the emanated diffraction signal on the detector frame. The comparison of the HR-3DXRD datasets collected from the AA1050 sample in ESRF ID11 and ID06 experiments confirms this deduction, as the measured width of the observed diffraction peaks were found to be substantially narrower in the ID06 case. Hence, as expected, the bandwidth has a reciprocal relationship with the observed width of the diffraction peaks. Albeit providing better definition for observed peaks, the choice of narrow incident bandwidth also implies a respective decrease in the incident X-ray flux on the sample. Therefore, the use of a narrow bandwidth should be justified if only the diffraction peaks are observed with adequate S/N, or in other words, statistics.

Lastly, as mentioned above, this experiment was originally designed as a demonstration of a complex multi-modal X-ray microscopy experiment with the dedicated aim of observation of a deformed grain/recrystallized grain boundary in the mentioned AA1050 sample (see Section 5.1.2). The experiment aimed to track the deformed-grain-side of the boundary microstructure with HR-3DXRD; whereas, the recrystallized grain was aimed to be mapped with DFXM. In short, the alignment of the boundary was commenced by determination of the recrystallized-grain of interest. The recrystallized grain was chosen through on-line inspection of far-field diffraction patterns. Then, the vicinity of the found recrystallized grain was inspected for the presence of a deformed grain through extended scanning in the "roll" direction of the DFXM setup [88, 89, 91]. Following the confirmation, the found recrystallized grain was aligned for the DFXM scanning procedure, enabling observation of the real-space image of the chosen recrystallized grain. Then, by utilizing such real-space information, the determined deformed/recrystallized grain boundary was translated to the pre-aligned CoR of the goniometer. Therefore, the gauge volume aligned in the microscope had the desired deformed grain/recrystallized grain boundary for both HR-3DXRD and DFXM to study. We should note that, due to such alignment, the HR-3DXRD dataset contained the information for the recrystallized grain, yet, the analysis of this particular grain would only provide the grain-averaged information (e.g. for orientation and strain). In contrast, the reconstruction of the DFXM scan from the recrystallized grain would provide the intragranular variation of orientation and strain of the analyzed grain with superior real and reciprocal space resolution. The further details of this experiment is out of scope of this thesis and the finding will be reported elsewhere. Nevertheless, in this experiment, we have successfully showed that alignment of particular microstructural features are in fact possible, provided that the grain-mapping instrument have direct microscopy techniques at its gamut of offered techniques.

5.2.3 APS 1-ID-E beamline

In this experiment, oligocrystalline Au and ARB-processed interstitial-free steel samples were studied by combining classical FF-3DXRD and HR-3DXRD scans.

Photon energy of 52 keV was selected with the 1-ID's high-energy monochromator; Si(111) bent Laue double crystal monochromator that is 29 m away from the source. The bandwidth of the incident beam was estimated as $\frac{\Delta E}{E} = 8 \times 10^{-4}$. The vertical collimation of the monochromatized beam was done 33 m away from the source with 38 1-D Al-CRLs. For each lenslet, web thickness was $20\,\mu$m and cylindrical radius was $500\,\mu$m. The beam was further collimated at 62 m away from the source with 18 2D paraboloid Al-CRLs. For each lenslet, web thickness was $20\,\mu$m and cylindrical radius was $500\,\mu$m. The horizontal collimation of the incident beam was done at $\approx$68 m away from the source with two sets of Al sawtooth CRLs. The lens sets were 160 mm long and they are composed of triangular tooth with base angle of $30\,^\circ$ and groove depth of $150\,\mu$m. The condenser was overfo-

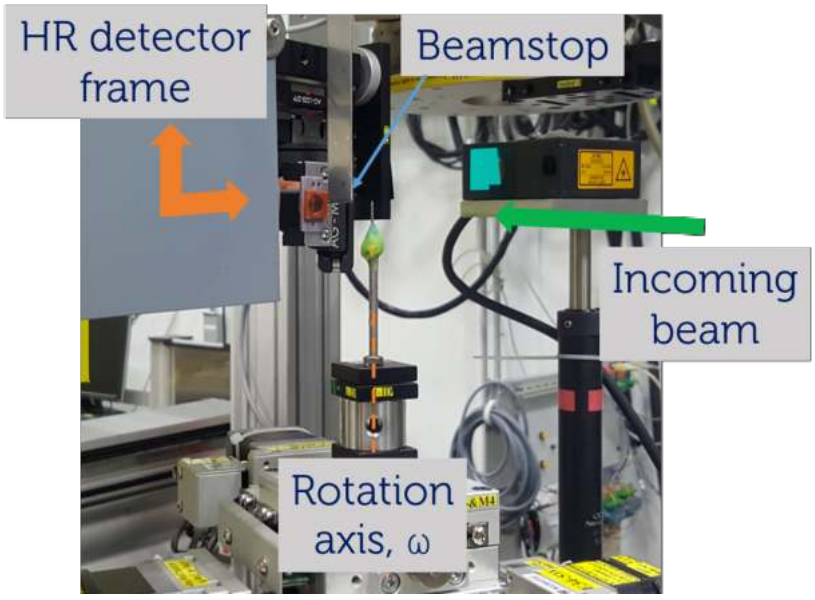

Figure 5.11: The experimental configuration of APS 1-ID-E experiment. High resolution detector was translated on the plane defined by y and z axes (shown in orange). During FF-3DXRD scans, the high resolution detector was translated out of the beam.

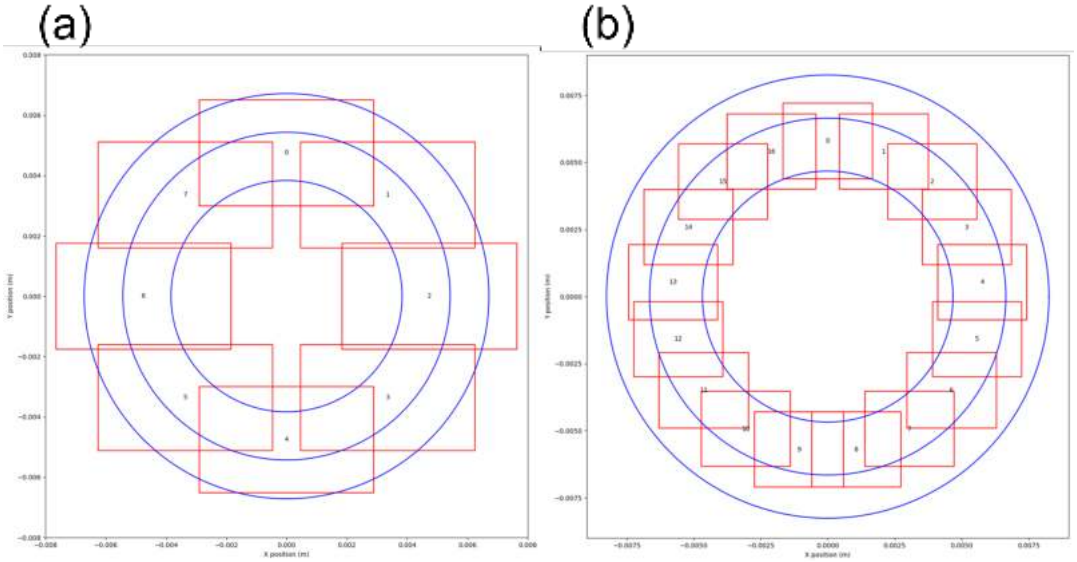

Figure 5.12: HR-3DXRD detector configurations utilized in (a) APS 1-ID-E and (b) DESY Petra II P21.2 experiments. The positions of the first three Debye-Scherrer rings of α-Fe (blue) are given with respect to the employed X-ray energies.

cused with respect to sample position. The height of the beam on the sample position was measured as $\approx 10\,\mu$m. The samples were place on the vertical rotation stage. CoR of the rotation stage was aligned to coincide with the defined optical axis. The detector frame for HR-3DXRD was placed 70 mm downstream of the sample position. HR-3DXRD scan was collected using a FLIR Grasshopper3 CCD camera with a visible light optics system. The native pixel size of the $5.86\,\mu$m in both vertical and horizontal directions. FoV of the camera was 1920 x 1200 pixels $\times$ pixels. The optical system consisted of a scintillator screen, a static eyepiece with $1x$ magnification and a secondary objective. A free-standing $25\,\mu$m thick LuAG crystal was used as a scintillator screen. The secondary objective was chosen as $2x$ magnification, providing an effective pixel size of $2.93\,\mu$m and FoV of 5.626 x 3.516 mm^2.

The detector frame for FF-3DXRD was placed 822 mm downstream of the sample position. FF-3DXRD scans were collected using a single GE-41RT flat panel detectors with a pixel size of $200\,\mu$m. FoV of the camera was 2048 x 2048 pixels $\times$ pixels. The camera was screened by a lead plate for reduction of noise from background radiation. For both scans beamstop made from a ≈ 3 mm thick W wire and placed 5 mm downstream of the sample.

The employed detector configuration for HR-3DXRD scans is shown in Figure 5.12(a). The experiment was performed with 8 detector positions, covering $\approx 45\,^\circ$ in η direction. Detector positions were adjusted such that each panel has ≈ 25% overlap with its neighboring position. With this configuration, each panel contains 2 full rings and 1 partial ring of the α-Fe phase. Considering a $1\,\mu$m subgrain size of the ARB-processed interstitial-free steel sample, Fresnel number of the setup was calculated as 0.57. ω-scans were done on the full range of $[0\,^\circ, 360\,^\circ]$ with steps of $0.1\,^\circ$.

The APS 1-ID-E experiment was the penultimate experimental trial of the multi-panel acquisition HR-3DXRD technique. As mentioned above, the experiment utilized the ARB IF steel samples introduced in Section 5.1.4. Furthermore, in this experiment we had tried to collect HR-3DXRD datasets from the oligocrystalline Au sample, Section 5.1.3, and a calibration dataset with CeO_2 powder. The aims for the experiment can be explained as follows:

- High incident X-ray energy configuration: APS 1-ID-E experiment was conducted with 52 keV incident X-ray energy. The incident energy choice was encouraged by the experience in ESRF ID06, such that the chosen energy was known to be one of the optimized incident energies offered by 1-ID-E beamline.
- Large choice of effective pixel size: In the first day of the experiment, the employed high resolution imaging detector was observed to fail the required adequate S/N for the observed diffraction peaks. Therefore, in order to increase the photon collection performance of the employed detector, the experiment was performed with an effective pixel size of $\approx 3\,\mu$m.
- Trial of calibration datasets: In this experiment, we had collected experimental calibrant datasets with the established HR-3DXRD experimental setup with two different calibrant materials: oligocrystalline Au and CeO_2 powder. These datasets were expected to serve as potential inputs for possible detector calibration work (for details, see Chapter 6).

Upon the experience gained from the ESRF experiments, the APS 1-ID-E experiment was performed with one of the optimized energies of the beamline, at 52 keV incident X-ray energy. Naturally, the high energy choice optimized the $\boldsymbol{L}$ to a comparably larger values than the previous experiments.

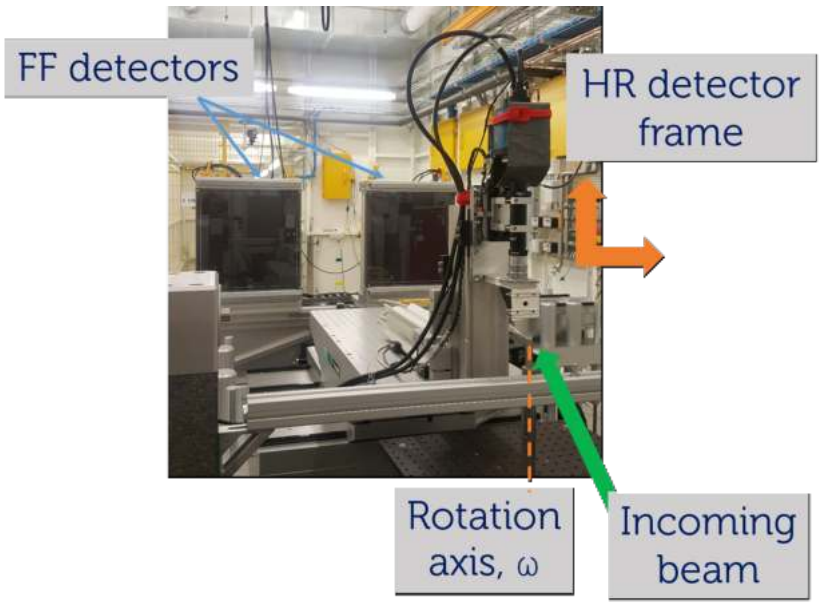

Figure 5.13: The experimental configuration of DESY Petra III P21.2 experiment. High resolution detector was translated on the plane defined by y and z axes (shown in orange). During FF-3DXRD acquisition, the high resolution detector was translated out of the beam.

As mentioned above, the initial efforts had shown that the employed high resolution imaging detector underperformed with respect to the previous experiences. Thus, in order to increase the effective S/N of the observed diffraction peaks, the effective pixel size was adjusted to $\approx 3\,\mu$m via changing the visible light objective of the optical microscopy setup attached to the detector unit. The increased effective pixel size comparably improved the observed S/N ratio, providing observation of smaller sized diffraction peaks.

Lastly, we had collected two calibrant datasets from the mentioned oligocrystalline Au sample and from a calibrant-grade CeO_2 powder provided from the beamline resources. The high crystallinity of the oligocrystalline Au sample had provided a good S/N for the observed diffraction peaks. Yet, the oligocrystalline nature of the sample provided only a small number of observed diffraction peaks in both 2θ and η directions. Moreover, the depressed number of orientations in the microstructure further caused no observable diffraction signal for some detector positions. In the CeO_2 (space group # 225, $Fm\bar{3}m$) powder case, the observed intensities of the diffraction signal from the calibrant material was extremely weak; the peak intensity of the first diffraction ring was observed to be ≈ 2% higher than the fluctuating background of the employed detector. Hence, we can say that both efforts of obtaining a good calibration dataset was failed. The problem of calibrant data collection will be further discussed in the upcoming chapter, in Section 6.2.

5.2.4 DESY Petra III P21.2 beamline

In this experiment, only ARB-processed interstitial-free steel samples were studied by combining classical FF-3DXRD and HR-3DXRD scans.

Photon energy of 38 keV was selected with the P21's broad band monochromator; Si(111) bent Laue double crystal monochromator that is 100 m away from the source. The bandwidth of the incident beam was estimated as $\frac{\Delta E}{E} = 1 \times 10^{-3}$. The monochromated primary beam was initially collimated with vertically focusing 1D Al CRLs located 112 m away from the source, comprising 9 lenslets with a radius of $200\,\mu$m and 1 lenslet with a radius of $500\,\mu$m. Horizontal focusing was done using 1D Al CRLs, located at 133 m away from the

source, comprising 8 lenslets with a radius of $100\,\mu$m, 1 lenslet with a radius of $300\,\mu$m and 1 lenslet with a radius of $200\,\mu$m. The physical aperture of all CRLs was 0.622 mm. The resulting focused beam at the sample position — 150 m from the source — had a Gaussian shape with FWHM of $20\,\mu$m and $40\,\mu$m in the vertical and horizontal directions, respectively. At a distance of 1.5 m upstream of the sample, the shape of the incoming beam was defined with a slit with $10\,\mu$m and $50\,\mu$m in the vertical and horizontal directions, respectively.

The samples were place on the vertical rotation stage. CoR of the rotation stage was aligned to coincide with the defined optical axis. The detector frame for HR-3DXRD was placed 28.85 mm downstream of the sample position. HR-3DXRD scans were collected using a PCO.edge 5.5 CCD camera with a visible light optics system. The native pixel size of the $6.5\,\mu$m in both vertical and horizontal directions. FoV of the camera was 2560 x 2160 pixels^2. The optical system consisted of a scintillator screen and an objective lens. A free-standing $20\,\mu$m thick Eu-doped GGG crystal (purchased from ESRF) was used as a scintillator screen. The objective lens was chosen as $5x$ magnification, providing an effective pixel size of $1.3\,\mu$m and FoV of 3.328 x 2.808 mm^2. The camera was screened by a thin lead plate for reduction of noise from background radiation. The detector frame for FF-3DXRD was placed 1.75 m downstream of the sample position. FF-3DXRD scans were collected using two Varex XRD4343CT flat panel detectors with a pixel size of $150\,\mu$m. FoV of the camera was 2880 x 2880 pixels^2. The camera was screened by a lead plate for reduction of noise from background radiation.

The employed detector configuration for HR-3DXRD scans is shown in Figure 5.12(b). The experiment was performed with 17 detector positions, covering $\approx 21\,^\circ$ in the η direction. Detector positions were adjusted such that each panel has $\approx$22% overlap with its neighboring position. With this configuration, each panel contains 2 full rings of the α-Fe phase. Considering a $1\,\mu$m subgrain size of the ARB-processed interstitial-free steel sample, Fresnel number of the setup was calculated as 1.06. ω-scans were done on the full range of $[0\,^\circ, 360\,^\circ]$ with steps of $0.1\,^\circ$.

DESY Petra III P21.2 experiment was the final experimental trial of the multi-panel acquisition HR-3DXRD technique. As mentioned above, the experiment utilized only one sample, ARB IF steel (see Section 5.1.4). In this experiment, the experience gained in the previous ESRF and APS experiments were utilized for optimization of the HR-3DXRD related experimental parameters. The optimized experimental setup provided adequate S/N, enabling observation of weak diffraction spots from the ARB IF steel sample that were not available in the previous APS experiment.

The main aim of this experiment can be explained as the suppression of systematic errors. The main strategical difference in P21.2 experiment could be seen as the randomized acquisition of the individual detector position steps along the HR-3DXRD scanning. In the previous experiments, the acquisitions were made on the manually calculated detector positions in a successive manner along the azimuthal direction; i.e. once an HR-3DXRD acquisition was made at a certain detector position, the HR-3DXRD scan was continued by translating the detector to the neighboring detector position in positive-η direction. Whereas, in the P21.2 experiment, the pre-calculated detector positions were shuffled in a randomized manner, such that the acquisitions did not follow a continuous path along the azimuthal direction. The shuffled acquisition strategy was aimed to suppress and account for the systematic errors that could arise from mechanical instabilities along the detector motion along the η-direction. Therefore, any potential drifts in the experimental configuration will not be correlated to the azimuthal angle.

Our initial analysis of the acquired datasets from DESY Petra III P21.2 experiment had shown that the acquired experimental diffraction images possessed an adequate S/N ratio. Hence, in the next chapter, (Chapter 6), a dataset acquired from this beamtime will be utilized as the input dataset for the discussion of pre-processing and demonstration purposes of HR-3DXRD.

5.3 Experimental data analysis

In Section 4.1, we have discussed a software pipeline for HR-3DXRD data analysis over the numerical simulation examples. In the following sections, we have successfully validated the analysis pipeline with phantoms of both randomly oriented subgrains and also with two physically representative phantoms. The results given in Chapter 4 shows that the proposed analysis software pipeline, gathered from readily available 3DXRD analysis softwares, are capable of analyzing and refining HR-3DXRD datasets.

The analysis pipeline presented in Figure 4.1 was given for two routes of direct and harvested analysis of the synthetic data. It was mentioned that the former operates on the calculated diffraction spot positions, whereas the latter operates on produced synthetic diffraction images. The latter was hypothesized to reflect the real experiments, as experimental diffraction images from $2D$ detectors are known to suffer from spot overlap for polycrystals of low misorientation [119]. It was later shown in Section 4.7.2 that the harvested analysis have partially suffered from spot overlap due to high local texture of the analyzed phantom.

In principle, the software pipeline for harvested analysis route should be readily usable for analysis of experimental HR-3DXRD data. However, we should remind that in the given numerical simulations, the diffraction signal was simulated on large synthetic detector frames. In the experimental demonstrations, the complete diffraction signal was caught partially in multiple detector frames. Hence, in order to use the proposed software pipeline[2] the complete diffraction signal needs to be merged into a common detector frame, to form a *compound image* of the detected diffraction signal.

The discussion about the compound image formation procedures will be presented with a through analysis in Chapter 6. Therefore, in this section, we will focus on the outline of the experimental data analysis procedure for HR-3DXRD technique.

Following the data analysis pipeline presented in Section 4.1, the experimental data analysis procedure can be outlined as the following:

- **Pre-processing**: The experimentally acquired diffraction images should be pre-processed for background and dark-field subtraction. Then, optionally, intensities of the background corrected images should be normalized with respect to the synchrotron current.
- **Compound image formation**: Datasets acquired with the multi-panel acquisition strategy should be merged into the pseudo-large detector frame, called the compound image. Depending on the choice of the compound image formation route, the observed diffraction spots should be harvested either before or after the compound image production (see Chapter 6). Also, the global parameters of the experimental setup should be determined, with respect to the chosen compound image formation route.

[2] In the rest of the text, software pipeline shall refer to its harvested analysis side.

- **Indexing**: The observed diffraction peaks should be converted to normalized scattering vector form (c.f. Equation (2.6)). Then, the calculated normalized scattering vectors should be subjected to indexing for determination of the grains in the analyzed gauge volume, following the descriptions given in Section 4.1.3.
- **Fitting and refinement**: The indexed grains should be subjected to a refinement stage. The initial refinement of the indexed grains can be done with the methodology given in Section 4.1.4. Such refinement approach would increase the statistical confidence of the indexed grains, as well as providing refined results for their orientation and CoM position.
  The refinement stage can be further extended to perform a multi-parameter refinement with the complete set of harvested diffraction peaks, experimental global parameters, indexed and refined grains. Such procedure can be exemplified with the minimization of the FitAllB software [2, 57]. Such type of multi-parameter refinement procedures enable derivation of the elastic strain matrices for the indexed grains.
- **Volume determination**: If the expected number of grains are identified in the previous indexing and refinement stages, the volume of the refined grains can be calculated with the explained procedure in Section 4.1.5.
- **Tessellation**:If the expected number of grains are identified in the previous indexing and refinement stages, the indexed grains can be subjected to tessellation procedure for $3D$ visualization of analyzed the gauge volume. The tessellation procedure could be conducted with respect to Section 4.1.6.

5.4 Strain determination

The explained approaches are proposed to be the experimental variant for the pre-processing step of the analysis pipeline. This procedure produces the three inputs for the following indexing and refinement stages: the list of diffraction spots in the pseudo-large detector frame, the list of normalized scattering vector calculated from thereof and global parameters of both individual panels and their combination. These inputs can be fed to indexing and refining schemes (given in sections 4.1.3 and 4.1.4) for determining the orientation, CoM positions and volumes of the subgrains.

In classical FF-3DXRD analysis, the determination of strain tensors of the found grains requires an extra refinement stage following the described indexing and refinement stages. In this further refinement, the strain tensors, determined orientation, CoM positions and volume of all grains are refined (in other words ”re-indexed”) together by minimising the global error of the entire grain ensemble. Oddershede and co-workers have implemented such refinement in *FitAllB* software of the FABLE package and presented its application in [57] and [2]. To illustrate, in the former example, FitAllB was also demonstrated for refinement of simultaneously collected NF and FF-3DXRD data with two detectors at different $\boldsymbol{L}$. Here, the global parameters of each detector were refined in tandem for minimizing the determined grain properties.

In Sections 2.1 and 3.1, we state that a subgrains lying in a deformed microstructure is a near-perfect crystals. We have further stated that individual subgrains have a homogeneous constant strain due low dislocation concentration in their matrix [14, 17]. For reasons of simplicity, such homogeneous strain was assumed to be zero in the presented simulation work. Hence, the proposed analysis pipeline performs refinement only for increasing the accuracy of the determined orientation and CoM position and disregards the possible strain contribution. From HR-3DXRD’s perspective, *FitAllB*-type refinement procedures could have a possible application for serving as an advanced refinement tool over

the adopted *makemap.py* procedure (see Section 4.1.4). The multi-detector minimization scheme of FitAllB can potentially be exploited for HR-3DXRD, by letting FitAllB to optimize the global parameters of all panels simultaneously for all identified grains [140]. Such calculations are expected to be computationally expensive due to increased complexity with respect to number of detector positions. Aforementioned above, the detector's motion in the $y_L - z_L$ plane is expected to have minute effect on $\boldsymbol{L}$ and detector tilts. Thus, application of tight boundary conditions for optimizing these global parameters would expected to remedy the computational expense. During the writing of the text, the multi-panel implementation of FitAllB software is still under development. The resulting software is planned to become a part of the analysis pipeline, according to Section 5.3.

5.5 Experimental challenges

Over five beamtimes carried out on different grain mapping beamlines, the demonstration experiments have provided useful insights about the proposed *high resolution* concept for 3DXRD. In this section, we will discuss the challenges faced in the experimental equipment and data collection.

In Chapter 3, we state that HR-3DXRD experiment adopts the classical 3DXRD setup, with the addition of the detector movements in the surface defined by y_L and z_L axes. From an experimentalist's point of view, one would expect from series of scans with the movement of a high resolution detector to suffer from stability issues. This was in fact the case in all of the experiments. Our experience have shown that such positional instabilities are generally induced due to the lack of a thermal equilibrium inside the experimental hutch. Such a case was observed in APS 1-ID-E experiment, in which the thermal equilibrium of the experimental hutch was tracked via in-hutch thermometers. In this experiment, we had measured that the temperature profile inside the hutch alters by approximately $5\,$K, with respect to its equilibrated state, whenever an experimenter enters the hutch. This may lead to a low frequency oscillation of the high resolution detector mount, therefore, leading to inaccuracies in determining the positions of the observed diffraction spots.

In the explained beamtimes, we have observed that the thermal stability of the hutch can be improved by mere avoidance of the unnecessary entry to the hutch. If entry is unavoidable (e.g. due to change of samples, etc.), we suggest that such entry should be done by the least amount of experimenters within a short time window. Moreover, our experience have shown that the modern grain-mapping beamline hutches require $\approx 0.5 - 1\,$h to reach the thermal stability. We suggest that this dead-time can be leveraged for the alignment procedures of the beamline optics. Additionally, such dead-time could be utilized for collection of datasets that are less prone to thermal stability, such as FF-3DXRD or classical tomography experiments.

Experimentation-wise, HR-3DXRD follows a similar sample alignment procedure to classical NF or FF-3DXRD techniques. Similar to any diffraction experiment, we should point that placing the sample (or a ROI of the sample) in the CoR of the goniometer is of crucial importance. Secondly, determination of the precession for the sample rotation stage may enable an extra set of corrections for the determined ω positions of the observed diffraction spots.

One of the main challenges of HR-3DXRD experimentation is the efficiency of the high resolution detector. Considering the fact that subgrain boundaries are less defined at low deformation levels, the complete mapping of the deformed microstructure requires observation of the weak diffraction spots emanated from sub-μm sized subgrains. Our analysis have shown that detectors of high efficiency enable better collection of these

weak spots, therefore, offering high resolution 3D maps with high completeness.

We should note three major points about the high resolution imaging detectors:

- In Chapter 3, we mention that the effective pixel size of a $2D$ detector could be adjusted by changing the optical objective of its visible microscopy setup. We should note that such an adjustment requires the focusing of the mounted visible light optical objective of detector's microscopy attachment. We suggest such focusing scans are not to be done through the diffraction spots, but it should be done with an object with sharp features. The shape of the diffraction spots from the deformed microstructures may not provide enough sharpness required for the objective focusing, thus, it should be avoided.
- The change of the optical objective may require an adjustment on the thickness of the utilized scintillator screen. We should note that in order to depress the instrumental effect on the diffraction spots, one needs to use an adequately thin scintillator crystal. However, it is known that the efficiency of X-rays to visible light conversion increases with increasing scintillator thickness. Therefore, the thickness (and if available, chemistry) of the scintillator screen should be optimized for the highest attainable intensity on the detector without compromising the sharpness of the diffraction spots.
- The microscopy setup of $2D$ detectors pose a distortion of the detected image, due to imperfections of the optical objective. It is known that such distortion gets pronounced on the edges of the detector frame. As HR-3DXRD observes its signal from the whole active area of the $2D$ detector, the distortion correction of the diffraction images is one of the most crucial step for attaining a good accuracy and precision in the produced 3D volumetric maps.

Lastly, we would like to digest our experience with HR-3DXRD proof-of-concept experiments for describing an *ideal HR-3DXRD experiment*:

- The optical alignment of the grain-mapping instrument should be done for optimizing the highest attainable high incident X-ray flux. The incident X-ray beam should be monochromatized with a low bandwidth. The monochromatic beam should be collimated with multiple condenser units for attaining a high X-ray flux, with a uniform and defined shape.
- The sample should be placed on the CoR of an ordinary rotation stage (or preferably a four-circle goniometer). The precession of the rotation stage must be determined and should be corrected on the observed diffraction spots.
- The sample-to-detector distance, $\boldsymbol{L}$, and the number of HR-3DXRD panels should be optimized with respect to the number of diffraction rings desired on the detector frame and the detector's pixel size.
- An ideal experiment shall be done with a high resolution detector with $\approx 0.5 - 1.5\,\mu$m effective pixel size with high efficiency. In the detector's configuration, the magnification of the objective lens and the scintillator thickness should be optimized for the highest achievable intensity and least amount of blurring on the spot shapes. The distortion profile of the detector configuration should be experimentally determined.
- The experimental hutch where the ideal experiment held should further have adequate climate control. The thermal equilibrium of the experimental hutch should be kept closed at all times.

6 Detector Calibration of Compound Diffraction Images

Section 3.1 has introduced two experimental acquisition strategies for the realization of the HR-3DXRD technique under laboratory conditions. As illustrated previously in Figure 3.3, the proposed strategies utilize a high resolution imaging detector with adequately small effective pixel sizes in two different configurations. The first strategy assumes the use of a single detector with a large innate FoV ($\gg 10,000$ pixel $\times\, 10,000$ pixel). Similar to classical near and far-field 3DXRD experimentation, such a configuration will enable capturing the desired diffraction signal in single image frames. At the time of writing this text, the single frame strategy is experimentally not possible due to commercial unavailability of high resolution large FoV imaging detector. As presented in Section 3.1, the usage of a large FoV detector strategy in this thesis is solely limited to numerical simulation studies.

The second strategy, depicted in Figure 3.3(b), aims to capture the desired diffraction signal in multiple acquisitions around the azimuthal direction with a regular FoV high resolution imaging detector ($\approx 2,400$ pixel x $2,400$ pixel). For simplicity, we shall recall this strategy as *multi-panel acquisition strategy for HR-3DXRD*. This strategy aims to observe the complete diffraction signal through registering and/or calibrating the individual partial diffraction images. The calibrated partial diffraction images are then combined on a single detector frame. Throughout the text, we will call this composite large diffraction image frame *the compound image*. Note that once compound images have been created the data analysis chain for the two strategies are identical, and can be performed according to the description given in Section 5.3.

In the large FoV detector approach, the calibration of the diffraction images would follow the well-established diffraction detector calibration routines of powder diffraction and 3DXRD. The detector calibration procedure would provide the global parameters of the experimental setup. Calibration tools for such analysis are readily available as standalone software, e.g. pyFAI [31], or within 3DXRD software suites, e.g. FABLE/ImageD11 [111], HEXRD [30].

The multi-panel acquisition strategy requires the absolute position and tilt of the detector for each panel to be known with sub-pixel precision for accurately producing the compound image. This calibration is not trivial. The main problem is that each individual panel does not contain sufficient information for an independent calibration. The η range covered by a single panel is too small for the fit of the global parameters to converge with good statistics.

In general, the calibration of a multi-detector diffraction setup is a well-known problem. A recent example can be seen in novel photon counting active pixel detectors, in which diffraction signal is captured on multiple active chips. In such a setup, the diffraction signal is detected simultaneously on the chip assembly. Then, the composite diffraction image is obtained by calibrating the global parameters of individual chips in tandem. At times, the multi-panel strategy is also being performed for the classical FF-3DXRD studies. Several beamline around the world (e.g. 1-ID-E of APS, P21.2 of Petra III) use multiple so-called *far-field* detectors for extending the FoV, and therefore the *Q-range* of their experimental setup. For both examples, the calibration of the multi-panel diffraction setup is done via

high quality diffraction images of a calibrant material (e.g. polycrystalline LaB_6, single crystal Si, polycrystalline Si, etc.) with adequate S/N.

In this work, we have seen that the established multi-panel diffraction setup calibration strategies are not suitable for the posed calibration problem of HR-3DXRD. For the examples given above, the mentioned detectors possess very high quantum efficiencies. Therefore, the calibration images of adequately high S/N can be easily produced from aforementioned calibrant materials in sub-second exposure times. Conversely for the HR-3DXRD setting, we were not able to produce diffraction images of different calibrant materials in numerous beamlines of different light sources (Section 5.2). In our experimental trials, the diffraction signal of the calibrant material were observed to have impractically low S/N. Over an experimentally suitable exposure time, the observed signals were found to smeared out over a large number of pixels in both radial and azimuthal directions. This behavior can be attributed to the following reasons:

1. The high resolution imaging detectors have inherently low quantum efficiency at mid-to-high X-ray energies.
2. The microstructure of the calibrant materials is not suitable for the HR-3DXRD setting.

The low quantum efficiency of the high resolution imaging detectors require long exposure times for attaining diffraction signal of adequate S/N on the detector. In our experimental attempts, we have experienced that such detectors may require $\approx 40 - 60$ seconds exposures for obtaining a good quality diffraction signal from the calibrant material. Furthermore, we had experienced that some high resolution imaging detectors may even limit their exposure to $\approx 1 - 2$ seconds, hindering collection of any usable signal. In both cases, we were unable to produce calibration images with sharp diffraction features and good S/N.

The microstructure of the calibrant materials can be regarded as the material limitation of the posed calibration problem. In general, the powder diffraction studies utilize well annealed pure materials for calibration purposes. The microstructure materials are usually composed of

- Single crystals with no discernible structural features, or
- Polycrystals of micro-to-nanometer sized grains or powders, ensuring a random orientation distribution.

In the single crystal case, the diffraction signal comprises only a very few diffraction spots in each panel (if any), insufficient for the relevant multi-dimensional fits. The polycrystalline case produces multiple powder lines that are continuous along the azimuthal direction. However, due to the aforementioned low efficiency characteristic of the high resolution imaging detectors, the diffraction signal was observed to be smeared out in both radial and azimuthal directions with impractically low S/N.

The aim of this chapter is to present and discuss different methods of producing the compound image and its calibration to serve as an input for a HR-3DXRD collected with multi-acquisition strategy. Thus, we should note that the methods presented in this chapter are not specific to HR-3DXRD experimentation, but rather applicable to any diffraction experiment having similar experimental configuration; multi-acquisition, detector motion, regions of overlap, S/N issues etc.

Since we were unable to collect any usable calibration data in our multiple experimental

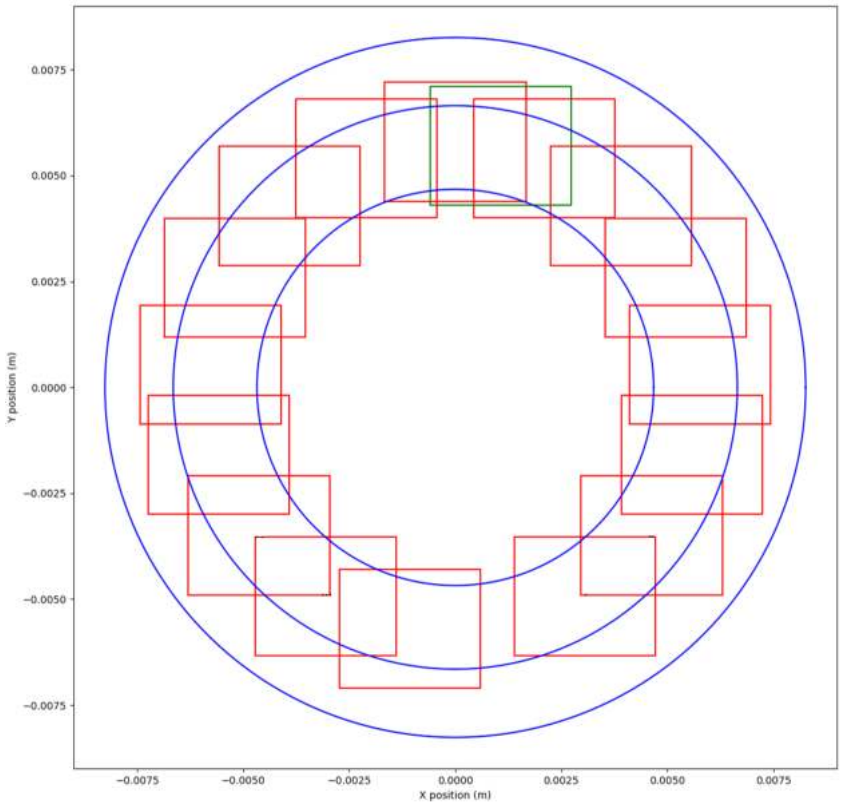

Figure 6.1: Schematic representation of the HR-3DXRD acquisition in DESY Petra III P21.2 beamline. Owing to an experimental error, the panel indicated in green was collected at $\eta \approx \pi/10$, instead of $\eta \approx \pi$.

demonstration beamtimes, the efforts in this chapter will utilize the experimental diffraction images and their derivatives as an input dataset. The analyses presented in this chapter will utilize a data set of the ARB processed IF steel sample annealed at $620\,^{\circ}$C from the Petra III P21.2 experiment. The scan utilized 17 detector positions around the azimuthal direction with mean overlap of $\approx 20\%$. The multi-panel acquisition HR-3DXRD geometry enabled observation of the full-azimuthal coverage of the first two Debye-Scherrer rings of $\alpha-$Fe phase. The angular coverage of the complete set of 17 detector positions at the employed sample-to-detector distance, $\boldsymbol{L}$, is previously illustrated in Figure 5.13(b). Further details of the specimen microstructure and the experimental configuration of the acquisition can be found in Sections 5.1.4 and 5.2.4, respectively.

We should note that the scans acquired in this beamtime had a misplaced detector position as shown in Figure 6.1. Due to a typing error in the experiment's acquisition scheme, the detector position indicated as green in Figure 6.1 was mistakenly collected at $\eta \approx \pi/10$, instead of $\eta \approx \pi$. Furthermore, a visual inspection of all data sets collected in the same beamtime had revealed that the $\eta = \pi$ part of the diffraction signal from the first Debye-Scherrer ring (i.e. 110 for $\alpha-$Fe) was physically obstructed and it was not observed in the FoV of the compound image. Such mistakes could be deemed as detrimental for the accuracy of the experiment. Yet, we argue that the extent of accuracy loss may not be on the expected level. In the mentioned experiment, the tomographic rotation axis was aligned parallel to the height axis of the sample. This suggests that the subgrains with orientations aligned on the proximity of the tomographic axis would satisfy the diffraction condition throughout the tomographic rotation scan. Therefore, the diffraction spots emanated from these subgrains would be located at the north and south poles of the observed diffraction signal and they should visible at each rotation step.

The chapter will introduce two routes for calibration, with increased complexity. Firstly, the use of classical image registration and stitching to generate the compound image will be presented. Secondly, a multi-panel calibration procedure with a custom script, build on the dedicated powder diffraction calibration pyFAI software [31] will be presented. The quality and performance of compound image production via different methods will be compared and discussed through a common set of quality parameters.

6.1 Image Registration and Stitching

The image registration route offers a fast and easy solution for producing the compound image out of partial detector images, provided that each partial contains a certain amount of overlap with its immediate neighbors. The algorithm calculates the spatial correlation of an image pair by choosing one as the reference image, then registering the other image through aligning the common intensity features present in both images. Therefore, the image registration approach assumes that *the associated tilts at each detector position are constant and also they are independent of the experimental motor positions*. Hence, the spatial correlation between the images acquired at different detector positions are determined *solely* by varying the spatial position of the images with respect to each other. The resulting spatial correlation can be used for stitching the registered image pair.

Considering HR-3DXRD experimentation, image registration can be applied for all possible detector position pairs of the acquisition. Such registration can be set as the default alignment of the experimental detector pairs. Then, these settings can be used for driving a stitching process for producing the compound image.

This section will present the procedure, implementation and quality assessment of image registration and stitching for production and calibration of the compound image. The

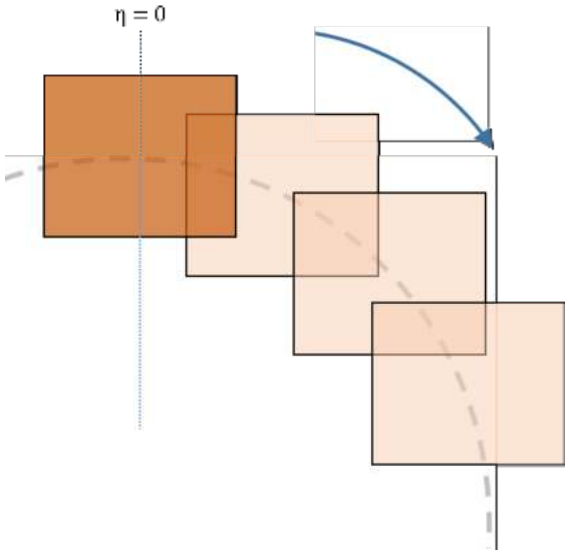

Figure 6.2: Schematic representation of the image registration process. An arbitrary detector position (dark orange) is selected as the reference image. Then, the neighboring detector positions are registered successively on the clockwise direction of the azimuth. The process is terminated when all detector positions are registered, i.e. by reaching the starting reference position.

presented image registration and stitching process were performed with the built-in 2D pair-wise image stitching plug-in of ImageJ [141].

6.1.1 Procedure

The adopted image registration procedure can be explained as follows:

- The procedure commences with pre-processing of the experimental data for preparation of the input files. Firstly, for each detector position, the acquired experimental images (in HR-3DXRD case, the set of images represent a tomographic rotation scan, i.e. ω-scan) are summed into a single image frame with an appropriate choice of image filter (e.g. maximum intensity, median, etc.). This through-stack summation is done for increasing the density of intensity features for the image registration process to benefit. The same procedure should be repeated for the set of experimentally acquired dark detector images. The input images are produced by subtracting the dark images from the experimental images. (If available, distortion correction must be employed after background subtraction.)
- The pre-processed input files are fed to the image registration algorithm. For each image pair, the overlapping regions should be manually selected. The registration process takes one image as the reference starting position, then, its azimuthal neighbor is registered to the reference image by varying the spatial position of the image to be registered. This process should be repeated successively for all detector positions around the azimuth (Figure 6.2). The resulting alignment is used for stitching the registered input images, thus producing the compound image.
- The quality assessment of the registration process can be done by employing a detector calibration routine on the compound image. After calibration and refinement steps, the resulting global parameters can be used converting the observed diffraction signal from the detector coordinate system to $2\theta - \eta$ plots. Further, azimuthal integration of the compound image can be utilized for tracking the mean 2θ position

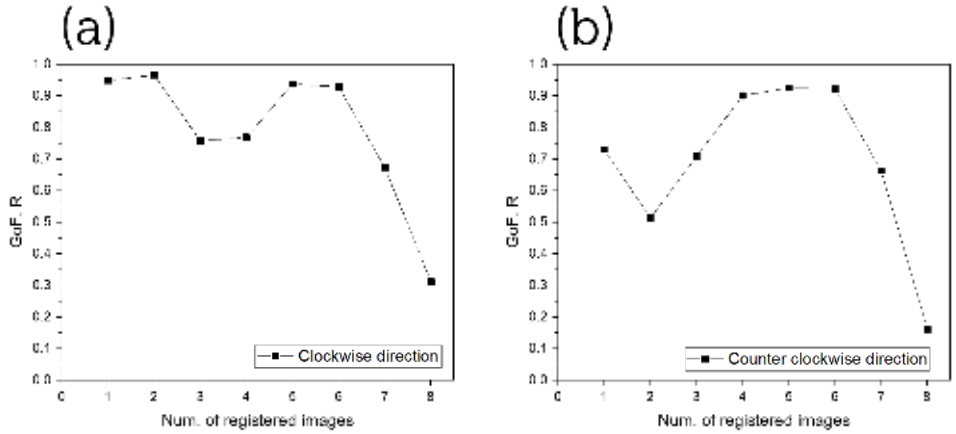

Figure 6.3: The evolution of calculated statistical correlation of the image registration process for (a) clockwise and (b) counter clockwise directions.

of the diffraction signal.

In regard to HR-3DXRD methodology, we should emphasize that the acquired partial diffraction images collected along the ω-scan at each detector position had observed a spotty pattern on both 2θ and η directions. In the pre-processing stage of the given procedure, we explain the through-stack summation of these partial diffraction images at each detector position for increasing the number density of intensity features. We should further emphasize that such through-stack summation of the partial diffraction images did not produce thin and sharp powder lines. Rather, the obtained signal on the summed images had retained their spotty nature. Therefore, these through summed images should intrinsically contain more information than a classical powder diffraction pattern.

If the quality assessment of the given procedure provides satisfactory results, then, the image stitching procedure is repeated for the individual diffraction images with the obtained parameters. This would provide a full data set of compound images to serve as an input for the Mode II HR-3DXRD analysis. Moreover, the global parameters derived from detector calibration can be employed for calculating the scattering vectors from the compound images data set.

6.1.2 Implementation

The pre-processing step was carried out with the image averaging/summation tool of the pyFAI software suit [31]. Firstly, the dark detector images (collected at each particular detector position) were summed with a maximum intensity filter[1]. Then, for each detector position, all acquired images were subjected to background removal with their respective dark images, and then summed with a maximum intensity filter.

The resulting summed images were then subjected to image registration following the procedure presented in Section 6.1.1. The reference position was chosen as the detector position at $\eta = 0$ and the neighboring detector positions were successively registered in the clockwise direction (CW) up to $\eta = \pi$. As pointed out in the introduction section of this chapter, the data set had a misplaced panel that produced a missing detector position

[1]When two images are averaged and/or summed through the *maximum intensity filter*, if a pixel has an intensity feature that is brighter than its counterpart in the other image, the pixel with the higher intensity is selected for the resulting image.

around $\eta = \pi$. The visual inspection of the intermediate compound image have revealed this missing position around $\eta = \pi$, therefore limiting the registration of the next panel.

Owing to the presence of a missing detector position in the data set, the proposed registration procedure was modified such that, the procedure starts and follows the original process up to $\eta = \pi$. Then, the resulting intermediate image is taken as the reference image for the second half of the registration step. The detector position at $\eta = 0$ is again chosen as the reference and the registration procedure is repeated in the counter-clockwise (CCW) direction up to $\eta = -\pi$.

For each registration step, the employed ImageJ plug-in outputs the the spatial correlation of the panel pair, along with its statistical correlation. The evolution of this goodness-of-fit parameter is given in Figure 6.3, for both CW and CCW directions. The figure shows that the upper half of the image ensemble had registered with appreciable statistics. However, as the azimuthal angle reaches towards the $\eta = \pi$, the statistical correlation of the registration falls gradually. Considering the missing diffraction signal -and hence, the depressed density of signal- around this region, such behavior is highly expected.

Albeit the missing signal, we should further note the variation of goodness-of-fit parameter of the registration process. This variation could can be explained by the adopted experimental procedure for the DESY Petra P21.2 beamtime (c.f. Section 5.2.4). In this experiment, firstly, the set of detector positions were calculated. Then, rather than following a circular path around the azimuth, acquisitions at each detector position were done in a random fashion. Through this strategy, we had aimed to suppress the systematic positional errors, as well as the monotonic S/N depression in consecutive acquisitions. Therefore, we can say that the intensity variation between detector positions has no systematic, but rather it is deliberately scattered around the azimuthal direction. Considering the fact that image registration is strongly affected by the S/N and number density of intensity features, the described acquisition strategy may had caused the observed variation in the calculated goodness-of-fit parameter of the image registration.

The obtained registrations results were employed with the stitching option of the mentioned ImageJ plug-in. During the process, intermediate stitching products were also saved for analysis purposes. The resulting compound image is shown in Figure 6.4. The field of view of the resulting compound image is $11,239$ pixels in horizontal and $10,803$ pixels in vertical direction. It can be seen from the figure that the compound image reveals the high resolution image of the complete azimuthal spread of observed diffraction peaks over the observable 2θ range. The initial quality assessment of the compound image was done by inspecting the overlap regions around the azimuthal direction. Close inspection of these regions have shown no discernible intensity defects. This observation was applicable to all overlap regions, both for image pairs of good statistical correlation, but also for pairs of bad correlation, as well. Figure 6.4(b) shows an example close-up look of the overlap region located at $\eta = \approx \pi 3$. It can be seen that the registered image pair was fused with well, with no observable defects.

In terms of HR-3DXRD analysis, the compound image shown in Figure 6.4 should be seen as the last intermediate product of the procedure. Following along the registration pipeline, we should remind that the compound image presented in the figure is produced from through-stack sum images at each detector position. The individual diffraction spots from the complete ω angles were deliberately posed on top of each other for increasing the density of intensity features. Therefore, the close-up image shown in Figure 6.4 should not mislead the reader about any spot overlap issue in the acquired diffraction frames. Rather, the compound image in Figure 6.4(a) was built off of images representing the cumulative

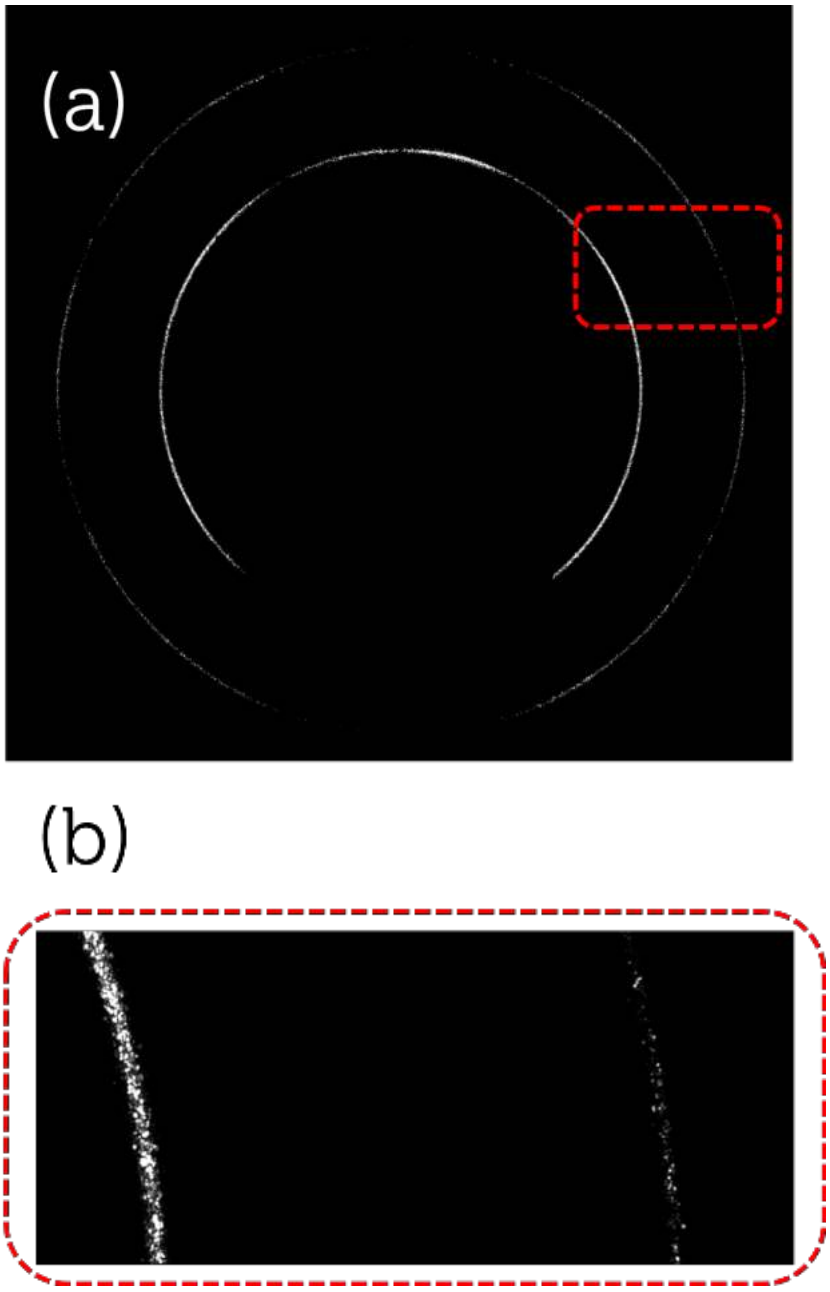

Figure 6.4: (a) The compound image produced with image registration approach. The presented compound image was produced out of through stack sum images at each detector position. The resulting FoV is $11,239$ pixels in horizontal and $10,803$ pixels in vertical direction. In the experimental setup, the radial portion around $\eta = \pi$ had erroneously obstructed the diffraction signal, causing a loss of diffraction signal. (b) A zoom-in look on the compound image of the region is indicated with red markers in (a).

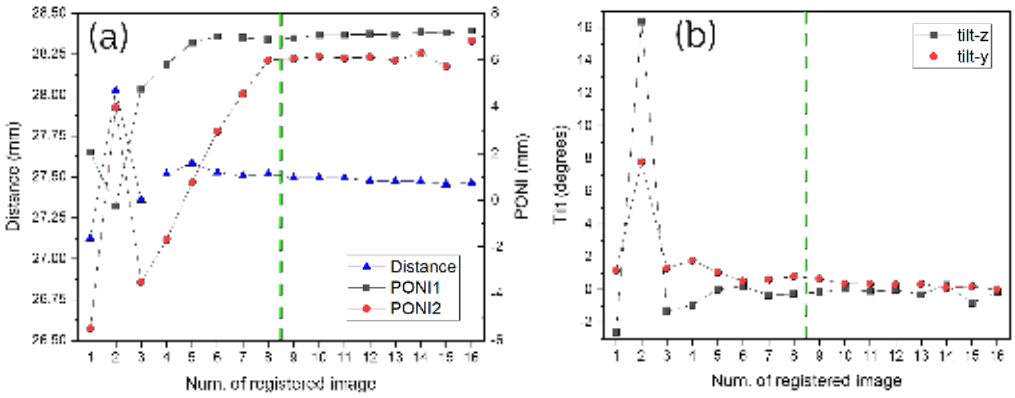

Figure 6.5: The evolution of global parameters during the image registration/stitching process. The parameters were obtained by subjecting the intermediate stitched images to detector calibration. The green dashed lines indicate the point of direction change, from CW to CCW. In figure (a), PONI1 and PONI2 indicates the respective z and y distances between the center-of-rotation of the HR-3DXRD detector motion and the origin of the image frame. For further details, please consult the text.

diffraction signal at each detector position. In order to produce the HR-3DXRD data set, the obtained registration results should be employed to individual diffraction images at each ω angle for building the compound image data set .

6.1.3 Quality Assessment

In this section,the quality assessment of the image registration procedure is presented. First, detector calibration of the stitching processes will be presented. The evolution of the global parameters will be presented via detector calibration of the stitched intermediate images. This part will end by presenting the detector calibration of the stitched compound image. The section will continue with analysis of the visual overlay of a chosen stitched image pair. The analysis will focus on the registration behavior of the diffraction peaks lying in the overlap region. Then, the overlap analysis will be repeated on the harvested diffraction peaks of the mentioned image pair. The registration performance will be statistically analyzed with calculated mismatches of CoM positions on detector frame, scattering angles 2θ and η and scattering vectors (in reciprocal space, Å^{-1}).

6.1.3.1 Calibration of the compound image

The produced intermediate images and the compound image, shown in Figure 6.4, were subjected to detector calibration, for derivation of their global parameters. The detector calibration routines were performed with the calibration module of pyFAI software [31]. The required inputs for the calibration were wavelength, polarization, effective pixel size, a calibration file indicating the *d-spacings* of the sample and a set of manually chosen *control points* defining regions with discernible intensity around Debye-Scherrer rings. Then, the global parameters of the image of concern was calculated through initial calibration and refinement stages. The resulting parameters were regarded as to be fully refined when the obtained global parameters do not refine with further refinement steps. The obtained refined global parameters were employed on the images for $1D$ and/or $2D$ azimuthal integration with the mentioned software.

In order to observe the performance of individual steps throughout the image registration process, the intermediate stitched images were subjected to detector calibration. The evolution of calibrated global parameters are given in Figure 6.5. The figure shows the evolution of the entire stitching process. The half-way point of the procedure, i.e. the point

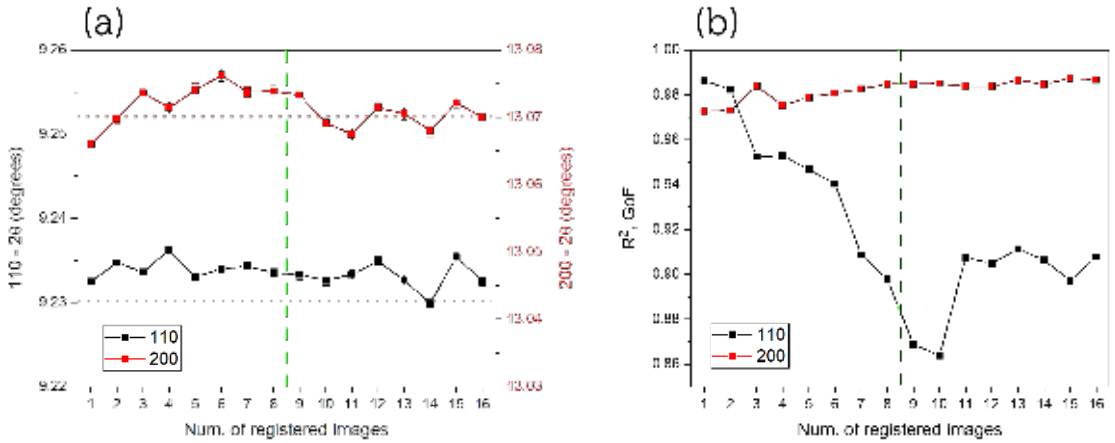

Figure 6.6: (a) Evolution of peak positions of 110 and 200 diffraction rings in image registration/stitching process. Peak positions are calculated by fitting a Lorentzian function to the corresponding diffraction peaks in azimuthally integrated $1-D$ patterns. Theoretical peak positions are indicated with black and red dotted lines, respectively. The green dashed lines indicate the point of direction change, from CW to CCW. (b) Corresponding evolution of goodness of fit, R^2, parameter for the fitted Lorentzian functions in (a).

where the stitching direction changes from clockwise (CW) to counter-clockwise direction (CCW), is indicated with green lines.

Figure 6.5(a) shows the evolution of calibrated sample-to-detector distance and the so-called *PONI* parameters. In pyFAI environment, PONI parameter is defined as the point of normal incidence of the direct beam with respect to the origin of the detector frame [31]. In HR-3DXRD context, the definition of PONI parameter narrows down to a more specific manner. Owing to its novel detector motion scheme of moving the detector on $y-z$ plane around the optical axis, PONI parameter indicates the distance between the the center-of-rotation of the HR-3DXRD detector motion (i.e. the intercept of the optical axis on the extended detector plane) and the origin of the image frame of concern.

In the first stage of image registration, the calibrated global parameters show large deviations from the experimentally measured values. Around the half-way point of the process, it can be seen that the calibrated parameters reach a steady value. Figure 6.5 shows that the reached values stay approximately constant for the rest of the registration process.

The bad calibration performance of the intermediate images composed of four images or less can be explained by the limited azimuthal range of the observed signal. It is known that pyFAI software is optimized for calibration of powder diffraction datasets, in which the sharp Debye-Scherrer rings are observed in a continuous manner around the azimuthal direction. Therefore, regardless of the statistics of the registration, the calibration of the intermediate images from the initial steps would provide lesser accuracy with respect to its compound image counterpart.

The explained evolution behavior can be also observed in the calibrated tilt angles, as well. In Figure 6.5, it can be seen the calibrated tilt angles refines from questionable values, from tens of degrees, to $\approx 0.5\,^{\circ}$. Similar to spatial parameters, the refinement reaches a steady state around the half-way point of the process. Therefore, upon these observations, we can make the following deductions:

- In order to derive good global parameters, the compound image should cover an azimuthal range, $\eta_{range} \geq \pi$,
- Extending the azimuthal range further provides a refinement of the found global parameters,
- Calibration of datasets with limited azimuthal coverage ($\eta_{range} \leq \pi/2$) is not trivial. Any derived global parameters should be checked carefully, with special emphasis on detector tilt-y and tilt-z.

The performance of the stitching process can be further assessed by calculating $1-$ and $2-$dimensional azimuthal integration of the intermediate and stitched compound images. In case of $1-D$ integration analysis, the peak positions of the two available diffraction peaks were obtained by fitting a Lorentzian function. Figure 6.6(a) shows the evolution of the fitted peak positions of 110 and 200 diffraction rings with respect to number of registered images. It can be seen that for both diffraction rings, the peak positions were found to be on the theoretical positions of pure $\alpha-$Fe. Contrary to observed behavior on global parameters, the fitted peak positions showed minute variation around the theoretical positions.

Figure 6.6(b) shows the goodness-of-fit, R^2, values obtained from the Lorentzian fitting analysis. It can be seen that the 200 diffraction ring showed a monotonic behavior around $R^2 \approx 0.985$ throughout the registration process. Whereas for 110 ring,the slope of calculated R^2 values changes from negative to positive, whilst registration direction changes from CW to CCW. This observation can be explained through the azimuthal coverage of the observed diffraction rings. Figure 6.4(a) shows the complete FoV of the stitched compound image. Here, it can be seen that the second/outer diffraction ring has a larger azimuthal coverage with respect to first/inner ring (c.f. the misplaced panel at $\eta = \pi$). Therefore, we can say that the second/outer diffraction ring has a higher weight in the calibration procedure, since it provides a better definition of the circular nature of the polycrystalline diffraction rings. Albeit having lesser azimuthal definition, the calibration algorithm uses the first/inner diffraction ring as its on-line reference for further refinement of global parameters.

Figure 6.7 shows the $1-$ and $2-dimensional$ azimuthal integration of the stitched compound image. The derived $1-D$ pattern in Figure 6.7(a) reveals that observed diffraction peaks showed no discernible shape irregularities. Figure 6.7(b) shows the polar decomposition representation of the calibrated stitched compound image, in terms of 2θ and η angles. In the figure, the straight diffraction rings implies that the derived global parameters are well refined. As such straight alignment of the diffraction rings is regarded to be crucial for any 3DXRD work, Figure 6.7(b) provides a positive assessment for the stitching procedure.

6.1.3.2 Analysis of overlapping regions

In order to visually analyze the performance of the result of the image registration procedure two detector position/image pairs were chosen (acquisition numbers 7&9 and 0&10[2]). Image pair 1 is arbitrarily chosen to reflect the general behavior, whereas image pair 2 presents a special case. This particular pair consists of the first detector position of the HR-3DXRD acquisition, positioned exactly at $\eta = 0$. The second image of the pair is the aforementioned *misplaced detector*, positioned at $\eta \approx \pi/10$ (see Figure 6.1). Owing to this misplacement, image pair 2 has the highest overlap area within the entire data set.

The input images of the analyses were prepared by stitching the first ten diffraction images

[2] In the following text, these pairs will be referred to as image pairs 1 and 2, respectively.

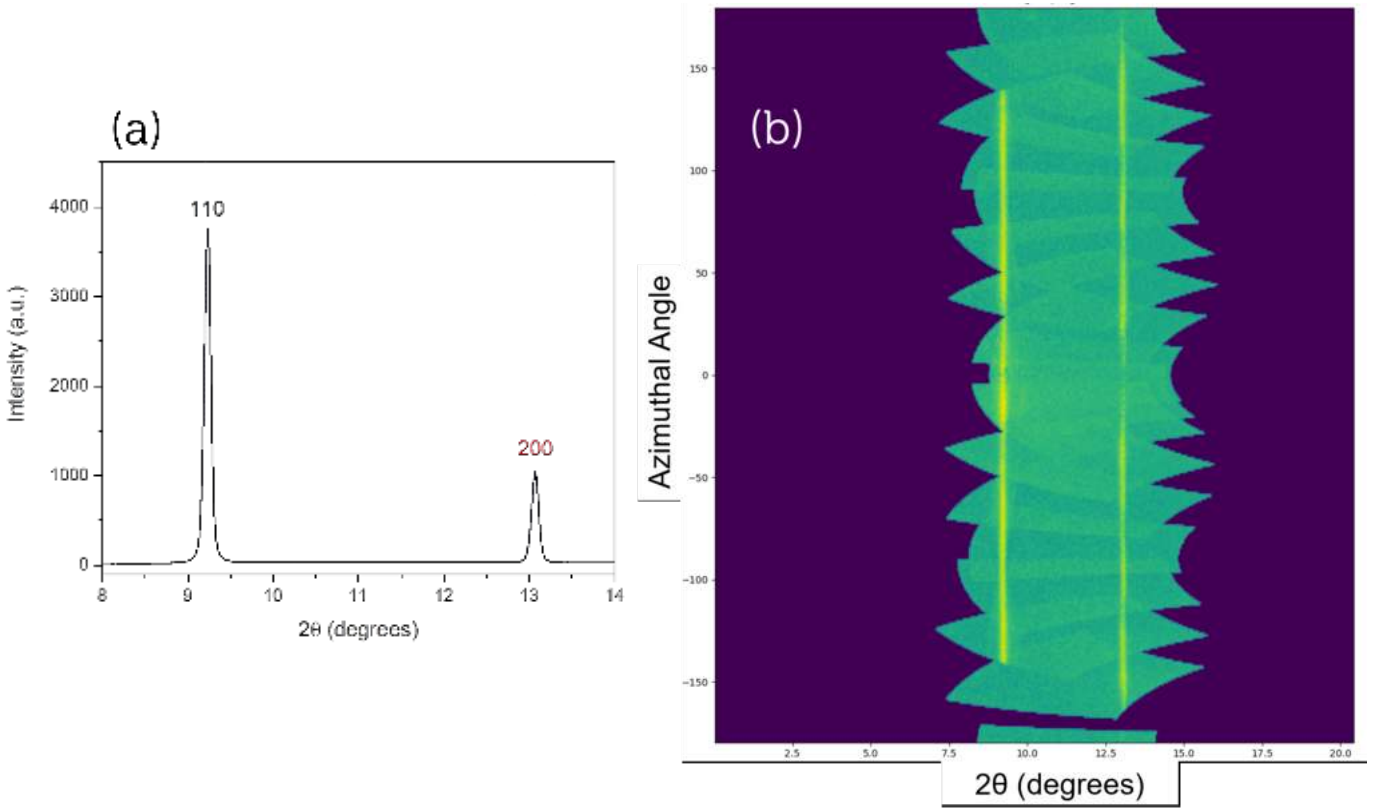

Figure 6.7: (a) 1D azimuthal integration and (b) 2D polar decomposition of the stitched compound image. In (a), theoretical scattering positions of $\alpha - Fe$ are indicated as dotted lines.

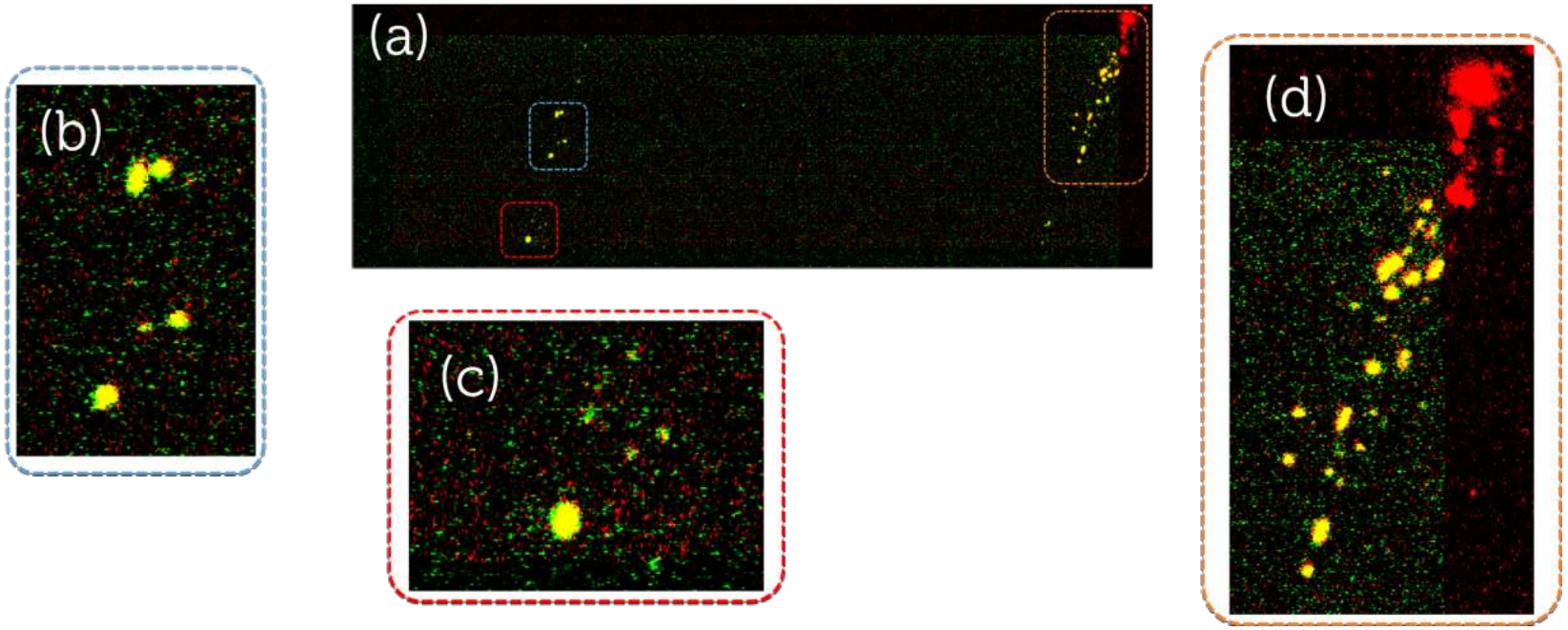

Figure 6.8: (a) An overlay of an image pair 1, showing the same ω slice from two neighboring detector positions, located at $\eta \approx 1.5\pi$. The images were converted from greyscale to red and green scales for left and right hand sides, respectively. Therefore, the overlapping diffraction signal is observed in yellow. (b-d) Zoom-in views of the respective boxes in (a).

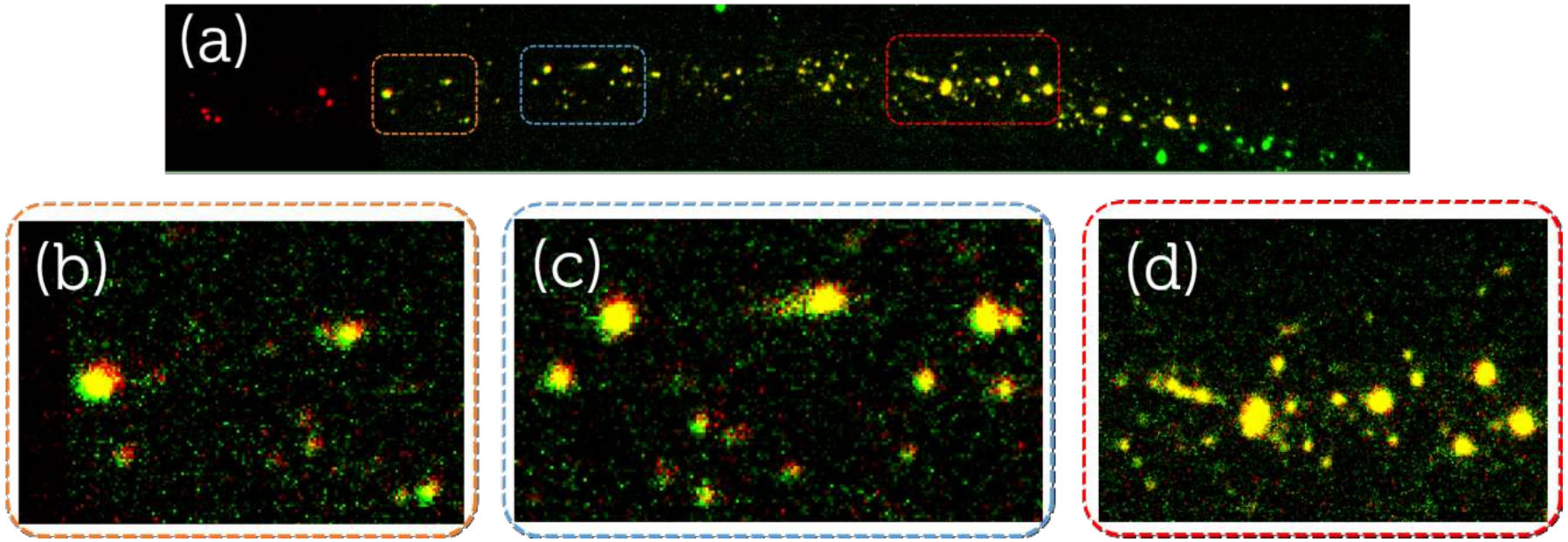

Figure 6.9: (a) An overlay of image pair 2, showing the same ω slice from two neighboring detector positions, located at $\eta \approx 0$. The images were converted from greyscale to red and green scales for left and right hand sides, respectively. Therefore, the overlapping diffraction signal is observed in yellow. (b-d) Zoom-in views of the respective boxes in (a).

from mentioned image pairs with the found registration parameters in Section 6.1.2. In order to ease the analysis, individual images of the pairs were assigned different colors with their respective greyscale intensities. The colors were changed to red for acquisition numbers 0 and 7, green for acquisition number 10 and 9. As a result of respective colors, a matching signal attains a yellow color in the overlap region of the stitched image.

Figures 6.8(a) and 6.9(a) shows a stitched image pair of an arbitrary ω-slice. Inspection of this example reveals three distinct behavior:

- Regions of good registration, e.g. Figure 6.9(d),
- Regions of acceptable registration, e.g. Figure 6.8(d) & Figure 6.9(c)
- Regions of bad registration, e.g. Figure 6.9(b).

Visual inspection of the regions with good registration reveals that observed diffraction signals from both detector positions have a large overlap on the compound image frame. Due to this overlap, we can estimate the error in detector CoM positions of diffraction peaks lying on the overlap region to be lower than effective pixel size. In regions with acceptable registration the diffraction peaks lying in the overlap region were observed to have a diagonal separation of ≈ 1 pixel. Thus, these region show slightly worse registration with respect to its better registered counterparts. Figures 6.8(d) and 6.9(c) reveals these diagonal misalignments, as well as the adequate overlap between two detector positions. Lastly, the diffraction peaks that lie specifically in the extremities of its FoV constitute the regions of bad registration. In these regions, the observed peaks have a distinct diagonal misalignment of $2 - 4$ pixels.

The observation of such behaviors in a single image registration step is rather unexpected. As explained in Section 6.1.1, the image registration process tries to find the possible shifts between two images in 2D by considering all available intensity features in the overlap region. Therefore, the resulting registration was expected to have a uniform positional error over the entire registered field of view. The cause of this discrepancy could be attributed to:

- The inadequate statistics of image registration,
- Combined effect of the spatial arrangement of the detectors and detector distortion.

As previously shown in Figure 6.3, the calculated statistical correlation of the image registration varies for different detector positions. We have attributed these variations to heterogeneous azimuthal spread of the diffracted intensity (see Section 6.1.2). Such errors could be avoided by increasing the number density of the intensity features by attaining a higher S/N in the captured experimental diffraction images.

The observed discrepancy can also be attributed to a combined effect of the spatial arrangement of the detector positions in HR-3DXRD and the associated optical distortion of the employed high resolution imaging detector. The effect will be illustrated through the given sketch of the image pairs in Figure 6.10. In the figure, red-framed images were used as references, then, the green-framed images were registered with the previously described procedure. In Section 6.1.1 we have explained that before the registration step, the overlap regions were selected manually as regions of interest (ROI) in both reference and registered image. We have discussed that these regions were used to calculate the spatial relation between a image pair. Hence, this explanation implies that image registration process is strongly affected by the consistency of intensity feature's position in both images.

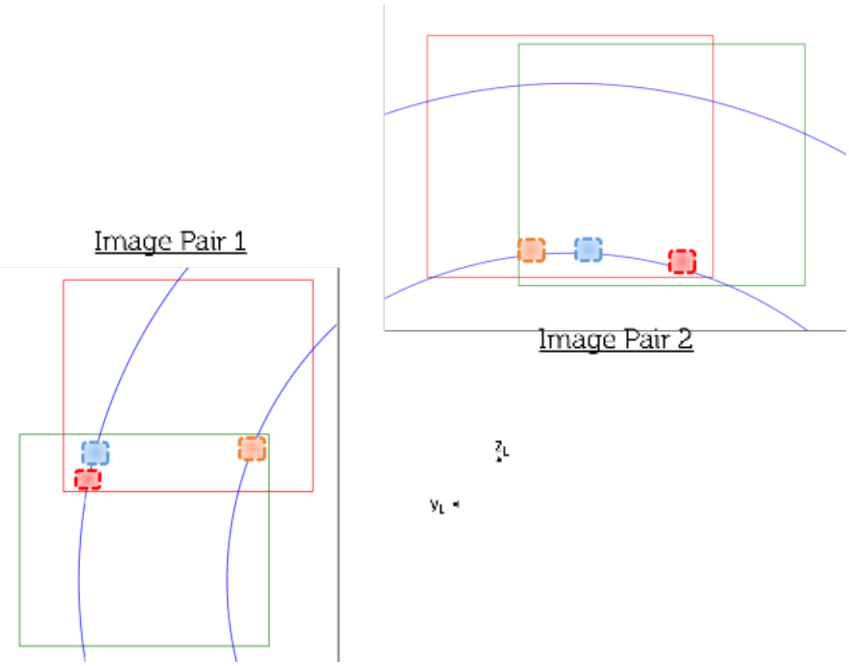

Figure 6.10: Schematic representation of image pair 1 and 2 in laboratory coordinates. Acquisition 7 & 0 are shown in red and 9 & 10 are shown in green. For both image pair, the analyzed regions of interest (ROI) in figures 6.8 and 6.9 are indicated with their respective colors.

Considering the CCD detectors used for diffraction studies, such inconsistencies could be arise on the observed diffraction signal via the so-called *detector distortion* effect. The detector distortion can be seen as the cumulative effect that accounts for all innate errors from the optical elements in the detector unit [1]. In practice, it is known that these distortion effects are a strong function of position on the detector frame. The distortion effect has little to no impact to the around the center of the FoV, but it can pose notable spatial distortions on the observed intensity if only it lies on the close proximity of the edges of the employed detector's FoV.

Figure 6.10 shows the schematic representation of the spatial arrangement of the analyzed image pairs. In the figure, the analyzed regions of interest in figures 6.8 and 6.9 were indicated with respect to their respective color coding. In order to observe the full extent of spatial distortion, we shall first focus on the relationship between image pair 2. Recall that this pair has the largest mutual overlap among the entire dataset. Therefore, we expect the distortion effects to be more pronounced with respect to image pair 1.

In the given schematics for image pair 2, we can see that selected ROIs lie on different parts of the detector's FoV. Firstly, we shall consider the red ROI in image pair 2. The red ROI lie on the lower right edge of the red frame. Whereas in the green frame, it is located in the mid-lower edge of the FoV. Considering the positional dependency of detector distortion, we can expect the signal observed in both images to suffer from distortion effects. But the affect in the red-frame is expected to be far more stronger with respect to the green-frame, due being on close proximity of the lower-right corner of the detector's FoV. Therefore, in the stitched image, we can formalize the overall effect as a convolution of mild distortion (from the red-frame) and a soft/negligible distortion (from the green-frame).

The analysis can be extended to the blue and orange ROIs of image pair 2, as well. In

Table 6.1: Results of the overlay study performed on peak lists from image pairs 1 & 2 for the image registration and stitching procedure.

	Image pair 1	Image pair 2
Number of harvested peaks	11,211/11,985	8,226/9,966
Number of matched peaks	2718	1556
Median mismatch in detector position (pixels)	0.87	0.64
Median mismatch in scattering vectors ($Å^{-1}$)	0.0008	0.0001

case of blue ROI, it can be said that it is located sufficiently far away from the edge of the FoV in both red and green-frames ($\approx\gg 50$ pixels from the edge). Thus, with the same formalization, we can say that the overall effect here can be seen as a convolution of soft/negligible and soft/negligible distortion. In case of the orange ROI, its location in the red-frame is quite similar to the blue ROI. Conversely for the green-frame, the orange ROI is located on the close proximity of the left-hand-side edge of the FoV. Therefore, the overall effect here can be seen as a convolution of soft/negligible and heavy distortion.

A similar analysis can be done for image pair 1. Here, the red and orange ROIs show a similar behavior to the red ROI of image pair 2. Therefore, these two cases can be assessed as a convolution of soft/negligible distortion and mild distortion. Similarly, the blue ROI has a direct positional correspondence to its image pair 1 counterpart, showing a convolution of soft/negligible and soft/negligible distortion.

The above analysis can be directly related to the observed co-habitation of the well registered, acceptable and badly registered regions, e.g. the bad registration in Figure 6.9d, or acceptable registrations in Figure 6.8c-d. In the presented study, no distortion correction was applied to the experimental images due to lack of such information for the used high resolution imaging detector. Therefore, in the registered and stitched images, we can say that the distortion field of detector frame is convoluted by itself in a shifted manner. We believe that this convoluted distortion field causes a spatial inconsistency for the diffraction peaks that are observed in both image pairs. As these particular diffraction peaks are used for calculating the shifts of image registration, we deduce that detector distortion has a crucial negative impact on the accuracy of the compound image formation.

Distortion correction is known to be a trivial pre-processing step. For most of the detectors used in diffraction studies, the distortion field information is measured and it is available in a cubic-spline function form. However, in our experimental trials with high resolution imaging detectors, such information was not available for any of the employed detector configurations. We think that this is not surprising at all, as high resolution imaging detectors are almost never used for conventional diffraction or grain mapping studies. Measurement of the distortion field of a detector is also not trivial. In practice, a grid sample with known hole separation should be placed on the place of detector's scintillator screen. Then, a series of images of the grid should be collected. As this procedure probes the visible-optics side of the detection system, it can be performed either with a visible light source or with X-ray radiation. The acquired images are then analyzed for fitting the effective pixel size and distortion field of the detector in cubic-spline function form[3].

In order the quantify the analysis made above, we have repeated the overlay study study

[3] An example fitting routine can be found in the pyFAI tutorials: https://pyfai.readthedocs.io/en/master/usage/tutorial/Detector/CCD_Calibration/CCD_calibration.html

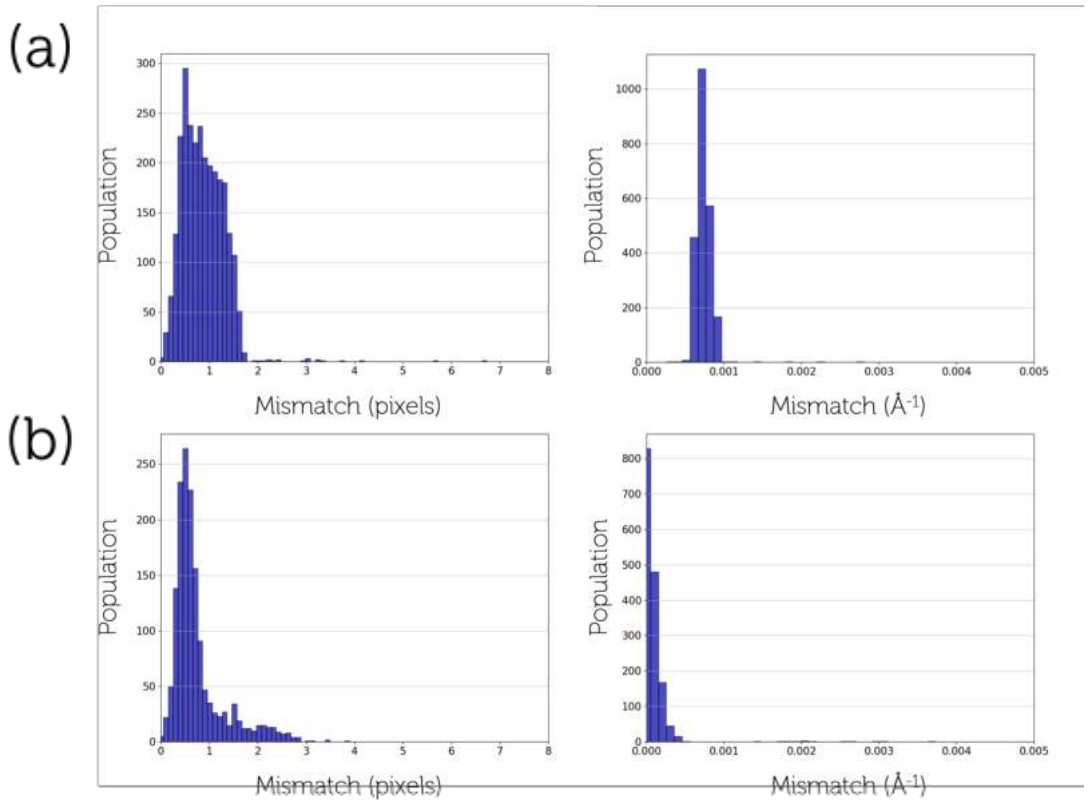

Figure 6.11: Calculated mismatch of CoM position distance on compound image frame (left) and on scattering vectors (right) for (a) image pair 1 and (b) image pair 2 for the image registration and stitching procedure.

of the same image pairs on harvested peaks level. Both image pairs were pre-processed and subjected to peak harvesting, according to the given simulation pipeline in Section 4.1. Then, the shifts calculated by image registration were posed on the obtained peak lists. This step ensures that for each image pair, the individual images share a common FoV. The global parameters from detector calibration of the compound image were employed on the resulting peak lists for calculating the scattering angles and scattering vectors for each harvested peak. For each image pair, the resulting peak lists were analyzed with a similar approach adopted for the simulation studies (c.f. Section 4.2). All peaks of an image pair were subject to a matching process. The matching is done by determining each peaks counterpart for an image pair by minimising the distance on the common detector frame through a spatio-angular search kernel. For each peak, a match was searched within a kernel of ± 20 pixels in y and z CoM positions on the common detector frame and ± 0.005 degrees in ω angle.

Considering the observed peak position of the diffraction peaks lying on the overlap regions, we can suggest that the observed ω angle position determination is less prone to systematic errors than their determined CoM position on the compound image frame. Such statement is build on the fact that the ω angle of a diffraction spot is determined along the diffraction image stack at its detector position. As all detector positions utilize the same ω range and step size, the observed ω angle of a diffraction peak in two neighboring detector positions would be highly accurate. Therefore, in order to increase the accuracy of the matching process, the angular part of the search kernel was deliberately set to a tight angular range, corresponding to two fifths of the experimental ω-step

size. Hence, the obtained set of matched diffraction peaks were assumed to be of good precision.

The results of the matching procedure is summarized in Table 6.1. For both image pairs, the number of matched peaks correspond to approximately $15-20\%$ of the total number of peaks in the respective individual images. We should note that the analysis considered all available peaks in the images, rather than focusing on the overlap region. Considering the fact that the η-range of the overlap region is considerably narrower that the η coverage of a single detector frame, we think that the percent correspondence of the number of matched peaks is actually much higher that the given value. Thus, we think that obtained set of matched peaks are statistically representative of the analyzed image pairs.

By utilizing the resulting set of matched peaks, the mismatch in the compound image frame and the mismatch in derived scattering vectors were calculated. The distribution of these mismatches are presented Figure 6.11. In case of mismatch in the compound image frame, the bulk of the matched diffraction peaks were found to be matched within a single pixel. This observation is supported with the calculated median of the given distributions. For both cases, the median was found to be lower than 1 pixel. In case of image pair 1, the largest observed mismatch values reach up to ≈ 1.5 pixels. Whereas in image pair 2, the distribution shows an extended tail reaching up to 3 pixels.

We should note that, these results should be interpreted through the lens of compound image formation in HR-3DXRD. During the stitching process, image pairs are first shifted with respect to each other, and then the merging of the two images are done with the help of maximum filter (see Section 6.1.1). Let us consider stitching of an image pair with a calculated mismatch of 1 pixel on the compound image frame. In such condition, we can expect the detector CoM position of diffraction peaks lying on the overlap region to have the same positional mismatch in the two image frames. When the image pair is registered and stitched, these diffraction peaks would merge together with an error of 1 pixel; i.e. the diameter of the observed diffraction peak on the compound image would enlarge by 1 pixel. Hence, when these diffraction peaks are harvested from the compound image, the determined detector CoM position of these peaks will be 0.5 pixels away from their positions in their respective detector frame. Therefore, a calculated mismatch of 1 pixel should reflect as 0.5 pixel error in the compound image dataset.

Table 6.1 also shows the calculated mismatch for the respective scattering vectors of the matched peaks. Recall that in derivation of the scattering vectors of an image pair, the refined calibration of the compound image (presented in Section 6.1.2) was used for both parts of the image pair. The distributions given in the figure shows that for both image pair, all scattering vectors are matched within $0.001\,\text{Å}^{-1}$. Albeit this result is on the limit of being acceptable, we assess that the attained accuracy in both detector CoM positions and scattering vectors would be sufficient enough for the demonstration purpose of HR-3DXRD.

6.2 Simultaneous multi-panel detector calibration

In the previous section, we have shown that the compound image can be physically formed by means of image registration and stitching processes. In this section, we are going to present a multi-panel calibration approach, in which the diffraction signal obtained in all detector positions are calibrated simultaneously. Rather than forming a stitched compound image, the resulting refinement here presents an analytical formalization of the experimental setup in term of experimentally recorded motor positions. The resulting overall calibration of the experimental setup is used for calculating the scattering vec-

tors of each individual detector positions. Hence, a compound image is formed both in pseudo-large detector form and also in scattering vector form.

This section will present the procedure, implementation and quality assessment of multi-panel detector calibration for simultaneous production and calibration of the compound image. The presented process was performed with a specialized version of the pyFAI script explained in [142]. The mentioned script was thoroughly customized to accommodate and refine the proposed multi-acquisition HR-3DXRD experimentation strategy. The final version of the script can be found as an *ipython notebook* form in Appendix C.

6.2.1 Procedure

The adopted multi-panel detector calibration procedure can be explained as follows:

- The procedure commences with pre-processing of the experimental data for preparation of the input files. This step strictly follows the same operations of the pre-processing stage of image registration and stitching process. For details please refer to the first item in Section 6.1.1.
- Initial calibration of individual panels: The refinement script requires initial global parameter guesses. These guesses are derived via manual calibration of all detector positions. During this process, control points (see Section 6.1.3.1) are also obtained for all detector positions.
- Definitions 1: The user is asked to provide the experimental (pre-processed) diffraction images and their associated motor positions, definition of the used detector unit (in terms of FoV, effective pixel size, -if available- a cubic spline function for defining the detector distortion) and definition of the calibrant material.
- Definitions 2: This step is dedicated for further definitions of the experimental geometry, initial guesses and boundary conditions of the global parameters. In the experimental geometry definition, the user have the option of defining analytical expressions of the global parameters in terms of motor positions. Practically, experimental measurements of the global parameters can be used as initial guesses.
- Refinement: A fitting/refinement instance is created with the provided definitions. The derived initial guesses and control points are provided to the instance. Then, the script performs the multi-panel detector calibration process and refines it thoroughly to obtain analytical form of global parameters. This step can be repeated several times for reaching the optimal refinement.
- The resulting global parameters can be converted to different geometry definitions, such as ImageD11, HEXRD, etc., and they are saved for each detector position.
- The obtained result is subjected to an on-line quality assessment via $1D$ and $2D$ integration of the calibrated images. Fitted 2θ positions of the diffraction rings and 2θ-η plots of the compound image are derived for quality assessment.

If the quality assessment provides satisfactory results, then, the obtained result for each detector position is used respectively for calculating the scattering vectors from the harvested diffraction peaks. These scattering vectors can be merged to serve as a “reciprocal space version” of the compound images to serve as an input for the Mode II HR-3DXRD analysis.

6.2.2 Implementation

The pre-processing step was carried out with the image averaging/summation tool of the pyFAI software suit [31]. The adopted procedure follows the exact route pre-processing

route of the image registration and stitching procedure. For details, please refer to the first paragraph of Section 6.1.2.

Following the procedure, all pre-processed images were subjected to detector calibration routine for derivation of an initial guess of their global parameters. The resulting set of global parameters and control points were then fed to the aforementioned pyFAI-powered customized multi-panel calibration script.

The current section will start by presenting the calibration results of the individual panels. Then, the customized multi-panel calibration script and its application will be explained in detail. The analysis of the produced results will be presented and discussed in the following section.

6.2.2.1 Calibration of individual panels

The pre-processed experimental diffraction images were subjected to detector calibration, for derivation of their global parameters. The detector calibration routines were performed with the calibration module of pyFAI software [31]. The required inputs for the calibration were wavelength, polarization, effective pixel size, a calibration file indicating the *d-spacings* of the sample and a set of manually chosen *control points* defining regions with discernible intensity around Debye-Scherrer rings. The global parameters of the image of concern was calculated through initial calibration and refinement stages. The resulting parameters were regarded as to be fully refined, when the obtained global parameters do not refine with further refinement steps. The obtained refined global parameters were employed on the images for $1D$ azimuthal integration with the mentioned software.

As stated above, the main motivation of this step is to obtain sensible initial parameters for each individual acquisition step of the HR-3DXRD scan. However, the initial efforts of calibrating detector images from a single detector position with pyFAI's calibration module have failed numerous times. These efforts have shown that the obtained results provide only partial calibration; i.e. a calibration result containing physically meaningful[4] values for only $1-2$ out of 5 global parameters. We think that the innate low azimuthal range but also the low S/N nature of the acquired HR-3DXRD datasets hinder derivation of the complete set of refined global parameters for each detector position.

We can state that the adopted tools were found to be unsuccessful for providing the complete set of initial parameters with the desired accuracy. However, we can still derive a partial calibration providing physically meaningful values for a small set of global parameters. Therefore, to remedy this problem, one can select a narrow set of global parameters in terms of their significance to the experimental setup. Then, in the detector calibration process, these parameter(s) can be sought to calibrate to physically meaningful values, while letting the rest of the parameters to end up with non-physical values. Such strategy would provide a partial calibration for all detector positions of the HR-3DXRD scan.

Regarding the multi-panel acquisition strategy of HR-3DXRD, the most critical global parameters for performing a successful detector calibration are the detector center positions, or in terms of pyFAI notation, *PONI* parameters. The PONI definition can be narrowed down on the HR-3DXRD frame by stating that PONI parameters relate to the motor position of an individual detector position[5]. Considering the rest of the global parameters,

[4] Here, the term "physical" connotes the experimenters' objective observation of the mentioned experimental observable. In the all of the presented experiments in this thesis, the beamlines' alignment had ensured that the detector tilts around y_L and z_L are less than a degree. In this regard, we call a calibrated tilt value of e.g. $15\,^{\circ}$ as non-physical due to not reflecting the observed objective reality.

[5] This concept will be further explained in the upcoming section on multi-panel calibration script. In short, assuming a tilt-free detector configuration, the experimental motor positions can be expressed as summation

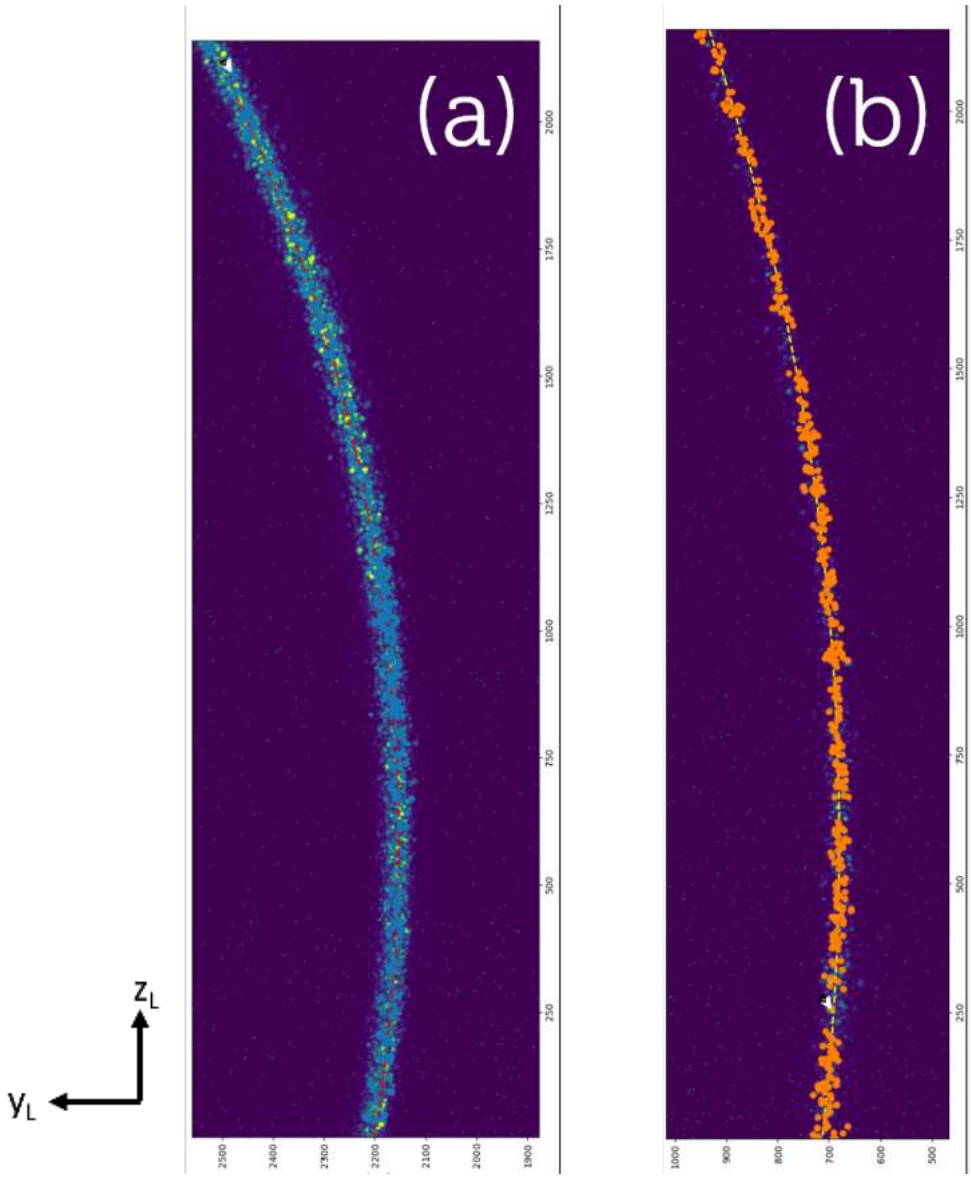

Figure 6.12: The calibration result of (a) 110 and (b) 200 diffraction rings observed at the detector position located around $eta \approx \pi/2$. The control point used for this detector position are indicated as blue and orange for (a) and (b), respectively. The calibrated powder lines for both rings are indicated red and yellow dashed lines for (a) and (b), respectively.

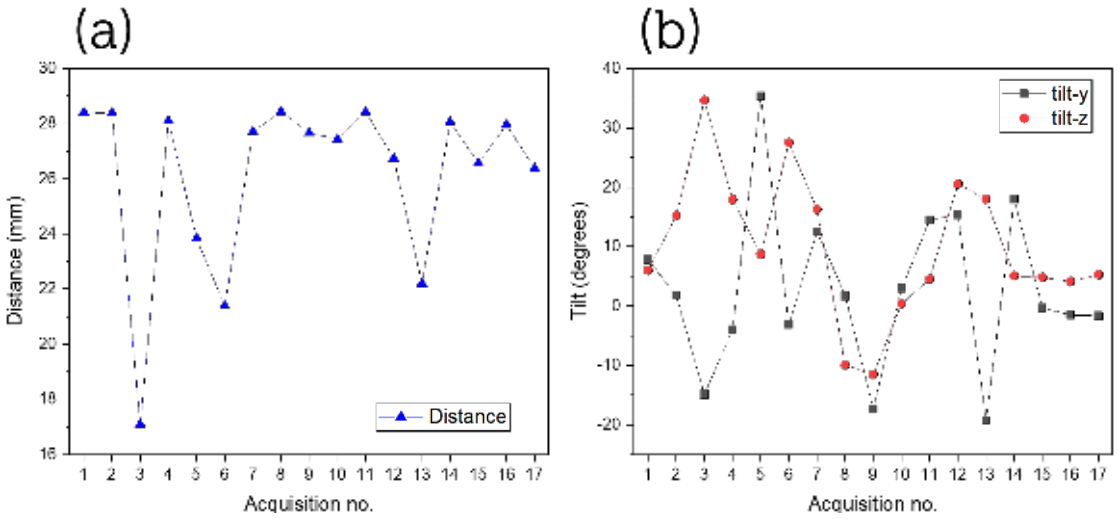

Figure 6.13: Detector calibration results for the individual detector positions of the HR-3DXRD dataset: (a) sample-to-detector distance, $\boldsymbol{L}$ and (b) detector tilts-y and z. The detector center (or PONI) parameters are not shown, as coordinate system of the calibration is different for individual images.

initial parameters for both $\boldsymbol{L}$ and detector tilts were measured during the experiment. Sample-to-detector distance, $\boldsymbol{L}$ was manually measured at the time of data collection, whereas detector all tilts were carefully aligned to their zero positions during the experiment. Therefore, we expect the derived partial calibration result to have good initial parameters for the PONI parameters, but not for the rest of the global parameters. In the upcoming multi-panel calibration process, these initial parameters can be overridden with the manual definition of initial parameters as the experimentally measured and aligned values.

Regarding the explanation above, the success criteria of the obtained partial calibrations was set to be the accuracy of the PONI parameters. After each fitting and subsequent refinement step of the calibration, the quality of these parameters can assessed by by a visual comparison between the experimentally observed diffraction signal and the overlaid powder diffraction signal calculated from the resulting partial calibration. Our trials have shown that obtaining a good correspondence implies that PONI parameters are found with sufficient accuracy. An example of such visual assessment is given in Figure 6.12: the resulting partial calibration shows a good correspondence with the observed diffraction signal implying that refined PONI parameters are sufficiently accurate. Thus, the obtained partial calibration was regarded as successful.

The calibration of individual detector positions were performed for the dataset of concern. The obtained partial calibrations were thoroughly refined until the explained success criteria has satisfied. The derived global parameters from individual detector positions are presented in Figure 6.13. Please not that, the figure presents only the $\boldsymbol{L}$, and detector tilt-y & tilt-z; but omits the found PONI positions for each detector position. Such choice was made due to the definition of the PONI parameters. Recall that PONI is defined as the vector between the origin of the detector frame and the optical axis' intercept of the extended surface defined by the detector frame. Thus, considering the fact that the image origin is not fixed for diffraction images collected at different detector positions, the

of $-\overrightarrow{PONI}$ and $\overrightarrow{FOV/2}$ vectors in the laboratory coordinate system. For details please check Section 6.2.2.2.

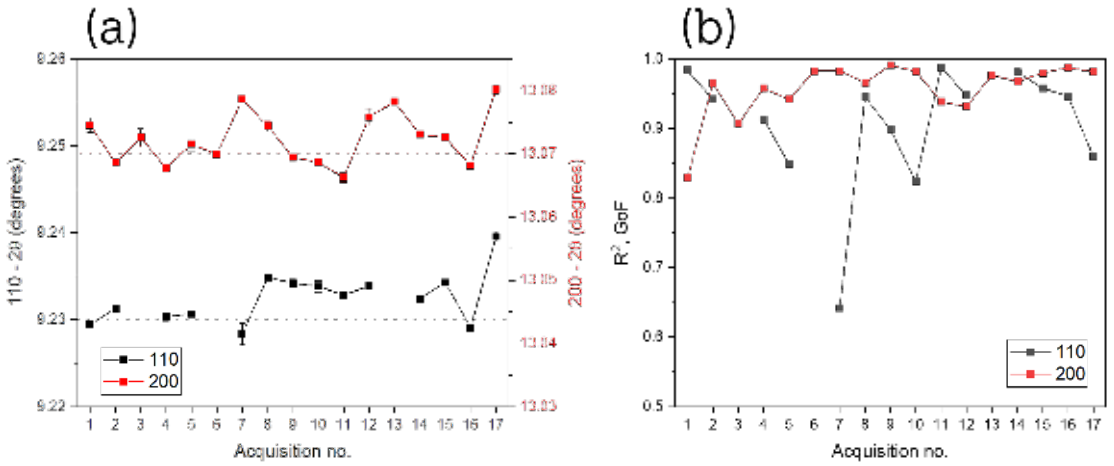

Figure 6.14: (a) Determined peak positions of 110 and 200 diffraction rings for the individual detector positions of the HR-3DXRD dataset. Peak positions are calculated by fitting a Lorentzian function to the corresponding diffraction peaks in azimuthally integrated $1-D$ patterns. Theoretical peak positions are indicated with black and red dotted lines, respectively. (b) Corresponding evolution of goodness of fit, R^2, parameter for the fitted Lorentzian functions in (a).

obtained PONI parameters are not directly related, nor it is trivial to do a comparison.

The results given in Figure 6.13 should be discussed with respect to the characteristics of the dataset of concern. In Figure 6.4, we have shown that the dataset of concern has two major artifacts: the obstructed signal around $\eta \approx \pi$ and the *missing panel* at $\eta \approx \pi$. In the experimental dataset, the former artifact had affected the detector positions (i.e. acquisition number along the HR-3DXRD scan) number 3, 5 and 13. In other words, the diffraction images from these detector positions provides little to information about the inner 110 diffraction ring. Figure 6.13(a) shows that for these particular detector positions, the obtained partial calibrations were stand out to be worse than the rest of the dataset. Due to the missing information from the 110 diffraction ring, calibrated $\boldsymbol{L}$ values of these detector positions were found to be off by 10 mm with respect to the experimentally measured $\boldsymbol{L}$. Conversely for the rest of the dataset, $\boldsymbol{L}$ was determined within ≈ 1 mm.

Figure 6.13(b) shows the determined detector tilt-y and tilt-z of the dataset of concern. Following our perspective, the results showed non-physical values for both detector tilts. The obstructed detector positions have shown tilt values reaching $\gg 10\,^{\circ}$, confirming that obtained individual partial calibration of these detector positions were particularly worse than the rest of the rest of the dataset.

The quality and accuracy of the obtained partial calibrations of the individual detector positions were done through the $1D$ azimuthal integration and subsequent Lorentzian fitting of the 2θ position of the diffraction peaks. Figure 6.14 shows the determined peak positions of the 110 and 200 diffraction peaks and their corresponding goodness-of-fit parameters. The figure shows that peak positions of all detector positions were found around the vicinity of the theoretical diffraction angles. Considering the success criteria of individual detector calibration scheme, the results shown in Figure 6.14(a) quantitatively confirms our visual assessment that obtained PONI parameters were found with adequate accuracy.

Lastly, we should point out that the Lorentzian fitting of the outer 200 diffraction ring pro-

vided relatively more consistent statistics with respect to the inner 110 diffraction ring. Such inconsistencies can be attributed to the chosen experimental HR-3DXRD configuration for $\boldsymbol{L}$ and number of detector positions, and the aforementioned detector distortion. In the current HR-3DXRD configuration, the signal from the inner diffraction ring fell on to the vicinity of the edge of the detector frame, whereas the bulk of the signal from the outer ring was mostly observed on the middle portion of the FoV. Considering the discussed spatial errors due to detector distortion, we can comment that the inner ring may have suffered from such distortion effects with respect to the outer ring. Therefore, the affected positional error of the inner ring may led to produce results with less accuracy with respect to the outer diffraction ring. Hence, we comment that such effects should be kept in mind whislt determining the experimental configuration of any multi-acquisition HR-3DXRD scanning.

The individual detector position calibration procedure was successfully performed by obtaining partial calibrations of all acquisitions for the entire dataset. The resulting partial calibrations possess good initial parameters for the detector center positions (or analogously, PONI parameters). The found $\boldsymbol{L}$ and detector tilt parameters have shown large inaccuracies. Yet, in the multi-panel calibration process, these parameters is planned to be replaced by the experimentally measured (or aligned) values.

6.2.2.2 Geometrical definitions of global parameters

Before starting the details of the implemented pyFAI-based multi-panel detector calibration script, we should discuss the correlation between the proposed HR-3DXRD experimental geometry (Section 3.2) to the geometry definitions of the calibration software pyFAI and the 3DXRD-analysis software FABLE/ImageD11.

As mentioned in Section 3.1, the same geometrical definitions given in [1] are strictly followed by the proposed experimental geometry of HR-3DXRD and also FABLE/ImageD11 software suit [111]. In comparison, the pyFAI geometry has the same definitions for detector tilts, but not for the the spatial parameters (i.e. $\boldsymbol{L}$ and detector center/PONI parameters). In [1], these spatial parameters are defined on the 'tilt-corrected' detector frame, such that the detector frame is assumed re-oriented to zero positions by the amount of the determined tilts. Therefore, the spatial parameters are defined with respect to the origin of the detector frame in such tilt-corrected condition. In contrast, the pyFAI geometry defines its spatial parameters in the 'tilted' detector frame. In this case, in order to convert the obtained distance and PONI parameters to the laboratory coordinate system, the resulting values should be corrected with the found detector tilt values. Therefore, the obtained calibrations with the pyFAI software should be converted[6] to the geometry defined in [1] before employing them with the proposed analysis pipeline in Section 4.1.

The conversion from pyFAI geometry to laboratory coordinate system has another essential implication for the HR-3DXRD analysis. Let us consider the experimental configuration given in Figure 6.15. In this schematic, the spatial relations are expressed in laboratory coordinates with the assumption that the utilized detector is free of any angular misalignments (i.e. detector tilts are zero). Following the geometrical definitions given above, the condition presented in the schematic can be regarded as a special case in which the pyFAI geometry falls to the same definitions given in [1]. In this schematic, $O_{optical}$ is defined as the intersection of the optical axis vector and surface defined by y_L and z_L axes and $O_{detector}$ is the origin of the detector frame in the defined HR-3DXRD geometry. In the actual experiments, the beamline alignment ensures that the motor position of the employed

[6] The details of geometry conversion between pyFAI to FABLE/ImageD11 can be reached from https://github.com/kif/pyFAI/blob/master/doc/source/geometry.tex.

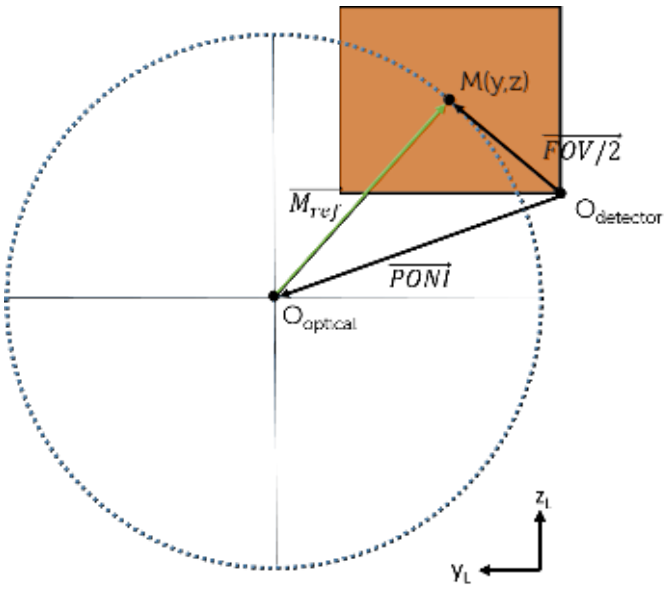

Figure 6.15: A schematic depicting the definition of the refined motor positions. Assuming that all detector tilts are aligned to zero, the refined motor position of acquisitions at detector position can be calculated by redefining the calibrated detector center (i.e. in pyFAI terms, PONI parameters) from origin of the detector frame to the center of the detector frame.

detector is positioned at the center of employed detector's FoV. Thus, the motor position of an arbitrary detector position lying on the surface defined by y_L and z_L axes is defined as $M(y, z)$. Furthermore, following the definitions given in (Section 2.2.1.1), the detector center (or in pyFAI terms, PONI parameters) can be expressed in vector form as,

$$\overrightarrow{PONI} = \left|O_{detector}O_{optical}\right|, \tag{6.1}$$

and the vector between $O_{detector}$ and the defined motor position can be expressed as,

$$\frac{\overrightarrow{FOV}}{2} = \left|O_{detector}M(y,z)\right|. \tag{6.2}$$

Therefore, assuming that the calibration of the detector frame is obtained with sufficient accuracy, then, one can calculate the so-called *refined motor positions* from the calibration result the following relation:

$$\overrightarrow{M_{refined}} = \left|O_{optical}M(y,z)\right| = -\overrightarrow{PONI} + \frac{\overrightarrow{FOV}}{2}. \tag{6.3}$$

Hence, the presented analysis shows that the result of the multi-panel calibration procedure can be used for calculating the attained spatial errors at each detector position. In terms of multi-acquisition HR-3DXRD scanning, these calculated spatial errors can be regarded as corrections of the experimental motor positions of each acquisition. Analogous to image registration results, the calculated refined motor positions provide the overall spatial arrangement of all detector positions of the multi-acquisition scan. Then, the resulting refined motor positions can be utilized for calculation of

- The attained size of the compound image frame (i.e. its FoV),

- Spatial position of individual detector positions in the compound image frame.

The calculation of refined motor positions enables determination of the extent of detector frames traveling ranges in the surface defined by y_L and z_L axes. As refined motor positions are defined to follow a circular path around the azimuthal direction, then, the horizontal and vertical sizes of the compound image frame can be calculated by,

$$FoV_{multi-panel,h} = \left|M_{refined,y-max} - M_{refined,y-min}\right| + FoV_{detector,h}, \tag{6.4}$$

$$FoV_{multi-panel,v} = \left|M_{refined,z-max} - M_{refined,z-min}\right| + FoV_{detector,v}, \tag{6.5}$$

where $M_{refined}$ denotes the calculated maximum and minimum refined motor positions along y_L and z_L and $FoV_{detector}$ is the field of view of the high resolution imaging detector frame. The calculated refined motor positions further enables the calculation of the spatial position of each individual detector position (i.e. each acquisition at an arbitrary motor position) on the compound image frame. In laboratory coordinate system, the horizontal and vertical shifts required for placing each detector position on the compound image frame is determined as,

$$Shift_y = M_{refined,y} + \frac{FoV_{multi-panel,h}}{2} - \frac{FoV_{detector,h}}{2}, \tag{6.6}$$

$$Shift_z = M_{refined,z} + \frac{FoV_{multi-panel,v}}{2} - \frac{FoV_{detector,v}}{2}, \tag{6.7}$$

where $M_{refined}$ denotes the motor position in laboratory coordinate system. The calculated shifts can be applied to the dataset for production of the compound image. Please not that, the production of the compound image is not limited to image stitching on the extended detector frame. One can apply these shifts to the harvested diffraction peaks for forming the compound image frame on peak lists level.

6.2.2.3 Multi-panel calibration script

The multi-panel calibration procedure was implemented as a custom pyFAI script and presented as an ipython notebook in Appendix C. Following Section 6.2.1, the script initializes by loading the pre-processed diffraction images of each panel, description of the detector parameters and the calibration material[7]. If the experimental diffraction images do not contain its motor position information, the experimental motor positions should be provided by the user.

The script continues with the definitions of the detector translation function and user-specified initial and boundary conditions of the refinement. Then, the script utilizes the given information for calibration of the individual panels and outputs the refined global parameters in ASCII format.

The script determines and refines the global parameters in three successive steps. The adopted methodology is influenced by the calibration procedures of classical 3DXRD work. In general, the calibration procedure starts with finding physically meaningful $\boldsymbol{L}$ and detector center values with the assumption that detector frame is free of tilts. In the second step, the detector tilts are determined by simultaneous fitting and refinement of all global parameters. Regarding multi acquisition HR-3DXRD scanning, we hypothesize that spatial global parameters, i.e. $\boldsymbol{L}$ and detector center-y and z, of the detector frame are prone to attain errors due to its $2D$ motion on the surface defined by y_L and z_L. The current implementation of multi-panel calibration offers the possibility of deriving analytical

[7] As mentioned before, in the absence of calibration data, the diffraction signal of the sample can also be used. In this case, the calibrant file should be prepared manually. For various examples of calibrant files, please refer to https://github.com/silx-kit/pyFAI/tree/master/pyFAI/resources/calibration.

expressions with respect to experimental variables. Therefore, the script is constructed in such a way that one can first fit these spatial global parameters through the set of initial guesses and then the refinement can be performed via fitting of mentioned analytical expressions.

Following the mentioned ideology, the fitting and refinement of the global parameters was implemented in four steps:

- Step 1: Fit $\boldsymbol{L}$=const. and detector center as a function of motor position. Assume all $tilts = 0$.
- Step 2: Fit both $\boldsymbol{L}$ and detector center as a function of motor position. Assume all $tilts = 0$.
- Step 3: Fit all global parameters. Assume all tilts as constant.
- Step 4: (Optional) Repeat previous step for further refinement.

We should note that each step adopts the result of its predecessor as its initial guess of the refinement. The script enables definition of different boundary conditions for each step. In the presented implementation, although boundary conditions were defined for each step, we have used the same set of boundary conditions throughout the multi-panel calibration process. Lastly, we should remind the reader that throughout these calculations, the detector center points will expressed through PONI parameters, as the calculation is being made in pyFAI geometry.

In previous sections, we have discussed the significance of detector center parameter determination for creation of the compound image. Considering these discussions, Step 1 of the multi-panel calibration focuses on initial fitting of the spatial global parameters. In this steps, $\boldsymbol{L}$ was assumed to be fixed to its experimentally measured value and PONI parameters were further assumed to be linearly dependent to the experimental motor positions. The PONI parameters were expressed as,

$$\text{PONI1}_{refined} = -M_i, z \times \text{PONI1}_{scale} + \text{PONI1}_{offset}, \tag{6.8}$$

$$\text{PONI2}_{refined} = -M_i, y \times \text{PONI2}_{scale} + \text{PONI2}_{offset}, \tag{6.9}$$

where M_i is the experimental motor position, PONI1 and PONI2 denotes the fitted detector-z and y center positions in the pyFAI geometry, and PONI1_{scale}, PONI1_{offset}, PONI2_{scale} and PONI2_{offset} are the fitted free variables. The resulting refined calibration outputs the refined $\boldsymbol{L}$ as a constant and PONI parameters as a linearly dependent function of experimental motor positions.

Step 2 can be regarded as the second iteration of spatial global parameters' determination. In this step, the PONI expressions from the previous step is kept, whereas $\boldsymbol{L}$ was further assumed to be linearly dependent to the experimental motor positions. The sample-to-detector distance parameter, $\boldsymbol{L}$ was expressed as,

$$\text{L}_{refined} = \text{L}_0 + \text{L}_{scale,1} \times -M_i, z + \text{L}_{scale,2} \times -M_i, y, \tag{6.10}$$

where M_i is the experimental motor position, L_0 is the initial guess for $\boldsymbol{L}$ of the current refinement stage, and $\text{L}_{scale,1}$ and $\text{L}_{scale,2}$ are the fitted free variables. The resulting refined calibration outputs both $\boldsymbol{L}$ and PONI parameters as linearly dependent functions of experimental motor positions.

In Step 3, the detector tilts-y and z were determined by keeping the adopted expressions for $\boldsymbol{L}$ and PONI parameters. Here, we made the assumption that during its travel along

the azimuth on a multi acquisition HR-3DXRD scan, the detector tilts were not affected and kept a constant value. We should stress that, albeit being a mere simplification of the problem, our attempts of adopting an expression similar to Equations 6.8 and 6.10 had led no further refinement of the resulting calibration. The resulting refined calibration output presents $\boldsymbol{L}$ and PONI parameters as linearly dependent functions of experimental motor positions and detector tilts-y and z as constants.

The result of Step 3 can be regarded as the end product of the multi-panel calibration script. However, considering the noticeable number of free variables, further refinement of the resulting calibration could be done via repeating the third step, optionally for a desired number of times. In the current implementation given in Appendix C, such further refinement was done twice on 4^{th} and 5^{th} refinement stages.

The last step of the presented multi-panel calibration script is dedicated for on-line analysis of the produced refined calibration. Firstly, the resulting calibration was utilized for $1D$ azimuthal integration and $2D$ polar decomposition of the produced compound image. Secondly, the refined motor positions (see Section 6.2.2.2) were calculated for all detector positions. These results were then used for calculating the FoV of the compound image with Equation (6.4). Lastly, the obtained refined calibration was converted from pyFAI to FABLE/ImageD11 geometry and ImageD11-style parameter files were created for all detector positions.

6.2.2.4 Results

The explained multi-panel calibration implementation was performed twice on the dataset of concern. In the first run, the input images consisted of the complete set of 17 detector positions in the HR-3DXRD dataset. In the second run, the dataset was narrowed down to set of 14 images by removing the 3 detector positions that had failed to observe the first diffraction ring. In the following text, these datasets will be referred as the complete dataset and the narrow dataset, respectively.

For these multi-panel calibration efforts, the initial guesses of the $\boldsymbol{L}$ and detector tilts-y and z were assumed as their experimentally measured and/or aligned values. As mentioned before, detector tilts were aligned to its zero position with better than $1\,^{\circ}$ degree precision during the time of data collection. The initial guess of $\boldsymbol{L}$ was estimated as 28.85 mm and the detector tilts were estimated as $1\,^{\circ}$ in clockwise direction, to reflect the upper-most observed angular error.

The calibrated and refined global parameters derived from the refined multi-panel calibration efforts are given in Table 4.3. In the given results, instead of providing the calibrated $\boldsymbol{L}$ and PONI parameters, each component of their respective expressions (c.f. Equations 6.8 and 6.10) are presented. The table presents the experimental initial guesses of the parameters, as well as the final cost function value of the minimization scheme of the refinement stage. The final cost function value can be seen as the statistical metric that implies the quality of the performed fitting procedure.

Table 6.2 shows that the narrow dataset (i.e. the dataset with omitted images) has attained a final cost function value that is an order of magnitude better than the complete dataset. This conclusion can also be observed from the refined values of global parameters. The table shows that omission of 3 detector positions with bad initial guesses provided an obvious refinement of the resulting global parameters. It can be seen that the refined detector tilts decreased from non-physical values (e.g. $\gg 5\,^{\circ}$) to experimental observations of below $1\,^{\circ}$ rotations.

The field of view (FoV) of the produced compound images of the complete and narrow

Table 6.2: Results of multi-panel detector calibration procedure. Experimentally observed initial guesses are given, where applicable. The results are presented in the pyFAI geometry.

	L_0 (mm)	$L_{scale,1}$	$L_{scale,2}$	$PONI1_{scale}$	$PONI1_{offset}$ (mm)	$PONI2_{scale}$	$PONI2_{offset}$ (mm)	Det. tilt-y (°)	Det. tilt-z (°)	Final cost func. value
Exp. observation	28.85	$\approx$ 0.0	$\approx$ 0.0	$\approx$ 0.0	$\approx$ 0.0	$\approx$ 1.0	$\approx$ 0.0	$\approx$ 0.0	$\approx$ 1.0	NA
Complete dataset	26.963	-0.017	0.007	0.964	-0.914	0.955	1.908	-4.494	-0.606	3.25E-06
Narrow dataset	27.486	0.004	-0.004	0.977	1.554	0.977	1.428	0.480	0.413	3.09E-07

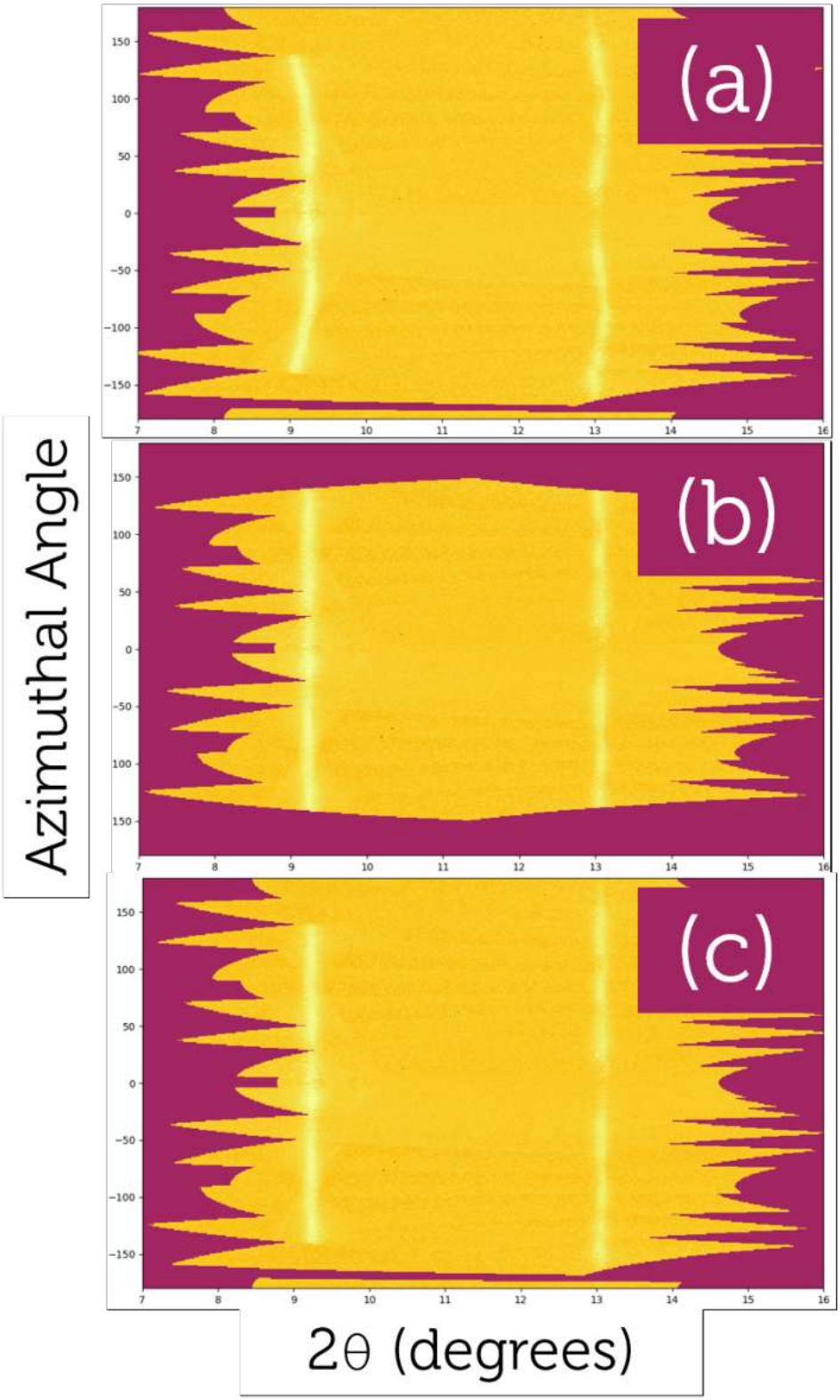

Figure 6.16: Polar decomposition of (a) the complete dataset and (b) the narrow dataset calculated from their respective refined calibrations. (c) Polar decomposition of the complete dataset with the refine calibration of the narrow dataset.

datasets were calculated with the procedure explained in Section 6.2.2.2. The refined calibration of the complete dataset had produced the compound image with the FoV of $10,996$ pixels in horizontal and $10,707$ pixels in vertical direction. In comparison, the refined calibration of the narrow dataset had produced the compound image with the FoV of $11,186$ pixels in horizontal and $10,818$ pixels in vertical direction.

Unlike image registration and stitching procedure, the multi-panel calibration script does not explicitly produces a compound image, but rather it provides the refined location of individual detector positions on the formed compound image. However, the obtained refined calibrations can be used directly for deriving the polar decomposition of the calibrated datasets. Figure 6.16(a) and (b) presents these polar decomposition plots of complete and narrow datasets.

The discussed performance of the obtained results can be further validated through the polar decomposition plots. Visual inspection of Figure 6.16(a) shows that the obtained refine calibration was not successful. It can be seen from the figure that the observed diffraction rings did not aligned well with their expected 2θ positions, but rather they had a wavy shape. In 3DXRD literature, such wavy patterns are usually attributed to insufficient calibration of the global parameters[1, 111]. Furthermore, considering the compound image formation efforts in HR-3DXRD, any misalignment of the detector positions would also produce a similar effect in the produced compound image. Figure 6.16(b) shows that such is not the case for the refined calibration of the narrow dataset. The figure reveals the straightly positioned diffraction rings around their expected 2θ positions.

In addition to the presented results for complete and narrow datasets, the latter calibration result was extrapolated to complete dataset. Please recall that the obtained calibration results are presented as a function of experimental motor positions. Therefore, in the analysis of the narrow dataset, the calibration of the omitted images were calculated from the obtained refined calibration result with their experimental motor positions. Figure 6.16(c) shows the polar composition of the complete set of images calculated with the refined calibration derived from the narrow dataset. It can be clearly seen that the calculated refined calibration from the narrow dataset had produced the desired “physically meaningfull” result, with respect to calibration of the complete dataset.

6.2.3 Quality Assessment

In this section,the quality assessment of the multi-panel detector calibration efforts are presented. First, the performance of the multi-panel calibration procedure will be discussed through by azimuthal integrated $1D$ plots, via tracking the 2θ position and FWHM of the observed diffraction rings. Then, the performance of the refined calibrations will be further analyzed and discussed through the calculated errors in $\boldsymbol{L}$ and detector center parameters. The quality assessment will continue by repeating the overlap analysis of the image pairs analyzed in Section 6.1.3.2. Please note that the overlap analysis will not be done on the diffraction image level, due to the nature of the obtained calibration result. Therefore, the presented overlap analysis will be narrowed down to harvested diffraction peaks level. The performance of the multi-panel calibration procedure will be statistically analyzed with calculated mismatches of CoM positions on detector frame, scattering angles 2θ and η and scattering vectors (in reciprocal space, Å^{-1}).

6.2.3.1 Analysis of calibration performance with azimuthal integration

In order to track the evolution of the derived refined calibration results during the multi-panel calibration procedure, both datasets were subjected to $1D$ azimuthal integration with the obtained intermediate calibration solutions for each calibration step given in Section 6.2.2. Figure 6.17 presents the determined 2θ angle and widths of the diffraction

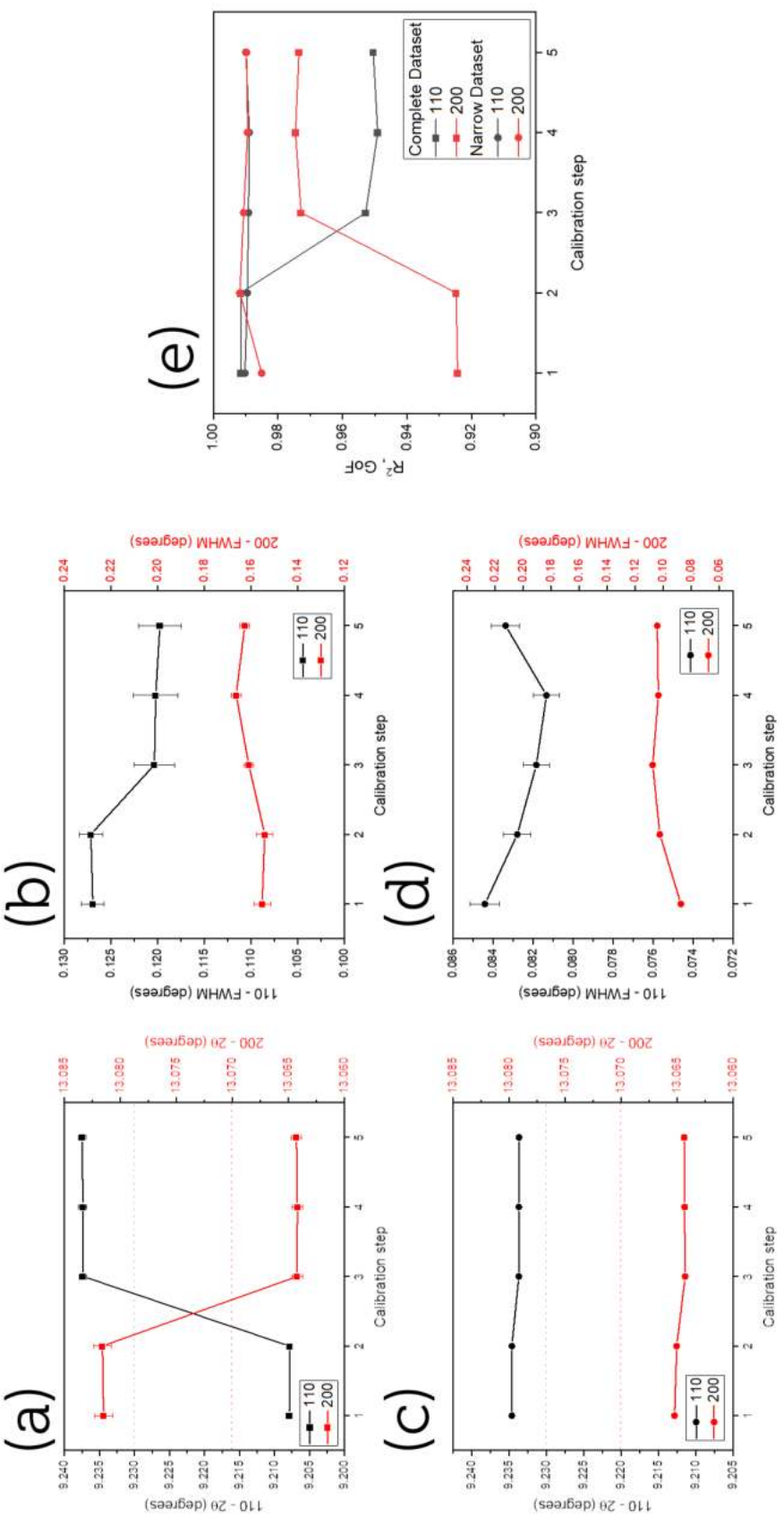

Figure 6.17: The evolution of Lorentzian fitted 2θ position and FWHM of the observed diffraction rings during the multi-panel calibration process. The results are given for both (a-b) complete dataset and (c-d) narrow dataset. (e) The calculated statistical goodness-of-fit parameter, R^2, of Lorentzian fits given in (a-d).

rings via Lorentzian fitting of the calculated $1D$ patterns. Figures Figure 6.17(a) and (c) shows the fitted 2θ angle for complete and narrow datasets, respectively. Firstly, we should point out that these figures confirm our assessment about the calibration behavior of the implementation, such that it can be seen that the multi-panel calibration process had found an optimized solution in Step 3. The found solutions were subjected to further refinement in Steps 4 & 5, yet providing minute changes in the fitted and refined global parameters. Secondly, the mentioned figures further show the consistency of the found solutions for datasets of differing confidence. For the complete dataset, it can be seen that the script's solution for Step 1 provided 2θ angles that were approximately $0.2\,^{\circ}$ away from their theoretical values. As mentioned, a stable solution was found in Step 3 for both rings. In comparison, for the narrow dataset, the initial determination of 2θ angles via the calibration result from Step 1 had provided a better estimation. During Step 3, the found estimation was refined to the proximity of its final value. Lastly, we should say that both calibrations had provided similar values for the determined 2θ angle of the second diffraction ring. Whereas, for the first diffraction ring, the value obtained from the complete dataset was observed to have a higher deviation from its theoretical value, with respect to the narrow dataset.

In addition to the 2θ positions of the diffraction rings, the width of the rings were also determined. Considering the multi-panel calibration procedure, any errors on the refined spatial position of a detector positions could reflect as formation of wavy diffraction rings in the polar decomposition plots (e.g. Figure 6.16(a)). As such misalignment is defined to be in the azimuthal direction, determined peak widths were used for quantifying these misalignments. Figure 6.17(b) and (d) shows the fitted widths, i.e. full-width-at-half-maximum (FWHM), values for the observed diffraction rings for complete and narrow datasets, respectively. The figures confirm the observations from the polar decomposition plots such that the narrow dataset provides relatively narrow rings with respect to complete dataset. The polar decomposition plot of the complete dataset implies that the obtained diffraction peaks its integrated $1D$ pattern should be a composed of convolution of misaligned diffraction signal around the vicinity of their determined 2θ position. Therefore, the obtained diffraction peaks in the pattern derived from the complete dataset provided a worse Lorentzian fit with respect to the narrow dataset. This can be observed in the statistical goodness-of-fit parameters given in Figure 6.17(e). The figure reveals that the fits of the resulting calibration step provides a better result for the narrow dataset.

Figure 6.18 shows the azimuthally integrated $1D$ plots of both datasets from their respective refined calibration result. The figure also shows the $1D$ plot of the complete dataset of images with the refined calibration result of the narrow dataset (i.e. dataset presented in Figure 6.16(c)). The shown figure supports the previous discussion of the peak width difference for complete and narrow datasets. It can be seen that the refined calibration of the narrow dataset provides sharper diffraction peaks around 2θ angles. Lastly, we should also point the observed intensity discrepancy between the narrow dataset and its extension to the complete set of experimental images. For the second diffraction peak, the observed intensity for both datasets were found to be comparable. Yet, the observed intensity of the first diffraction peak was found to be higher for the narrow dataset than its extension to complete dataset. Considering the fact that $1D$ azimuthal integration operation provides the average intensity over the observed azimuthal range, the mentioned discrepancy can be explained by the observed intensity characteristics of the omitted detector positions for the narrow dataset. Recall that the narrow dataset was formed by omitting detector positions that had practically no diffraction signal on the first diffraction ring. Thus, when the obtained good calibration of the narrow dataset was extended to

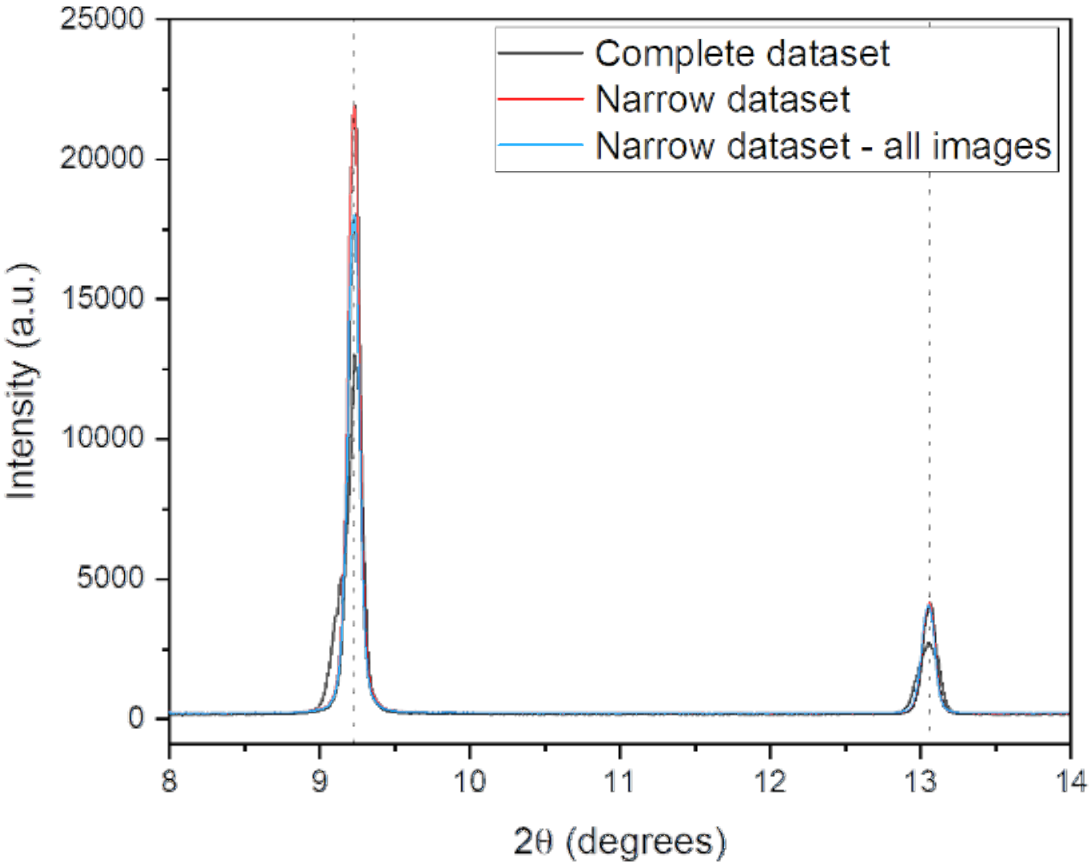

Figure 6.18: Comparison of the $1D$ azimuthal integral plots for the complete dataset, the narrow dataset and the calibration of the narrow dataset extended to consider all experimental images. Theoretical 2θ positions of the diffraction peaks are indicated as black dotted lines for both 110 and 200 reflections.

Table 6.3: Calculated positional errors of the experimental motor positions in laboratory coordinates.

Calculated error	Mean (μm)	Standard deviation
x_L	2.60	24.23
y_L	24.79	93.16
z_L	51.92	91.63

Table 6.4: Results of the overlay study performed on peak lists from image pairs 1 & 2 for the multi-panel calibration procedure.

	Image pair 1	Image pair 2
Number of harvested peaks	11,211/7,773	8,262/10,165
Number of matched peaks	1698	1370
Median mismatch in detector position (pixels)	0.87	21.95
Median mismatch in scattering vectors ($Å^{-1}$)	0.0003	0.0024

the complete set of experimental diffraction images, we think that aforementioned loss of diffraction signal around $\eta \approx \pi$ might have caused such discrepancy.

In previous sections, we have explained that the result of the multi-panel calibration is defined through user-specified experimental motor positions. We have further explained that the obtained result can be interpreted as the refined 3D position of the experimental motor positions. Therefore, we can estimate the calculated error between the calculated refined and experimentally employed/recorded motor positions. The calculated errors cover not only the y_L and z_L, but if further calculates the errors along x_L direction, as well. As discussed in Section 6.2.2.2, the adopted geometry of [27] states that $\boldsymbol{L}$ is defined along x_L, thus, these error can be discussed as the calculated error of $\boldsymbol{L}$ at each detector position.

The positional errors of at each detector position was obtained by calculating the difference between the experimentally recorded motor positions and $\boldsymbol{L}$ and the global parameters produced by the multi-panel calibration script. Please note that, the produced refined calibration result was converted to the adopted geometry of [27] for redefining all spatial parameters in the laboratory coordinate system. Table 6.3 shows the calculated positional errors of all acquisitions of the analyzed HR-3DXRD dataset. The table shows that determined $\boldsymbol{L}$ of detector positions vary by $\approx 25\,\mu$m along x_L direction. Furthermore, the difference between the experimentally recorded and calculated refined motor positions vary by $\approx 100\,\mu$m on the surface defined by y_L and z_L axes.

6.2.3.2 Analysis of overlapping regions

Following a similar procedure to Section 6.1.3.2, the characteristics of the obtained refined calibrations were further inspected though analysis of the overlapping regions. For comparability reasons, the presented study was performed with the same procedure (explained in Section 6.1.3.2) on the same image pairs studied in Section 6.1.3.2. As the multi-panel calibration procedure does not provide the physical merger of the experimental diffraction images, the current study will narrow its focus to calculation of mismatches on harvested diffraction peaks level. Lastly, this study will further narrow down its focus to the analysis of the derived refined calibration of the narrow dataset, as we have shown that it had outperformed the resulting refined calibration derived from the complete dataset.

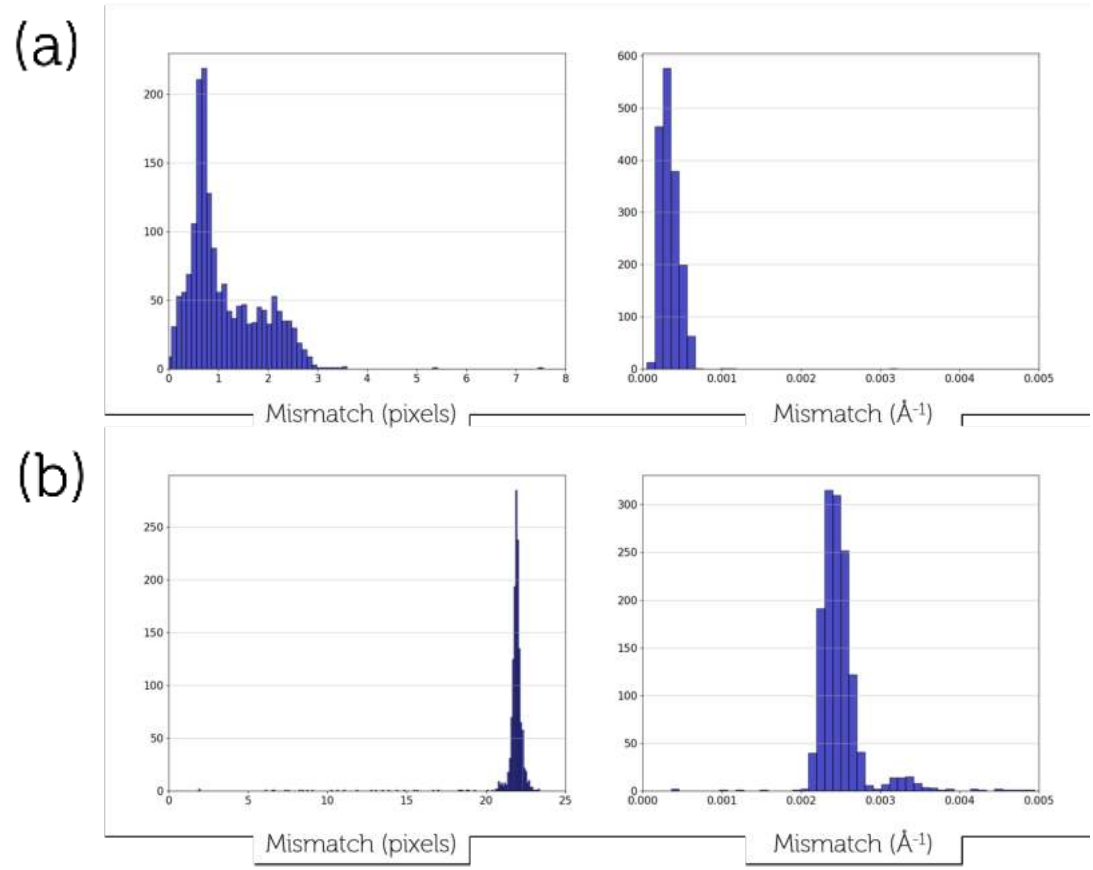

Figure 6.19: Calculated mismatch of CoM position distance on compound image frame (left) and on scattering vectors (right) for (a) image pair 1 and (b) image pair 2 for the multi-panel calibration procedure.

The results of the matching procedure is summarized in Table 6.4. For both image pairs, the number of matched peaks correspond to approximately $10 - 15$% of the total number of peaks in the respective individual images. Again, We should stress that the analysis considered all available peaks in the images, rather than focusing on the overlap region. By utilizing the resulting set of matched peaks, the mismatch in the compound image frame and the mismatch in derived scattering vectors were calculated. The distribution of these mismatches are presented Figure 6.19.

In case of mismatch in the compound image frame, the bulk of the matched diffraction peaks were found to be matched within a single pixel. This observation is supported with the calculated median of the given distributions. In case of image pair 1, the median was found to be lower than 1 pixel and the largest observed mismatch value reached up to ≈ 3 pixels. The calculated mismatch for image pair 2 showed a worse performance; the median was found to be around ≈ 22 pixels. In contrast to image pair 2, the calculated set of mismatch for image pair 2 showed a narrow distribution. The highest observed mismatch reached up to ≈ 23 pixels.

Table 6.4 also shows the scattering vector mismatch of matched peaks. Recall that in derivation of the scattering vectors of an image pair, the specific global parameters from the refined calibration result was calculated with respect to their experimental motor position. The distributions given in the figure shows a successful matching of scattering

vector for image pair 1. For this case, the observed scattering vectors were matched within $0.001\,\text{Å}^{-1}$. Following its detector position mismatch behavior, the scattering vectors in image pair 2 were matched within $\approx 0.0025\,\text{Å}^{-1}$.

The results of the overlay study reflects that the resulting refined calibration obtained from the multi-panel calibration procedure have shown different behaviors for different detector positions. The refined calibration result provided an acceptable result for image pair 1. However, for image pair 2, the calculated mismatch of CoM positions of diffraction peaks reached up to ≈ 23 pixels, displaying a bad registration of the two images. Through our current understanding of generalized concept of compound image formation and the multi-panel detector calibration routine, the observed inaccuracies of the procedure can be attributed to:

- The experimental problems regarding the acquisition,
- Inadequate statistics of multi-panel detector calibration, and
- Possible distortion posed by the detector frame.

During the course of this chapter, we have meticulously explained the undesired artefacts present in the analyzed dataset. Please recall that the dataset had suffered an obstruction of the diffraction signal at the detector positions located around $\eta \approx \pi$. Also, we have mentioned the so-called *misplaced detector*, which caused the complete miss of the diffraction signal around $\eta = \pi$. Considering the fact that detector calibration software like pyFAI performs better with large number of continuous and sharp powder rings, we can discuss that the analyzed dataset of concern is not the most suitable case for the proposed multi-panel calibration routine.

Another issue about the analyzed dataset is the attained S/N for the observed diffraction peaks. Owing to its unique acquisition strategy, a complete scanning of a single layer with HR-3DXRD would require multiple hours of data collection. Therefore, the extended scanning times require the optimization of the exposure of each acquisition of diffraction images, for optimization of the total scanning time. The inadequate S/N may also be enforced by the characteristics of the employed detector frame. As we have mentioned before in one of the presented experiments (APS 1-ID-E, Section 5.2.3), the employed detector limited the exposure time to ≈ 1 second, therefore, limiting any option of longer acquisitions.

The observed discrepancy between the mismatch results of image pairs 1 and 2 can be compared and discussed to the analysis of overlap regions from the image registration and stitching procedure. In Section 6.1.3.2, we argued that the detector distortion had a profound effect on the spatial positioning of individual diffraction peaks on the detector frame. As both analysis were performed on the same dataset of experimental images, we believe that a similar distortion effect may be responsible for the observed inaccuracies. As mentioned before, the current analysis can not include such distortion correction, due to the unavailability of the required information. If the distortion map of the detector was available, the provided distortion map (i.e. the fitted cubic-spline function) can be introduced in the detector definitions part of the multi-panel calibration script.

Lastly, we should mention that the explained analysis of multi-panel calibration should be ideally performed with the experimentally collected diffraction images of a calibrant material. However, as we've discussed in the beginning of this chapter, we have failed to collect any usable calibration data in our experimental efforts. Hence, in future uses of HR-3DXRD, remedying this problem can potentially provide accurate determination of

the global parameters. Then, the obtained global parameters can be used as initial guess of the data analysis scheme of HR-3DXRD.

6.3 Summary

In this section we have introduced two different strategies for producing the pseudo-large detector image, *the compound image*, to serve as an input for the analysis of a HR-3DXRD dataset collected with multi-panel acquisition strategy. The first strategy of image registration and stitching provided an *ad hoc* solution to the problem of compound image formation, via registration of the multiple observation of the intensity features in different detector positions. The second strategy of multi-panel detector calibration took a more systematic approach to compound image production. In this procedure, the compound image was produced implicitly through simultaneously fitting of all global parameters of the experimental setup with respect to the complete set of diffraction images acquired at the experimentally recorded detector positions.

In Sections 6.1.3.2 and 6.2.3.2 we have presented the characteristics of the produced compound images by focusing on the overlap regions of individual detector positions. The presented analysis had shown that the image registration and stitching procedure had produced a compound image in which the calculated CoM position of the diffraction peaks on the detector frame was found to be lower than ≈ 1 pixel. In comparison, the same analysis for the multi-panel detector calibration had produced inconsistent results. In this case, the calculated CoM position of the diffraction peaks on the detector frame had provided ≈ 1.5 pixels and ≈ 22 pixels error for the inspected image pairs.

The presented results for image registration and multi-panel detector calibration shows that the former approach provides the rule-of-thumb requirement of 1 pixel mismatch for diffraction peaks' CoM positions on the produced compound images. Therefore, image registration and stitching procedure can be used for demonstration of applicability of the multi-panel acquisition HR-3DXRD scanning technique.

Besides its systematic approach, the explained multi-panel detector calibration procedure requires a more demanding input preparation for producing physically meaningful initial guesses. Furthermore, one can argue that such procedure require a calibration dataset to function properly. As we have discussed before, neither of the acquired experimental data in four different experiments has the required confidence to satisfy the innate requirements of the procedure. Lastly, we should note that for future experimental applications of the multi-panel acquisition HR-3DXRD scanning, the experimenters should address the issue of calibrant dataset collection and utilize the calibrant dataset for the multi-panel detector calibration procedure.

7 Experimental demonstration of HR-3DXRD

In this chapter, I will present the first experimental application of the HR-3DXRD technique with the explained multi-panel acquisition strategy. In Chapter 6, I have shown that image registration and stitching procedure provides the required precision of $\lessapprox 1$ pixel for producing the compound image frame out of experimentally acquired partial diffraction images. In general, regarding the multi-panel acquisition HR-3DXRD scanning, I foresee that increasing the precision even further would require an extensive *FitAllB*-type of minimization [2, 57], in which the determined (sub)grain properties should be further refined through simultaneous fitting and refinement of the complete set of global parameters of each detector position as well as the orientation and CoM position (and, possibly, the elastic strain tensor) of the sub-grains. Yet, I assess that the attained precision in the presented image registration and stitching procedure is encouraging. Below, I show that the observed sub-pixel mismatch enables indexing of (sub)grains, without the need of FitAllB-type minimization scheme. These indexed (sub)grains can then serve as starting point for future refinements efforts using an adapted multi-panel version of *FitAllB* (see Section 5.4).

In this demonstration effort, I will adopt and show the applicability of image registration and stitching as the pre-processing tool for the experimental data analysis pipeline (Section 5.3) for producing Mode-II type three-dimensional CoM mapping. I should stress that the complete analysis of the experimental demonstration could not be completed due to the time limitations of the Thesis work. Therefore, results presented in this chapter will present the current state of the data analysis at the time of writing.

The demonstration of the multi-acquisition HR-3DXRD scanning dataset was performed with the image registration and stitching procedure, due to providing better performance over multi-panel calibration procedure, cf. Section 6.3. Therefore, this section will focus on presenting the analysis procedure of the multi-acquisition HR-3DXRD scanning dataset. After presenting the current state of the data analysis, we will discuss the potential improvements about the explained procedure.

In Chapter 6, we have presented two different approaches of producing the compound image. We have concluded that HR-3DXRD datasets can be converted into the compound image dataset with $\leq 1\,\mu$m positional errors with image registration and stitching approach. The compound image dataset was produced by employing the registration results presented and discussed in Section 6.1 on the experimental dataset of ARB processed IF steel sample annealed at $620\,^{\circ}$C from the Petra III P21.2 experiment. As explained in the begining of Chapter 6, the initial assessment of the dataset revealed that the observed diffraction peaks showed good S/N with no obvious sign of peak overlap. The stitching procedure was conducted with the built-in $2D$ pair-wise image stitching plug-in of ImageJ [141] in an automated fashion. Following the procedure given in Section 6.1, formation of the compound image observed at each ω angle was done by stitching the pre-processed (i.e. background subtracted) experimental diffraction images of individual detector positions to their registered position around the azimuth.

The image stitching process was performed on a common desktop personal computer. The production of a single stitched compound image took $3-5$ minutes and the produced

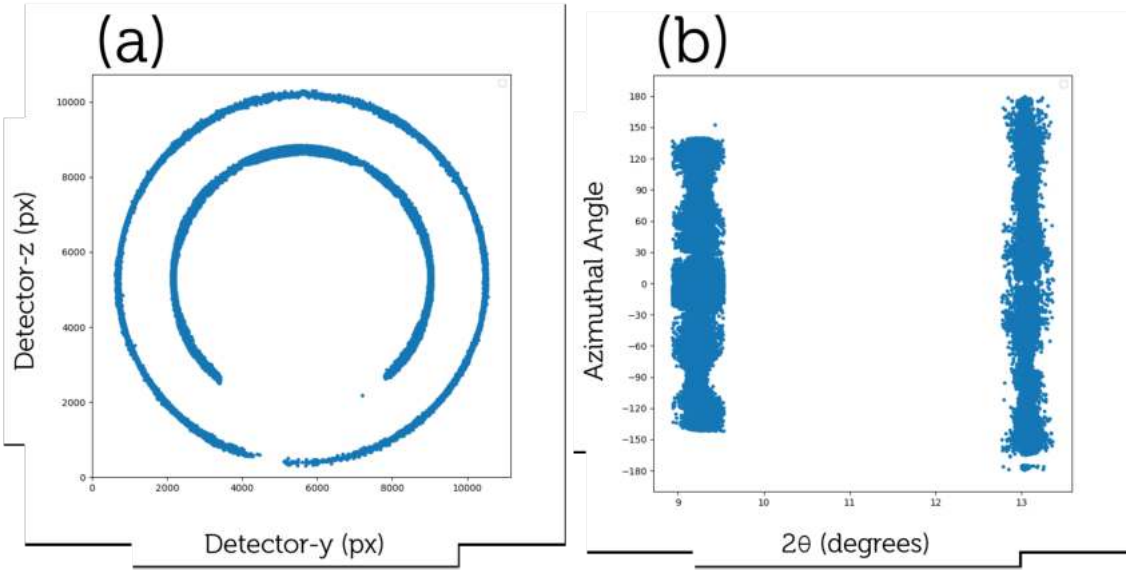

Figure 7.1: The representation of the harvested diffraction peaks from the stitched compound image in (a) detector frame and (b) its polar decomposition in 2θ and η angles of the ARB processed IF steel sample annealed at $620\,^{\circ}$C from the Petra III P21.2 experiment. The detector frame representation shows the complete set of observed diffraction peaks along the ω-range. The polar decomposition was performed by employing the refined calibration of the stitched compound image given in Section 6.1.3.1.

file size of a single image was 231 MB. The stitching of the complete dataset took approximately 4 days. We have further observed that the processing time is a strong function of the computing power. For comparison, the partial repetition of the same procedure with a common workstation computer showed that processing of a single stitched compound image can be depressed to $0.5 - 1$ minutes, reducing the total processing time to ≈ 1 day.

The analysis of the obtained compound image dataset was done by employing the explained data analysis pipeline in Section 4.1. Following the analysis pipeline, the peak harvesting was performed with the *peaksearcher* module of FABLEImageD11 software package [111]. The harvesting procedure was performed on a series of intensity thresholds, covering finer steps in lower intensities and relatively coarser steps in higher intensity ranges. The obtained peak lists of differing intensity thresholds were merged and subjected to a clean-up procedure. The clean-up process was performed by thresholding the number of pixels observed for each identified spot. This procedure ensured elimination of most of the erroneous signal, such as hot pixels and stray diffraction signal from the surroundings of the experimental setup. The resulting cleaned harvested peak list yielded $290,314$ diffraction peaks; 110-ring contains $103,687$ and 200-ring contains $38,682$. Assuming that all observed grains had 100% completeness, the expected number of observed grains can be estimated by dividing the theoretical multiplicity of the respective diffraction ring. Therefore, we can estimate the total number of observed grains as $8,641$ and $6,444$ for 110 and 200 rings, respectively.

The resulting harvested peak list is visualized in Figure 7.1, presented in both detector frame and as polar decomposition format. Inspection of Figure 7.1(a) shows that the stitching and subsequent peak harvesting procedures was successfully reproduced the observed intensity features in the through-stack sum version of the stitched compound im-

age given in Figure 6.4. Figure 7.1(b) shows the 2θ-η polar decomposition of the stitched compound image calculated by utilizing the derived refined calibration of the stitched compound image. The polar plot clearly shows the straight diffraction rings around their determined 2θ positions.

The normalized scattering vectors from the obtained harvested peak list of the stitched compound image were calculated by employing the aforementioned refined calibration. Following the analysis pipeline, calculated scattering vectors were fed to *Grainspotter* software for indexing [59]. In the initial trial, the indexing was performed on the complete set of two diffraction rings by adopting the indexing cuts and tolerances from Section 4.7. Among the set of indexing tolerances, only the diffraction angle tolerance $\sigma_{2\theta}$ was adjusted with respect to its reference value. In Grainspotter software, $\sigma_{2\theta}$ tolerance acts as an angular filter around the theoretical 2θ angle of the analyzed material. Considering the fact that the experimentally analyzed gauge volume was substantially larger than the simulated volumes, the increase in $\sigma_{2\theta}$ tolerance was necessary for accounting all of the observed diffraction peaks.

The initial indexing effort had failed to index any grains with the employed indexing thresholds. This failure was attributed to the large number of observed diffraction peaks. In the first stage of the indexing algorithm, Grainspotter generates the possible set of orientations from the observed peaks in the given 2θ range. Considering the extremely high number of observed diffraction peaks, the examination of the complete set of guess orientations took an exceedingly long time, reaching 10 hours. The long analysis time resulted in indexing of only 50 grains with questionable statistics.

In order to remedy the long analysis time of the Grainspotter indexing, we have made small alterations on the adopted analysis pipeline. In the original described pipeline, the indexing was conducted on the complete set of diffraction rings. The indexed orientations were then subjected to a refinement procedure with FABLE/ImageD11's *makemap* module [111], in which the observed diffraction peaks were reassigned to the observed orientations with successive depression of hkl_{tol} (see Section 4.1.4). As this approach turned out to be computationally longer than our expectation, the indexing and refinement stage of the analysis pipeline is changed as the following:

- Indexing with Grainspotter: Rather than accounting for the complete set of harvested diffraction peaks, the indexing was performed only with one of the measured rings. Indexing of rings with lower multiplicity are expected to be more robust than its high multiplicity counterpart.
- Refinement of the obtained orientations with *Makemap*: The indexed orientations (derived from a single diffraction ring) can be subjected to refinement with the complete set of harvested diffraction peaks.

Thus, the altered pipeline aims to index a high number of diffraction peaks by considering only one of the observed diffraction rings. Then, the indexed orientations are aimed to be thoroughly refined by accounting both of the observed diffraction rings. The main hypothesis behind this idea assumes that the successive depression of hkl_{tol} should distinguish the statistically significant solutions and eliminate the false-positives out of the set of indexed orientations. Once a set of grains are identified, the unassigned diffraction spots can be segmented. The remainder of the un-indexed harvested peaks can be fed to the altered analysis pipeline again, until the expected number of grains are identified.

The second indexing trial was performed with the explained altered analysis pipeline. Due to time restrictions of the PhD project, the altered analysis pipeline was performed for only

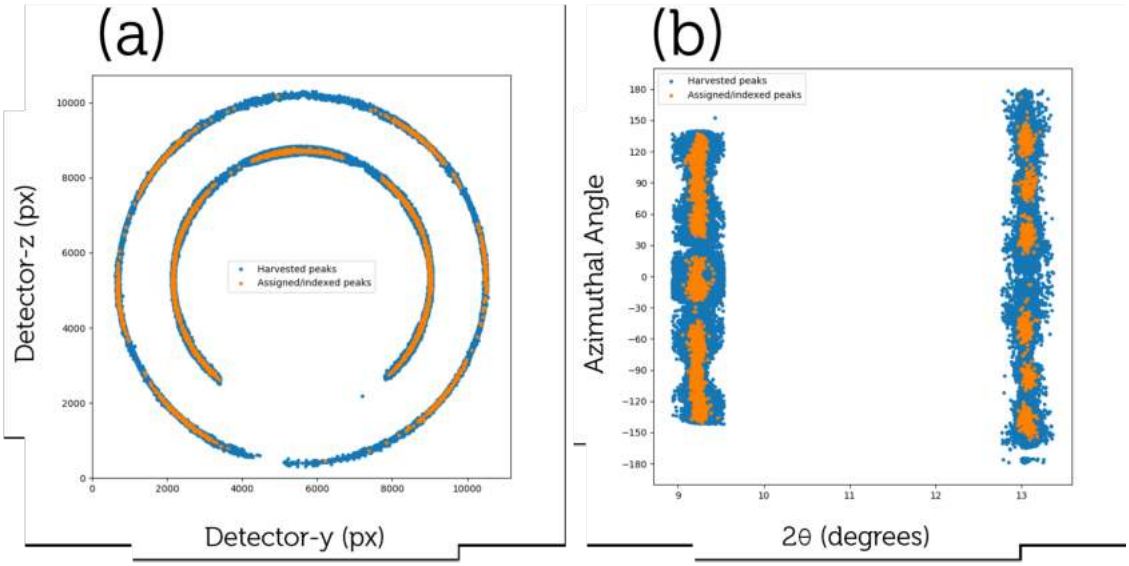

Figure 7.2: The representation of the harvested (blue) and assigned/indexed (orange) diffraction peaks from the stitched compound image on (a) the detector frame and (b) its respective polar decomposition in 2θ and η angles. The polar decomposition was performed by employing the refined calibration of the stitched compound image given in Section 6.1.3.1.

one cycle of indexing and refinement processes. Therefore, the results presented below will be concerned with this partial grain map.

The indexing step was performed on the observed 200 diffraction ring, owing to its lower multiplicity of 6 in the scanned ω-range$= \pi$. Grainspotter was let to produce guess orientations with at least 4 diffraction peaks and the rest of the tolerances were kept as the same in Section 4.7. The single indexing run identified $1,749$ orientations along with their candidate CoM positions in laboratory coordinates. The identified orientations were subjected to *makemap* refinement with the complete set of harvested diffraction peaks. The refinement was commenced with an extremely loose tolerance of $hkl_{tol} = 0.5$. Then, the identified orientations were thoroughly refined by decreasing the tolerance up to $hkl_{tol} = 0.003$ in steps of $0.0005\,\text{Å}^{-1}$. The final result of the refinement had identified 497 orientations with their determined CoM positions. The identified grains were found with mean number of 8.56 ± 0.79 peaks, with a mean hkl_{tol} of 0.0015 ± 0.0002. Hence, the mean completeness of the indexed grains was calculated as 0.476. The visual comparison of the complete set of harvested peaks against the indexed (i.e. assigned) diffraction peaks are shown in Figure 7.2.

The resulting partial 3D CoM map and its corresponding inverse pole figure are given in Figure 7.3 along the laboratory axes. The shown partial CoM maps reveals the identification of individual grains separated within $\approx 1 - 2\,\mu$m, suggesting that our assessment for the adequacy of pre-processing with image registration and stitching for multi-panel acquisition HR-3DXRD datasets was indeed correct.Figure 7.3(d) shows the derived inverse pole figure (IPF) of the determined orientations. In order to make direct comparison to the literature, the determined orientations were rotated by $\pi/2$ in clockwise direction, in order to align the rolling direction parallel to the setting given in Figure 5.7(c). The comparison of the IFP coloring between Figures 7.3(d) and 5.7(c) suggest that approximately half of the

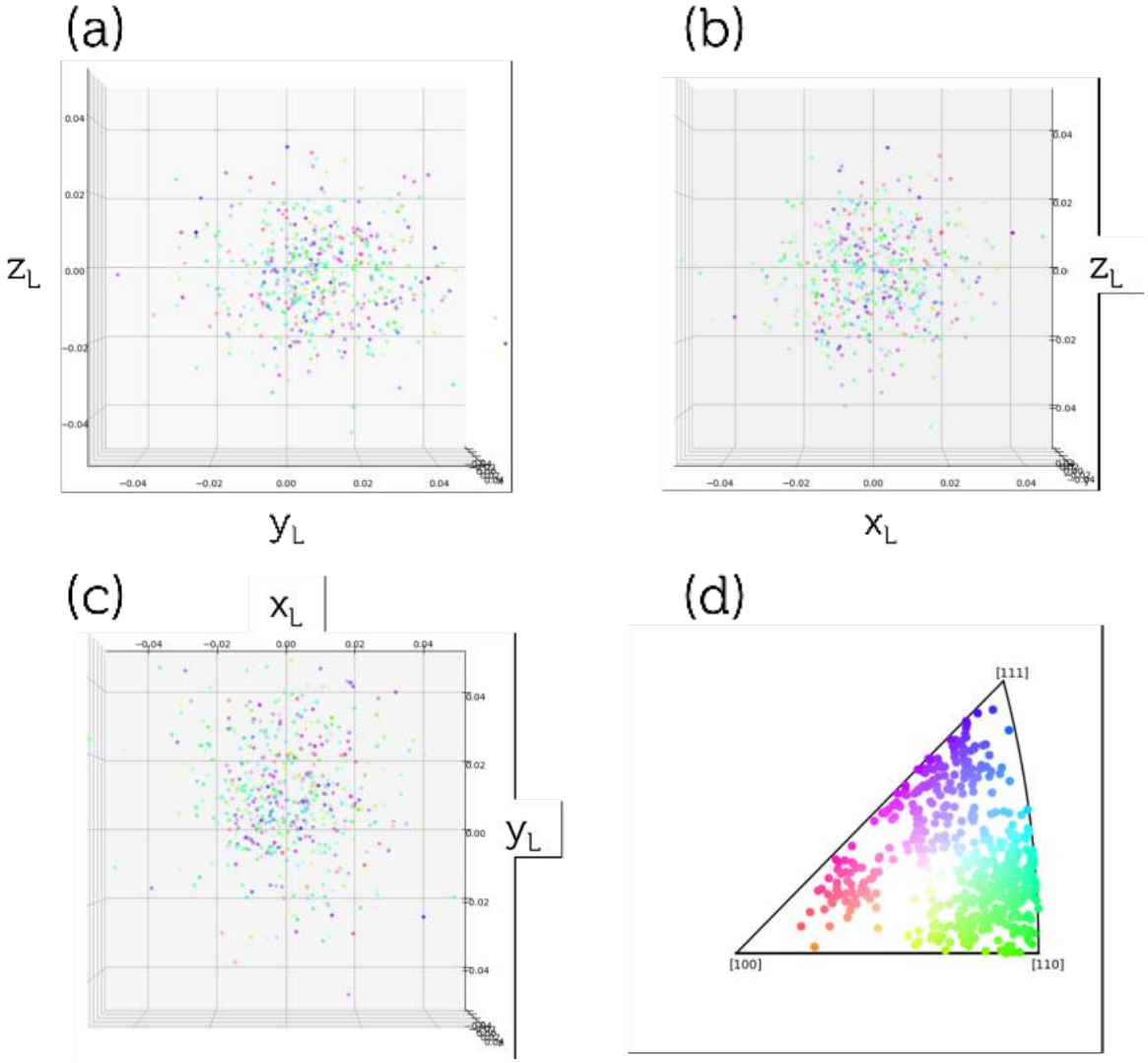

Figure 7.3: 3D CoM map of the indexed and refined grains from DESY Petra III P21.2 experiment, along (a) x_L, (b) y_L, (c) z_L directions and (d) corresponding inverse pole figure (IPF). All grains are represented with its respective IPF coloring. The determined orientations were rotated by $\pi/2$ in clockwise direction, for aligning the rolling direction to the coordinate axes given in Figure 5.7.

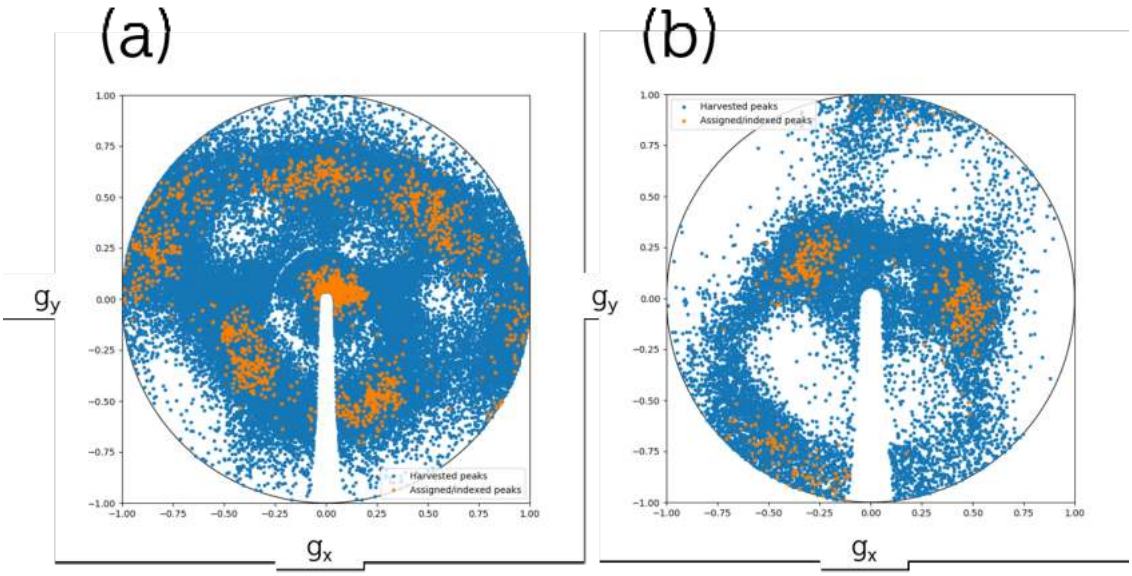

Figure 7.4: (a) 110 and (b) 200 pole figures of the harvested and indexed diffraction peaks, projected on z_L axis.

determined grains have similar orientations — between the $\langle 100 \rangle$ and $\langle 111 \rangle$ directions. We should note that the reported EBSD map in Figure 5.7(c) had shown a depressed number of orientations around the vicinity of $\langle 110 \rangle$ portion of the IPF. Whereas, the partial 3D CoM map derived with HR-3DXRD has shown that such particular orientations are present in the gauge volume in a substantial amount.

The observation of unexpected number of orientations around the $\langle 110 \rangle$ direction could be explained with two different reasoning. Firstly, one should recall that EBSD is a surface sensitive technique, with typical electron penetration depths of few hundreds of nanometers [143]. Therefore, the 2D EBSD map given in Figure 5.7(c) should be inspected with caution, as it does not provide enough statistics about the bulk distribution of the present orientations. In this regard, we can hypothesize that the experimentally chosen gauge volume could be selected from a region, in which the grains are oriented towards the $\langle 110 \rangle$ direction.

The observed discrepancy could also be attributed to the attained quality level from the indexing and refinement procedures with the mentioned altered analysis pipeline. As explained above, the grains were determined through considering only the lowest multiplicity diffraction ring, and the refinement was done with the complete set of harvested peaks. Thus, the motivation behind the devised altered analysis pipeline was to an abundant number of trial orientations with loose statistics, which were expected to get successively refined and also, eliminate the ”false-positive” results. During the processing of the presented refinement results, the elimination of these ”false-positive” orientations was observed to show less robustness than our expectation. Yet, we should note that the ”green”-colored grains had shown comparable statistics with respect to the rest of the identified grains, implying an absence of systematic errors in refinement stage.

We should note that, the experience on *makemap* refinement scheme [111] is known to perform better, if the true number of orientations get indexed from the pool of harvested diffraction peaks. Hence, the discussion made above should be taken as an intermediate assessment of the presented partial analysis of HR-3DXRD dataset. We foresee that with

the complete analysis via indexing the (expected) complete set of grains in the gauge volume, the statistics of the presented results would improve drastically.

Figure 7.4 shows the derived 110 and 200 pole figures from the harvested and indexed diffraction peaks. The figure clearly reveals the innate texture of the analyzed sample in both 110 and 200 directions. The given figure further shows that the texture of the indexed peaks agrees well with the texture of the complete set of harvested peaks. This indicates that the indexed (sub)grains are statistically representative of the (sub)grain population in the gauge volume. Such statistical representation can be seen as a validation of the altered analysis pipeline, suggesting enough confidence that further indexing and refinement cycles would allow indexing of more (sub)grains. At this point, however, it is impossible to comment on the level of completeness that indexing can be reached in the adopted analysis approach.

Lastly, we should note that due to the partial nature of the identified grain ensemble, the volume of the identified (sub)grains (and therefore, its equivalent spherical diameter) can not be calculated. The volume determination procedure (explained in Section 4.1.5) assumes that the obtained 3D CoM is space-filling. Hence, due to the partial nature of the presented analysis, we cannot comment on the size of the identified grains. Similarly, the obtained partial 3D CoM map could not be visualized through means of tessellation, due to the same reasoning. The analysis presented in this chapter is still on-going, and its final results will be reported elsewhere.

8 Conclusions and outlook

8.1 Conclusions

X-ray diffraction based imaging is typically performed in the near-field or far-field limit, for enhanced spatial and angular resolution, respectively. In this thesis, I introduce diffraction imaging in an intermediate field, corresponding to Fresnel numbers around ≈ 1. For science cases involving $1\,\mu$m-sized grains, I argue that imaging in this regime can provide 3D center-of-mass maps with up to ten times better spatial and angular resolution than classical far-field imaging. This insight also is relevant beyond metallic microstructures, e.g. for the 3D visualisation of solar cell materials and nano-crystalline grain ensembles.

Realising this potential for 3D microstructure mapping implies enlarging the ratio between field of view (FoV) and spatial resolution of a (compound) 2D detector. Establishing such a method vastly improves options for multiscale imaging. This again is of generic interest to hierarchically organised crystalline materials. As an example, the proposed set-up is very relevant for *in situ* studies of recrystallisation.

In this thesis, I specifically investigate the potential for generalising 3DXRD in this way and for using the resulting new modality HR-3DXRD for mapping plastically deformed metal microstructures in 3D and at the subgrain level. For simplicity, mapping of elastic strains was not included in the project, although this aspect is one motivation factor for establishing the method. As there are no existing set-ups optimised for this type of work, the feasibility of the HR-3DXRD technique has been studied by a combination of full-scale numerical simulations and exploratory tests at existing grain-mapping beamlines.

The numerical study focused on establishing an indexing procedure — if possible — and revealing the intrinsic limitations of HR-3DXRD for the case of a perfectly aligned and calibrated instrument. For two phantoms, representative of a deformation-induced intragranular structure consisting of subgrains delineated by geometrically necessary boundaries (GNBs) in medium-to-high γ_{SFE} metals, I found that an existing far-field indexing method, GrainSpotter, could be adapted to generate high quality CoM maps that can be extrapolated to generate space-filling 3D maps with tessellation methods. Following additional refinement, the simulations revealed that 3D mapping of deformation microstructures comprising ≈ 1000 subgrains is feasible. The proof-of-concept simulations on Phantom B showed mean spatial and angular resolutions of $0.1\,\mu$m and $5 \times 10^{-4}\,^{\circ}$, respectively.

A systematic study of various error sources revealed that errors due to alignment (e.g. detector tilt) are manageable at a dedicated instrument. The two central limitations encountered in the simulation work are the spot density on the detector and signal-to-noise (S/N) issues. Following the previous work on FF-3DXRD [119], the indexing algorithm demands a maximum spot overlap of 10%. In regard to the S/N study, the simulations show that all diffraction spots with an intensity above threshold will be associated within acceptable errors on their center-of-mass positions.

The most obvious experimental challenge is the construction of the large FoV compound image. The classical detector calibration of using reference powders failed for S/N reasons. Instead, I investigated two approaches for using the HR-3DXRD data acquired from the actual measurement for aligning and calibrating the individual detector positions. In

the first approach, individual detector positions are registered and stitched together using image processing tools — this solution implicitly assumes all panels to lie in the same plane and in particular to have the same tilts. Using experimental data from the DESY Petra III P21.2 experiment, involving 17 detector positions, the average uncertainty on spot position is in this case estimated to be better than 1 pixel. This is within the specifications required for HR-3DXRD as determined in my simulations. The second approach, based on pyFAI software package, involved successive optimisation of both tilts and positions for each detector position through means of simultaneous multi-panel detector calibration. I applied this method to the same dataset and obtained discrepant results for different detector positions. I speculate that the innate issues of the dataset hindered derivation of global parameters with sufficient precision with respect to the first approach.

The experimental proof-of-concept of HR-3DXRD, turned out to be challenging. The experiments at the four different grain-mapping beamlines all suffered from the fact that the beamline set-ups were not optimised to HR-3DXRD and had to altered in an *ad hoc* fashion that varied from beamline to beamline. This is at odds with the tolerances required for HR-3DXRD being tighter than for conventional 3DXRD. Suitable calibrants and spatial distortion corrections were missing. Progress on data analysis was also hampered by the lack of software for the registration/calibration of the compound image — the mentioned solution was established late in the PhD study.

The experiments were performed on samples of varying microstructures, representing differences in mean grain size, number of phases, deformation and heat treatment history and associated differences in local texture, spot density etc. The four beamtimes have provided a wealth of information on best practice, in relation to instrumentation, data analysis procedure, calibration as well as how the microstructure effect the feasibility of HR-3DXRD.

The applicability of multi-panel acquisition HR-3DXRD has been shown with adopting the image registration and stitching approach as the pre-processing tool. I have applied the proposed experimental analysis pipeline to the mentioned DESY Petra III P21.2 dataset and determined 497 grains with 0.476 completeness. The complete analysis of the dataset is not presented due to time limitations of the PhD project.

In conclusion, in this thesis I have shown the feasibility of a *high resolution* modality for 3DXRD microscopy technique through a set of numerical simulations and experimental demonstrations. The current limitations of this HR-3DXRD technique can be listed as the unavailability of large FoV imaging detectors, the maximum number of observed subgrains — due to possible spot overlap — and the absence of a dedicated and optimized experimental configuration with known detector calibration and distortion, optimized stability characterized at the sub-μm level. I should state that neither of these limitations are fundamental. One can foresee that remedies regarding these limitations will be addressed in the near future, e.g. especially large FoV high resolution imaging detectors.

8.2 Outlook

The proposed HR-3DXRD technique shows unprecedented potential not only for the visualization of deformation microstructures, but also for 3D mapping of sub-micrometer sized grains. In this last section of the thesis, I will discuss the potential improvements for HR-3DXRD, the experimental ideas that could not be realized during the PhD project and some future recommendations.

Although the experimental realization of HR-3DXRD was not completed during the PhD project, the HR-3DXRD project will be continued in a post-doctoral study by the candi-

date. The project called “Predicting **W**hy, **W**here and **W**hen metals fail (Triple-W)” will utilize HR-3DXRD for studying the fundamental mechanisms for ductile failure of metals. Ductile failure is mediated by the formation of voids in the microstructure [17]. With increasing deformation, the multiple voids nucleate and coalesce in regions of high stress concentration. The presence of the voids further increase the local stress concentration, therefore leading to the occurrence of complex stress states in a uniaxial testing scheme. Further coalescence of the voids may increase the local stress concentration above a critical level, hence leading to catastrophic failure. The main objective of the project is to investigate the interaction between the intragranular substructure with the so-called *voids*.

The work presented in the thesis had relied on existing single phase multigrain indexing algorithms, such as GrainSpotter [59] and ImageD11 [111]. These codes are designed specifically for Mode-II FF-3DXRD operation, in which strain and positional degrees of freedom can be treated as perturbations on the diffraction spot position. Therefore, one can perform indexing primarily based on grain orientation, and then derive the associated strain and position in a subsequent “refinement” step. The natural next step for the HR-3DXRD data analysis chain is the exploration of the limits for determination of finite elastic strain. In regard to the simulated phantoms, we assume that strain values of 10^{-3} should be feasible for HR-3DXRD operation. For larger elastic strains, one may consider the grains to belong to different (un-strained) phases instead. Hence, we propose to replace the adopted indexing software, GrainSpotter, with a multi-phase multigrain indexing algorithm. An example of such an algorithm is presented in [119]. We expect that the remainder of the data analysis chain would be the same.

In Chapter 3, I have derived the HR-3DXRD concept with respect to the properties and scattering characteristics of the deformation microstructures. Furthermore in Section 4.4, I have successfully validated the HR-3DXRD technique with a series of randomly oriented phantoms with μm-to-sub-μm grain sizes. These numerical studies imply an extended generalization of HR-3DXRD beside the deformation microstructure imaging to 3DXRD mapping grain ensembles with sub-μm grain sizes. In other words, the detector pixel size and sample-to-detector distance of the HR-3DXRD setup can be adjusted to account for grain ensembles in with sub-μm regime. This approach may provide a useful tool for characterization of a variety of microstructures. For example, HR-3DXRD can be used to track the sintering reactions in novel nanocrystalline bioceramics via in situ heating experiments. In a similar sense, HR-3DXRD may be used for studying the grain growth in additive manufacturing (AM) parts. AM processing is known to produce microstructures with sub-μm grain sizes. In an in-situ AM experiment, the evolution of the grain properties in each processing step can be visualized with 3D CoM maps with HR-3DXRD.

The HR-3DXRD experiment can be improved in several different ways. These can be listed as follows:

- **Improving the collection efficiency of experimental data**: The current experimental data collection scheme of HR-3DXRD chooses a 2θ range for covering multiple Debye-Scherrer rings. Then, the complete η-range is scanned in multiple panels of HR-3DXRD scans. For microstructures of high local texture, this approach was observed to be rather inefficient, as the diffraction images from certain diffraction angles may comprise little-to-no diffraction signal. The efficiency of the HR-3DXRD scans can be increased with a fast pre-FF 3DXRD scanning. This pre-scan can be used to determine the η and ω distribution of the diffraction signal and therefore, can be used to constraint the ranges and extents of HR-3DXRD scans. In case of substantially high texture, the pre-scan may provide invaluable information for de-

termining the panel positions. Such approach may decrease the overall acquisition time quite drastically.

- **Scanning half range in η and full range in ω**: NF-3DXRD techniques are known to be performed by letting the upper half of the Debye-Scherrer rings on the detector frame and scanning the full 2π range in ω-direction. With this approach the complete pole figure of the sample can be obtained through observation of the Friedel pairs. This idea can be extended to HR-3DXRD scanning, as well. Referring to Equation (3.2), the number of panels needed for such HR-3DXRD scan would be

$$N'_{\text{detector}} \geq (\frac{2\pi}{2})/\Delta\eta = \pi/\Delta\eta. \tag{8.1}$$

  Therefore, considering the default full range ω-rotation, the acquisition speed of HR-3DXRD scan can improve by 2, as the number of panels are decreased by half.

- **Ray tracing from FF to HR-3DXRD**: A grain size distribution with an average value of $\approx 1\ \mu$m would imply the presence of low population of larger grains (i.e. $\approx 2-5\ \mu$m) in the microstructure. These relatively larger grains may be big enough to be identified by FF-3DXRD, as well as HR-3DXRD. Thus, in a HR-3DXRD experiment, one can collect an extra FF-3DXRD scan and identify these large grains. Then, after determining the properties of these grains, their diffraction spots may be propagated back to the HR-3DXRD detector frame by simple ray tracing. The indexed FF-information traced back to the HR-3DXRD frame may be used for refining the local global parameters of individual panels in a multi-parameter minimization scheme.

- **Analysis by forward modelling approach**: Unlike the proposed analysis scheme given in Section 5.3, HR-3DXRD analysis could also be performed with a HEDM-type forward modelling approach. This would result in a Mode-II type CoM maps, but may also provide determination of grain orientation envelopes (GOEs) [85] of the indexed orientations. Considering an in situ deformation experiment, the GOE derivation would provide a better definition of the possible rotational movement of the indexed orientations. However, we foresee that the approach given in [84] may not be suitable for HR-3DXRD, as the possible complementation with NF-3DXRD methods would be compromised by diffraction spot overlap. Furthermore, such analysis could result in redundant information, as the interior microstructure of subgrains are known to be free of crystal defects, therefore, it is expected to be mostly free from orientation variations.

In Chapter 5, all experiments were explained as purely proof-of-concept studies for HR-3DXRD. However, we would like to mention that in the ESRF ID06 experiment (Section 5.2.2) this does not reflect the actuality. In fact, this experiment was designed and performed as an in-situ multi-modal microscopy experiment for observing the boundary motion between a recrystallized and a deformed grain with HR-3DXRD, *RSM* and *DFXM*. The goal was to acquire an experimental movie of the growth of the recrystallized grain by consumption of the deformed grain with different techniques. In order to perform this experiment, a recrystallized grain-deformed grain pair was found in the sample. The boundary is aligned to the center-of-rotation of the goniometer by translating the real space image of the recrystallized grain with DFXM. Then, the motion of the pair was devised to be tracked with multi-modal microscopy; the deformed grain was mapped with HR-3DXRD, whereas the recrystallized grain was mapped with RSM and DFXM. We should further note that combination of HR-3DXRD and DFXM requires quite tedious experimentation and non-trivial alignment challenges. The current development in the beamline control software and advanced alignment procedures are expected to diminish this complexity.

The data analysis of the multi-modal microscopy experiment is still undergoing and it is planned to be finish after the completion of the PhD project.

The multi-modal microscopy procedure proposed a great potential for visualization of deformation microstructures. Considering the large gamut of X-ray microscopy techniques, the microstructure evolution during a deformation process (e.g. in situ uniaxial testing, 4-point bending, cyclic loading, etc.) can be mapped with a combination of these techniques for resolving different properties. An ideal multi-modal X-ray microscopy experiment could start by obtaining bright field tomograms of the unloaded sample, for determining the presence and volume fraction possible e.g. crystallographic phases, microstructural features such as voids. The unloaded sample can be further characterized by NF and/or FF-3DXRD microscopy methods. The combination of these 3D maps for the unloaded state may be used for determining a regions-of-interest (ROI) in the sample for further analysis during the in situ mechanical testing. During each interrupted loading step, grain averaged properties of the ROI can be mapped with NF and FF-3DXRD. Then, zoom-in maps of specific regions in the ROI can be further studied with HR-3DXRD and/or DFXM. With increasing deformation levels, NF-3DXRD technique would start to fail owing to increased probability of diffraction spot overlap. Then, the mapping procedure could be adjusted for replacing NF-3DXRD with HR-3DXRD, at the expense of depressed FoV. Similarly, at extremely large deformation levels ($\varepsilon \gg \approx 2.0 - 3.0$), the zoom-in scans with DFXM may be replaced with RSM, as well.

Lastly, the emergence of the fourth generation X-ray sources pose a great potential for materials science research. These new sources, such as ESRF-Extremely Brilliant Source, APS-II, Petra IV, MAX IV, offer few orders-of-magnitude brilliant and coherent X-ray beams with substantially lower emittance. HR-3DXRD microscopy, but also X-ray microscopy techniques in general, is expected to benefit from the increased X-ray flux by optimizing the S/N ratio of the acquired maps. Furthermore, the decreased beam divergence would lead to a decrease in the FWHM of the observed diffraction spots (see Equation (3.1)), which will improve the accuracy of determined diffraction spot positions. We may further expect to observe a positive improvement on the diffraction spot overlap issue with the depressed beam divergence.

The main question about grasping the full potential of the fourth generation sources is the need of efficient and fast detection instruments. The discussion in Section 5.5 tells that the performed HR-3DXRD microscopy experiments got limited from low S/N levels due to low X-ray flux and efficiency issues of high resolution imaging detectors. Regarding HR-3DXRD, the introduction of the new sources can be seen to remedy the S/N problem with their increased brilliance. Yet, the experience have shown that the detector efficiency is the current limiting factor of HR-3DXRD technique. In Section 3.3, we have also shown that new generation detectors provide better signal detection at reasonable acquisition times. Therefore, we can project the acquisition times of HR-3DXRD in a fourth generation synchrotron with a new generation detector to decrease from ≈ 1 s to few hundreds of a second.

Another demand of HR-3DXRD from the developing detector technology is the need of a high dynamic range. This can be exemplified with the ESRF ID06 experiment explained above: The experiment was designed to track a microstructure in which a strongly scattering grain, e.g. a recrystallized grain, and weakly scattering grains/crystallites, e.g. subgrain structures in deformed grains, co-exist as neighbours. The boundary between this neighbour pair was of the interest. In the diffraction images, the vicinity of recrystallized grain's diffraction spots will be dominated by its strongly intensity, obscuring the detection

of weakly scattering subgrains of similar orientations. Clearly, this analysis may lead to production of a partial grain map due to these missed reflections. An improvement in the detector's dynamic range may remedy such problems.

An ideal detector to be utilized for HR-3DXRD would have sub-μm sized pixels over an active area of $1 - 2$ cm, with low fluctuating background, high collection efficiency and high dynamic range. Over these five requirements, we foresee that development of a large active area detector with small and efficient pixels may occur in a moderately distant future. Besides the active area requirement, the modern detectors have already started to fulfill the ideal condition. Therefore, the data collection efficiency of HR-3DXRD technique is bound to improve in parallel with the developments in the X-ray detection technology.

Bibliography

1. Poulsen, H., Margulies, L., Schmidt, S. & Winther, G. Lattice rotations of individual bulk grains. *Acta Mater.* **51,** 3821–3830. ISSN: 13596454 (2003).
2. Oddershede, J., Wright, J., Beaudoin, A. & Winther, G. Deformation-induced orientation spread in individual bulk grains of an interstitial-free steel. *Acta Mater.* **85,** 301–313. ISSN: 1359-6454 (2015).
3. Miller, M. P., Pagan, D. C., Beaudoin, A. J., Nygren, K. E. & Shadle, D. J. Understanding Micromechanical Material Behavior Using Synchrotron X-rays and In Situ Loading. *Metall. Mat. Trans. A* (2020).
4. Gundlach, C. *et al.* Direct observation of subgrain evolution during recovery of cold-rolled aluminium. *Scr. Mater.* **50,** 477–481. ISSN: 13596462 (2004).
5. Ahl, S., Simons, H., Detlefs, C., Juul Jensen, D. & Poulsen, H. F. Subgrain dynamics during recovery of partly recrystallized aluminium. *Acta Mater.* **185,** 142–148 (2020).
6. Warren, B. E. *X-ray Diffraction* Reprint Ed, 402. ISBN: 0486663175 (Dover Publications, 1990).
7. Guinier, A. *X-ray Diffraction in Crystals, Imperfect Crystals, and Amorphous Bodies* 400. ISBN: 0486141349 (Dover Publications, 1994).
8. Als-Nielsen, J. & McMorrow, D. *Elements of Modern X-Ray Physics* 319. ISBN: 0471498580 (2001).
9. Willmott, P. *An Introduction to Synchrotron Radiation* ISBN: 9781119970958 (John Wiley & Sons, Ltd, Chichester, UK, 2011).
10. Hansen, N. & Barlow, C. in *Physical Metallurgy* (eds Laughlin, D. & Hono, K.) 5th edition, 1681–1765 (Elsevier B.V., Amsterdam, 2014). ISBN: 978-0-444-59597-3.
11. *Glossary of TEM Terms, JEOL* https://www.jeol.co.jp/en/words/emterms/search%7B%5C_%7Dresult.html?keyword=dislocation (2020).
12. Weertman, J. & Weertman, J. *Elementary Dislocation Theory* 213 (Macmillan, New York, 1967).
13. Hull, D. & Bacon, D. *Introduction to Dislocations* 272. ISBN: 978-0-08-096672-4 (Elsevier, Butterworth-Heinemann, 2011).
14. Humphreys, F. & Hatherly, M. *Recrystallization And Related Annealing Phenomena* 2nd (Elsevier BV, 2004).
15. Porter, D. & Easterling, K. *Phase Transformations in Metals and Alloys* Third Edition, 520. ISBN: 0412450305 (2014).
16. Hansen, N. New discoveries in deformed metals. *Metallurgical & Materials Trans. A* **32,** 2917–2935 (2001).
17. Dieter, G. *Mechanical Metallurgy* 3rd Edition, 751. ISBN: 0071004068 (McGraw-Hill, 1988).
18. Huang, X. & Winther, G. Dislocation structures. Part I. Grain orientation dependence. *Phil. Mag.* **87,** 5189–5214 (2007).
19. Sumino, K. & Imai, M. Interaction of dislocations with impurities in silicon crystals studied by in situ X-ray topography. *Philos. Mag. A Phys. Condens. Matter, Struct. Defects Mech. Prop.* **47,** 753–766. ISSN: 01418610 (1983).
20. Ahmad, S. & Whitworth, R. W. Dislocation motion in ice: A study by synchrotron X-ray topography. *Philos. Mag. A Phys. Condens. Matter, Struct. Defects Mech. Prop.* **57,** 749–766. ISSN: 01418610 (1988).

21. Wilkens, M. APPLICATION OF X-RAY TOPOGRAPHY TO THE ANALYSIS OF THE DISLOCATION ARRANGEMENT IN DEFORMED COPPER SINGLE CRYSTALS. *Can. J. Phys.* **45,** 567–579. ISSN: 0008-4204 (1967).
22. Dudley, M. *et al.* White-beam synchrotron topographic studies of defects in 6h-sic single crystals. *J. Phys. D. Appl. Phys.* **28,** A63–A68. ISSN: 13616463 (1995).
23. Collingwood, J. F. & Adams, F. Chemical imaging analysis of the brain with X-ray methods. *Spectrochim. Acta Part B At. Spectrosc.* **130,** 101–118. ISSN: 05848547 (2017).
24. Wang, J. *et al. 3D chemical and elemental imaging by STXM spectrotomography* in *AIP Conf. Proc.* **1365** (American Institute of Physics, 2010), 215–218. ISBN: 9780735409255.
25. Baruchel, J., Buffière, J. Y., Maire, E., Merle, P. & Peix, G. *X-Ray Tomography in Material Science* (Hermes Science Publications, Cachan cedex, France, 2000).
26. Busing, W. R. & Levy, H. A. Angle calculations for 3- and 4-circle X-ray and neutron diffractometers. *Acta Crystallogr.* **22,** 457–464. ISSN: 0365110X (1967).
27. Poulsen, H. *Three Dimensional X-Ray Diffraction Microscopy* (Springer Verlag, 2004).
28. Bernier, J. V., Suter, R. M., Rollett, A. D. & Almer, J. D. High-Energy X-Ray Diffraction Microscopy in Materials Science. *Annu. Rev. Mater. Res.* **50,** 395–436. ISSN: 1531-7331 (2020).
29. Engler, O. & Randle, V. *Introduction to Texture Analysis* ISBN: 9780429191909 (CRC Press, 2009).
30. Bernier, J. V., Barton, N. R., Lienert, U. & Miller, M. P. Far-field high-energy diffraction microscopy: A tool for intergranular orientation and strain analysis. *J. Strain Anal. Eng. Des.* **46,** 527–547 (2011).
31. Ashiotis, G. *et al.* The fast azimuthal integration Python library: pyFAI. *J. Appl. Crystallogr.* **48,** 510–519. ISSN: 1600-5767 (2015).
32. Paganin, D. *Coherent X-Ray Optics* ISBN: 9780198567288 (Oxford University Press, Jan. 2006).
33. Poulsen, H. An introduction to three-dimensional X-ray diffraction microscopy. *J. Appl. Cryst.* **45,** 1084–1097 (2012).
34. Williams, D. B. & Carter, C. B. *Transmission Electron Microscopy: A Textbook for Materials Science* Second Edition, 760. ISBN: 9780387765006 (Springer Science+Business Media, 2009).
35. Poulsen, H. Multi scale hard x-ray microscopy. *Curr. Opin. Solid State Mater. Sci.* **24,** 100820. ISSN: 1359-0286 (Apr. 2020).
36. Ludwig, W. *et al.* Three-dimensional grain mapping by x-ray diffraction contrast tomography and the use of Friedel pairs in diffraction data analysis. *Rev. Sci. Instrum.* **80,** 033905. ISSN: 0034-6748 (2009).
37. Li, S. F. & Suter, R. M. Adaptive reconstruction method for three-dimensional orientation imaging. *Journal of Applied Crystallography* **46,** 512–524 (2013).
38. Ludwig, W., Schmidt, S., Lauridsen, E. M. & Poulsen, H. F. X-ray diffraction contrast tomography: a novel technique for three-dimensional grain mapping of polycrystals. I. Direct beam case. *J. Appl. Crystallogr.* **41,** 302–309. ISSN: 0021-8898 (2008).
39. Johnson, G., King, A., Honnicke, M. G., Marrow, J. & Ludwig, W. X-ray diffraction contrast tomography: A novel technique for three-dimensional grain mapping of polycrystals. II. The combined case. *Journal of Applied Crystallography* **41,** 310–318. ISSN: 00218898 (2 2008).
40. Viganò, N. *et al.* Three-dimensional full-field X-ray orientation microscopy. *Sci. Rep.* **6,** 20618. ISSN: 2045-2322 (2016).

41. Renversade, L. *et al.* Comparison between diffraction contrast tomography and high-energy diffraction microscopy on a slightly deformed aluminium alloy. *IUCrJ* **3,** 32–42. ISSN: 2052-2525 (2016).
42. King, A., Reischig, P., Adrien, J. & Ludwig, W. First laboratory X-ray diffraction contrast tomography for grain mapping of polycrystals. *J. Appl. Crystallogr.* **46,** 1734–1740. ISSN: 00218898 (2013).
43. Van Aarle, W., Ludwig, W., King, A. & Penumadu, D. An accurate projection model for diffraction image formation and inversion using a polychromatic cone beam. *J. Appl. Crystallogr.* **48,** 334–343. ISSN: 16005767 (2015).
44. McDonald, S. A. *et al.* Non-destructive mapping of grain orientations in 3D by laboratory X-ray microscopy. *Sci. Rep.* **5,** 14665. ISSN: 20452322 (2015).
45. Peetermans, S., King, A., Ludwig, W., Reischig, P. & Lehmann, E. H. Cold neutron diffraction contrast tomography of polycrystalline material. *Analyst* **139,** 5765–5771. ISSN: 13645528 (2014).
46. Cereser, A. *et al.* Time-of-Flight Three Dimensional Neutron Diffraction in Transmission Mode for Mapping Crystal Grain Structures. *Sci. Rep.* **7,** 9561. ISSN: 2045-2322 (2017).
47. Li, S. F. *et al.* Three-dimensional plastic response in polycrystalline copper via near-field high-energy X-ray diffraction microscopy. *J. Appl. Crystallogr.* **45,** 1098–1108. ISSN: 0021-8898 (2012).
48. Pokharel, R. *et al.* In-situ observation of bulk 3D grain evolution during plastic deformation in polycrystalline Cu. *Int. J. Plast* **67,** 217–234 (2015).
49. 3-D growth of a short fatigue crack within a polycrystalline microstructure studied using combined diffraction and phase-contrast X-ray tomography. *Acta Mater.* **59,** 590–601. ISSN: 13596454 (2011).
50. King, A. *et al.* Three-dimensional in situ observations of short fatigue crack growth in magnesium. *Acta Mater.* **59,** 6761–6771. ISSN: 13596454 (2011).
51. Gonzalez, D. *et al.* Three-dimensional observation and image-based modelling of thermal strains in polycrystalline alumina. *Acta Mater.* **61,** 7521–7533. ISSN: 13596454 (2013).
52. Zhang, J. *et al.* Three-dimensional grain growth in pure iron. Part I. statistics on the grain level. *Acta Mater.* **156,** 76–85 (2018).
53. Menasche, D. B., Shade, P. A. & Suter, R. M. Accuracy and precision of near-field high-energy diffraction microscopy forward-model-based microstructure reconstructions. *J. Appl. Crystallogr.* **53,** 107–116. ISSN: 1600-5767 (2020).
54. Hefferan, C. M. *et al.* Statistics of High Purity Nickel Microstructure From High Energy X-ray Diffraction Microscopy. *C. Comput. Mater. Contin.* **14,** 209–220 (2009).
55. Hefferan, C. M. *et al. Acta Mater.* **60,** 4311–4318 (2012).
56. Bhattacharya, A. *et al.* Three-dimensional observations of grain volume changes during annealing of polycrystalline Ni. *Acta Mater.* **167,** 40–50. ISSN: 13596454 (2019).
57. Oddershede, J. *et al.* Determining grain resolved stresses in polycrystalline materials using three-dimensional X-ray diffraction. *J. Appl. Cryst.* **43,** 539–549 (2010).
58. Pokharel, R. in *Mater. Discov. Des.* 167–201 (Springer, Cham, 2018).
59. Schmidt, S. GrainSpotter: a fast and robust polycrystalline indexing algorithm. *J. Appl. Cryst.* **47,** 276–284 (2014).
60. Nervo, L. *et al.* Comparison between a near-field and a far-field indexing approach for characterization of a polycrystalline sample volume containing more than 1500 grains. *J. Appl. Crystallogr.* **47,** 1402–1416. ISSN: 1600-5767 (2014).

61. Pagan, D. C. *et al.* Modeling slip system strength evolution in Ti-7Al informed by in-situ grain stress measurements. *Acta Mater.* **128,** 406–417. ISSN: 13596454 (2017).
62. Pagan, D. C. *et al.* Measuring Ti-7Al slip system strengths at elevated temperature using high-energy X-ray diffraction. *Scr. Mater.* **142,** 96–100. ISSN: 13596462 (2018).
63. Lauridsen, E., Poulsen, H., Nielsen, S. & Jensen, D. J. Recrystallization kinetics of individual bulk grains in 90% cold-rolled aluminium. *Acta Mater.* **51,** 4423–4435 (2003).
64. Poulsen, S. O. *et al.* In situ measurements of growth rates and grain-averaged activation energies of individual grains during recrystallization of 50% cold-rolled aluminium. *Scr. Mater.* **64,** 1003–1006. ISSN: 13596462 (2011).
65. Oddershede, J. *et al.* Grain-resolved elastic strains in deformed copper measured by three-dimensional X-ray diffraction. *Mater. Charact.* **62,** 651–660. ISSN: 1044-5803 (2011).
66. Oddershede, J. *et al.* in *Strain Dislocation Gradients from Diffr.* (eds Rozaliya Barabash & Ice, G.) chapter 6, 254–279 (Imperial College Press, May 2014). ISBN: 9781908979636.
67. Lyckegaard, A., Lauridsen, E., Ludwig, W., Fonda, R. & Poulsen., H. Generalized balanced power diagrams for 3D representations of polycrystals. *Adv. Eng. Mater.* **13,** 165–170 (2011).
68. Alpers, A., Brieden, A., Gritzmann, P., Lyckegaard, A. & Poulsen, H. F. Generalized balanced power diagrams for 3D representations of polycrystals. *Phil. Mag.* **95,** 1016–1028 (2015).
69. Schmidt, S. *et al.* Direct observation of 3-D grain growth in Al-0.1% Mn. *Scr. Mater.* **59,** 491–494. ISSN: 13596462 (2008).
70. Rodek, L., Poulsen, H. F., Knudsen, E. & Herman, G. T. A stochastic algorithm for reconstruction of grain maps of moderately deformed specimens based on X-ray diffraction. *J. Appl. Crystallogr.* **40,** 313–321. ISSN: 0021-8898 (2007).
71. Lienert, U., Ribárik, G., Ungár, T., Wejdemann, C. & Pantleon, W. High-Resolution Single-Grain Diffraction of Polycrystalline Materials. *Synchrotron Radiat. News* **30,** 35–40. ISSN: 0894-0886 (2017).
72. Jakobsen, B. *et al.* Formation and subdivision of deformation structures during plastic deformation. *Science* **312,** 889–92. ISSN: 1095-9203 (2006).
73. Jakobsen, B., Lienert, U., Almer, J., Poulsen, H. & Pantleon, W. Direct observation of strain in bulk subgrains and dislocation walls by high angular resolution three-dimensional X-ray diffraction. *Mater. Sci. Eng. A* **483-484,** 641–643. ISSN: 0921-5093 (2008).
74. Jakobsen, B., Poulsen, H. F., Lienert, U. & Pantleon, W. Direct determination of elastic strains and dislocation densities in individual subgrains in deformation structures. *Acta Mater.* **55,** 3421–3430. ISSN: 1359-6454 (2007).
75. Diederichs, A. M., Lienert, U. & Pantleon, W. *Monitoring microstructural evolution in-situ during cyclic loading with high-resolution reciprocal space mapping* in *IOP Conf. Ser. Mater. Sci. Eng.* **580** (Institute of Physics Publishing, 2019), 012004.
76. Hayashi, Y., Hirose, Y. & Seno, Y. Polycrystal orientation mapping using scanning three-dimensional X-ray diffraction microscopy. *J. Appl. Crystallogr.* **48,** 1094–1101. ISSN: 16005767 (2015).
77. Hektor, J. *et al.* Scanning 3DXRD Measurement of Grain Growth, Stress, and Formation of Cu6Sn5 around a Tin Whisker during Heat Treatment. *Materials* **12,** 446. ISSN: 1996-1944 (2019).

78. Hayashi, Y., Setoyama, D., Hirose, Y., Yoshida, T. & Kimura, H. Intragranular three-dimensional stress tensor fields in plastically deformed polycrystals. *Science* **366,** 1492–1496. ISSN: 1095-9203 (2019).
79. Henningsson, N. A., Hall, S. A., Wright, J. P. & Hektor, J. Reconstructing intragranular strain fields in polycrystalline materials from scanning 3DXRD data. *J. Appl. Crystallogr.* **53.** ISSN: 1600-5767 (2020).
80. Vaughan, G. B. M. *et al. The extension of ID11 for nanoscale and hierarchical characterization* in *Proc. Risø International Symp. Mater. Sci.* **31** (Risø National Laboratory, 2010), 457–476.
81. Schuren, J. C. *et al.* New opportunities for quantitative tracking of polycrystal responses in three dimensions. *Curr. Opin. Solid State Mater. Sci.* **19,** 235–244. ISSN: 13590286 (2015).
82. Juul, N. Y. *et al.* Elastic interaction between twins during tensile deformation of austenitic stainless steel. *Scr. Mater.* **120,** 1–4. ISSN: 13596462 (2016).
83. Turner, T. J. *et al.* Crystal Plasticity Model Validation Using Combined High-Energy Diffraction Microscopy Data for a Ti-7Al Specimen. *Metall. Mater. Trans. A Phys. Metall. Mater. Sci.* **48,** 627–647. ISSN: 10735623 (2017).
84. Nygren, K. E., Pagan, D. C., Bernier, J. V. & Miller, M. P. An algorithm for resolving intragranular orientation fields using coupled far-field and near-field high energy X-ray diffraction microscopy. *Mater. Charact.* **165,** 110366. ISSN: 1044-5803 (2020).
85. Nygren, K. E., Pagan, D. C. & Miller, M. P. Sub-grain orientation resolution during continuous loading using only far-field HEDM. *IOP Conf. Ser. Mater. Sci. Eng.* **580,** 012018. ISSN: 1757-899X (2019).
86. Reischig, P. & Ludwig, W. *Three-dimensional sub-grain mapping of elastic strain state and orientations in the bulk of polycrystals* in *40th Risø Int. Symp. Met. Microstruct. 2D, 3D 4D* (Risø, Denmark, 2019). https://hal.archives-ouvertes.fr/hal-02404435.
87. Sun, J., Yu, T., Xu, C., Ludwig, W. & Zhang, Y. 3D characterization of partially recrystallized Al using high resolution diffraction contrast tomography. *Scr. Mater.* **157,** 72–75. ISSN: 1359-6462 (2018).
88. Kutsal, M. *et al.* The ESRF dark-field x-ray microscope at ID06. *IOP Conf. Ser. Mater. Sci. Eng.* **580,** 012007. ISSN: 1757-899X (2019).
89. Simons, H. *et al.* Dark field x-ray microscopy for multiscale structural characterization. *Nat. Commun.* **6,** 6098 (2015).
90. Murray, K. T. *et al.* Multilayer Laue lenses at high X-ray energies: performance and applications. *Opt. Express* **27,** 7120 (2019).
91. Poulsen, H. F. *et al.* X-ray diffraction microscopy based on refractive optics. *J. Appl. Cryst.* **50,** 1441 (2017).
92. Simons, H., Jakobsen, A. C., Ahl, S. R., Detlefs, C. & Poulsen, H. F. Multiscale 3D characterization with dark-field x-ray microscopy. *MRS Bulletin* **41,** 454 (2016).
93. Ahl, S. *et al.* Ultra-low-angle boundary networks within recrystallizing grains. *Scripta Mater.* **139,** 87–91 (2017).
94. Simons, H. *et al.* Long-range symmetry breaking in embedded ferroelectrics. *Nat. Materials* **17,** 814–819 (2018).
95. Mavrikakis, N. *et al.* A multi-scale study of the interaction of Sn solutes with dislocations during static recovery in α-Fe. *Acta Materialia* **174,** 92–104 (2019).
96. Jakobsen, A. C. *et al.* Mapping of individual dislocations with dark-field X-ray microscopy. *J. Appl. Cryst.* **52,** 122 (2019).
97. Yildirim, C., Kutsal, M. & co-workers. *Dark field x-ray microscopy study of in-situ annealing of a highly deformed steel sample* in preparation. 2020.

98. Poulsen, H. F. *et al.* Reciprocal space mapping and strain scanning using X-ray diffraction microscopy. *J. Appl. Cryst.* **51,** 1428–1436 (2018).
99. Simons, H., Ahl, S. R., Poulsen, H. F. & Detlefs, C. Simulating and optimizing compound refractive lens-based X-ray microscopes. *J. Synchrotron Rad.* **24,** 392 (2017).
100. Larson, B. C., Yang, W., Ice, G. E., Budai, J. D. & Tischler, J. Z. *Nature* **415,** 887–890 (2002).
101. Zhang, Y. B. *et al.* Boundary migration in a 3D deformed microstructure inside an opaque sample. *Sci. Rep.* **7,** 1–8. ISSN: 20452322 (2017).
102. Zhou, B. *et al.* Study of the dislocation activity in a Mg–Y alloy by differential aperture X-ray microscopy. *Mater. Charact.* **156,** 109873. ISSN: 10445803 (2019).
103. Arnold, M. & Rossmann, E. *Crystallography of biological macromolecules* (eds Rossmann, M. G. & Arnold, E.) ISBN: 978-0-7923-6857-1 (International Union of Crystallography, Chester, England, 2006).
104. Poulsen, H. F. & Vaughan, G. B. M. *International Tables for Crystallography* (eds Gilmore, C. J., Kaduk, J. A. & Schenk, H.) 601–616. ISBN: 978-1-118-41628-0 (International Union of Crystallography, Chester, England, 2019).
105. Delannay, L., Mishin, O. V., Jensen, D. J. & Van Houtte, P. Quantitative analysis of grain subdivision in cold rolled aluminium. *Acta Mater.* **49,** 2441–2451. ISSN: 13596454 (2001).
106. Ehrenfest, P. Bemerkung über die angenäherte Gültigkeit der klassischen Mechanik innerhalb der Quantenmechanik. *Zeitschrift für Phys.* **45,** 455–457. ISSN: 14346001 (1927).
107. Detlefs, C. & Paganin, D. M. *Private communication.* (2021).
108. Lauridsen, E. M., Schmidt, S., Suter, R. M. & Poulsen, H. F. Tracking: a method for structural characterization of grains in powders or polycrystals. *J. Appl. Cryst.* **34,** 744–750 (2001).
109. Moscicki, M. *et al.* Friedel-pair based indexing method for characterization of single grains with hard X-rays. *Mater. Sci. Engineering A* **524,** 64–68 (2009).
110. Sørensen, H. O. 2008. https://sourceforge.net/p/fable/wiki/PolyXSim/.
111. Wright, J. *ImageD11 package* 2005. https://github.com/FABLE-3DXRD/ImageD11 (2019).
112. Lauridsen, E., Jensen, D. J., Poulsen, H. & Lienert, U. Kinetics of individual grains during recrystallization. *Scripta Mater.* **43,** 561–566 (2000).
113. Quey, R. *Neper: Polycrystal Generation and Meshing* version 3.5.0. Oct. 2019. http://neper.sourceforge.net.
114. Quey, R. & Renversade, L. Optimal polyhedral description of 3D polycrystals : Method and application to statistical and synchrotron X-ray diffraction data. *Comput. Methods Appl. Mech. Engrg* **330,** 308–333 (2018).
115. Menasche, D. *Error Analysis of near-field High Energy Diffraction Microscopy* PhD thesis (Carnegie Mellon University, 2016).
116. Wilkinson, A. J. & Britton, T. B. Strains, planes, and EBSD in materials science. *Mater. Today* **15,** 366–376 (2012).
117. Zaefferer, S., Wright, S. & Raabe, D. Three-Dimensional Orientation Microscopy in a Focused Ion Beam–Scanning Electron Microscope: A New Dimension of Microstructure Characterization. *Metall. Mater. Trans. A* **39,** 374–389. ISSN: 1073-5623 (2008).
118. Polonsky, A. T., Charpagne, M.-A., Echlin, M. P., Manjunath, B. & Pollock, T. M. Acquisition, Reconstruction and Curation of Multimodal 3D TriBeam Data. *Microsc. Microanal.* **25,** 354–355. ISSN: 1431-9276 (2019).

119. Sørensen, H. O. *et al.* Multigrain crystallography. *Z. Kristallogr.* **227,** 63–78 (2012).
120. Chang, H. *et al.* Advanced denoising for X-ray ptychography. *Opt. Express* **27,** 10395. ISSN: 1094-4087 (2019).
121. Coan, P. *et al.* Evaluation of imaging performance of a taper optics CCD 'FReLoN' camera designed for medical imaging. *J. Synchrotron Rad.* **13,** 260–270 (2006).
122. Peeters, B., Bacroiz, B., Teodosiu, C., van Houtte, P. & Aernoudt, E. Work-hardening/softening behavior of B.C.C. polycrystals during changing strain paths: II. TEM observations of dislocation sheets in an IF steel during two-stage stage strain paths and their representation in terms of dislocation densities. *Acta Materialia* **49,** 1621–1632 (2001).
123. Haldar, A., Huang, A., Leffers, T., Hansen, N. & Ray, R. Grain orientation dependence of microstructures in a warm rolled IF steel. *Acta Materialia* **54,** 5405–5418 (2004).
124. Quey, R., Dawson, P. R. & Barbe, F. Large-scale 3D random polycrystals for the finite element method : Generation , meshing and remeshing. *Comput. Methods Appl. Mech. Engrg* **200,** 1729–1745 (2018).
125. Liu, Q., Juul Jensen, D. & Hansen, N. Effect of grain orientation on deformation structure in cold-rolled polycrystalline aluminium. *Acta Mater.* **46,** 5819–5838 (1998).
126. Wani, I. S. *et al.* Ultrafine-Grained AlCoCrFeNi2.1 Eutectic High-Entropy Alloy. *Mater. Res. Lett.* **4,** 174–179. ISSN: 2166-3831 (2016).
127. Miracle, D. & Senkov, O. A critical review of high entropy alloys and related concepts. *Acta Mater.* **122,** 448–511. ISSN: 13596454 (2017).
128. Wani, I. S. *et al.* Tailoring nanostructures and mechanical properties of AlCoCrFeNi2.1eutectic high entropy alloy using thermo-mechanical processing. *Mater. Sci. Eng. A* **675,** 99–109. ISSN: 09215093 (2016).
129. Schmidt, S. *et al.* Watching the Growth of Bulk Grains During Recrystallization of Deformed Metals. *Science* **305,** 229–232 (2004).
130. Ahl, S. R. *Elements of a Method for Multiscale Characterization of Recrystallization in Deformed Metals* PhD Thesis (Technical University of Denmark, 2018).
131. Shade, P. A. *et al.* Fiducial marker application method for position alignment of in situ multimodal X-ray experiments and reconstructions. *J. Appl. Crystallogr.* **49,** 700–704. ISSN: 1600-5767 (2016).
132. Cottrell, A. H. & Bilby, B. A. Dislocation Theory of Yielding and Strain Ageing of Iron. *Proc. Phys. Soc. Sect. A* **62,** 49–62. ISSN: 0370-1298 (1949).
133. Gao, S., Chen, M., Joshi, M., Shibata, A. & Tsuji, N. Yielding behavior and its effect on uniform elongation in IF steel with various grain sizes. *J. Mater. Sci.* **49,** 6536–6542. ISSN: 0022-2461 (2014).
134. *Non-equilibrium Processing of Materials* (ed Suryanarayana, C.) ISBN: 0-08-042697-2 (Pergamon, 1999).
135. Gao, S. *et al.* Yielding Behavior and Its Effect on Uniform Elongation of Fine Grained IF Steel. *Mater. Trans.* **55,** 73–77. ISSN: 1345-9678 (2014).
136. Faust, C. L. *Method of electropolishing steel* 1944.
137. Vaughan, G. B. *et al.* X-ray transfocators: Focusing devices based on compound refractive lenses. *J. Synchrotron Radiat.* **18,** 125–133. ISSN: 09090495 (2011).
138. Labiche, J.-C. *et al.* The fast readout low noise camera as a versatile x-ray detector for time resolved dispersive extended x-ray absorpiton fine structure and diffraction studies of dynamic problems in materials science, chemistry, and catalysis. *Rev. Sci. Instrum.* **78,** 091301 (2007).
139. Snigirev, A. *et al.* High energy X-ray transfocator based on Al parabolic refractive lenses for focusing and collimation. *J. Phys. Conf. Ser.* **186,** 012073. ISSN: 1742-6596 (2009).

140. Oddershede, J. *Private communication.* (2021).
141. Preibisch, S., Saalfeld, S. & Tomancak, P. Globally optimal stitching of tiled 3D microscopic image acquisitions. *Bioinformatics* **25,** 1463–1465. ISSN: 13674803 (2009).
142. *Calibration of a 2 theta arm with a Pilatus 100k detector — pyFAI 0.18.0a0 documentation* https://pyfai.readthedocs.io/en/latest/usage/tutorial/Goniometer/Rotation-Pilatus100k/Multi120_Pilatus100k.html (2020).
143. *Electron Backscatter Diffraction in Materials Science* (eds Schwartz, A. J., Kumar, M., Adams, B. L. & Field, D. P.) ISBN: 978-0-387-88135-5 (Springer US, Boston, MA, 2009).
144. Bastiaans, M. J. Application of the Wigner distribution function to partially coherent light. *J. Opt. Soc. Am. A* **3,** 1227. ISSN: 1084-7529 (1986).

A Appendix A Linear motion of the centre-of-mass of a partially coherent beam

The following text describes the theoretical analysis of CoM position of diffracted electromagnetic beams along their propagation direction, through geometrical optics formalisms. The author would like to express his kindest gratitude to Carsten Detlefs of European Synchrotron Radiation Facility and David M. Paganin of Monash University for sharing the discussion below [107].

Although derived in terms of Fourier optics, the description of optical signals by a Wigner distribution function (WDF) closely resembles the ray concept in geometrical optics [144]. Here, we apply the WDF to look at the change of a beam's centre-of-mass as function of free-space propagation distance, d.

Let $F_z(x,u)$ be the WDF of a monochromatic, partially coherent beam at the position z along the optical axis [144]. Here x is a real-space position and u a transverse momentum or spatial frequency.

The intensity as function of position is given by [144]

$$I_z(x) = \int F_z(x,u)\,\mathrm{d}u. \tag{A.1}$$

For simplicity, we assume the intensity to be normalized, $\int I_z(x)\,\mathrm{d}x = 1$. We then define the centre-of-mass of the beam as the first-order moment of the intensity with respect to the position x,

$$\langle x \rangle_z = \int x I_z(x)\,\mathrm{d}x = \iint x F(x,u)\,\mathrm{d}u\,\mathrm{d}x. \tag{A.2}$$

For this integral to converge, the beam has to be spatially confined, i.e. $\lim_{x\to\pm\infty} xI(x) \to 0$.

The WDF after free-space propagation through a distance d is simply given by [144]

$$F_{z=d}(x,u) = F_{z=0}(x - du, u). \tag{A.3}$$

The corresponding centre-of-mass position is then,

$$\langle x \rangle_{z=d} = \iint x F_{z=d}(x,u)\,\mathrm{d}x\,\mathrm{d}u \tag{A.4}$$

$$= \iint x F_{z=0}(x-du,u)\,\mathrm{d}x\,\mathrm{d}u \tag{A.5}$$

$$= \iint (x'+du) F_{z=0}(x',u)\,\mathrm{d}x'\,\mathrm{d}u \tag{A.6}$$

$$= \underbrace{\iint x' F_{z=0}(x',u)\,\mathrm{d}x'\,\mathrm{d}u}_{\langle x \rangle_{z=0}} + d \underbrace{\iint u F_{z=0}(x',u)\,\mathrm{d}x'\,\mathrm{d}u}_{\langle u \rangle} \tag{A.7}$$

$$= \langle x \rangle_{z=0} + d \langle u \rangle . \tag{A.8}$$

We identify the first moment of the WDF with respect to the transverse momentum, $\langle u \rangle = \iint u F(x,u)\,\mathrm{d}x\,\mathrm{d}u$, as the average beam direction. From its definition and Eq. A.3 it is clear that this does depend on the propagation distance d.

We have thus shown that the centre-of-mass of the intensity travels in a straight line, for all distances d — the WDF is equally valid for the near-, mid- and far-field regimes, as well as for fully and partially coherent beams.

Note that the calculations remain equally valid when x and u describe two transverse coordinates. The same result can be obtained from the Helmholtz equations of Fourier optics, which are equivalent to the Schrödinger equation [106].

B Appendix B Simulation analysis script peakpurity.py

This code can be reached in the “Scripts” section of the following URL: https://github.com/mkutsal/hr-3dxrd.

```
###############################################################################
### A script for checking the purity of peaks in peak lists
### with respect to a provided reference (e.g. PolyXSim output)
###
### The input requires a GFF file NOT a UBI or MAP file. You can use
### the polyxsim output gff file.
###
### M. Kutsal
### v0.1, April 2020
### DTU Physics & ESRF ID06-HXRM
###############################################################################

from __future__ import absolute_import
from __future__ import print_function
import numpy as np
from ImageD11.columnfile import columnfile as cl
import ImageD11.columnfile as cl2
from ImageD11 import transformer
from sys import exit,argv
import time

start_time = time.time()

###############################################################################
## Inputs
###############################################################################
try:
    gff_ref = argv[1]
    flt_ref = argv[2]
    par_ref = argv[3]
    ubi_1 = argv[4]
    flt_1 = argv[5]
    par_1 = argv[6]

except:
    print ("peakpurity.py [gff_ref] [flt_ref] [par_ref] [ubi_1] [flt_1] [par_1]")
    exit()

###############################################################################
## Few function and object definitions
###############################################################################

# Converting from ubi format to gff format using ubi_to_gff.py [code copy-pasted from
# ImageD11 package]
```

```
def ubi_to_gff(ubi,par):
    from ImageD11 import grain as ig
    from ImageD11 import parameters as ip
    from string import split
    from xfab import tools
    from six.moves import range

    list of grains = ig.read_grain_file(ubi)
    p = ip.parameters()
    p.loadparameters(par)
    uc = [p.parameters['cell__a'],p.parameters['cell__b'],p.parameters['cell__c'],
          p.parameters['cell_alpha'],p.parameters['cell_beta'],p.parameters['cell_gamma']]
    #print(uc)


    grain_id = []
    x = []
    y = []
    z = []
    rodx = []
    rody = []
    rodz = []
    unitcell_a = []
    unitcell_b = []
    unitcell_c = []
    unitcell_alpha = []
    unitcell_beta = []
    unitcell_gamma = []
    U11 = []
    U12 = []
    U13 = []
    U21 = []
    U22 = []
    U23 = []
    U31 = []
    U32 = []
    U33 = []
    eps11 = []
    eps22 = []
    eps33 = []
    eps23 = []
    eps13 = []
    eps12 = []
    titles = ["grain_id","x","y","z",
```

```
            "rodx","rody","rodz",
            "U11","U12","U13","U21","U22","U23","U31","U32","U33",
            "unitcell_a","unitcell_b","unitcell_c","unitcell_alpha","unitcell_beta",
            "unitcell_gamma","eps11","eps22","eps33","eps23","eps13","eps12"]
for i in range(len(list_of_grains)):
    grain_id.append(eval(split(list_of_grains[i].name,':')[0]))
    x.append(list_of_grains[i].translation[0]/1000.)
    y.append(list_of_grains[i].translation[1]/1000.)
    z.append(list_of_grains[i].translation[2]/1000.)
    ubi = list_of_grains[i].ubi
    (U,eps) = tools.ubi_to_u_and_eps(ubi,uc)
    uc_a, uc_b, uc_c, uc_alpha, uc_beta, uc_gamma = tools.ubi_to_cell(ubi)
    unitcell_a.append(uc_a)
    unitcell_b.append(uc_b)
    unitcell_c.append(uc_c)
    unitcell_alpha.append(uc_alpha)
    unitcell_beta.append(uc_beta)
    unitcell_gamma.append(uc_gamma)
    rod = tools.u_to_rod(U)
    rodx.append(rod[0])
    rody.append(rod[1])
    rodz.append(rod[2])
    U11.append(U[0,0])
    U12.append(U[0,1])
    U13.append(U[0,2])
    U21.append(U[1,0])
    U22.append(U[1,1])
    U23.append(U[1,2])
    U31.append(U[2,0])
    U32.append(U[2,1])
    U33.append(U[2,2])
    eps11.append(eps[0])
    eps12.append(eps[1])
    eps13.append(eps[2])
    eps22.append(eps[3])
    eps23.append(eps[4])
    eps33.append(eps[5])

gff = cl2.newcolumnfile(titles)
gff.ncols = len(titles)
gff.nrows = len(grain_id)
gff.bigarray = np.zeros((gff.ncols,gff.nrows))
gff.set_attributes()
gff.addcolumn(grain_id,"grain_id")
```

```
    gff.addcolumn(x,"x")
    gff.addcolumn(y,"y")
    gff.addcolumn(z,"z")
    gff.addcolumn(rodx,"rodx")
    gff.addcolumn(rody,"rody")
    gff.addcolumn(rodz,"rodz")
    gff.addcolumn(U11,"U11")
    gff.addcolumn(U12,"U12")
    gff.addcolumn(U13,"U13")
    gff.addcolumn(U21,"U21")
    gff.addcolumn(U22,"U22")
    gff.addcolumn(U23,"U23")
    gff.addcolumn(U31,"U31")
    gff.addcolumn(U32,"U32")
    gff.addcolumn(U33,"U33")
    gff.addcolumn(unitcell_a,"unitcell_a")
    gff.addcolumn(unitcell_b,"unitcell_b")
    gff.addcolumn(unitcell_c,"unitcell_c")
    gff.addcolumn(unitcell_alpha,"unitcell_alpha")
    gff.addcolumn(unitcell_beta,"unitcell_beta")
    gff.addcolumn(unitcell_gamma,"unitcell_gamma")
    gff.addcolumn(eps11,"eps11")
    gff.addcolumn(eps22,"eps22")
    gff.addcolumn(eps33,"eps33")
    gff.addcolumn(eps23,"eps23")
    gff.addcolumn(eps13,"eps13")
    gff.addcolumn(eps12,"eps12")
    return gff, uc

class Umatrix(np.ndarray):
    ''' 3x3 orthogonal matrix corresponding to a rotation '''
    def __new__(cls, val=None):
        '''
        Create. If no argument given, create a completely random matrix,
        otherwise use argument to initialize
        '''
        if val is None:
            self = np.zeros((3,3), dtype=np.float).view(cls)
        else:
            self = np.array(val, dtype=np.float).view(cls)
        return self

class mygrain:
```

```
    ''' grain object having its orientation, x,y,z positions, unit cell parameters,
        its (arbitrary) index and its assigned peaks'''

    def __init__(self,U,xyz,unitcell,grainname,peaks):
        self.U=U
        self.xyz=xyz
        self.unitcell=unitcell
        self.grainno=grainname
        self.peaks=peaks
    def __str__(self):
        return str(self.grainno)


def calc_dist(grain1,grain2):
    """
    A function calculating the distance between two reconstructed grains
    """
    dist=np.sqrt((grain1.xyz[0][0]-grain2.xyz[0][0])**2+(grain1.xyz[0][1]-grain2.xyz[0][1])**2
         +(grain1.xyz[0][2]-grain2.xyz[0][2])**2)
    return dist

class mypeak:
    ''' peak entry having its detector-y (px), detector-z (px), omega (deg) positions,
    g-vector, hkl and intensity information'''
    def __init__(self,detector_y,detector_z,omega,num_of_px,avg_intensity,sum_intensity,gx,gy,
                 gz,h,k,l,hr,kr,lr,diff,spot3d_id,labels,tth,eta,tth_per_grain,eta_per_grain):
        self.detector_y = detector_y
        self.detector_z = detector_z
        self.omega = omega
        self.num_of_px = num_of_px
        self.avg_intensity = avg_intensity
        self.sum_intensity = sum_intensity
        self.gx = gx
        self.gy = gy
        self.gz = gz
        self.diff = 0
        try:
            self.h = h
            self.k = k
            self.l = l
            self.hr = hr
            self.kr = kr
            self.lr = lr
        except:
```

```
            pass
        self.spot3d_id=spot3d_id
        self.labels=labels
        self.tth=tth
        self.eta=eta
        self.tth_per_grain=tth_per_grain
        self.eta_per_grain=eta_per_grain
    def __str__(self):
        return str(self.spot3d_id)

def introduce_gvectors(flt_file,par_file):

    obj = transformer.transformer()
    obj.loadfiltered( flt_file )
    obj.loadfileparameters( par_file )
    obj.colfile.sortby('omega')
    obj.compute_tth_eta()
    obj.addcellpeaks()
    obj.computegv()
    obj.write_colfile( str(flt_file.split(".")[0])+"_with_gvec.flt")


def get_attributes(flt_file, counter):
    #peak_name = 'peak_no_' + str( flt_file.spot3d_id[counter] )
    detector_y = flt_file.sc[counter]
    detector_z = flt_file.fc[counter]
    omega = flt_file.omega[counter]
    num_of_px = flt_file.Number_of_pixels[counter]
    avg_intensity = flt_file.avg_intensity[counter]
    sum_intensity = flt_file.sum_intensity[counter]
    gx = flt_file.gx[counter]
    gy = flt_file.gy[counter]
    gz = flt_file.gz[counter]
    if hasattr(flt_file,'h') == False:
        h = 1
        k = 1
        l = 1
    else:
        h = flt_file.h[counter]
        k = flt_file.k[counter]
        l = flt_file.l[counter]
    if hasattr(flt_file,'hr') == False:
        hr = h
        kr = k
        lr = l
```

```
        else:
            hr = flt_file.hr[counter]
            kr = flt_file.kr[counter]
            lr = flt_file.lr[counter]
        diff = 0
        spot3d_id = flt_file.spot3d_id[counter]
        labels = flt_file.labels[counter]
        tth=flt_file.tth[counter]
        eta=flt_file.eta[counter]
        if hasattr(flt_file,'tth_per_grain') == False:
             tth_per_grain=flt_file.tth[counter]
             eta_per_grain=flt_file.eta[counter]
        else:
             tth_per_grain=flt_file.tth_per_grain[counter]
             eta_per_grain=flt_file.eta_per_grain[counter]

        return detector_y,detector_z,omega,num_of_px,avg_intensity,sum_intensity,gx
        return gy,gz,h,k,l,hr,kr,lr, diff,spot3d_id,labels,tth,eta,tth_per_grain
        return eta_per_grain

    def getU_xyz_from_gff(gff_file,counter):

        grain_name = 'grain_no_' + str(    gff_file.grain_id[counter] ).split('.')[0]
        U_matrix = np.zeros((3,3))
        xyz_matrix = np.zeros((1,3))

        U_matrix[0][0] = gff_file.U11[counter]
        U_matrix[0][1] = gff_file.U12[counter]
        U_matrix[0][2] = gff_file.U13[counter]
        U_matrix[1][0] = gff_file.U21[counter]
        U_matrix[1][1] = gff_file.U22[counter]
        U_matrix[1][2] = gff_file.U23[counter]
        U_matrix[2][0] = gff_file.U31[counter]
        U_matrix[2][1] = gff_file.U32[counter]
        U_matrix[2][2] = gff_file.U33[counter]

        xyz_matrix[0][0] = gff_file.x[counter]
        xyz_matrix[0][1] = gff_file.y[counter]
        xyz_matrix[0][2] = gff_file.z[counter]

        return U_matrix, xyz_matrix, grain_name

    def calculate_dist_on_gvector(peak1, peak2):
        ''' A function calculating the difference of g-vectors for two peaks.
```

```
        Idea based on CD's suggestions. '''

    dist = np.sqrt((peak1.gx-peak2.gx)**2 +
                   (peak1.gy-peak2.gy)**2 + (peak1.gz-peak2.gz)**2 )
    return dist


def calculate_dist_on_detector(peak1, peak2):
    ''' A function calculating the difference of detector positions for
        two peaks. MK's original idea.. '''

    dist = np.sqrt((peak1.detector_y-peak2.detector_y)**2 +
                   (peak1.detector_z-peak2.detector_z)**2  )
    return dist


def calculate_dist_on_gvector_HFP(peak1, peak2):
    ''' A function calculating the difference of g-vectors for two peaks.
        Idea based on HFP's suggestions.'''

    g1 = np.array([peak1.gx, peak1.gy, peak1.gz])
    g2 = np.array([peak2.gx, peak2.gy, peak2.gz])

    gv_dot = float(g1[0]*g2[0]) + float(g1[1]*g2[1]) +
             float(g1[2]*g2[2])

    norm_g1 = float(np.sqrt( float(g1[0]*g1[0]) + float(g1[1]*g1[1]) +
                             float(g1[2]*g1[2]) ) )
    norm_g2 = float(np.sqrt( float(g2[0]*g2[0]) + float(g2[1]*g2[1]) +
                             float(g2[2]*g2[2]) ) )

    dist =  float(np.degrees(float(np.arccos(float((gv_dot/(norm_g1*norm_g2)))))))

    return dist

#####
## Open the input files
#####

gff_ref = cl(gff_ref)

if ubi_1.split(".")[-1] == "ubi" or ubi_1.split(".")[-1] == "map":
    gff_1, cellpars_1 = ubi_to_gff(ubi_1,par_1)
```

```
elif ubi_1.split(".")[-1] == "gff":
    gff_1 = cl(ubi_1)

if flt_ref.split(".")[0].split("_")[-1] != "gvec":
    introduce_gvectors(flt_ref, par_ref)
    flt_ref = cl(str(flt_ref.split(".")[0])+"_with_gvec.flt")
else:
    flt_ref = cl(str(flt_ref))

if flt_1.split(".")[0].split("_")[-1] != "gvec":
    introduce_gvectors(flt_1, par_1)
    flt_1 = cl(str(flt_1.split(".")[0])+"_with_gvec.flt")
else:
    flt_1 = cl(str(flt_1))


#####
## Dictionaries holding the grains to be matched  and peak lists
#####

grains_ref = {}
grains_1 = {}
peaks_ref = {}
peaks_1 = {}

for i in range(len(gff_ref.U11)):
    u_temp, xyz_temp, name_temp = getU_xyz_from_gff(gff_ref,i)
    peaks_temp = []
    unitcell_temp = []
    grain_temp =  mygrain(u_temp, xyz_temp, unitcell_temp, name_temp, peaks_temp)
    grains_ref[name_temp]=grain_temp

for i in range(len(gff_1.U11)):
    u_temp, xyz_temp, name_temp = getU_xyz_from_gff(gff_1,i)
    peaks_temp = []
    unitcell_temp = []
    grain_temp = mygrain(u_temp, xyz_temp, unitcell_temp, name_temp, peaks_temp)
    grains_1[name_temp] = grain_temp

for m in range(len(flt_ref.sc)):
    detector_y_temp,detector_z_temp,omega_temp,num_of_px_temp,avg_intensity_temp,sum_intensity_temp,
    gx_temp,gy_temp,gz_temp,h_temp, k_temp, l_temp, hr_temp,kr_temp,lr_temp, diff_temp, name_temp,
    labels_temp, tth_temp, eta_temp, tth_per_grain_temp, eta_per_grain_temp  =  get_attributes(flt_ref, m)
```

```
        peak_temp   =  mypeak(detector_y_temp,detector_z_temp,omega_temp,num_of_px_temp,avg_intensity_temp,
                              sum_intensity_temp,gx_temp,gy_temp,gz_temp,h_temp, k_temp, l_temp, hr_temp,kr_temp,
                              lr_temp, diff_temp, name_temp, labels_temp, tth_temp, eta_temp, tth_per_grain_temp,
                          eta_per_grain_temp )
        peaks_ref[name_temp]   =  peak_temp

for i in range(len(flt_1.sc)):
    detector_y_temp ,detector_z_temp ,omega_temp ,num_of_px_temp ,avg_intensity_temp ,sum_intensity_temp,
    gx_temp ,gy_temp ,gz_temp , h_temp, k_temp, l_temp, hr_temp ,kr_temp ,lr_temp, diff_temp, name_temp,
    labels_temp, tth_temp, eta_temp, tth_per_grain_temp, eta_per_grain_temp =  get_attributes(flt_1, i)

    peak_temp   =  mypeak(detector_y_temp ,detector_z_temp ,omega_temp ,num_of_px_temp ,avg_intensity_temp,
                          sum_intensity_temp ,gx_temp ,gy_temp ,gz_temp , h_temp, k_temp, l_temp, hr_temp ,kr_temp ,
                          lr_temp, diff_temp, name_temp, labels_temp, tth_temp, eta_temp, tth_per_grain_temp, eta_per_grain_temp )
    peaks_1[name_temp]   =  peak_temp


for grain in grains_ref:
    for peak in peaks_ref:
        if peaks_ref[peak].labels == float(grains_ref[grain].grainno.split(' ')[-1]):
            grains_ref[grain].peaks.append(peaks_ref[peak])

print("Reference grains are populated with their peaks")


for grain in grains_1:
    for peak in peaks_1:
        if peaks_1[peak].labels == float(grains_1[grain].grainno.split(' ')[-1]):
            grains_1[grain].peaks.append(peaks_1[peak])

print("Analyzed grains are populated with their peaks")


#########################################################################################
## Grain matching
#########################################################################################
diff_dist_list = []
matched_grains_ref_1 = {}

from xfab.symmetry import Umis
for keys_ref in grains_ref:
    temp_listtt = []
    print()
```

```
        print()
        print("try to match grain ", keys_ref," of reference with grain list 1")
        for keys_1 in grains_1:
                    dist_diff = calc_dist(  grains_1[keys_1], grains_ref[keys_ref] )
                    test = Umis(grains_ref[keys_ref].U,grains_1[keys_1].U, 7)      #7 for cubic
                    or_diff = min(test[:,1])
                    diff_dist_list.append((or_diff,dist_diff))
                    ranking =  (dist_diff)/0.01  +  (or_diff)
                    temp_listtt.append(ranking)
                    if min(temp_listtt) == ranking  and or_diff < 0.2 and  dist_diff*1e3 < 0.5:
                        print("#####")
                        print("new minimum: ", ranking)
                        print("dist_diff: ",dist_diff*1e3)
                        print("or_diff: ",or_diff)
                        print("Ref grain: ",keys_ref,"  matched to grain list's ",keys_1)
                        print("#####")
                        matched_grains_ref_1[ grains_1[keys_1] ] = grains_ref[keys_ref]
print("#####")

completeness = []
purity_graindex = []
purity_grainspotter = []

dist_diff = 0

dummy_equal = True

all_purity_graindex_good=[]
all_purity_graindex_bad=[]
all_purity_grainspotter_good=[]
all_purity_grainspotter_bad=[]
all_completeness_good=[]
all_completeness_bad=[]


all_t_hkl_good=[]
all_t_hkl_bad=[]
all_t_tth_good=[]
all_t_tth_bad=[]
all_t_eta_good=[]
all_t_eta_bad=[]
all_t_omega_good=[]
all_t_omega_bad=[]
```

```
all_ref_peaks=[]

all_gx=[]
all_gy=[]
all_gz=[]

for keys in matched_grains_ref_1:

    matched_peaks = {}
    unmatched_peaks = []

    for peak_1 in keys.peaks:
        temp_dist = []
        temp_list = []
        unmatched = True
        for peak_ref in matched_grains_ref_1[keys].peaks:
                if peak_ref.omega < (peak_1.omega+0.2) and peak_ref.omega > (peak_1.omega-0.2):
                    dist_diff = abs(calculate_dist_on_gvector (peak_ref, peak_1))
#                   #dist_diff = abs(calculate_dist_on_detector (peak_ref, peak_1))
#                   #dist_diff = abs(calculate_dist_on_gvector_HFP(peak_ref, peak_1))
                    temp_list.append(dist_diff)
                    if min(temp_list) == dist_diff and float(dist_diff) < 0.1:
                        temp_dist.append(dist_diff)
                        matched_peaks[ peak_1 ] = peak_ref
                        unmatched = False

        if unmatched == True:
            unmatched_peaks.append(peak_1)
            dummy_equal = False

        det_y_ref_1_diff_temp=[]
        det_z_ref_1_diff_temp=[]
        omega_ref_1_diff_temp=[]
        num_of_px_ref_1_diff_temp=[]
        avg_intensity_ref_1_diff_temp=[]
        sum_intensity_ref_1_diff_temp=[]
        gx_diff_ref_1_temp=[]
        gy_diff_ref_1_temp=[]
        gz_diff_ref_1_temp=[]

    for peaks_per in matched_peaks:
```

```
            peaks_ref = matched_peaks[peaks_per]

            det_y_ref_1_diff_temp.append(float( (peaks_per.detector_y - peaks_ref.detector_y)  ))
            det_z_ref_1_diff_temp.append(float( (peaks_per.detector_z - peaks_ref.detector_z) ))
            omega_ref_1_diff_temp.append(float( (peaks_per.omega - peaks_ref.omega) ))
            num_of_px_ref_1_diff_temp.append(float( (peaks_per.num_of_px - peaks_per.num_of_px) ))
            avg_intensity_ref_1_diff_temp.append(float( (peaks_per.avg_intensity - peaks_ref.avg_intensity) ))
            sum_intensity_ref_1_diff_temp.append(float( (peaks_per.sum_intensity - peaks_ref.sum_intensity) ))
            gx_diff_ref_1_temp.append(float( (peaks_per.gx - peaks_ref.gx) ))
            all_gx.append(float( (peaks_per.gx - peaks_ref.gx) ))
            gy_diff_ref_1_temp.append(float( (peaks_per.gy - peaks_ref.gy) ))
            gz_diff_ref_1_temp.append(float( (peaks_per.gz - peaks_ref.gz) ))

    print(np.mean(temp_dist))
    print(" ")
    print(str(len(keys.peaks)))
    print(str(len(matched_grains_ref_1[keys].peaks)))
    all_ref_peaks.append(len(matched_grains_ref_1[keys].peaks))
    print(str(len(matched_peaks)))
    print(str(len(unmatched_peaks)))
    print(" ***** ")

    p_gd = float( float(len(matched_peaks)) / float(len(keys.peaks)) )
    p_gs = float( float(len(matched_peaks)) / float(len(matched_grains_ref_1[keys].peaks)) )
    comp = float(float(len(keys.peaks))/len(matched_grains_ref_1[keys].peaks))

    purity_graindex.append( p_gd )
    purity_grainspotter.append( p_gs )
    completeness.append(comp)

    print("purity_graindex: ",p_gd)
    print(" ")
    print("purity_grainspotter: ",p_gs)
    print(" ")
    print("completeness: ",comp)
    print(" ")

    if len(unmatched_peaks) < 100:
        all_purity_graindex_good.append(p_gd)
        all_purity_grainspotter_good.append(p_gs)
        all_completeness_good.append(comp)

    elif len(unmatched_peaks) > 100:
        all_purity_graindex_bad.append(p_gd)
```

```
        all_purity_grainspotter_bad.append(p_gs)
        all_completeness_bad.append(comp)

    def tol_hkl(peak_1, peak_ref):
        err = float(np.sqrt( float((peak_1.hr-peak_ref.h)**2) + float((peak_1.kr-peak_ref.k)**2) + float((peak_1.lr-peak_ref.l)**2) ) )
        return err

    def tol_tth(peak_1, peak_ref):
        err = float(peak_1.tth) - float(peak_ref.tth)
        return err

    def tol_eta(peak_1, peak_ref):
        err = float(peak_1.eta) - float(peak_ref.eta)
        return err

    def tol_omega(peak_1, peak_ref):
        err = float(peak_1.omega) - float(peak_ref.omega)
        return err

    error_hkl=[]
    error_tth=[]
    error_eta=[]
    error_omega=[]

    for peak in matched_peaks:

        error_hkl.append( tol_hkl(peak, matched_peaks[peak]) )
        error_tth.append( tol_tth(peak, matched_peaks[peak]) )
        error_eta.append( tol_eta(peak, matched_peaks[peak]) )
        error_omega.append( tol_omega(peak, matched_peaks[peak]) )

        if len(unmatched_peaks) == 0 or len(unmatched_peaks) != 0:
            all_t_hkl_good.append(tol_hkl(peak, matched_peaks[peak]) )
            all_t_tth_good.append(tol_tth(peak, matched_peaks[peak]) )
            all_t_eta_good.append(tol_eta(peak, matched_peaks[peak]) )
            all_t_omega_good.append(tol_omega(peak, matched_peaks[peak]) )

    print("mean hkl_error: ",np.mean(error_hkl),"with stdev: ",np.std(error_hkl))
    print("mean tth_error: ",np.mean(error_tth),"with stdev: ",np.std(error_tth))
    print("mean eta_error: ",np.mean(error_eta),"with stdev: ",np.std(error_eta))
    print("mean omega_error: ",np.mean(error_omega),"with stdev: ",np.std(error_omega))
    print(" \n")
    print(" \n")
    print(" \n")
```

```
    print("**************************** \n")
    print(" \n")
    print(" \n")

print(" ")
print("Mean purity_graindex: ",np.mean(purity_graindex),
      "with stdev: ",np.std(purity_graindex))
print(" ")
print("Mean purity_grainspotter: ",np.mean(purity_grainspotter),"with stdev: ",np.std(purity_grainspotter))
print(" ")
print("Mean completeness: ",np.mean(completeness),"with stdev: ",np.std(completeness))
print(" \n")
print(" \n")
print("Good grains:\n")
print("Mean purity_graindex: ",np.mean(all_purity_graindex_good),"with stdev: ",np.std(all_purity_graindex_good))
print("Mean purity_grainspotter: ",np.mean(all_purity_grainspotter_good),"with stdev: ",np.std(all_purity_grainspotter_good))
print("Mean completeness: ",np.mean(all_completeness_good),"with stdev: ",np.std(all_completeness_good))
print("mean hkl_error: ",np.mean(all_t_hkl_good),"with stdev: ",np.std(all_t_hkl_good))
print("mean tth_error: ",np.mean(all_t_tth_good),"with stdev: ",np.std(all_t_tth_good))
print("mean eta_error: ",np.mean(all_t_eta_good),"with stdev: ",np.std(all_t_eta_good))
print("mean omega_error: ",np.mean(all_t_omega_good),"with stdev: ",np.std(all_t_omega_good))
print(" \n")
print(" \n")
print("Bad grains:\n")
print("Mean purity_graindex: ",np.mean(all_purity_graindex_bad),"with stdev: ",np.std(all_purity_graindex_bad))
print("Mean purity_grainspotter: ",np.mean(all_purity_grainspotter_bad),"with stdev: ",np.std(all_purity_grainspotter_bad))
print("Mean completeness: ",np.mean(all_completeness_bad),"with stdev: ",np.std(all_completeness_bad))
print("mean hkl_error: ",np.mean(all_t_hkl_bad),"with stdev: ",np.std(all_t_hkl_bad))
print("mean tth_error: ",np.mean(all_t_tth_bad),"with stdev: ",np.std(all_t_tth_bad))
print("mean eta_error: ",np.mean(all_t_eta_bad),"with stdev: ",np.std(all_t_eta_bad))
print("mean omega_error: ",np.mean(all_t_omega_bad),"with stdev: ",np.std(all_t_omega_bad))
print(" \n")
print(" \n")
print("Total execution time: %.3fs"%(time.time() - start_time))
print(" \n")
print(" \n")
print(str(len(matched_grains_ref_1)))
print(np.mean(all_ref_peaks))


per_=[]
ref_=[]

for keys in matched_grains_ref_1:
```

```
        per_.append(int(keys.grainno.split("_")[-1]))
        ref_.append(int(matched_grains_ref_1[keys].grainno.split("_")[-1]))


print("Checking for possible duplicates")

def checkIfDuplicates_3(listOfElems):
    ''' Check if given list contains any duplicates '''
    for elem in listOfElems:
        if listOfElems.count(elem) > 1:
            return True
    return False

result = checkIfDuplicates_3(per_)

if result:
    print('Yes, reference list contains duplicates')
else:
    print('No duplicates found in the reference list')


result = checkIfDuplicates_3(ref_)

if result:
    print('Yes, analyzed list contains duplicates')
else:
    print('No duplicates found in the analyzed list')

print("Duplicate check done!")


##########

filename = "matchinglist.flt"
f2 = open(filename, "w")
f2.write("\n")
f2.write("#  gs_grain ref_grain com_diff misori gs_x gs_y gs_z ref_x ref_y ref_z\n")
fmt = "%f "*4 + "%.9g "*6 + " \n"


for keys in matched_grains_ref_1.keys():

        com_diff = calc_dist( matched_grains_ref_1[keys], keys )*1e3
        or_diff = Umatrix()
```

```
        or_diff = or_diff.angle(keys.U,matched_grains_ref_1[keys].U)

        per_x = keys.xyz[0][0]*1e3
        per_y = keys.xyz[0][1]*1e3
        per_z = keys.xyz[0][2]*1e3

        ref_x = matched_grains_ref_1[keys].xyz[0][0]*1e3
        ref_y = matched_grains_ref_1[keys].xyz[0][1]*1e3
        ref_z = matched_grains_ref_1[keys].xyz[0][2]*1e3

        per_grain = float(keys.grainno.split("_")[-1])
        ref_grain = float(matched_grains_ref_1[keys].grainno.split("_")[-1])

        f2.write(fmt % ( per_grain, ref_grain, com_diff, or_diff, per_x, per_y, per_z, ref_x, ref_y , ref_z  ))

f2.close()


k=cl("matchinglist.flt")

k.sortby("gs_grain")
k.writefile("matchinglist.flt")

U_difference_ref_1 =[]
xyz_difference_ref_1 =[]

for keys in matched_grains_ref_1:
    test = Umis(keys.U,matched_grains_ref_1[keys].U, 7)      #7 for cubic
    misori = min(test[:,1])
    U_difference_ref_1.append(misori)

U_error_ref_1_mean = np.mean(U_difference_ref_1)
U_error_ref_1_stdev = np.std(U_difference_ref_1)

for keys in matched_grains_ref_1:
    xyz_difference_ref_1.append(calc_dist( keys, matched_grains_ref_1[keys] ))

xyz_error_ref_1_mean = np.mean(xyz_difference_ref_1)
xyz_error_ref_1_stdev = np.std(xyz_difference_ref_1)


U1="Average difference in U matrices per grain for reference and grain list 1 is "+str(U_error_ref_1_mean)+
    " (in degrees) with std. deviation of "+str(U_error_ref_1_stdev)
print(U1)
```

```
XYZ1 = "Average difference in CoM position of grains per grain for grain list 1 w.r.t reference is "+str(xyz_error_ref_1_mean*1000)+
    " (in micrometers) with std. deviation of "+str(xyz_error_ref_1_stdev*1000)
print(XYZ1)


print()
print()
print("Maximum U error (degrees): ", max(U difference ref 1))
print("Maximum CoM error (microns): ", max(xyz_difference_ref_1)*1000)


print("Unmatched grains: ")

temp_1 = set()
temp_2 = set()
temp_7 = set()
temp_8 = set()

if len(matched_grains_ref_1) == len(grains_1):
        print("All grains are matched in both grain lists!")
        dummy_equal = True
else:
    dummy_equal = False
    for keys in matched_grains_ref_1:
        temp_1.add(keys.grainno)
        temp_2.add(matched_grains_ref_1[keys].grainno)
    for keys_ref in grains_ref:
        temp_7.add(grains_ref[keys_ref].grainno)
    for keys_1 in grains_1:
        temp_8.add(grains_1[keys_1].grainno)

    unmatched_grains_1 = temp_7 - temp_1    #ref vs. grain list 1 -  ref
    unmatched_grains_2 = temp_8 - temp_2    #ref vs. grain list 1 - 1

    print("Reference vs. grain list 1: ")
    print("Found ",len(unmatched_grains_1)," unmatched grains in the grain list ", gff_ref.filename.split('/')[-1])
    print("Found ",len(unmatched_grains_2)," unmatched grains in the grain list ", gff_1.filename.split('/')[-1])
    print("#####")

    f8 = open("ref_not_found.gff", "w")
    f8.write("#  grain_id x y z U11 U12 U13 U21 U22 U23 U31 U32 U33\n")
```

```
    fmt = "%i " + "%9f "*12 + " \n"
    for i in unmatched_grains_1:
        grain_id = int(i.split("_")[-1])
#        i="grain_no "+str(i)
        x=float(grains_ref[i].xyz[0][0])
        y=float(grains_ref[i].xyz[0][1])
        z=float(grains_ref[i].xyz[0][2])
        U11=float(grains_ref[i].U[0][0])
        U12=float(grains_ref[i].U[0][1])
        U13=float(grains_ref[i].U[0][2])
        U21=float(grains_ref[i].U[1][0])
        U22=float(grains_ref[i].U[1][1])
        U23=float(grains_ref[i].U[1][2])
        U31=float(grains_ref[i].U[2][0])
        U32=float(grains_ref[i].U[2][1])
        U33=float(grains_ref[i].U[2][2])
        f8.write(fmt % (grain_id, x, y, z, U11, U12, U13, U21, U22, U23, U31, U32, U33 ))
    f8.close()

    print("########################")
```

C Appendix C HR-3DXRD Pre-processing: Multi-panel calibration script

The presented *ipython notebook* was employed in the studies presented in Section 6.2. The digital version of the script can be reached in the “Scripts” section of the following URL: https://github.com/mkutsal/hr-3dxrd.

Procedure

This script is an HR-3DXRD adaptation of the workflow presented in https://pyfai.readthedocs.io/en/master/usage/tutorial/Goniometer/Rotation-Pilatus100k/Multi120_Pilatus100k.html (https://pyfai.readthedocs.io/en/master/usage/tutorial/Goniometer/Rotation-Pilatus100k/Multi120_Pilatus100k.html) (access date May 31st, 2021).

!!! The current version of the script requires the following input files present in the working directory:

- Calibrant file, '.D'
- Image files, '.tif, .edf, etc.'
- Control points file for each image, '.npt'
- Detector calibration file for each image, '.PONI'

Step 1 - Initial calibration 1: Define experimentally measured distance. Calibration guesses of individual detector positions should be provided (as control points, '.npt.' and '.PONI' files). Initial calibration of sample-to-detector distance and PONI parameters. All tilts are set to zero.

Step 2 - Initial calibration 2:
Inherit the refined calibration from the previous step. Calibrate sample-to-detector distance and PONI parameters with new expression. All tilts are set to zero.

Step 3 - Complete calibration: Inherit the refined calibration from previous step. Calibrate all global parameters. Initial guess of both tilts are set to zero.

Step 4 & 5 - Refinement: Inherit all parameters from previous step. Repeat the 3rd step with non-zero initial guesses for both detector tilts.

Step 6 - Analysis: 1D azimuthal integration and 2D polar decomposition of the HR-3DXRD compound image. Refined motor positions are calculated. Conversion from pyFAI to FABLE/ImageD11 geometry and producing the parameter files, '.par'.

Initialization

Definitions of working directory, input images, motor positions and its reader function, and definitions of calibrant, detector, etc.

In [ ]:

```
%pylab nbagg

import time, pyFAI
print("Using pyFAI version", pyFAI.version)

start_time = time.time()

#Loading required libraries
import os
import random
import fabio
from pyFAI.goniometer import GeometryTransformation, GoniometerRefinement, Goniometer
from pyFAI.gui import jupyter

# Image/working directory:

im_dir = '/home/esrf/kutsal/desy_oct21_analysis_ann2_ep1_nf2/single_panel_ponis/testing/'
os.chdir(im_dir)

# Loading images...

all_files = []
image_files = []

for f in os.listdir(im_dir):
    if f.split('.')[-1] == 'tif':
        if f.split('.')[0].split('_')[-3] == str(2) :
            continue
        if f.split('.')[0].split('_')[-3] == str(5) :
            continue
        if f.split('.')[0].split('_')[-3] == str(12) :
            continue
        else:
            all_files.append(im_dir + f);

image_files = [i for i in all_files if i.split('.')[-1] == 'tif']
image_files.sort()

print('Number of loaded images: '+str(len(image_files)))
```

In [ ]:

```
# Testing: Did we loaded the images successfully?

#fimg = fabio.open(image_files[1])

#plt.figure()
#plt.imshow(fimg.data,cmap="gray", vmin=50, vmax=350)
#plt.title('Raw Image of '+fimg.filename )
#plt.colorbar()
```

In [ ]:

```
# Definition of the motor position function

# The refinement procedure requires a function that reads
# the experimental motor position of the acquired image.
# Works with '.edf' files, or any format with headers
# containing its motor positions. In case, please change the
# reading format according to your header's data structure.


#def get_pos(header):
#    #print("get_pos: ", img_basename)
#    #for_header = fabio.open(img_basename);
#    #header = for_header.header;
#    motor_mne = header["motor_mne"].split(" ");
#    motor_pos = header["motor_pos"].split(" ");
#    a = dict(zip(motor_mne, motor_pos));
#    d2ty = float(a.get("d2ty"));
#    d2tz = float(a.get("d2tz"));
#    return d2ty , d2tz
```

In [ ]:

```
# Definition of the position function - manual way: No
# header info in .tif images. Experimental motor positions
# are provided manually and they are called from a list,
# instead of image header.

motorpos_list = [(0, (5.8, 0)),(1, (0.535, -5.775)),(2, (-5.7, 1.066)),(3, (-1.587, -5.578)
                 (4, (5.408, 2.095)),(5, (-4.931, -3.05)),(6, (4.286, -3.907)),
                 (7, (2.585, 5.19)),(8, (-3.495, 4.628)),(9, (0.535, 5.77)),
                 (10, (5.7, -1.065)),(11, (2.585, -5.192)),(12, (-4.931, 3.05)),
                 (13, (5.408, -2.095)),(14, (-1.587, 5.578)),(15, (-3.495, -4.628)),
                 (16, (4.286, 3.907))]

def get_pos(img_basename):
    i=img_basename.split('/')[-1].split('_')[1]
    k,yz = motorpos_list[int(i)]
    if k == int(i):
        return yz[0]*1e-3, yz[1]*1e-3  #returns in meters
```

In [ ]:

```
# Definition of the employed detector and the calibrant

frelon = pyFAI.detector_factory("frelon")

# PCO edge is not avaiable. Going for a way-around...
# Please comment out the part below, if your detector is
# available in pyFAI's database.

frelon.pixel1=1.3e-6
frelon.pixel2=1.3e-6
frelon.shape=(2540,2140)
frelon.MAX_SHAPE=(2540,2140)
print(frelon)


# Manual definition of the calibrant.
# The user-made calibrant files may require further manual definition
# of the d-spacings and the wavelength... Please comment out the part
# below, if your calibrant/material is available in pyFAI's database.

d_list = [2.027, 1.433, 1.170]
wavelength = 3.2627e-11

calib = pyFAI.calibrant.Calibrant()
calib.load_file("aFe.d")
calib.dSpacing= d_list
calib.wavelength= wavelength

print("Calibrant loaded: ", calib.filename)
print("d-spacings: " + str(calib.dSpacing))
print("Wavelength to be used: " + str(calib.wavelength))
```

In [ ]:

```
# If the input images may lose their header information during the
# through-stack summation of pre-processing. This step re-intorduces
# the header information to the summed images, from the respective
# experimental diffraction images. This step is required  if only the
# images have header info...

#def copy_headers(fn):
#    eta1 = fabio.open(fn)
#    orig = eta1.header["merged_file_0000"]
#    header = fabio.open("/data/id06/inhouse/2019/MKutsal/ID11_HEA_x10_data/
#                    HEA_x10_eta_all/"+os.path.split(eta1.header["merged_file_0000"])[-1]).h
#    eta1.header.update(header)
#    print(eta1.header)
#    eta1.write(fn)




#copy_headers("maxi_eta1.edf")
#copy_headers("maxi_eta2.edf")
#copy_headers("maxi_eta3.edf")
#copy_headers("maxi_eta4.edf")
```

Step 1: Initial calibration I

Distance= constant, tilts y&z=0. PONI=PONI(posY, posZ). -> Fit the distance and PONI only.

In [ ]:

```
# Definition of the goniometer translation function:
# The detector moves in y_L and z_L axes, (presumably) with no rotation

goniotrans = GeometryTransformation(param_names = ["dist", "poni1_scale", "posY_offset",
                                                   "poni2_scale", "posZ_offset", "rot1",
                                                   "rot2"],
                                    pos_names = ["posY", "posZ"],
                                    dist_expr= "dist",
                                    poni1_expr="-posZ * poni1_scale + posZ_offset",
                                    poni2_expr="-posY * poni2_scale + posY_offset",
                                    rot1_expr="0.0",
                                    rot2_expr="0.0",
                                    rot3_expr="0.0")

# Initial guesses of the refinement
# The parameter order is the same as the param_names of the output file.

param = {"dist":0.02885, # in meters
         "poni1_scale": 1.0,
         "posZ_offset": 0.0,
         "poni2_scale": 1.0,
         "posY_offset": 0.0,
         "rot1":0.0, # in radians
         "rot2":0.0,
         "rot3":0.0
          }

# Boundary conditions of the refinement

bounds = {"dist": (0.025, 0.035),
          "poni1_scale": (-1.0,1.0),
          "poni2_scale": (-1.0,1.0),
          "posZ_offset": (-1.0,1.0),
          "posY_offset": (-1.0,1.0)
         }

# Initialization of the refinement object

gonioref = GoniometerRefinement(param, #initial guess
                                pos_function=get_pos,
                                trans_function=goniotrans,
                                bounds=bounds,
                                detector=frelon, wavelength=wavelength)


print("Empty refinement object:")
print(gonioref)
```

In [ ]:

```
# Populating the goniometer refinement object with control point and PONI files:

for image in image_files:
    fimg = fabio.open(image)

    basename = os.path.splitext(fimg.filename)[0]

    which_eta = 'pos_'+basename.split('_')[-3]
    print(basename, which_eta)

    sg =gonioref.new_geometry(which_eta, image=fimg.data, metadata=fimg.filename,
                              control_points=which_eta+"_max.npt", geometry=which_eta+"_max
    sg.control_points.calibrant = calib
    sg.geometry_refinement.wavelength = wavelength

    print(sg.label," Detector Position: ",sg.get_position())
    print(sg.geometry_refinement)
    print()


print("Filled refinement object:")
print(gonioref)
```

In [ ]:

```
# Display all images with associated calibration:

nimg = len(gonioref.single_geometries)
fig,ax = subplots(nimg, 1, figsize=(8,nimg*3))
for i, sg in enumerate(gonioref.single_geometries.values()):
    jupyter.display(sg=sg, ax=ax[i])
```

In [ ]:

```
# Repeat the refinement for determining the local minimum

i=0
while i<6:
    gonioref.refine2(maxiter=100000000)
    i=i+1
```

In [ ]:

```
# Check the calibration results...

def print_geo(key):
    print("expected")
    print(gonioref.single_geometries[key].geometry_refinement)
    print("refined")
    print(gonioref.get_ai(gonioref.single_geometries[key].get_position()))

print_geo("pos_0")
print_geo("pos_10")
print_geo("pos_13")
print_geo("pos_16")
```

Step 2: Initial calibration II

Distance=Distance(posY, posZ) and PONI=PONI(posY, posZ). Tilts y&z=0. -> Fit the distance and PONI only.

In [ ]:

```
goniotrans2 = GeometryTransformation(param_names = ["dist", "poni1_scale", "posY_offset",
                                                    "poni2_scale", "posZ_offset",
                                                    "dist1_scale", "dist2_scale"],
                                     pos_names = ["posY", "posZ"],
                                     dist_expr= "dist + dist1_scale * -posZ + dist2_scale *
                                     poni1_expr="-posZ * poni1_scale + posZ_offset",
                                     poni2_expr="-posY * poni2_scale + posY_offset",
                                     rot1_expr="0.0",
                                     rot2_expr="0.0",
                                     rot3_expr="0.0")



#Defines the bounds for some variables
bounds2 = {"dist": (0.025, 0.035),
           "poni1_scale": (-1.0,1.0),
           "poni2_scale": (-1.0,1.0),
           "posZ_offset": (-1.0,1.0),
           "posY_offset": (-1.0,1.0),
           "dist1_scale":(-5.0,5.0),
           "dist2_scale":(-5.0,5.0),
          }



param2 = (gonioref.nt_param(*gonioref.param))._asdict()

# Initial guesses for dist_scale parameters
param2["dist1_scale"]= 0.0
param2["dist2_scale"]= 0.0



gonioref2 = GoniometerRefinement(param2, #initial guesses from previous steps results
                                 pos_function=get_pos,
                                 trans_function=goniotrans2,
                                 bounds=bounds,
                                 detector=frelon, wavelength=wavelength)



gonioref2.single_geometries = gonioref.single_geometries.copy()
print(gonioref2)
```

In [ ]:

```
for image in image_files:
    fimg = fabio.open(image)

    basename = os.path.splitext(fimg.filename)[0]

    which_eta = 'pos_'+basename.split('_')[-3]
    print(basename, which_eta)




    sg =gonioref2.new_geometry(which_eta, image=fimg.data, metadata=fimg.filename, control_
                               geometry=gonioref.get_ai(gonioref.single_geometries[which_eta
                                calibrant=calib)
    sg.control_points.calibrant = calib
    sg.geometry_refinement.wavelength = wavelength


    print(sg.label," Detector Position: ",sg.get_position())
    print(sg.geometry_refinement)
    print()



print("Filled refinement object:")
print(gonioref2)
```

In [ ]:

```
# Repeat the refinement for determining the local minimum


i=0
while i<6:
    gonioref2.refine2("slsqp", eps=1e-13, maxiter=100000000, ftol=1e-12)
    i=i+1
```

In [ ]:

```
# Check the calibration results...

def print_geo2(key):
    print("expected")
    print(gonioref.single_geometries[key].geometry_refinement)
    print("refined")
    print(gonioref2.get_ai(gonioref.single_geometries[key].get_position()))



print_geo2("pos_0")
print_geo2("pos_10")
print_geo2("pos_13")
print_geo2("pos_16")
```

Step 3: Complete calibration

Distance=Distance(posY, posZ) and PONI=PONI(posY, posZ). Tilt-y and tilt-z=constant. -> Fit all global parameters.

In [ ]:

```
goniotrans3 = GeometryTransformation(param_names = ["dist", "poni1_scale", "posY_offset",
                                                    "poni2_scale", "posZ_offset", "rot1", "r
                                                    "dist1_scale", "dist2_scale"],
                                     pos_names = ["posY", "posZ"],
                                     dist_expr= "dist + dist1_scale * -posZ + dist2_scale *
                                     poni1_expr="-posZ * poni1_scale + posZ_offset",
                                     poni2_expr="-posY * poni2_scale + posY_offset",
                                     rot1_expr="rot1",
                                     rot2_expr="rot2",
                                     rot3_expr="0.0")



#Defines the bounds for some variables
bounds3 = {"dist": (0.025, 0.035),
           "poni1_scale": (-1.0,1.0),
           "poni2_scale": (-1.0,1.0),
           "posZ_offset": (-1.0,1.0),
           "posY_offset": (-1.0,1.0),
           "rot1": (-0.1,0.1),
           "rot2": (-0.1,0.1),
           "dist1_scale":(-5.0,5.0),
           "dist2_scale":(-5.0,5.0),
          }

param3 = (gonioref2.nt_param(*gonioref2.param))._asdict()

# Initial parameters for tilt-z and tilt-y, respectively
param3["rot1"]= 0.0174533 #in radians
param3["rot2"]= 0.0174533



gonioref3 = GoniometerRefinement(param3, #initial guesses from previous steps results
                                 pos_function=get_pos,
                                 trans_function=goniotrans3,
                                 bounds=bounds3,
                                 detector=frelon, wavelength=wavelength)

gonioref3.single_geometries = gonioref2.single_geometries.copy()
print(gonioref3)
```

In [ ]:

```
for image in image_files:
    fimg = fabio.open(image)

    basename = os.path.splitext(fimg.filename)[0]



    which_eta = 'pos_'+basename.split('_')[-3]
    print(basename, which_eta)


    sg =gonioref3.new_geometry(which_eta, image=fimg.data, metadata=fimg.filename, control_
                               geometry=gonioref2.get_ai(gonioref2.single_geometries[which_e
                                calibrant=calib)


    sg.control_points.calibrant = calib
    sg.geometry_refinement.wavelength = wavelength



    print(sg.label," Detector Position: ",sg.get_position())
    print(sg.geometry_refinement)
    print()


print("Filled refinement object:")
print(gonioref3)
```

In [ ]:

```
# Repeat the refinement for determining the local minimum

i=0
while i<6:
    gonioref3.refine2("slsqp", eps=1e-13, maxiter=100000000, ftol=1e-12)
    i=i+1
```

In [ ]:

```
# Check the calibration results...

def print_geo3(key):
    print("expected")
    print(gonioref.single_geometries[key].geometry_refinement)
    print("refined")
    print(gonioref3.get_ai(gonioref.single_geometries[key].get_position()))



print_geo3("pos_0")
print_geo3("pos_10")
print_geo3("pos_13")
print_geo3("pos_16")
```

Step 4: Refinement I

Repeat of Step 3.

In [ ]:

```
goniotrans4 = GeometryTransformation(param_names = ["dist", "poni1_scale", "posY_offset",
                                                    "poni2_scale", "posZ_offset", "rot1", "r
                                                    "dist1_scale", "dist2_scale"],
                                     pos_names = ["posY", "posZ"],
                                     dist_expr= "dist + dist1_scale * -posZ + dist2_scale *
                                     poni1_expr="-posZ * poni1_scale + posZ_offset",
                                     poni2_expr="-posY * poni2_scale + posY_offset",
                                     rot1_expr="rot1",
                                     rot2_expr="rot2",
                                     rot3_expr="0.0")



#Defines the bounds for some variables
bounds4 = {"dist": (0.025, 0.035),
           "poni1_scale": (-1.0,1.0),
           "poni2_scale": (-1.0,1.0),
           "posZ_offset": (-1.0,1.0),
           "posY_offset": (-1.0,1.0),
           "rot1": (-0.1,0.1),
           "rot2": (-0.1,0.1),
           "dist1_scale":(-5.0,5.0),
           "dist2_scale":(-5.0,5.0),
          }


param4 = (gonioref3.nt_param(*gonioref3.param))._asdict()


gonioref4 = GoniometerRefinement(param4, #initial guesses from previous steps results
                                 pos_function=get_pos,
                                 trans_function=goniotrans4,
                                 bounds=bounds4,
                                 detector=frelon, wavelength=wavelength)


gonioref4.single_geometries = gonioref3.single_geometries.copy()
print(gonioref4)
```

In [ ]:

```
for image in image_files:
    fimg = fabio.open(image)



    basename = os.path.splitext(fimg.filename)[0]


    which_eta = 'pos_'+basename.split('_')[-3]
    print(basename, which_eta)



    sg =gonioref4.new_geometry(which_eta, image=fimg.data, metadata=fimg.filename, control_
                               geometry=gonioref3.get_ai(gonioref3.single_geometries[which_e
                                calibrant=calib)



    sg.control_points.calibrant = calib
    sg.geometry_refinement.wavelength = wavelength

    print(sg.label," Detector Position: ",sg.get_position())
    print(sg.geometry_refinement)
    print()



print("Filled refinement object:")
print(gonioref4)
```

In [ ]:

```
# Repeat the refinement for determining the local minimum


i=0
while i<6:
    gonioref4.refine2("slsqp", eps=1e-13, maxiter=100000000, ftol=1e-12)
    i=i+1
```

In [ ]:

```
# Check the calibration results...

def print_geo4(key):
    print("expected")
    print(gonioref.single_geometries[key].geometry_refinement)
    print("refined")
    print(gonioref4.get_ai(gonioref.single_geometries[key].get_position()))


print_geo4("pos_0")
print_geo4("pos_10")
print_geo4("pos_13")
print_geo4("pos_16")
```

Step 5: Refinement II

Repeat of Step 3.

In [ ]:

```
param5 = (gonioref4.nt_param(*gonioref4.param))._asdict()

# Bounds are inherited from previous calibration step

gonioref5 = GoniometerRefinement(param5, #initial guesses from previous steps results
                                 pos_function=get_pos,
                                 trans_function=goniotrans4,
                                 bounds=bounds4,
                                 detector=frelon, wavelength=wavelength)

gonioref5.single_geometries = gonioref4.single_geometries.copy()
print(gonioref5)
```

In [ ]:

```
for image in image_files:
    fimg = fabio.open(image)

    basename = os.path.splitext(fimg.filename)[0]

    which_eta = 'pos_'+basename.split('_')[-3]
    print(basename, which_eta)


    sg =gonioref5.new_geometry(which_eta, image=fimg.data, metadata=fimg.filename, control_
                               geometry=gonioref4.get_ai(gonioref4.single_geometries[which_e
                               calibrant=calib)
    sg.control_points.calibrant = calib
    sg.geometry_refinement.wavelength = wavelength

    print(sg.label," Detector Position: ",sg.get_position())
    print(sg.geometry_refinement)
    print()


print("Filled refinement object:")
print(gonioref5)
```

In [ ]:

```
# Repeat the refinement for determining the local minimum

i=0
while i<6:
    gonioref5.refine2("slsqp", eps=1e-13, maxiter=100000000, ftol=1e-12)
    i=i+1
```

In [ ]:

```
# Check the calibration results...

def print_geo5(key):
    print("expected")
    print(gonioref.single_geometries[key].geometry_refinement)
    print("refined")
    print(gonioref5.get_ai(gonioref.single_geometries[key].get_position()))

print_geo4("pos_0")
print_geo4("pos_10")
print_geo4("pos_13")
print_geo4("pos_16")

# Save the refined calibration in ASCII format
gonioref5.save("multipanel_geometry_all.json")

print("Refined calibration execution time: "+str(time.time() - start_time)+" seconds")
```

Step 6: Analysis

- 1D azimuthal integration & 2D polar decomposition plots.
- Calculation of refined motor positions and derivation of errors with respect to experimental observations.
- Conversion from pyFAI to FABLE/ImageD11 geometry, production of ImageD11-type parameter files.

In [ ]:

```
#Reload all images, for extrapolating the refined calibration to the omitted images...

all_files=[]
image_files=[]


for f in os.listdir(im_dir):
    if f.split('.')[-1] == 'tif':
            all_files.append(im_dir + f);

print('Number of loaded images: '+str(len(all_files)))


image_files = [i for i in all_files if i.split('.')[-1] == 'tif']
image_files.sort()


# Restore the translation table setting (i.e. the refined calibration) from the file

transtable = Goniometer.sload("multipanel_geometry_all.json")
transtable.detector.pixel1= 1.3e-6
transtable.detector.pixel2= 1.3e-6
transtable.detector.MAX_SHAPE=(2540,2140)
print("Translation table: \n",transtable)

# Complete motor positions list, including the images omitted from the calibration

mt = [(0.0058, 0.0), (0.0057, -0.001065), (0.002585, -0.005192), (-0.004931, 0.00305), (0.0
      (-0.001587, 0.005578), (-0.003495, -0.004628), (0.004286, 0.003907), (0.000535, -0.00
      (-0.001587, -0.005578), (0.005408, 0.002095), (-0.004931, -0.00305), (0.004286, -0.00
      (-0.003495, 0.004628), (0.000535, 0.00577)]

print("Motor pos: \n", mt)


# Create a multi-geometry object for all images in this refinement set:

multigeo = transtable.get_mg(mt)
multigeo.radial_range=(7, 16)
print(multigeo)

from pyFAI.method_registry import IntegrationMethod

#Selection of the methods for integrating
method = IntegrationMethod.parse("full", dim=1)
method2d = IntegrationMethod.select_one_available(("pseudo","histogram","cython"), dim=2)


# Integrate the set of images in a single run:

res = multigeo.integrate1d([fabio.open(fn).data for fn in image_files], 10000, method=metho

filename = "multipanel_geometry_all_1dint.xy"
f1 = open(filename, "w")
f1.write("\n")
f1.write("#  2theta intensity \n")
fmt = "%6f "*2 + " \n"
for i in range(len(res[0])):
    f1.write(fmt % ( res[0][i], res[1][i]))
f1.close()

# Display the result using matplotlib
fig, ax = subplots()
ax.plot(*res)
ax.set_xlabel(res.unit.label)
ax.set_ylabel("Intensity")
#ax.set_xlim(17, 22)
#ax.set_title("Zoom on the two first rings")

fig, ax = subplots(2, 1, figsize=(12,16))
jupyter.plot1d(*res,ax=ax[0])

res2d = multigeo.integrate2d([fabio.open(fn).data for fn in image_files], 1000,360)
jupyter.plot2d(res2d, ax=ax[1])
```

In [ ]:

```
#Display all images with associated calibration:

nimg = len(gonioref5.single_geometries)
fig,ax = subplots(nimg, 1, figsize=(8,nimg*3))
for i, sg in enumerate(gonioref5.single_geometries.values()):
    jupyter.display(sg=sg, ax=ax[i])
```

Generation of FABLE/ImageD11 parameter files

Conversion from pyFAI to ImageD11 geometry. Takes motor positons and the refined calibration result, and generates '.par' files, containing global parameters for each panel in ImageD11-formatting.

In [ ]:

```
# Statics: Load refined calibration parameters
panel_fov = frelon.shape #transposed!!
dist = gonioref5.param[0]
poni1_scale = gonioref5.param[1]
posY_offset = gonioref5.param[2]
poni2_scale = gonioref5.param[3]
posZ_offset = gonioref5.param[4]
rot1 = gonioref5.param[5]
rot2 = gonioref5.param[6]
rot3 = 0.0
dist1_scale = gonioref5.param[7]
dist2_scale = gonioref5.param[8]
```

In [ ]:

```
# Save .par files in ImageD11 formatting

os.mkdir('ImD11_pars')
os.chdir('/home/esrf/kutsal/desy_oct21_analysis_ann2_ep1_nf2/single_panel_ponis/testing/ImD

mt_ref=[]

del_x = []
del_z = []
del_y = []


print('The refined motor positions calculated from the refined calibration result\n')
print('Panel no.  RMP_y (mm)  RMP_z (mm)\n')

for i,(posY, posZ) in motorpos_list:

    posY = posY*1e-3 #now in m
    posZ = posZ*1e-3 #now in m

    dist_exp = eval(goniotrans4.dist_expr)
    poni1_exp = eval(goniotrans4.poni1_expr)
    poni2_exp = eval(goniotrans4.poni2_expr)

    ImageD11 = {}
    ImageD11["wavelength"] = float(calib.wavelength*1e10)
    ImageD11["distance"] = dist_exp/cos(rot1)/cos(rot2)*1e6 #Convert to um for ImD11 format
    ImageD11["y_size"] = frelon.pixel2*1e6 #Convert to um for ImD11 formatting
    ImageD11["z_size"] = frelon.pixel1*1e6 #Convert to um for ImD11 formatting
    ImageD11["y_center"] = (poni2_exp - dist_exp * tan(rot1))/float(frelon.pixel2)
    ImageD11["z_center"] = (poni1_exp + dist_exp * tan(rot2)/cos(rot1))/float(frelon.pixel1
    ImageD11["tilt_x"] = rot3
    ImageD11["tilt_y"] = rot2
    ImageD11["tilt_z"] = -rot1
    ImageD11["o11"] = 1
    ImageD11["o12"] = 0
    ImageD11["o21"] = 0
    ImageD11["o22"] = -1

    #Below are for my own convenience. Take out for general distribution...
    ImageD11["cell__a"] = 2.866
    ImageD11["cell__b"] = 2.866
    ImageD11["cell__c"] = 2.866
    ImageD11["cell_alpha"] = 90.0
    ImageD11["cell_beta"] = 90.0
    ImageD11["cell_gamma"] = 90.0
    ImageD11["cell_lattice_[P,A,B,C,I,F,R]"] = 'I'
    ImageD11["omegasign"] = 1
    ImageD11["chi"] = 0.0
    ImageD11["fit_tolerance"] = 0.005

    outfile = 'pos_'+str(i)+'_pycalib.par'
    f1 = open(outfile,'w')


    for key in sorted(ImageD11):
        #print("{0:s}: {1:g}".format(key, ImageD11[key]))
        fmt = str(key)+' '+ str(ImageD11[key])+'\n'
        f1.write(fmt)
    f1.close()


    mtref_z = (ImageD11["z_center"]-panel_fov[1]*0.5)* frelon.pixel1*-1
    mtref_y = (ImageD11["y_center"]-panel_fov[0]*0.5)* frelon.pixel1*-1

    mt_ref.append((i,(mtref_y,mtref_z)))

    del_x.append((dist_exp-dist)*1e6) #in microns
    del_z.append((mtref_z-posZ)*1e6) #in microns
    del_y.append((mtref_y-posY)*1e6) #in microns

    print i, mtref_y*1e3, mtref_z*1e3 #in millimeters


# Calculated error of detector motor pos. in 3D
print('Average error in x_L position: ',np.mean(del_x)*1e3,' mm with st.dev. of ',np.std(de
print('Average error in y_L position: ',np.mean(del_y)*1e3,' mm with st.dev. of ',np.std(de
print('Average error in x_L position: ',np.mean(del_z)*1e3,' mm with st.dev. of ',np.std(de


ylab_list=[]
zlab_list=[]
for i,(y,z) in mt_ref:
    ylab_list.append(y)
    zlab_list.append(z)


# Calculated FoV of the compound image
fov_big_h = (abs(max(ylab_list))+abs(min(ylab_list)))/frelon.pixel1+panel_fov[1]
fov_big_v = (abs(max(zlab_list))+abs(min(zlab_list)))/frelon.pixel1+panel_fov[0]

print('FoV of the compound image: hor= ',fov_big_h,',  vertical= ',fov_big_v' pixels\n')
print
print("Total execution time: "+str(time.time() - start_time)+" seconds")
```

Technical
University of
Denmark

Fysikvej, Building 307
2800 Kgs. Lyngby
Tlf. 4525 1700

www.fysik.dtu.dk